

Branislav Avramov

DYNAMICAL EVOLUTION OF MASSIVE BLACK HOLES  
IN GALACTIC NUCLEI

Heidelberg  
2021

Dissertation  
submitted to the  
Combined Faculties for the Natural Sciences and for Mathematics  
of the Ruperto-Carola University of Heidelberg, Germany  
for the degree of  
Doctor of Natural Sciences

Put forward by

Branislav Avramov

born in: Zrenjanin, Serbia

Oral examination: 22<sup>nd</sup> July 2021

DYNAMICAL EVOLUTION OF MASSIVE BLACK HOLES  
IN GALACTIC NUCLEI

Referees:

Apl. Prof. Dr. Andreas Just  
Prof. Dr. Ralf Klessen

---

## ABSTRACT

---

In this work, I investigate the dynamical evolution of supermassive black hole (SMBH) binaries and triples using high-resolution  $N$ -body simulations. Starting from cosmological initial conditions, I characterize the effects of stellar dynamics on the formation and evolution of SMBH binaries. I perform numerical tests and benchmarks of the novel  $N$ -body code  $\varphi$ -GRAPE-hybrid and discuss how numerical parameters affect the evolution of SMBH binaries. I then simulate a hard SMBH binary system embedded in a triaxial and gas-poor galaxy merger remnant. I investigate the properties of loss cone stars that interact strongly with the SMBH binary and find that the summed energy changes of these stars match very well with the overall binary energy change, demonstrating that stellar interactions are the primary drivers of SMBH binary hardening in triaxial, gas-poor systems. I also investigate the orbital and phase-space properties of these stars and distinguish three different populations based on their apocenter. Then, I investigate the population of SMBH triple systems in the IllustrisTNG100-1 cosmological simulation. Using the tree code `bonsai2`, I perform zoom simulations of six of these triple SMBH candidates. I then present the orbital evolution of the black holes following the mergers of their host galaxies and examine prospects for their coalescence.

---

## ZUSAMMENFASSUNG

---

In der vorliegenden Arbeit untersuche ich mithilfe hochauflösender  $N$ -Körper-Simulationen die dynamische Entwicklung supermassereicher Schwarzer Löcher (engl. "supermassive black hole", kurz "SMBH") in Binär- und Dreifachsystemen. Ausgehend von kosmologisch motivierten Anfangsbedingungen charakterisiere ich die Auswirkungen der stellaren Dynamik auf die Entstehung und Entwicklung von SMBH-Binärssystemen. Ich führe numerische Tests sowie Benchmarks-Tests des neuartigen  $\varphi$ -GRAPE-Hybrid- $N$ -Körper-Codes durch und diskutiere, wie numerische Parameter die Entwicklung von SMBH-Binärssystemen beeinflussen. Dann simuliere ich ein hartes SMBH-Binärssystem, das in einem triaxialen und gasarmen Überrest einer Galaxienverschmelzung eingebettet ist. Ich untersuche die Eigenschaften von Sternen im Verlustkegel, die stark mit dem SMBH-Binärssystem wechselwirken und finde, dass die summierten Energieänderungen dieser Sterne sehr gut mit der gesamten Energieänderung des Binärsystems übereinstimmen, was zeigt, dass stellare Wechselwirkungen die Haupteinflussfaktoren für die Schrumpfung von SMBH-Binärssystemen in triaxialen, gasarmen Galaxien sind. Ich untersuche auch die Bahn- und Phasenraumeigenschaften dieser Sterne und unterscheide drei verschiedene Populationen basierend auf ihrem Apozentrum. Im letzten Teil der Arbeit untersuche ich dann die Population von SMBH-Dreifachsystemen in der kosmologischen Simulation "IllustrisTNG100-1". Unter Verwendung des Baum-Codes `bonsai2` führe ich Zoom-Simulationen von sechs dieser SMBH-Dreifach-Kandidaten durch. Anschließend stelle ich die orbitale Entwicklung der Schwarzen Löcher nach der Verschmelzung ihrer Wirtsgalaxien dar und untersuche die Aussichten für ihre Verschmelzung.

---

## CONTENTS

---

<b>Contents</b>	<b>v</b>
<b>List of abbreviations</b>	<b>vii</b>
<b>1 Introduction</b>	<b>3</b>
<b>2 Supermassive black holes</b>	<b>7</b>
2.1 Spin . . . . .	8
2.2 Accretion . . . . .	9
2.3 Formation . . . . .	10
2.4 Effect on the host galaxy . . . . .	11
2.4.1 Active Galactic Nuclei and black hole feedback . . . . .	11
2.4.2 Scaling relations . . . . .	12
2.5 Dynamics in galactic nuclei . . . . .	12
2.5.1 Captures and tidal disruptions . . . . .	12
2.5.2 The loss cone . . . . .	13
2.5.3 Non-spherical nuclei . . . . .	14
<b>3 Gravitational waves &amp; the Post-Newtonian expansion</b>	<b>17</b>
3.1 Gravitational wave spectrum . . . . .	18
3.2 Observatories . . . . .	19
3.2.1 Laser Space Interferometer Antenna . . . . .	19
3.2.2 Pulsar Timing Arrays . . . . .	20
3.2.3 TianQin . . . . .	21
3.3 Post-Newtonian expansion . . . . .	22
3.3.1 Validity and accuracy . . . . .	23
3.3.2 Equations of motion . . . . .	24
3.3.3 Energy and angular momentum . . . . .	25
3.3.4 Orbital elements . . . . .	27
3.3.5 Spinning binaries . . . . .	29
<b>4 Binary supermassive black holes</b>	<b>30</b>
4.1 Electromagnetic observations . . . . .	30
4.2 Dynamical evolution of SMBH binaries . . . . .	32
4.2.1 Pairing phase . . . . .	33
4.2.2 Stellar hardening . . . . .	35
4.2.3 Gravitational wave inspiral . . . . .	38

4.3	Final parsec problem	38
4.4	Solutions to the final parsec problem	39
4.4.1	Collisionless loss cone refilling	39
4.4.2	Gas and accretion	41
4.4.3	Massive stellar perturbers	42
4.4.4	Triple systems	42
4.4.5	Other effects	43
4.5	Khan et al. (2016)	43
<b>5</b>	<b>Numerical description</b>	<b>46</b>
5.1	Force calculation	47
5.1.1	Direct N-body	47
5.1.2	Self-consistent field method	48
5.1.3	Tree algorithm	50
5.2	Numerical codes	51
5.2.1	$\varphi$ -GRAPE and $\varphi$ -GPU	51
5.2.2	AR-CHAIN	53
5.2.3	Bonsai	55
5.2.4	ETICS	55
5.2.5	$\varphi$ -GRAPE-hybrid	56
5.3	Numerical tests and benchmarks of the $\varphi$ -GRAPE-hybrid code for galactic simulations	57
5.3.1	Benchmarks	58
5.3.2	Orders in the multiple expansion	61
5.3.3	Gravitational softening	62
5.3.4	Black hole integration timestep	66
5.3.5	Centering strategy	69
5.3.6	Summary and conclusions	71
<b>6</b>	<b>Numerical investigation of three-body scattering events with a SMBH binary in the Post-Newtonian regime</b>	<b>73</b>
6.1	Introduction	73
6.2	Initial conditions and setup	75
6.3	Initial velocity condition	76
6.4	Results	78
6.4.1	Merger rate	78
6.4.2	Pericenter distribution	79
6.4.3	Energy balance	80
6.4.4	PN energy correction terms	82
6.5	Summary and conclusions	85
<b>7</b>	<b>Properties of loss cone stars in a cosmological merger remnant</b>	<b>88</b>
7.1	Introduction	88
7.2	Initial conditions	89
7.2.1	Numerical parameters and performance	90
7.3	Results	91
7.3.1	SMBH binary properties	91
7.3.2	Merger remnant properties	93

7.3.3	Properties of centrophilic stars . . . . .	98
7.4	Discussion . . . . .	110
7.4.1	Inclination of loss cone stars . . . . .	110
7.4.2	Hybrid integration approach . . . . .	110
7.4.3	Merger timescale and numerical parameters . . . . .	111
7.5	Summary and conclusions . . . . .	111
<b>8</b>	<b>Dynamical evolution of massive black hole triplets in IllustrisTNG</b>	<b>113</b>
8.1	Introduction . . . . .	113
8.2	Illustris-TNG . . . . .	114
8.3	Selection criteria . . . . .	116
8.4	Numerical setup and initial conditions . . . . .	118
8.4.1	Data extraction . . . . .	118
8.4.2	Galaxy modeling . . . . .	120
8.4.3	Initialization of N-body runs . . . . .	124
8.5	Results . . . . .	125
8.6	Discussion . . . . .	129
8.7	Summary and conclusions . . . . .	131
<b>9</b>	<b>Summary and future outlook</b>	<b>132</b>
9.1	Summary . . . . .	132
9.2	Future outlook . . . . .	134
	<b>Acknowledgments</b>	<b>136</b>
	<b>Publications</b>	<b>138</b>
	<b>Bibliography</b>	<b>139</b>



---

---

## LIST OF ABBREVIATIONS

---

<b>AGN</b>	Active galactic nuclei
<b>AR</b>	Algorithmic regularization
<b>CPU</b>	Central Processing Unit
<b>CUDA</b>	Compute Unified Device Architecture
<b>DCBH</b>	Direct Collapse Black Hole
<b>E-ELT</b>	European Extremely Large Telescope
<b>EHT</b>	Event Horizon Telescope
<b>EM</b>	Electromagnetic
<b>EMRI</b>	Extreme mass-ratio inspiral
<b>ETICS</b>	Expansion Techniques in Collisionless Systems
<b>FoF</b>	Friends of friends
<b>FPP</b>	Final Parsec Problem
<b>GMR</b>	Galaxy merger remnant
<b>GPU</b>	Graphics Processing Unit
<b>GR</b>	General Relativity
<b>GRAPE</b>	GRAvity PipE
<b>GW</b>	Gravitational wave
<b>JWST</b>	James Webb Space Telescope
<b>IPTA</b>	International pulsar timing array
<b>ISCO</b>	Inner-most circular orbit
<b>KS</b>	Kustaanheimo & Stiefel
<b><math>\Lambda</math> CDM</b>	Lambda Cold Dark Matter
<b>LIGO</b>	Laser Interferometer Gravitational-Wave Observatory
<b>LISA</b>	Laser Interferometer Space Antenna
<b>MEX</b>	Multipole expansion method
<b>MPI</b>	Message Passing Interface
<b>NANOGrav</b>	Nanohertz Observatory for Gravitational waves
<b>PN</b>	Post Newtonian
<b>PTA</b>	Pulsar Timing Array
<b>SMBH</b>	Supermassive black hole
<b>SED</b>	Spectral Energy Distribution
<b>S-0</b>	Spin-orbit
<b>SPH</b>	Smooth particle hydrodynamics
<b>S-S</b>	Spin-spin
<b>TFlops</b>	Trillion floating point operations per second
<b>TNG</b>	The next generation
<b>TPM</b>	Tree particle-mesh
<b>VLBA</b>	Very Long Baseline Array
<b>VLBI</b>	Very Long Baseline Interferometry

---

## INTRODUCTION

---

Black holes are some of the most exotic objects known in the Universe. They are massive and extremely compact objects, occupying a region of space-time where the escape velocity due to their gravity exceeds the speed of light. As a result, their boundary, termed the event horizon, represents the point of no return for all matter and photons that cross it. The speculation on their existence dates back to the 18. century, but it was not until the formulation of Einstein's Theory of General Relativity (GR), that their existence was considered as a real possibility by the wide scientific community. Schwarzschild was the first to derive an exact solution for Einstein's equations of GR and derived the metric that describes the space-time surrounding a spherically symmetric body of mass  $M$  in a vacuum. This solution, now known as the Schwarzschild solution, exhibited a singularity at radius:

$$R_{sch} = \frac{2GM}{c^2}, \quad (1.1)$$

where  $G$  is the gravitational constant and  $c$  is the speed of light. As we know today, this singularity, termed the Schwarzschild radius, corresponds to the event horizon of an electrically uncharged, spherically symmetric and non-rotating black hole.

Since then, a wealth of observational evidence has pointed to the existence of black holes in different mass ranges. The stellar-mass black holes have masses in the range of  $3 M_{\odot} \lesssim M \lesssim 50 M_{\odot}$  and are formed through the collapse of massive stars at the end of their lifetime. While both the lower and upper boundaries of stellar black hole masses are not well constrained, it is generally thought that a gap must exist in the mass spectrum of black holes between  $\sim 50 - 100 M_{\odot}$ , in the regime of pair-instability supernovae. During a pair-instability supernova the entire star is disrupted, leaving no remnant behind, and consequently, no black hole. The second mass range comes in the form of supermassive black holes (hereafter SMBH), with masses in the range  $10^5 M_{\odot} \lesssim M \lesssim 10^{10} M_{\odot}$ . These black holes reside in the centers of galaxies, and are the main subject of this thesis. They are formed from massive black hole seeds and grow to their large size either through accretion or mergers with other black holes. A third black hole mass range, of masses in between these two regimes:  $10^2 M_{\odot} \lesssim M \lesssim 10^5 M_{\odot}$  consists of objects often termed the intermediate mass black hole (IMBH). These black holes are too massive to form through standard stellar collapse. Instead, they are thought to form

through direct collapse of gas clouds at high redshift (Latif et al., 2013), through the collapse of first generation, metal-free (Population III) stars (Madau and Rees, 2001; Spera and Mapelli, 2017), or in dense stellar environments such as global clusters, via runaway mergers (Portegies Zwart and McMillan, 2002; Mapelli, 2016). While the existence of this population has long been assumed, conclusive observational evidence remained illusive until recently when LIGO (Laser Interferometer Gravitational-Wave Observatory) and Virgo detected a  $142 M_{\odot}$  mass black hole through gravitational waves (GW, Abbott et al., 2020b).

Supermassive black holes were first proposed as central objects of quasars, as objects that are responsible for their large energy output and luminosity (Zel'dovich and Novikov, 1964; Salpeter, 1964; Robinson et al., 1965). Infalling matter spirals towards the black hole and feeds it through the process of accretion. Since accretion is very efficient in energy generation, the infalling matter emits radiation in a wide range of wavelengths. Since then, this energetic process has been linked to a wide array of objects known as Active Galactic Nuclei (AGN), which also include quasars. The existence of SMBHs has further been proven by measurements of stellar dynamics in galaxy centers. These measurements have shown that SMBH reside not only in AGN, but also in the centers of the vast majority of galaxies. The presence of the SMBH then affects both its immediate environment, as well as large-scale galactic properties. Measurements of the stellar velocity dispersion, bulge mass and total stellar mass have revealed a close correlation between these properties and the mass of the central black hole, pointing to a co-evolution of the black hole and its host galaxy (Kormendy and Ho, 2013). As a result, proper understanding of galaxy formation and evolution necessitates proper treatment of SMBH growth and AGN feedback.

The recent developments in GW astronomy have opened a new window into the Universe. Coalescing black hole binaries, which are characterized by their strong gravitational interaction, are obvious choices for progenitors of detectable GW signals. The first few observational runs of the LIGO/Virgo collaborations have already significantly expanded our knowledge of black hole demographics and merger rates, and have started to put robust constraints on black hole spin parameters and both lower and upper mass boundaries of stellar mass black holes (Abbott et al., 2019). However, signals from merging SMBHs fall outside of the frequency sensitivity ranges from these missions. Instead, these lower frequency signals must be detected with space-based interferometers, or ground-based precise pulsar timing measurements. For this reason, the Pulsar Timing Arrays (PTA) have already been in operation for more than a decade. While no conclusive detections have been made so far, the constantly improving accuracy of the measurements is already constraining the theoretical estimates of the stochastic GW background of SMBH binary mergers (Arzoumanian et al., 2020). In the next few decades, upcoming space-based missions such as LISA (Laser Space Interferometer Antenna, Amaro-Seoane et al., 2017) and TianQin (Luo et al., 2016) promise to shed light on the massive black hole population by directly detecting GW signals from their mergers.

The rapid development of GW astronomy has put a spotlight on theoretical modeling of close SMBH binaries in order to make robust predictions for detection rates of future GW observations. The dynamical evolution of SMBH binaries can be described in three main phases (Begelman et al., 1980). Following a galactic merger, the two black holes that were residing in the centers sink towards the center of the potential due to the effect of dynamical friction from the surrounding stars. Once their mutual separation sufficiently decreases, the black holes form a Keplerian binary system. At this point, along with dynamical friction, individual interactions with stars can extract energy from the binary via the gravitational slingshot effect. As the binding

energy of the binary increases, dynamical friction becomes less effective. In the second phase, termed the hardening phase, the main driver of the binary evolution become three-body stellar interactions. Stars that reach separations comparable to the binary semi-major axis come from a region in phase space known as the loss cone. These loss cone stars can extract energy and angular momentum from the binary, and are ejected with velocities comparable to the binary orbital velocity. Finally, once the separation between the two black holes decreases to  $\sim 0.01$  pc, the binary enters the third and final phase of its evolution. At this point, GW emission becomes the dominant mechanism of energy loss, and the binary mergers on a Peters timescale (Peters, 1964).

Direct N-body simulations of galaxy mergers are the most accurate method of studying the evolution of massive black hole binaries, but they require large amounts of computer resources. Nevertheless, the emergence of improved computer hardware, as well as parallel and GPU (Graphics Processing Unit) computing on large computer clusters have allowed for numerical simulations to study these systems with increasing accuracy. Studies at the start of the 21<sup>st</sup> century have shown that in spherical systems, the loss cone becomes emptied throughout the binary evolution, leading to the stalling of the binary at parsec separations in the hardening phase of the merger. This issue become known as the Final Parsec Problem (FPP, Berczik et al., 2005), and presented a theoretical bottleneck that estimated SMBH merger timescales longer than the Hubble time, posing a problem for any future GW detections. However, later studies have found that abandoning the assumption of spherical symmetry results in natural and efficient repopulation of the loss cone. Namely, in more realistic, triaxial systems, a large fraction of stellar orbits are centrophilic, and can get arbitrarily close to the binary, providing a constant supply of stars that can extract energy from it, and resolving the FPP (Preto et al., 2011; Khan et al., 2011). Apart from this, a number of other solutions to the FPP have since been proposed, such as the effect of gas clumps and molecular clouds (Goicovic et al., 2017, 2018), the presence of massive stellar clusters (Bortolas et al., 2018b; Arca Sedda et al., 2019) and the presence of a third black hole (Bonetti et al., 2018). As a result, the FPP is today thought of as a consequence of simplifying approximations or insufficient resolution, and merger timescales of SMBH binaries are now estimated to be  $t \lesssim 1$  Gyr (Rantala et al., 2017; Khan et al., 2018a).

The emergence of modern hydrodynamical cosmological simulations of structure and galaxy formation such as the EAGLE simulation (Schaye et al., 2015), Illustris (Vogelsberger et al., 2014), IllustrisTNG (Springel et al., 2018) and Horizon-AGN (Dubois et al., 2014) has opened the door to studies of SMBH mergers that do not assume idealized, equilibrium initial conditions, but rather take into account the full impact of the cosmological environment. This allows for modeling of the entire evolution of an SMBH binary, starting from cosmologically formed galaxy mergers, down to the GW-induced coalescence, covering a large range of scales. Additionally, the use of cosmological simulations as a starting point for higher resolution N-body simulations enables self-consistent investigation of different loss cone repopulation mechanisms and insight into the population of merging SMBHs in a large, cosmological volume.

The thesis is structured in the following way. In Chapter 2, we give an overview of the properties of massive black holes, including their formation, accretion, spin and their relation to the host galaxy. We also introduce the loss cone and discuss the loss cone refilling mechanism in non-spherical nuclei. Then, in Ch. 3 we give a brief summary on gravitational waves from an observational perspective, and detail the current and upcoming GW observational efforts that could detect SMBH binary signals. We then give an overview of Post-Newtonian (PN) theory and describe the formalism used to account for relativistic effects throughout this thesis. We

present the PN-corrected equations of motion of compact binaries up to order PN2.5, describe the relativistic corrections to the binary energy and angular momentum and give an overview of Keplerian orbital elements corrected for PN effects. Then, in Ch. 4 we describe the topic of binary SMBHs in the context of electromagnetic (EM) observations, as well as theoretical modeling. In Ch. 5 we present the numerical methods and codes used in this work, and present the results of the testing and benchmarking procedure we performed using the novel N-body code  $\varphi$ -GRAPE-hybrid, focusing on its application for the study of SMBH binary systems. Ch. 6 contains the results of our three-body scattering experiments, where we investigate energetic interaction of stars with a hard, SMBH binary. We present in Ch. 7 our study on the properties of loss cone stars interacting with an SMBH binary in a triaxial, gas-poor galaxy merger remnant originating from cosmological initial conditions. Then, in Ch. 8 we investigate the dynamical evolution of massive black hole triplets, using the cosmological simulation IllustrisTNG as a starting point for higher-resolution simulations. We conclude in Ch. 9, where we summarize and discuss our findings.

---

SUPERMASSIVE BLACK HOLES

---

Supermassive black holes are widely accepted today as an ever-present and crucial component of the vast majority of galaxies (Magorrian et al., 1998; Vestergaard et al., 2008). Their existence was first proposed in the 20<sup>th</sup> century after the discovery of the first quasar (Schmidt, 1963). The extremely large quasar luminosities and energy output posed a mystery as to what process could power these objects. Pioneering works (Zel’dovich and Novikov, 1964; Salpeter, 1964; Robinson et al., 1965) challenged the previously accepted paradigm and dared to propose an extremely compact and massive object at the center which powers quasars through the process of accretion. The mass of the central accreting object was inferred under the assumption of Eddington-limited luminosity (see Eq. 2.3), suggesting an object of mass  $M \sim 10^6 M_\odot$ . Accretion posed a natural solution to the problem of quasar luminosities since the efficiency by which the rest-mass of matter is converted into energy during accretion depends on the compactness of the central object. For an object such as an SMBH, this efficiency is on the order of 10% (Di Matteo et al., 2019; King et al., 2008; Zhang and Lu, 2017). This makes accretion far more efficient at energy generation than any other known process, including nuclear fusion processes that power stars, which release about 0.7% of their rest-mass as energy. As we know today, this is precisely why accretion is responsible for some of the brightest and most energetic phenomena in the Universe. At the turn of the century the claim of massive compact objects at the centers of galaxies, once regarded as outlandish, was finally accepted as fact when studies showed that such an object exists also in our own backyard, the center of the Milky Way (e.g. Ghez et al., 1998; Genzel et al., 2003). This discovery, which was awarded the Nobel prize twenty years later, analyzed stellar orbits around the radio source SgrA\* and conclusively showed that an object with mass  $M = 4 \times 10^6 M_\odot$  is contained within a region of 125 AU, in line with the SMBH hypothesis. After this, any slim remaining doubt about the existence of these objects was washed away by the ultra-high angular resolution observation of radio emission from the M87 SMBH (see Fig. 2.1) by the Event Horizon Telescope (EHT Akiyama et al., 2019a,b,c,d,e,f).

Generally, any compact object with mass  $10^5 M_\odot \lesssim M_{\text{BH}} \lesssim 10^{10} M_\odot$  is considered to be an SMBH (Ferrarese and Ford, 2005). Quasar searches have shown that SMBH masses can span a wide range of values across cosmic time  $10^6 M_\odot \lesssim M_{\text{BH}} \lesssim 10^{10} M_\odot$  (Kelly et al., 2008). A particularly interesting aspect is the detection of quasars powered by accretion onto SMBHs with masses of  $10^9 - 10^{10} M_\odot$  at redshifts  $z \sim 7.5$  (Bañados et al., 2018; Yang et al., 2020). The resulting evidence of massive black holes already within 0.8 Gyr since the Big Bang has

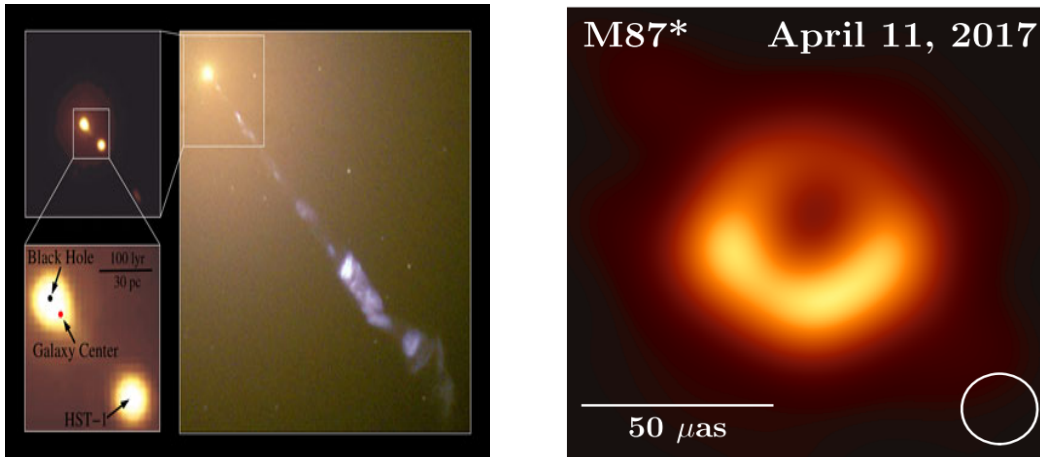


**Figure 2.1:** Left: Hubble image of M87, with the characteristic blue jet. The position of the SMBH is marked in the bottom-left. Credit: NASA/ESA/STSC/LAURA and D. Batcheldor and E. Perlman. Right: The M87\* detection, as captured by the EHT. Pictured is the shadow of the SMBH at the center of M87. Image credit: EHT collaboration, [Akiyama et al. \(2019a\)](#).

challenged previous SMBH formation mechanisms and pointed to a much faster growth rate of these objects than what was previously thought.

In this chapter, I will aim to introduce SMBHs in both the context of their galactic environment, as well as their own intrinsic properties. More specifically, I will introduce the black hole spin parameter, discuss different SMBH formation mechanisms, as well as the connection between the black hole and its host galaxy, in terms of feedback, scaling relations and dynamics.

## 2.1 SPIN

General relativity tells us that a stable, isolated black hole (either stellar, supermassive or of other mass ranges) can be completely characterized by a distant observer by finding its conserved quantities like mass-energy  $M$ , linear momentum  $\vec{p}$ , angular momentum  $\vec{J}$ , position  $\vec{X}$  and electric charge  $Q$ . Together, these quantities represent the 11 degrees of freedom a black hole can have (the vector quantities represent three degrees of freedom each). Appropriate choice of reference frame coordinates can remove 8 of these 11 degrees of freedom, leaving only three quantities that are independent of the choice of a coordinate system: mass, amplitude of angular momentum (spin) and charge. This conjecture is better known as the "*no hair theorem*". While the no hair theorem still lacks rigorous mathematical proof, it is widely accepted as fact, and has been expanded to include non-isolated black holes in astrophysical scenarios as well ([Gürlebeck, 2015](#)). Additionally, recent GW detections showed the first evidence in favor of black holes being "hairless" ([Isi et al., 2019](#)).

If we assume that black holes really have no "hair" (meaning, they have no other distinguishing features other than the 3 above mentioned quantities), then black holes outside of the event horizon would be astonishingly simple objects. In essence, they would be objects that are completely described by only three parameters:  $(M, J, Q)$ , the minimum set of parameters required to describe conservation laws in classical physics ([Reynolds, 2020](#)). Furthermore, black holes of all masses are generally assumed to be chargeless, since any electric charge the black hole could have would be dissipated to the electrically neutral surroundings, leaving only mass

and spin as the relevant black hole parameters. This would make the Kerr metric of a rotating, chargeless black hole the preferred description for investigation of black hole space-times (Kerr, 1963).

Black hole spin is almost always characterized in terms of the dimensionless black hole spin parameter  $a$ :

$$a = \frac{Jc}{GM_{\text{BH}}^2}, \quad (2.1)$$

where  $J$  is the amplitude of the black hole angular momentum,  $c$  is the vacuum speed of light,  $G$  is the Newtonian gravitational constant and  $M_{\text{BH}}$  is the black hole mass. The value of this parameter can impact many black hole features, such as the event horizon radius which, in the case of a rotating Kerr black hole, is defined as (Reynolds, 2020):

$$r_{\text{evt}} = (1 + \sqrt{1 - a^2}) \frac{GM_{\text{BH}}}{c^2}. \quad (2.2)$$

With this relation we can notice a hard limit on  $a$ , which must be confined to the range of  $a \in (-1, 1)$ . Namely, as per Eq. 2.2, if a black hole were to have  $|a| > 1$ , the event horizon would be undefined and the singularity at the center of the black hole would be naked and exposed, violating the cosmic censorship theorem.

Most observational estimates of black hole spin come from measuring spin in accreting systems using the X-ray reflection method (Reynolds and Fabian, 2007), showing that less massive black holes with masses  $M < 3 \times 10^7 M_{\odot}$  have very high spin  $a > 0.9$ , while more moderate spin values are found for more massive black holes (Reynolds, 2020). Recently, GW detections have proven to be a valuable additional insight into the spins of stellar black hole binaries, and in stark contrast to the X-ray, the first two observing runs of LIGO/Virgo show very low spins for their detected binaries (Abbott et al., 2019), pointing to different populations in the spin parameter landscape.

## 2.2 ACCRETION

Matter infalling to the black hole possesses its own intrinsic angular momentum, and naturally forms an optically-thick disk around the black hole, often termed the *accretion disk* (Shakura and Sunyaev, 1973; Rees, 1984). Viscosity in the disk heats up the matter up to temperatures of  $10^4 - 10^5$  K, which will produce thermal emission in a wide range of wavelengths (Hickox and Alexander, 2018). Accretion is an incredibly efficient process of energy generation (5% – 40% of the gravitational energy is converted into radiation, depending on the spin of the black hole (Shapiro and Teukolsky, 1983), and this excess energy is then radiated away, resulting in emission from objects known as Active Galactic Nuclei. However, there is an upper limit to the maximum accretion rate a black hole can have, termed the Eddington limit.

Namely, in the case of main-sequence stars, Eddington derived an upper limit to the luminosity that a star can have, in order for the radiation pressure of photons emitted from the star to be balanced with the gravitational force (i.e. for the star to be in hydrostatic equilibrium). This limit is specified only by the stellar mass and is widely known as the Eddington luminosity:

$$L_{\text{Edd}} = \frac{4\pi M m_{\text{p}} c}{\sigma_{\text{T}}}, \quad (2.3)$$

where  $M$  is the stellar mass,  $m_p$  is the proton mass,  $c$  is the vacuum speed of light,  $G$  is the gravitational constant and  $\sigma_T$  is the Thomson electron scattering cross-section. As matter accretes to a black hole (assuming spherical symmetry for the sake of simplicity), the electromagnetic radiation that is released during accretion also exerts radiation pressure on the infalling matter. The luminosity that arises from accretion is proportional to the mass accretion rate,  $L = \eta \dot{M} c^2$ , where  $\eta$  is the accretion efficiency (typically = 0.1) and  $\dot{M}$  is the mass accretion rate. Therefore, in a similar fashion to stars, the Eddington luminosity can be used to define a simple upper limit to the maximum accretion rate a black hole can have, before the radiation pressure becomes dominant and blows away the surrounding matter, stopping accretion. This upper limit is called the Eddington limit:

$$\dot{M}_{\text{Edd}} = \frac{L_{\text{Edd}}}{\eta c^2}, \quad (2.4)$$

and was used to estimate formation timescales for massive black holes since the Big Bang.

### 2.3 FORMATION

The detection of a large number of quasars hosting massive black holes within the first 1 Gyr of the Universe has caused a significant paradigm shift and revolutionized our view on the formation mechanisms of these objects (Bañados et al., 2016). Standard accretion models were challenged, since it was not clear whether black holes can grow to such large masses in such a short amount of time solely through Eddington-limited accretion.

This raised questions about how and when did massive black hole *seeds* form, what were their masses and how did they grow in the early Universe to the massive black holes we detect (Volonteri, 2010). The masses of the seeds are dependent on the formation mechanism and range from  $10 - 10^5 M_\odot$ . The literature agrees on three broadly different formation mechanisms of the black hole seeds, detailed below (see Volonteri (2010); Volonteri and Bellovary (2012); Haiman (2013); Latif and Ferrara (2016) for reviews on the subject). The first mechanism is the most straight-forward, with the seeds being formed from the core collapse of Population III stars. These first generation, massive and metal-free stars would collapse into stellar mass black holes beyond the pair-instability gap at redshifts of  $z \sim 15 - 20$ . Within the second mechanism, the black hole seeds would form from subsequent mergers and gravitational collapse of stars within a dense stellar cluster at redshifts  $z \sim 10$ . Alternatively, they could also form from stellar-mass black hole clusters with large gas inflows (Davies et al., 2011; Lupi et al., 2014). The third formation scenario is known as the Direct Collapse Black Hole model (DCBH), within which a protogalactic gas cloud would either directly collapse into a black hole, or first form a supermassive star, with mass  $10^4 - 10^6 M_\odot$ , and then driven by general-relativistic instabilities, the supermassive star would collapse into a black hole of the same mass.

While the exact formation mechanism is still not known, it is expected that the next generation of both ground-based and space-based observations could shed light on the formation of black hole seeds. In terms of detectors of electro-magnetic radiation, the Square Kilometer Array in the radio domain (Weltman et al., 2020), the James Webb Space Telescope (JWST) (Smith and Bromm, 2019) and the European Extremely Large Telescope (E-ELT) in the optical and near-infrared (Gilmozzi and Spyromilio, 2007), as well as Athena and Lynx in the X-rays will be invaluable to detect earliest black holes and dimmest AGN (Canton et al., 2019; McGee et al., 2020). On the other side, next generation gravitational wave observatories such as the LISA mission (Amaro-Seoane et al., 2017), TianQin (Luo et al., 2016), the Einstein Telescope

(Punturo et al., 2010) and the Cosmic Explorer (Reitze et al., 2019) will provide a new window into the mergers of black holes on all mass scales (Valiante et al., 2021).

Since the seed formation mechanism affects the possible growth rates of each model, numerous pathways for efficient black hole growth have since been proposed in the literature, which could result in the billion-solar-mass black holes detected in the earliest quasars, depending on seed type. These pathways provide efficient solutions to the conundrum of the formation of high-redshift quasars, and include efficient black hole growth via multiple subsequent black hole mergers, super-Eddington accretion episodes (accretion at rates higher than the Eddington limit), as well as accretion at Eddington rates in the *chaotic* accretion paradigm (Di Matteo et al., 2019).

## 2.4 EFFECT ON THE HOST GALAXY

### 2.4.1 Active Galactic Nuclei and black hole feedback

The large amount of energy released during accretion result in very large luminosities of AGN (up to  $L_{\text{bol}} \approx 10^{48} \text{ erg s}^{-1}$ , Padovani et al. 2017), which can be detected up to very high redshift, making them the most powerful non-explosive objects in the universe (Hickox and Alexander, 2018). While nonthermal emission can be detected in different parts of the spectrum, most of the emission from an AGN is thermal and its spectral energy distribution (SED) is very broad and ranges from the Infra-red, all the way down to the Gamma-ray part of the electromagnetic spectrum. This broad range of emission profiles has led to a complex plethora of different classifications, types and flavours of AGN, referred to as the "AGN zoo". These can depend on the orientation of the AGN with respect to the detector, on the presence (or lack of) a relativistic jet, as well as many other effects (for a more detailed overview we refer the reader to a more comprehensive review, found in Padovani et al. 2017).

Despite the fact that the gravitational region of influence of a black hole is contained only to the very central region of a galaxy ( $r_{\text{infl}} \sim 1 \text{ pc}$ ), the enormous amount of released energy through AGN outflows can also affect the large-scale properties of the galaxy itself, through a process known as *AGN feedback*. AGN feedback represents in essence the impact on the properties and evolution of the host galaxy, and is now an essential component of any simulation of galaxy evolution. It can take place over many different spatial scales throughout the galaxy and take many different forms. Two different modes of feedback can be differentiated: the *quasar (radiative) mode*, where the energy released in AGN drives outflows of gas and expels it from the galaxy, and the *jet (kinematic) mode*, dominant in lower power AGN, where the jet plasma prevents the gaseous atmosphere from cooling and returning to the galaxy (Morganti, 2017). AGN feedback can also significantly impact the star formation rate of galaxies in different ways. Namely, at high galaxy masses, this feedback can transport gas out of massive halos. The loss of gas results in a decrease in the star-formation rate of the host galaxy, causing a discrepancy between the simulated halo mass fraction and the observed galaxy luminosity function (Volonteri and Bellovary, 2012). Additionally, observational evidence shows that episodes of increased star-formation are followed by increased AGN activity, pointing to the fact that the starbursts (or the supernovae that follow them) can have a significant impact on the fueling of the central black hole (Davies et al., 2007). Today, constructing accurate feedback models is a necessary, although arduous feat for any modeling. Modern cosmological simulations in particular require accurate feedback models in order to properly account for suppressed star formation in massive galaxies, caused by AGN feedback. A notable example of this is the IllustrisTNG suite of

cosmological simulations, which used an improved feedback model with respect to the original Illustris simulations, resulting in proper quenching of galaxies in high and intermediate mass halos (Pillepich et al., 2018b).

#### 2.4.2 *Scaling relations*

The close relation between an SMBH and its host galaxy is best demonstrated by the existence of a number of scaling relations that correlate the mass of the black hole with various large-scale properties of the galaxy. These relations are empirical, and while the literature agrees that they are in large part caused by the aforementioned AGN feedback, the physical processes governing them are not yet fully understood. Nevertheless, the tight correlations shown by these relations demonstrate that large-scale galaxy properties, such as velocity dispersion or bulge mass, are intrinsically linked to the properties of the central black hole, pointing to a co-evolution of the galaxy and its SMBH. The constantly improving measurements that constrain the relations to higher and higher accuracy have made it possible to estimate the black hole mass with a high degree of certainty, solely by observing various other galactic properties. This has proven to be an invaluable and widely used tool for objects where dynamical measurements of central black holes are not possible.

Within the wealth of literature on the subject, the most prominent and well studied scaling relation relates the black hole mass  $M_{\text{BH}}$  to the stellar velocity dispersion  $\sigma$ , termed the  $M_{\text{BH}} - \sigma$  relation. The equation takes the following form:

$$\log \frac{M_{\text{BH}}}{10^9 M_{\odot}} = \alpha + \beta \log \left( \frac{\sigma}{200 \text{ km s}^{-1}} \right), \quad (2.5)$$

where  $\alpha$  and  $\beta$  are the dimensionless relation parameters, constrained by observations. Least square fits performed by Kormendy and Ho (2013) give values of  $\alpha = -0.51 \pm 0.049$  and  $\beta = 4.377 \pm 0.290$ .

Other commonly used relations include relations between black hole mass and the total mass of the stellar bulge ( $M_{\text{BH}} - M_{\text{bulge}}$  relation, see e.g. Häring and Rix 2004), the local total stellar mass of the galaxy ( $M_{\text{BH}} - M_{\star}$  relation, see e.g. Shankar et al. 2019), and the luminosity of the host spheroid ( $M_{\text{BH}} - L_{\text{sph}}$  relation, see e.g. Graham and Scott 2013), among others. For a comprehensive and detailed review on the topic of scaling relations, I refer the reader to Kormendy and Ho (2013).

## 2.5 DYNAMICS IN GALACTIC NUCLEI

### 2.5.1 *Captures and tidal disruptions*

The SMBH situated at the center of the galaxy dynamically interacts with the surrounding stars, and can act as a sink, either accreting, or directly swallowing stars, thereby increasing its own mass. This process can happen in two ways. In the first one, during close approaches stars can be disrupted by tidal forces coming from the black hole. They become pulled apart, and the stellar matter is distributed within the surroundings and is gradually accreted by the black hole via the accretion disk. The radius at which this happens depends on the mass of the black hole and the properties of the star, and is known as the tidal disruption radius:

$$r_t = \left( \eta^2 \frac{M_{\text{BH}}}{M_{\text{st}}} \right)^{1/3} R_{\text{st}}, \quad (2.6)$$

where  $M_{\text{BH}}$  is the mass of the black hole,  $M_{\text{st}}$  and  $R_{\text{st}}$  are the mass and radius of the star, and  $\eta$  is a dimensionless parameter of order unity that depends on the properties of the star. These events then result in bright flares of electromagnetic radiation in the X and UV parts of the spectrum, which can then be detected.

However, for very massive SMBHs, which have masses  $M_{\text{BH}} \gtrsim 10^8 M_{\odot}$ , the tidal disruption radius for main-sequence stars is smaller than the Schwarzschild radius of the SMBH,  $r_{\text{sch}}$ . In this case, instead of being tidally disrupted, the star directly plunges into the black hole, and the black hole mass increases as a result. Compact objects such as neutron stars and white dwarfs have higher binding energy than stars and can therefore directly plunge into SMBHs of all masses. When a star or a compact object is swallowed whole, no subsequent electromagnetic radiation is emitted.

However, in order for an object (let us assume it is a star) to end up within the event horizon, it needs to be on an orbit that allows it to be captured by the SMBH. For circular orbits around non-spinning black holes this boundary is defined by the ISCO radius (inner-most circular orbit), defined as  $r_{\text{ISCO}} = 6r_g$ , where  $r_g$  is the gravitational radius of the SMBH,  $r_g = GM_{\text{BH}}/c^2$ . However, most likely the star that is captured would be on an eccentric orbit, in which case its orbital angular momentum determines whether or not the star will be captured. For a star to be captured, the angular momentum has to be smaller than the critical angular momentum, which is defined as (Merritt, 2013a):

$$L < L_c = \sqrt{12} \frac{GM_{\text{BH}}}{c}. \quad (2.7)$$

The periapsis of this orbit then determines the critical capture radius:

$$r_c \sim 8r_g. \quad (2.8)$$

### 2.5.2 The loss cone

Since the fate of a star is determined by its closest distance to the SMBH compared to its disruption radius or its capture radius, we can define the loss cone radius,  $r_{\text{lc}}$ , as the radius which takes the value of larger out of the aforementioned two radii. Then, as soon as a star reaches separation of  $r \leq r_{\text{lc}}$  it will be either tidally disrupted or captured. For a stellar orbit that reaches  $r \leq r_{\text{lc}}$  at some point, the angular momentum obeys the inequality (Merritt, 2013a):

$$L \leq L_{\text{lc}}(E) = \sqrt{2r_{\text{lc}}^2 [E - \Phi(r_{\text{lc}})]} \approx \sqrt{2GM_{\text{BH}}r_{\text{lc}}}, \quad (2.9)$$

where we assume that  $|E| \ll \Phi(r_{\text{lc}})$ , suggesting that the semi-major axis of the orbit is much larger than  $r_{\text{lc}}$ . All orbits which have low enough angular momentum to satisfy Eq. 2.9 are then called *loss cone orbits*, and the collection of these orbits in phase space is called the *loss cone*.

Whether or not a star is part of the loss cone does not necessarily depend on its energy, but rather its angular momentum. As long as the angular momentum of the star is low enough to bring it within a distance of  $r_{\text{lc}}$  at some point in the orbit, it will be lost to the SMBH. In spherical nuclei, a stellar orbit has conservation of energy and the three components of angular momentum, which together correspond to its four integrals of motion (Binney and Tremaine,

1987). Because of this, in these idealized nuclei the population of stars that are in the loss cone is roughly constant, assuming the system is static and remains in equilibrium. In a spherical nucleus the population of stars that satisfy Eq. 2.9 is correspondingly quite low. These stars would be contained within the sphere of influence of the black hole, and would be lost rather quickly, within one orbital radial period. Unless the loss cone can be efficiently repopulated in some way, it would be emptied rather quickly, and the influx of stars into the black hole would cease. This would pose an issue for this method of SMBH growth, as well as for other mechanisms which require a constant supply of stars to the galactic center, which I will discuss in Chapter 4. While rapid changes in the gravitational potential, such as major galactic mergers, can efficiently refill the loss cone, these are one-off events, and afterwards the loss cone would quickly be emptied again.

One option for a loss cone refilling mechanism are two-body relaxation effects. Namely, individual gravitational encounters between stars in the galaxy can result in sufficiently large changes in the energy and more importantly, the angular momentum of a stellar orbit that can cause the star to scatter into the loss cone. If these changes in the angular momentum happen sufficiently quickly, these encounters could re-populate the loss cone as it is emptied. However, the timescale on which this happens is closely related to the relaxation timescale, which is defined as the time it takes for gravitational encounters to produce measureable changes in the velocity of a star:

$$t_r = \frac{0.34\sigma^3}{G^2 M_{st} \rho \ln \Lambda} \quad (2.10)$$

$$\approx 0.95 \times 10^{10} \left( \frac{\sigma}{200 \text{ km s}^{-1}} \right)^3 \left( \frac{\rho}{10^6 M_\odot \text{ pc}^{-3}} \right)^{-1} \left( \frac{M_{st}}{M_\odot} \right)^{-1} \left( \frac{\ln \Lambda}{15} \right)^{-1} \text{ yr},$$

where  $\sigma$  is the one-dimensional velocity dispersion,  $\rho$  is the stellar density. Finally,  $\ln \Lambda$  is a dimensionless factor termed the Coulomb logarithm, which will be touched upon in more detail in Chapter 4. As seen from the above equation, galaxies typically have relaxation timescales longer than the age of the Universe, meaning that the average star does not feel the effects of the surrounding stars throughout the galaxy lifetime. For this reason, galaxies are often termed as collisionless systems, since stars move within the galaxy on smooth orbits that are largely unperturbed by collisional effects caused by close interactions.

Since individual gravitational interactions do not play a significant role in galaxy dynamics and can be largely neglected, a problem arises for loss-cone refilling mechanisms in spherical nuclei. While relaxation effects may result in some stars being scattered into the loss cone, this happens in the so called "empty loss cone regime" (Merritt, 2013a), where it is assumed that the loss cone is largely empty at a given time.

### 2.5.3 Non-spherical nuclei

The number of orbital families that can enter the loss cone is significantly expanded when the assumption of sphericity is abandoned. In non-spherical nuclei, the flattening of the potential can result in gravitational torques that can change the stellar angular momentum over the course of its orbit, potentially bringing it into the loss cone region of phase space (Eq. 2.9). The timescales for these changes to become significant is on the order of many radial orbit timescales, suggesting a considerable amount of time is needed for stars on these orbits to be scattered into the loss cone. However, they are still much shorter than the respective relaxation

timescales. For this reason, non-spherical nuclei naturally provide a completely separate route for loss cone repopulation other than two body relaxation, via collisionless torques.

In the case of axisymmetric nuclei, stellar orbits no longer have conservation of the total angular momentum. Instead, their two classical integrals of motion are the total energy, and the  $z$  component of the angular momentum,  $L_z$ . In this type of nuclei there are two distinct families of orbits, the tube orbits and the saucer orbits. The tube orbits are similar to their spherical counterparts, since they have their total angular momentum conserved to a large degree, which gives a limit to the minimum distance they can reach from the center. Saucer orbits, on the other hand, have no such restrictions. While they have conservation of the  $z$  component of angular momentum, their total angular momentum can significantly vary, according to equation (Merritt, 2013a):

$$L_z = L \cos i = \text{const.}, \quad (2.11)$$

where  $i$  is their orbital inclination. Their inclination varies throughout their orbit, in turn causing changes in the total angular momentum, allowing them to reach much smaller distances from the center as  $L$  decreases. The lower limit for  $L$  is reached when the inclination goes to zero, and then  $L = L_z$ . From this we can see that condition 2.9 is relaxed in the case of saucer orbits, and can be written as:

$$L_z \leq L_{lc}(E) \approx \sqrt{2GM_{\text{BH}}r_{lc}}. \quad (2.12)$$

As such, a higher fraction of orbits in the galaxy would satisfy this condition. While the fraction of stars on loss cone orbits in spherical nuclei is comparable with  $\sim L_{lc}/L_c$ , the fraction of loss cone orbits in an axisymmetric system is  $\sim \sqrt{\epsilon}L_{lc}/L_c$ , where here  $\epsilon$  is a function of the short and long axis ratio ( $c/a$ ) of the system,  $\epsilon \approx (1 - c/a)/2$ .

In triaxial nuclei, on the other hand, orbits are dominated by boxy orbits, which support much of the structure of the galaxy (Gerhard and Binney, 1985). These boxy orbits are truly centrophilic in nature, meaning that they can reach arbitrarily close to the center. Therefore, they can attain arbitrarily small values of angular momentum, since their only classical integral of motion is the total energy. However, in the presence of an SMBH in the center, the black hole can serve as a reflecting surface for these orbits, reflecting the orbit by  $180^\circ$ , in which case they become pyramid orbits (Merritt and Vasiliev, 2011). The pyramid orbits are centered on the short axis of the ellipsoid, and the total angular momentum is equal to zero in the corners of the pyramid (Merritt and Poon, 2004; Merritt and Vasiliev, 2011; Merritt, 2013b; Vasiliev et al., 2014; Merritt, 2015). As such, all pyramid orbits will necessarily enter the loss cone, sooner or later. However, the time it takes for them to reach the point of minimum angular momentum is much longer than in the case of the saucers, giving the pyramid orbits much longer lifetimes. While the saucer (as well as tube) orbits are also present in triaxial nuclei, they are not as numerous as the pyramids. On Figure 2.2, I present the main different orbital families that can be found in a triaxial nucleus. The two possible orbital types in an axisymmetric nucleus are on the left side of the figure. The fraction of pyramid orbits with respect to the total population of stars is on the order of  $\sim \epsilon L_{lc}/L_c$ , a value much higher than the fractions of stars in spherical ( $\sim L_{lc}/L_c$ ) and axisymmetric nuclei  $\sim \sqrt{\epsilon}L_{lc}/L_c$  (Merritt, 2013a). Since many elliptical galaxies and galaxy bulges show signs of triaxiality, this would enable a large portion of galaxies to have consistent loss cone refilling through the pyramid orbits, resulting in SMBH growth through tidal captures and direct plunges.

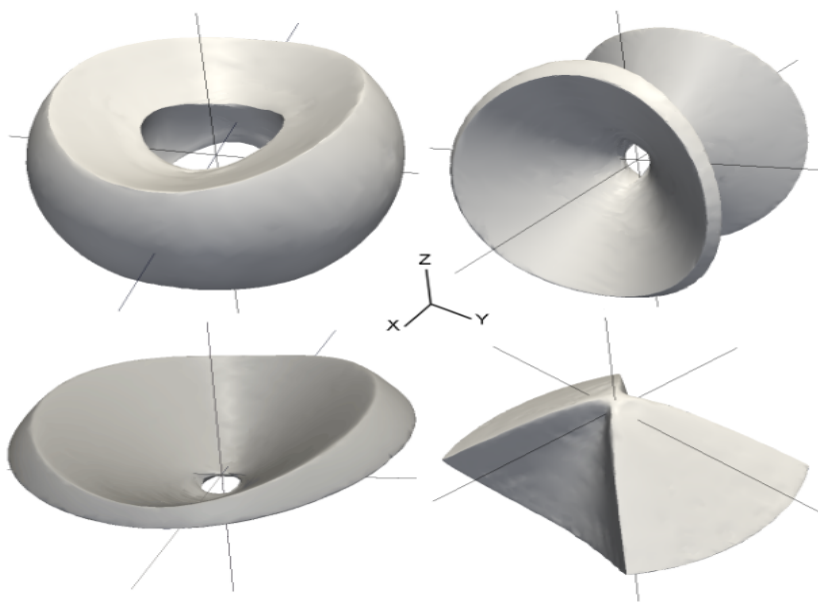


**Figure 2.2:** The four main orbital families in a triaxial system. The  $x$ ,  $y$  and  $z$  directions correspond to the directions of the long, middle and short axis respectively. The orbital families are, from left to right: the long-axis tube orbits, the short-axis tube orbits, the saucer orbits and the pyramids. Image credit: [Vasiliev \(2014\)](#).

# 3

---

## GRAVITATIONAL WAVES & THE POST-NEWTONIAN EXPANSION

---

After finally finishing work on his theory of General Relativity in 1915, Einstein focused further on the nature of gravity and the motions of bodies under its influence, and began to ponder if he could use his equations that describe the geometry of space-time, to derive a wave-like equation, analogous to the wave equation in electromagnetism, which is predicted by Maxwell's equations. These gravitational waves would then represent perturbations of space-time itself, and propagate through the Universe with the speed of gravity. Unlike EM waves, which represent dipole radiation, GWs are generated in the leading order by the Newtonian quadrupole moment of the mass distribution, demonstrated by the famous Quadrupole formula (see Eq. 3.16). While the idea of gravitational waves was not new at the time, his paper on the topic in 1918, now seen as a monumental part of the field, started a multi-decade-long debate on the existence of these phenomena. The notion of gravitational radiation existing in the physical world was scrutinized harshly by the scientific community. They were widely regarded as just as a formal mathematical construct with no real physical meaning, including Einstein himself, who was not convinced of the existence of the waves for many years (Cervantes-Cota et al., 2016). For the remainder of the century, the lack of robust observational detections made arguing for the existence of GWs difficult, although a very significant step was made with the first indirect detection by (Hulse and Taylor, 1975), within a now world-famous binary pulsar system.

However, the first direct detection of gravitational waves from a binary black hole system in 2015 by the LIGO and Virgo collaborations (Abbott et al., 2016) completely revolutionized the field, opening an entire new window of insight into the Universe. This is because gravitational waves, unlike EM radiation, interact very weakly with matter. Therefore, they are not subject to extinction, absorption and re-emission effects on their journey from the source to the detector, enabling the detection of undisturbed GW signals. Additionally, since they are emitted from extreme astrophysical systems, such as core-collapse supernovae and the mergers of compact objects, they enable us to peer into previously unreachable regions and robustly estimate physical parameters of highly relativistic objects and systems. Furthermore, when combined with electromagnetic observations (Abbott et al., 2017a), they open a path towards multi-messenger astronomical detections. The prospect of multi-messenger detections enables independent measures of distances in the form of standard sirens (Holz and Hughes, 2005), constraining the origin of short gamma-ray bursts (Abbott et al., 2017b), shedding light on the values of cosmological parameters (Wang et al., 2020) and uncovering the nature of compact objects, e.g.

the neutron star equations of state (Abbott et al., 2020a) as well as many other applications.

As described in Chapter 2, as SMBHs grow through cosmic time, it is expected that they would increase their mass at least in part due to mergers with other black holes, and therefore would emit GW in the process. Therefore, detections of these signals would be invaluable in shedding light on the growth mechanisms of massive black holes, their merger timescales, their masses and their spins. While GWs from these systems have yet to be detected, both current and future GW observatories are primarily aimed at detecting these signals.

This gives theoretical modeling of these events an important role in the field today, as well as in the future. While proper treatment of these events requires the use of numerical relativity, a number of approximation methods are present in the literature which provide great insight into relativistic effects of binary compact objects without the cumbersome ordeal that typically follows attempting to find exact solutions to Einstein's equations. By far the most widely used of these methods is the Post-Newtonian approximation, which expands Einstein's equations into an infinite series consisting of different orders, in the regime where gravity is considered weak.

With that in mind, in this chapter, I present an overview of massive black holes within the context of GW emission. In the first part of the chapter, I will describe the expected GW emission from massive black hole binaries from an observational perspective, including current and future observational projects. In the second part of the chapter, I will present an overview of the Post-Newtonian approximation and its formalism which will be used to study relativistic effects in this thesis.

### 3.1 GRAVITATIONAL WAVE SPECTRUM

Similar to electromagnetic waves, GWs can be characterized by their amplitude, wavelength and frequency. However, while the wavelengths in EM radiation are typically much smaller than their sources, GWs have wavelengths ranging from several kilometers to sizes comparable to the size of the observable Universe. The frequencies of the waves are determined by the parameters of the source and as a rough approximation can be estimated using the natural frequency of a self-gravitating body (Sathyaprakash and Schutz, 2009):

$$f_0 = \omega_0/2\pi = \sqrt{G\bar{\rho}/4\pi}, \quad (3.1)$$

where  $\bar{\rho} = 3M/(4\pi R^3)$  is the mean density of mass-energy of the source. In the case of black holes, the radius  $R$  is equal to its Schwarzschild radius, which determines the size of the event horizon  $R_{sch} = 2GM/c^2$ . If we substitute this in Eq. 3.1, we get:

$$f_0 \cong 0.15 \frac{c^3}{\pi GM}. \quad (3.2)$$

While this formula is Newtonian, and does not account the possibility of binary black hole system, it can serve as a good back-of-the-envelope estimation of the expected GW frequencies of black holes. Using Eq. 3.2 for a black hole of mass  $M = 10 M_\odot$  the obtained frequency is  $f_0 = 1$  kHz, while for a black hole of mass  $M = 10^6 M_\odot$  the expected frequency is  $f_0 = 10^{-2}$  Hz. The dependance of frequency on mass can be inferred from Fig. 3.1, where I present the GW spectrum, listing possible sources and detection techniques.

Since massive black holes emit GWs in the lower frequency range below 1 Hz, emissions

from these systems would be impossible to detect using ground-based interferometers like LIGO and Virgo, due to the presence of seismic noise and gravity variations due to mass motions on the Earth at these frequencies. Instead, space-based laser interferometers or other methods such as pulsar timing need to be utilized for detection of these systems. Below, we give an overview of current and future GW searches that promise to detect GW signals from massive black holes.

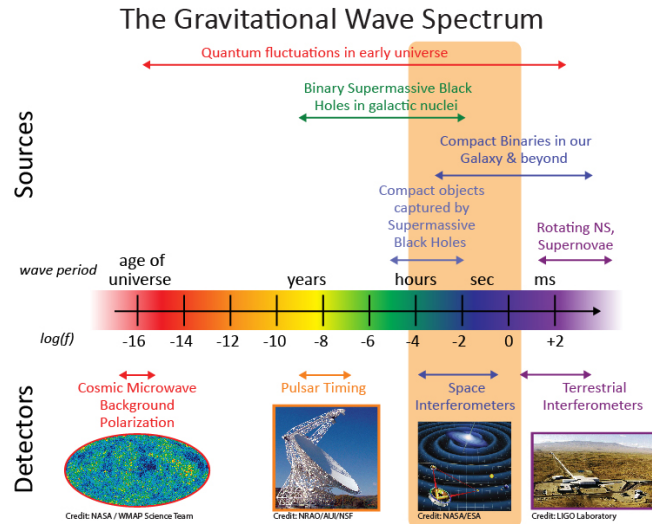


**Figure 3.1:** An overview of the GW spectrum with possible sources and detection techniques. Image credit: [www.lisa.nasa.gov](http://www.lisa.nasa.gov)

## 3.2 OBSERVATORIES

### 3.2.1 Laser Space Interferometer Antenna

The Laser Space Interferometer Antenna (LISA) (Amaro-Seoane et al., 2017) is an upcoming space-based gravitational wave observatory jointly funded by ESA and NASA, expected to launch in 2034. Similar to ground-based detectors, LISA plans to utilize laser interferometry to detect perturbations in space-time caused by GWs. It will consist of three spacecraft connected by lasers in a triangular configuration placed on a Solar orbit, where the side-length of the triangle is 2.5 million kilometers (Baker et al., 2019).

While the detection method functions similarly to LIGO/Virgo, the significantly longer arm lengths of the interferometer and the absence of Earth-based detector noise make the mission ideal to explore the mHz range of the GW spectrum. This is showcased on the left panel of Fig. 3.2. The characteristic strain shown on the plot is a measure of the amplitude of the GW.

With the ability to detect GWs in the lower frequency range, the main detection targets for LISA are massive black hole mergers, with the black holes masses ranging from  $10^4 M_\odot$  –  $10^7 M_\odot$  out to  $z \sim 20$  (see Fig. 3.2, right panel). These detections will give unique insight into the birth and early growth of massive black hole seeds, provide direct detections of massive black hole spins and illuminate the relationship and co-evolution of SMBHs and their host galaxies (Colpi et al., 2019).

While the primary focus of LISA is on the detection of SMBH binaries, other possible detection targets include compact object binaries, some of which would cross into the LIGO band, as well as intermediate mass black hole (IMBH) binaries, extreme mass-ratio inspirals

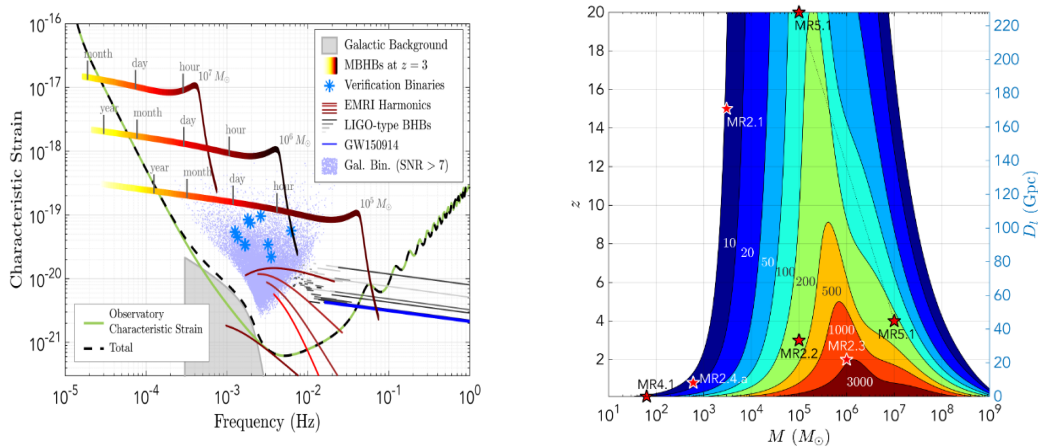


**Figure 3.2:** Left: LISA sensitivity curve represented by the green line, given in terms of the dimensionless strain amplitude as a function of frequency. Some examples of GW sources are overplotted. Image credit: LISA collaboration, [Amaro-Seoane et al. \(2017\)](#). Right: Contours of constant signal-to-noise ratios, as a function of redshift (y-axis, left), luminosity distance (y-axis, right) and total mass of the black hole binary (x-axis). Image credit: LISA collaboration, [Amaro-Seoane et al. \(2017\)](#).

(EMRI) and more exotic sources such as cosmic strings and early-universe phase transitions ([Baker et al., 2019](#)).

### 3.2.2 Pulsar Timing Arrays

Milisecond pulsars are widely regarded as the most accurate clocks in the Universe due to the very high stability of their rotational period, within 1 – 10 milliseconds. In principle, as a GW passes between the pulsar-Earth system, it would slightly alter the time of arrival of the pulse which could then be detected by ground-based radio telescopes. While this would not be sufficient for a robust GW detection, very precise timing data of a higher number of pulsars over longer periods of time (on the order of years and decades) could be used to identify GW signals and separate them from the detector noise. Namely, a joint analysis of different pulsar data could correlate the slight changes in frequencies measured in individual pulsars to extract information on the amplitude and direction of the GW signal ([Dahal, 2020](#); [Verbiest et al., 2021](#)). In this case, the distance between the Earth and the pulsar would serve as the effective arm length of the detector, enabling detections of low frequency GWs in the nHz range, making this method of detection highly complementary to the LISA and LIGO/Virgo sensitivity ranges. This frequency range would correspond to signals originating from SMBH of the highest masses ( $M \sim 10^8 M_\odot$ ).

For this purpose, Pulsar Timing Arrays (PTA) around the world have already been operational for more than a decade. They consist of the Australian Parkes PTA ([Reardon et al., 2016](#)), the European PTA ([Desvignes et al., 2016](#)) and the North-American Nanohertz Observatory for Gravitational waves (NANOGrav) ([Arzoumanian et al., 2016](#)), as well as the collective joint effort of the three before mentioned groups in the form of the International PTA (IPTA) ([Verbiest et al., 2016](#)).

It is expected that the most notable signal detected in this frequency range would be the stochastic gravitational wave background, which represents the superposition of many different incoherent GWs that are too weak to be resolved individually and would be generated primarily by SMBH binaries. Additionally, continuous signals could be detected from SMBH binaries,

assuming they are close enough in order to be resolved and that they are strong enough to stand out from the stochastic background. Other possible sources include burst events such as SMBH formation, close SMBH binary encounters, cosmic string interactions and so called "bursts with memories" (Favata, 2009; Verbiest et al., 2021). While no robust detections have been made yet, the constantly improving accuracy of the PTAs has started to put constraints on the theoretical estimates of the strain amplitude of the stochastic GW background (see Fig. 3.3). At the time of writing, the NANOGrav collaboration published results of a signal which could correspond to the stochastic GW background from merging massive binaries (Arzoumanian et al., 2020) and it is estimated that an astrophysical origin of the signal is possible (Middleton et al., 2021). However, the signal could also correspond to the stochastic background generated by cosmic strings (Ellis and Lewicki, 2021).

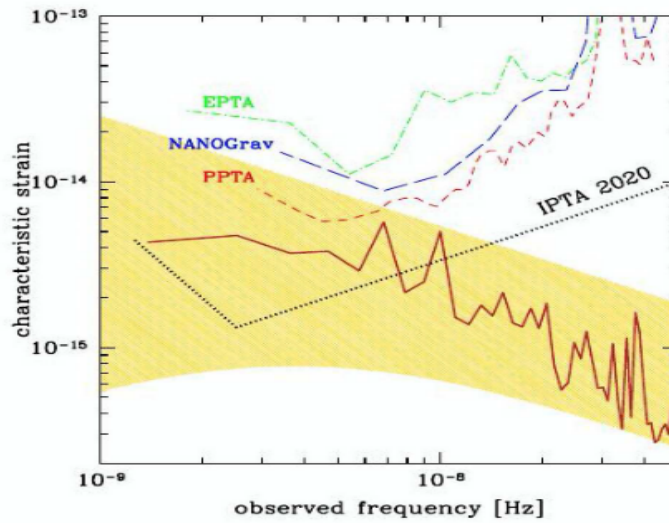


**Figure 3.3:** Characteristic strain amplitudes of different PTA collaborations as a function of GW frequency. The dashed line corresponds to the expected sensitivity reached at the end of 2020. The yellow shaded region and the full red line correspond to theoretical estimates of the stochastic GW background. Image credit: Hobbs and Dai (2017).

### 3.2.3 TianQin

TianQin is an upcoming Chinese space-based GW mission, expected to launch in the 2030s (Luo et al., 2016). Functioning on the same principle as LISA, it will consist of three spacecraft in a triangular configuration, and will be sensitive to the same frequency ranges. However, unlike LISA, the proposed mission is not envisioned as a full GW observatory, but rather as a detector, with the primary mission goal being the detection of a single, well-known GW source. Therefore, the sensitivity of TianQin is aimed at resolving the frequency and signal of one pre-chosen reference source, currently planned to be the white-dwarf binary RX J0806.3+1527. This detection would then serve as an important calibration tool for TianQin, as well as other future GW missions, with any other possible detections regarded as an additional result. This gives the mission a much more defined focus and goal, which combined with smaller arm lengths ( $\sim 10^5$  km) and a geocentric orbit results in significantly lower cost and complexity of the mission with respect to LISA.

Nevertheless, the sensitivity range of the mission leaves the door open to previously unknown and unexpected detections as well. It is estimated that the number of detections would

be on the order of  $\mathcal{O}(1 \sim 10)$  per year, with the ability to detect SMBH mergers up to  $z \sim 10$  (Wang et al., 2019). As such, it can be valuable towards giving early warning of SMBH mergers for other detections, by contributing to sky localization and in combination with LISA, has the potential to shed light on the formation of first black hole seeds.

### 3.3 POST-NEWTONIAN EXPANSION

The essence of Einstein’s theory of General Relativity is contained within Einstein’s field equations, which read:

$$G^{\alpha\beta} = \frac{8\pi G}{c^4} T^{\alpha\beta}, \quad (3.3)$$

where  $G^{\alpha\beta}$  is the Einstein curvature tensor, which describes the curvature of space-time, and  $T^{\alpha\beta}$  is the energy-momentum tensor, which describes the matter distribution. The existence of the equations signifies an intimate connection between matter and space-time, that is often described with the famous words of physicist John Wheeler: "Space-time tells matter how to move; matter tells space-time how to curve". This intrinsic coupling between matter and curvature already points on the surface level to the difficulties that arise when attempting to find a general solution of the equations. Namely, one cannot determine the space-time curvature, determined by the space-time metric  $g^{\alpha\beta}$ , without knowledge of the matter distribution whose motion is determined by that same metric. Similarly, one cannot determine the matter variables from the metric, since that metric is necessarily determined by the matter variables themselves. From a mathematical point of view, the equations themselves represent a coupled set of 10 non-linear second-order partial differential equations. Due to their high level of non-linearity, the equations are extremely difficult to solve. While exact solutions do exist, they are the exception, and not the norm. There are too few exact solutions for them to be applied in the general case of all matter configurations.

However, current and future GW searches need a large collection of pre-calculated waveform templates in order to match them to the detected signal and identify a detection among the noise. These templates can only be obtained by solving Eqs. 3.3 in the general case, for vastly different mass and spin configurations. For this purpose, a truly astonishing number of exact solutions have been found so far with the use of numerical relativity. However, the use of numerical relativity entails great computational and theoretical effort, making it out of reach for general studies of relativistic effects. Therefore, a variety of different approximation methods have been employed with great success to study these effects, in the domain where gravitational fields are considered to be weak. The flagship of approximation methods is the Post-Newtonian expansion, which is the most widely used and has provided us with most insight, particularly in the case of evolution of compact binary systems. Other approximation methods have also been highly successful, such as post-Minkowskian theory (Poisson and Will, 2014), the effective one-body approach (Buonanno and Damour, 1999) and the self-force (Poisson, 2004). Since the topic of PN theory is very vast, in this section I will present an overview of the most important results of the PN approach for their use in astrophysical modeling of compact binary systems, while omitting the mathematical description used to derive them. Instead, I refer the reader to Poisson and Will (2014) and Blanchet (2014) and the references therein, which give a much more comprehensive overview of the topic. Similarly, I will restrict the discussion to PN theory and refrain from detailing the results of other approximation methods and numerical relativity. An overview of numerical relativity can be found in Lehner and Pretorius (2014).

The Post-Newtonian approximation is a multipole expansion of Einstein’s field equations

where the expansion parameter is the ratio of the characteristic velocity of the massive object with respect to the speed of light,  $v^2/c^2$ . The velocity  $v$  can be represented by the characteristic internal velocity in the case of single objects  $v_c = r_c/t_c$ , where  $r_c$  is the characteristic length of the object and  $t_c$  is the characteristic timescale. In the case of binary systems,  $v$  takes the form of the orbital velocity  $v^2 \sim GM/r$ , where  $M$  is the total mass of the system and  $r$  is the orbital separation. The approximation is done under two very important assumptions. The first assumption is that the gravitational field in the domain of interest can be considered *weak*, meaning that the self-gravity of the source can be considered negligible (Blanchet, 2014). The second, equally important assumption is that the motions within the system in question are *slow*, so that  $v/c \ll 1$ . This condition is also the one that enables the field equations to be expanded in terms of this small parameter. The order of the PN expansion is then named according to the order of this parameter, where the N-th PN order corresponds to an expansion up to formal order  $O(1/c^{2N})$ . The expansion itself is divergent, meaning that it is possible to expand the equations up to an arbitrarily high number N without obtaining an exact solution of Einstein's equations. However, each subsequent order is increasingly difficult to derive and the current state-of-the-art is the 4PN order (Foffa et al., 2019), but progress is being made and incomplete terms of the 5PN order have been obtained as well (Blümlein et al., 2021).

The history of PN theory can be traced back to 1917, in the work of Lorentz and Droste (english translation, Lorentz and Droste, 1937) who derived the metric and motion of a N-body system up to PN1 order, as well as by Einstein himself, in Einstein et al. (1938). Since then PN theory has been used to great success in many applications in the solar system and beyond, with most notable examples being the calculation of the advance of the Mercury perihelion in 1915 by Einstein, the measurement of the relativistic deflection of light during a Solar eclipse, today known as the Eddington experiment (Dyson et al., 1920) and the damping of a pulsar's orbit due to GW emission (Hulse and Taylor, 1975).

### 3.3.1 Validity and accuracy

The assumptions of a weak gravitational field and slow motion of a compact binary system might seem counter-intuitive at first, since at first glance the study of objects such as merging binary black holes can hardly satisfy the notions of weak gravity and slow motions. After all, compact objects demonstrate some of the strongest gravity effects known and experience relativistic velocities comparable to the speed of light leading up to the merger. Namely, the notion of weak gravity holds true when the self-gravity of the source is negligible,  $|U/c^2|^{1/2} \ll 1/c$ , where  $U$  is the Newtonian potential of the source, which is not the case for compact objects such as neutron stars and black holes who have strong internal gravity. However, the requirement for the PN approximation is then, that the components of the binary system are well separated. Then, the gravitational interaction between them remains weak, despite allowing each body to be strongly self-gravitating (Poisson and Will, 2014). This is a consequence of the Strong Equivalence Principle, since orbital motion of well-separated bodies depends only on the total mass of the system, and not its internal structure (Will, 2011).

The situation is less clear in regards to the slow motion requirement, since inspiralling binaries can reach velocities up to 50% of light speed in the final few orbits before a merger (Blanchet, 2014). However, the PN approximation has proven to be very effective even in these cases, since comparisons with numerical relativity have shown that the use of higher order PN terms matches incredibly well with the numerically-obtained expected behavior. It is not exactly

clear why the approximation performs so well even in the case of violation of the slow motion assumption, and the PN expansion has been called *unreasonably effective* in this regard (Will, 2011). Nevertheless, it allows for smooth transitions between the different regimes, successfully bridging the gap between the domains of PN and numerical relativity and resulting in complete construction of waveforms of an inspiralling compact binary.

However, one caveat of the PN treatment is that it is only valid in the region near the source, namely where  $r \ll \lambda_c$ , where  $\lambda_c$  is the characteristic wavelength of the gravitational radiation of the source. This stems from the formalism of the theory itself, and means that the PN approximation fails to reproduce the boundary conditions at infinity. This is relevant since these boundary conditions determine the force the source experiences as a result of GW emission (termed the radiation-reaction force), and therefore influence the equations of motion. Because of this, PN formalism should be combined with Post-Minkowski theory, which expands Einstein's equations in terms of the gravitational parameter  $G$ , and is valid both in the region near the source, as well as at infinity (Blanchet, 2014).

### 3.3.2 Equations of motion

For the purposes of theoretical modeling of relativistic systems, it is most useful to present the equations of motion in a Newtonian-like fashion. Then, they can simply be implemented into the codes and calculations. In the context of compact binary systems, the relative acceleration between two bodies in the center of mass reference frame can be written as:

$$\vec{a} = \vec{a}_{Newt} + \vec{a}_{PN1} + \vec{a}_{PN1.5} + \vec{a}_{PN2} + \vec{a}_{PN2.5\dots}, \quad (3.4)$$

where  $\vec{a}_{Newt}$  is the standard Newtonian acceleration and the other terms denote the PN terms up to their respective orders. Firstly, we can make a distinction between conservative and dissipative dynamics in the equations of motion (this distinction can be clearly made up to order PN3.5, Blanchet and Iyer 2003). The *even* PN terms such as PN1, PN2, PN3 and so forth, signify terms where the dependence on  $c$  is an even number  $\mathcal{O}(1/c^{2N})$ . These are the *conservative* terms, meaning that they do not effectively carry away energy and angular momentum from the system. Instead, they may induce oscillations and perturbations, but these changes average to zero with time. *Odd* terms, such as PN1.5, PN2.5 and so on are *dissipative* terms, and their influence on the energy and angular momentum of the system is not invariant to time reversal, meaning that they induce permanent changes in the properties of the system. The PN2.5 term corresponds to the *radiation-reaction* term, and represents the acceleration the body feels as a result of GW emission. Therefore, in order to include the effects of GW emission, one needs to include PN corrections up to at least PN2.5 order.

Here, I will present ready-to-use equations of motion of a compact binary system, using the formalism of Blanchet (2014). Due to the great lengths of the expressions, I will present the equations of motion for non-spinning binaries, up to PN2.5 order. A brief overview of PN effects in spinning binaries is given at the end of the chapter.

Let us assume we have two massive bodies with their respective masses denoted  $m_1$  and  $m_2$  and position vectors  $\vec{r}_1$  and  $\vec{r}_2$ . Positioning ourselves in their center of mass reference frame, we will denote their relative position and velocity with:

$$\vec{r} = \vec{r}_1 - \vec{r}_2, \quad \vec{v} = \vec{v}_1 - \vec{v}_2. \quad (3.5)$$

The amplitudes of these vectors are then denoted simply by:

$$r = |\vec{r}|, \quad v = |\vec{v}|. \quad (3.6)$$

The mass variables take the usual form, with the inclusion of one additional helpful parameter:

$$\mu = \frac{m_1 m_2}{m_1 + m_2}, \quad m = m_1 + m_2 \quad \text{and} \quad \nu = \frac{\mu}{m} = \frac{m_1 m_2}{(m_1 + m_2)^2}, \quad (3.7)$$

denoting the reduced mass, the total mass of the system and the symmetric mass ratio, respectively. We will denote the scalar product between vectors  $\vec{a}$  and  $\vec{b}$  with  $\vec{a} \cdot \vec{b}$ . Finally, let us also introduce the following two helpful variables:

$$\vec{n} = \frac{\vec{r}}{r}, \quad \dot{r} = \vec{n} \cdot \vec{v}. \quad (3.8)$$

Then, we can write the 2.5PN equations of motion in the center of mass frame as:

$$\frac{d\vec{v}}{dt} = -\frac{Gm}{r^2} \left[ (1 + \mathcal{A})\vec{n} + \mathcal{B}\vec{v} \right] + \mathcal{O}\left(\frac{1}{c^6}\right), \quad (3.9)$$

where we have introduced coefficients  $\mathcal{A}$  and  $\mathcal{B}$ . It is evident from the above equation that the factor of unity in the bracket corresponds to the Newtonian acceleration. The dissipative PN1.5 term goes to zero for non-spinning binaries, so the coefficient  $\mathcal{A}$  takes the form of:

$$\begin{aligned} \mathcal{A} = & \frac{1}{c^2} \left\{ -\frac{3\dot{r}^2 v}{2} + v^2 + 3v\dot{v}^2 - \frac{Gm}{r}(4 + 2v) \right\} \\ & + \frac{1}{c^4} \left\{ \frac{15\dot{r}^4 v}{8} - \frac{45\dot{r}^4 v^2}{8} - \frac{9\dot{r}^2 v\dot{v}^2}{2} + 6\dot{r}^2 v^2 v^2 + 3v\dot{v}^4 - 4v^2 \dot{v}^4 \right. \\ & \left. + \frac{Gm}{r} \left( -2\dot{r}^2 - 25\dot{r}^2 v - 2\dot{r}^2 v^2 - \frac{13v\dot{v}^2}{2} + 2v^2 \dot{v}^2 \right) + \frac{G^2 m^2}{r^2} \left( 9 + \frac{87v}{4} \right) \right\} \\ & + \frac{1}{c^5} \left\{ -\frac{24\dot{r}v\dot{v}^2}{5} \frac{Gm}{r} - \frac{136\dot{r}v}{15} \frac{G^2 m^2}{r^2} \right\}. \end{aligned} \quad (3.10)$$

Similarly, the  $\mathcal{B}$  coefficient takes the form:

$$\begin{aligned} \mathcal{B} = & \frac{1}{c^2} \{-4\dot{r} + 2\dot{r}v\} \\ & + \frac{1}{c^4} \left\{ \frac{9\dot{r}^3 v}{2} + 3\dot{r}^3 v^2 - \frac{15\dot{r}v\dot{v}^2}{2} - 2\dot{r}v^2 v^2 \frac{Gm}{r} \left( 2\dot{r} + \frac{41\dot{r}v}{2} + 4\dot{r}v^2 \right) \right\} \\ & + \frac{1}{c^5} \left\{ \frac{8v\dot{v}^2}{5} \frac{Gm}{r} + \frac{24v}{5} \frac{G^2 m^2}{r^2} \right\}. \end{aligned} \quad (3.11)$$

### 3.3.3 Energy and angular momentum

Similar to Newtonian mechanics, PN theory allows for conservation of energy and angular momentum, although only when the conservative, non-dissipative PN terms are taken into account. Therefore, excluding the PN2.5 contribution from the above equations allows us to

obtain expressions for the PN conserved energy and angular momentum in the center of mass frame up to order PN2. Below, I present these expressions, adapted from [Blanchet and Iyer \(2003\)](#).

$$\begin{aligned} \frac{E}{\mu} = & \frac{v^2}{2} - \frac{Gm}{r} + \frac{1}{c^2} \left\{ \frac{3v^4}{8} - \frac{9v^4}{8} + \frac{Gm}{r} \left( \frac{\dot{r}v}{2} + \frac{3v^2}{2} + \frac{vv^2}{2} \right) + \frac{G^2 m^2}{2r^2} \right\} \\ & + \frac{1}{c^4} \left\{ \frac{5v^6}{16} - \frac{35v^6}{16} + \frac{65v^2 v^6}{16} \right. \\ & + \frac{Gm}{r} \left( -\frac{3\dot{r}^4 v}{8} + \frac{9\dot{r}^4 v^2}{8} + \frac{\dot{r}^2 v^2}{4} - \frac{15\dot{r}^2 v^2 v^2}{4} + \frac{21v^4}{8} - \frac{23vv^4}{8} - \frac{27v^2 v^4}{8} \right) \\ & + \frac{G^2 m^2}{r^2} \left( \frac{\dot{r}^2}{2} + \frac{69\dot{r}^2 v}{8} + \frac{3\dot{r}^2 v^2}{2} + \frac{7v^2}{4} - \frac{55vv^2}{8} + \frac{v^2 v^2}{2} \right) \\ & \left. + \frac{G^3 m^3}{r^3} \left( -\frac{1}{2} - \frac{15v}{4} \right) \right\}, \end{aligned} \quad (3.12)$$

$$\begin{aligned} \frac{\vec{L}}{\mu} = & \vec{r} \times \vec{v} \left[ 1 + \frac{1}{c^2} \left\{ (1-3v) \frac{v^2}{2} + \frac{Gm}{r} (3+v) \right\} \right. \\ & + \frac{1}{c^4} \left\{ \frac{3v^4}{8} - \frac{21vv^4}{8} + \frac{39v^2 v^4}{8} \right. \\ & + \frac{Gm}{r} \left( -\dot{r}^2 v - \frac{5\dot{r}^2 v^2}{2} + \frac{7v^2}{2} - 5vv^2 - \frac{9v^2 v^2}{2} \right) \left. \right\} \\ & \left. + \frac{G^2 m^2}{r^2} \left( \frac{7}{2} - \frac{41v}{4} + v^2 \right) \right]. \end{aligned} \quad (3.13)$$

Finding the time derivative of the above expressions by means of the equations of motion gives the energy correction due to the PN2.5 radiation-reaction term, which reflects the energy and angular momentum change due to GW emission (up to leading order in GW emission, represented by PN2.5):

$$\tilde{E} = E + \frac{8m^3 \dot{r} v^2}{5c^5 r^2} v^2, \quad (3.14)$$

$$\tilde{L} = \vec{L} - \left( \frac{8m^3 \dot{r} v^2}{5c^5 r^2} \right) \vec{r} \times \vec{v}. \quad (3.15)$$

Then, it can be easily checked that the total gravitational energy flux matches the famous Quadrupole formula, which describes the emission of GWs by the Newtonian quadrupole moment ([Blanchet, 2014](#)):

$$\left( \frac{d\tilde{E}}{dt} \right) = \frac{G}{5c^5} \left( \ddot{Q}_{ij} \ddot{Q}_{ij} + O\left(\frac{1}{c^7}\right) \right), \quad (3.16)$$

$$\left( \frac{d\tilde{L}_i}{dt} \right) = \frac{2G}{5c^5} \left( \epsilon_{ijk} \ddot{Q}_{jl} \ddot{Q}_{kl} + O\left(\frac{1}{c^7}\right) \right), \quad (3.17)$$

where  $i$  is a component of the angular momentum vector,  $\epsilon_{ijk}$  denotes the Levi-Civita symbol

and  $Q_{i,j}$  is the Newtonian trace-free quadrupole moment,  $Q_{ij} = \mu(x^i x^j - \frac{1}{3}\delta^{ij}r^2)$ .

These equations describe the instantaneous changes in energy and angular momentum due to GW emission, to leading order. However, since we are interested in secular changes over time, it is helpful to present the equations averaged over a characteristic timescale of the system. Averaged over the binary orbital period and expressed in terms of the Newtonian orbital elements, the well-known equations first derived in [Peters and Mathews \(1963\)](#) and [Peters \(1964\)](#) represent the secular changes in energy and angular momentum due to GW emission:

$$\left\langle \frac{dE}{dt} \right\rangle_{GW} = -\frac{32}{5} \frac{G^4 m_1^2 m_2^2 m}{c^5 a^5 (1-e^2)^{7/2}} \left( 1 + \frac{73}{24}e^2 + \frac{37}{96}e^4 \right), \quad (3.18)$$

$$\left\langle \frac{dL}{dt} \right\rangle_{GW} = -\frac{32}{5} \frac{G^{7/2} m_1^2 m_2^2 m^{1/2}}{c^5 a^{7/2} (1-e^2)^2} \left( 1 + \frac{7}{8}e^2 \right), \quad (3.19)$$

where  $L$  is the orbital angular momentum amplitude, and  $a$  and  $e$  are the Newtonian binary semi-major axis and orbital eccentricity.

### 3.3.4 Orbital elements

Similar to the energy and angular momentum, we can use the PN-corrected equations of motion to get Keplerian-like (often termed quasi-Keplerian) expressions for the binary orbital elements. These expressions were first derived at the PN1 order by [Damour and Deruelle \(1985\)](#), which I will present here based on the expressions in [Memmesheimer et al. \(2004\)](#).

Before presenting the PN corrections to the orbital equations, let us remind ourselves of some important quantities in standard, Keplerian motion. The Keplerian motion of the relative particle in the center of mass frame and in polar coordinates is characterized by :

$$R = a(1 - e \cos u), \quad (3.20)$$

$$\varphi - \varphi_0 = v = 2 \arctan \left[ \left( \frac{1+e}{1-e} \right)^{1/2} \tan \left( \frac{u}{2} \right) \right], \quad (3.21)$$

where  $R$  is the polar radial coordinate,  $\varphi$  is the azimuthal angle,  $u$  is the eccentric anomaly and  $v$  is the true anomaly. The Kepler equation, denoting the time dependence takes the form:

$$l = u - e \sin u, \quad (3.22)$$

where  $l$  is the mean anomaly. The Keplerian orbital elements are then expressed as:

$$a = \frac{Gm}{2\epsilon}, \quad (3.23)$$

$$e = \sqrt{1 + \frac{2\epsilon h^2}{G^2 m^2}}, \quad (3.24)$$

$$T = -Gm\sqrt{2\pi}\epsilon^{3/2}, \quad (3.25)$$

where we have expressed the semi-major axis, eccentricity and orbital period in terms of the specific energy and angular momentum,  $\epsilon = E/\mu$  and  $h = L/\mu$ .

The PN equations of motion given by Eq. 3.9 can be integrated in a similar manner as the

Keplerian equations, resulting in the Quasi-Keplerian description:

$$R = a_r(1 - e_r \cos u), \quad (3.26)$$

$$l = u - e_t \sin u, \quad (3.27)$$

$$2\pi k(\varphi - \varphi_0) = v = 2 \arctan \left[ \left( \frac{1 + e_\varphi}{1 - e_\varphi} \right)^{1/2} \tan \left( \frac{u}{2} \right), \right] \quad (3.28)$$

where  $2\pi k$  represents the periastron advance factor,  $2\pi k = 6\pi Gm/(c^2 a(1 - e^2))$ . The factors  $a_r, e_r, e_t, e_\varphi$  denote the PN1-corrected semi-major axis, the radial eccentricity, the time eccentricity and the angular eccentricity. When the equations are expressed in this form, they highly resemble the original Keplerian equations, with the biggest difference being the introduction of three different eccentricity parameters, which differ from one another by PN corrections. Already at order PN2, and especially at order PN3 the equations require the introduction of additional parameters and lose much of their Kepler-like appearance. For these higher order corrections, we refer the reader to [Memmesheimer et al. \(2004\)](#).

The orbital elements, including the three eccentricities, at order PN2 can then be expressed in terms of the specific energy and angular momentum:

$$a_r = \frac{Gm}{-2\epsilon} \left\{ 1 + \frac{-2\epsilon}{4c^2}(v+7) + \frac{(-2\epsilon)^2}{16c^4} \left[ (1 + 10v + v^2) + \frac{G^2 m^2 (44v - 68)}{-2\epsilon h^2} \right] \right\}, \quad (3.29)$$

$$e_r^2 = 1 + \frac{2\epsilon h^2}{G^2 m^2} + \frac{(-2\epsilon)}{4c^2} \left\{ 24 - 4v + 5(v-3) \frac{(-2\epsilon h^2)}{G^2 m^2} \right\} + \frac{(-2\epsilon)^2}{8c^4} \left\{ 52 + 2v + 2v^2 - (80 - 55v + 4v^2) \frac{(-2\epsilon h^2)}{G^2 m^2} - \frac{8G^2 m^2}{(-2\epsilon h^2)} (11v - 17) \right\}, \quad (3.30)$$

$$e_t^2 = 1 + \frac{2\epsilon h^2}{G^2 m^2} + \frac{(-2\epsilon)}{4c^2} \left\{ -8 + 8v - (7v - 17) \frac{(-2\epsilon h^2)}{G^2 m^2} \right\} + \frac{(-2\epsilon)^2}{8c^4} \left\{ 8 + 4v + 20v^2 - (112 - 47v + 16v^2) \frac{(-2\epsilon h^2)}{G^2 m^2} + \frac{4G^2 m^2}{(-2\epsilon h^2)} (-11v + 17) - 24 \sqrt{\frac{(-2\epsilon h^2)}{G^2 m^2}} (2v - 5) - \frac{24Gm}{\sqrt{(-2\epsilon h^2)}(5 - 2v)} \right\}, \quad (3.31)$$

$$e_\varphi^2 = 1 + \frac{2\epsilon h^2}{G^2 m^2} + \frac{(-2\epsilon)}{4c^2} \left\{ 24 + (-15 + v) \frac{(-2\epsilon h^2)}{G^2 m^2} \right\} + \frac{(-2\epsilon)^2}{16c^4} \left\{ -32 + 176v + 18v^2 - (160 - 30v + 3v^2) \frac{(-2\epsilon h^2)}{G^2 m^2} - \frac{G^2 m^2}{(-2\epsilon h^2)} (408 - 232v - 15v^2) \right\}. \quad (3.32)$$

Similar to energy and angular momentum, the orbital eccentricity and semi-major axis also change due to the radiation-reaction force and we can write the secular changes of the Newtonian definitions of these elements using relations in [Peters \(1964\)](#):

$$\left\langle \frac{da}{dt} \right\rangle_{GW} = -\frac{64}{5} \frac{G^3 m_1 m_2 m}{c^5 a^5 (1 - e^2)^{7/2}} \left( 1 + \frac{73}{24} e^2 + \frac{37}{96} e^4 \right), \quad (3.33)$$

$$\left\langle \frac{de}{dt} \right\rangle_{GW} = -\frac{304e}{15} \frac{G^3 m_1 m_2 m}{c^5 a^4 (1 - e^2)^{5/2}} \left( 1 + \frac{121}{304} e^2 \right). \quad (3.34)$$

### 3.3.5 *Spinning binaries*

In the description of the PN approximation so far, as well as throughout the thesis, I assume that the massive bodies are non-rotating, so that their spin parameter equals zero. This in turn vastly simplifies the PN equations of motion since all spin terms can be disregarded. However, in reality there is no reason to assume the bodies would not possess their own intrinsic rotation. In fact, as discussed in section 2.1, observations demonstrate high spin values for massive black holes.

The individual spin values and configurations can drastically affect the inspiral and subsequent GW emission of a compact binary merger, making proper treatment of spin effects crucial for current and future modeling of GW signals and black hole evolution in general. The PN spin terms can be distinguished between spin-orbit effects (SO) which are linear in the spin parameter, and the spin-spin effects (SS) which have a quadratic dependence on the spin parameter. The SO effects first appear in the equations of motion at the PN1.5 order, while SS effects appear at the PN2 order. The full corrections to the equations of motion including these terms can be found in [Faye et al. \(2006\)](#) and [Tagoshi et al. \(2001\)](#) as well as a more comprehensive review in [Blanchet \(2014\)](#) and [Poisson and Will \(2014\)](#).

One notable effect that arises from the presence of spins is spin precession. Namely, if the individual spins of the binary ( $\vec{S}_1$  and  $\vec{S}_2$ ) do not align with the orbital angular momentum of the binary ( $\vec{L}$ ), SO and SS interactions at PN2 order will cause the precession of these three vectors. On the other hand, the total angular momentum remains constant both in terms of direction and amplitude, where the total angular momentum vector has the form  $\vec{J} = \vec{L} + \vec{S}_1 + \vec{S}_2$ . The direction of  $\vec{J}$  will remain constant even at PN2.5 order where dissipative effects from the radiation-reaction force are present, and these dissipative effects will only decrease the amplitude of the total angular momentum.

# 4

---

## BINARY SUPERMASSIVE BLACK HOLES

---

Hierarchical galaxy formation models have established that massive galaxies are formed through a series of galactic mergers (White and Rees, 1978; White and Frenk, 1991). Since these events are crucial components for standard galaxy evolution models, they are expected to be common throughout the Universe. The question that arises then, is what happens to the massive black holes hosted within these galaxies. The natural assumption is that SMBHs would form binary systems, similar to stellar mass black holes, and eventually coalesce, emitting a burst of GWs in the process. In fact, in Ch. 2, this was named as one of the principal mechanisms by which SMBHs can grow in mass. In the previous chapter, I have further expanded on this, by detailing the theoretical framework of GW emission of SMBH binaries, and the observational efforts that plan to detect these signals. However, what was omitted from the discussion so far, was how pairs of SMBHs evolve, starting from  $\sim$  kpc separations during a galactic merger, down to sub-pc separations when their GW emission would become detectable. Therefore, the primary focus of this chapter will be to answer this question.

In this chapter, I will start by giving an overview of electromagnetic observations of dual and multiple AGN systems and close SMBH binaries. Then, I will proceed to introduce the theoretical framework of the evolution of SMBHs in merging nuclei. I will introduce the three main phases of SMBH binary coalescence, and discuss the theoretical bottleneck termed the Final Parsec Problem (FPP) and its possible solutions. Finally, I will give a detailed overview of the study of Khan et al. (2016)(hereafter Kh16), which served as the basis for much of the work in this thesis.

### 4.1 ELECTROMAGNETIC OBSERVATIONS

The topic of electromagnetic observation of dual SMBHs is vast and beyond the scope of this work. Only a brief overview will be given here, and the reader is referred to recent reviews on this topic for further details (De Rosa et al., 2019; Bogdanović, 2015). The topic can be distinguished between two main aspects. Namely, the observation of dual and multiple AGN at separations of  $\approx$  1kpc from each other, and the observation of bound SMBH systems at sub-parsec separations. In both cases however, despite large observational efforts, only a small number of detections have been confirmed so far, due to various difficulties involved with the observations. This has limited the ability to make robust comparisons with theoretical models

and gives even more importance to current and future GW detection efforts (De Rosa et al., 2019).

The observation of dual AGN at kpc separations have proven difficult for several reasons. The first is the insufficient angular resolution required to distinguish both AGN at these separations (the angular separation is comparable to  $\sim 1$  arcsecond at  $z \approx 0.05$ , Li et al. 2021). The second is due to the large amount of dust present in merging environments, which results in the obscuration of the source, posing a problem for optical observations. Additionally, observations in the radio domain of the spectrum may have difficulty in distinguishing AGN from star formation processes. This issue is further exacerbated by the fact that only 10% of AGN emit in the radio at all (De Rosa et al., 2019). Instead, X-ray and mid-infrared observations have proven valuable in tackling the issue, combined with optical and radio surveys. In cases where limiting spatial resolution prevents the detection of separate sources, spectroscopy can be used to distinguish separate kinematic sources by detecting double-peaks in their emission lines. Nevertheless, the appearance of new methods and improved techniques is proving effective in identifying dual (e.g. Foord et al., 2019, 2020) and triple systems (Kollatschny et al., 2020; Foord et al., 2021). It is expected that future missions in different parts of the electromagnetic spectrum would increase the number of candidates by orders of magnitude, and the combination of observations from different parts of the spectrum can be used to confirm those candidates (De Rosa et al., 2019).

The detection of close SMBH binaries at pc and sub-pc separations is even more challenging due to the even higher angular resolution necessary to identify separate sources. For example, a binary at separation of  $\approx 1$  pc at redshift  $z = 0.2$  would require a resolution of 3 milliarcseconds (Bogdanović, 2015). These resolutions can only be accomplished in the radio domain using VLBI (Very-Long-Baseline Interferometry), making direct observations in other domains of the spectrum highly unlikely. The most well-known case detected with this method is in the radio galaxy 0402 + 379, where two compact sources were identified at separation of  $\approx 7$  pc (Rodríguez et al., 2006).

The presence of an SMBH binary can also be revealed with periodic or periodic-like variations in the photometric measurements of the source that match the orbital period of the binary. Accurate optical measurements in the light curves over long periods of time can detect quasi-periodic double peaks in the light curve pattern, which can then be used to estimate the orbital period of the binary and put constraints on other orbital elements. However, this method is biased towards binaries with shorter orbital periods, on the order of 10 yr since then combining observational data from several decades can be used to observe the periodic behavior over several cycles (Bogdanović, 2015). The most well-known and studied case detected using this method is the blazar OJ 287, with observed light curve periodicity every 12 yr which is thought to host an eccentric SMBH binary with semi-major axis  $a = 0.05$  pc (Sillanpaa et al., 1988; Dey et al., 2019).

Another approach for detections is in detecting the Doppler shift of emission lines in AGN and quasars as a consequence of orbital motion of the binary. This method is similar to the one used for spectroscopic detections of stellar binaries and assumes that one or both of the SMBHs are actively accreting and with separate circumbinary disks, where the emission lines originate from. However this limits the detection range in terms of the binary orbital separation, since at higher orbital separations than the size of the emission region, the radial velocity variation of the black holes is indistinguishable from the motions within the emission region around it.

On the other hand, if the separation is considerably smaller than the size of the emission region, the emission region is subjected to the combined gravitational potential of both black holes, rather than each black hole individually. As a result, in this case there would only be a single, combined emission region, preventing detection of motions of the individual black holes (Krolik et al., 2019). Therefore, the detection range with this method translates to separations of about  $\sim 0.01 - 0.1$  pc for binaries with total mass  $10^7 - 10^8 M_{\odot}$  (De Rosa et al., 2019). Additionally, the observed Doppler shift can be caused by other mechanisms as well, making additional complimentary observations necessary to provide confirmation of the candidates.

#### 4.2 DYNAMICAL EVOLUTION OF SMBH BINARIES

Galaxy mergers are violent processes during which the shape and properties of the merging galaxies can be drastically changed. During a major galaxy merger, the gravitational potential starts to rapidly vary in time, causing significant energy changes in the stellar orbits which can completely change the orbital structure of the galaxy in a process called violent relaxation. The resulting redistribution of gas can trigger significant bursts of star formation as the system settles into a new equilibrium configuration, termed the galaxy merger remnant (hereafter GMR). The SMBHs which were originally hosted at the center of each galaxy now find themselves in the violently relaxed core of the newly merged galaxy, eventually forming a Keplerian binary system and either merging in a burst of GWs, or continuing to exist as a stalled binary. Famously, Begelman et al. (1980) described the dynamical evolution of the SMBH pair following a galaxy merger, distinguishing three main phases:

1. **Pairing phase:** At the onset of the merger, both SMBHs are surrounded by a dense stellar system denoting the central cores or cusps of their respective galaxies. During the merger the cusps sink towards the center of the remnant due to the effect of dynamical friction from the background stars, gas and dark matter. The individual cusps subsequently merge and undergo violent relaxation on a characteristic galaxy timescale. The black holes themselves sink towards the center of the gravitational potential due to dynamical friction and once they enter each other's sphere of influence, they form a stable Keplerian binary system.
2. **Stellar hardening phase:** As the separation between the black holes decreases, dynamical friction becomes less and less effective. As effects from dynamical friction decrease, the binary starts to experience many strong three-body interactions with incoming stars that cross its orbit. Via the gravitational slingshot effect, the interacting star extracts energy and angular momentum from the binary, thereby increasing its own kinetic energy and is then ejected from the binary surroundings.
3. **Gravitational wave inspiral:** The stellar three-body interactions bring the binary to sub-pc separations, where effects from GW emission start to become measurable. The GW emission effectively takes away energy and angular momentum from the binary, rapidly bringing it to coalescence.

While the presence of gas can significantly affect the SMBH binary inspiral, it is omitted from the discussion at this point since the focus of the thesis is on dynamical, stellar hardening of the binary. The effect of gas, and other hardening mechanisms will be further discussed in Sec. 4.4. Let us now investigate each of the above phases in more detail:

4.2.1 *Pairing phase*
**Dynamical friction**

The driving mechanism behind the pairing of two SMBHs following a galactic merger is the effect of dynamical friction. Dynamical friction is a well-known process that is crucial not just for SMBH pairing, but also for the orbital inspiral of satellite galaxies and mass segregation in star clusters. Chandrasekhar was the first to derive the theory of dynamical friction by examining the motion of a massive body embedded in an infinite, homogeneous, isotropic field of stars (Chandrasekhar, 1943). The field stars interact with the massive body as it moves throughout the field via small-angle scattering events and are deflected as a result. The deflected stars then form an overdensity of stars behind the massive body known as the *gravitational wake*. The massive body then feels a drag force from the wake opposite to the direction of its movement, resulting in the decrease in acceleration of the massive body, and therefore loss of energy and angular momentum. This drag force is opposite in the direction of the velocity vector of the massive body and is expressed by the Chandrasekhar dynamical friction formula (Binney and Tremaine, 1987):

$$\frac{d\vec{V}}{dt} = -\frac{16\pi^2}{3} \ln \Lambda G^2 (M+m) \frac{\int_0^V f(v) v^2 dv}{V^3} \vec{V}, \quad (4.1)$$

where  $\vec{V}$  and  $M$  are the velocity vector and mass of the massive object affected by the drag force.  $m$  and  $v$  are the mass and velocity of a field star and  $f(v)$  is the distribution function of field stars. In the above equation,  $\Lambda$  is a factor known as the Coulumb logarithm, and is defined as:

$$\Lambda = \frac{b_{\max}}{b_{\min}}, \quad (4.2)$$

where  $b_{\max}$  and  $b_{\min}$  are the maximum and minimum impact parameters for the gravitational encounters. For numerical studies, it is common to choose  $b_{\min}$  as the value of the gravitational softening of the encounter (see Ch. 5), while the value of  $b_{\max}$  is taken to be the typical length scale of the system. If  $M \gg m$  and if the velocity distribution is Maxwellian, Chandrasekhar's formula takes the following, commonly used form:

$$M \frac{d\vec{V}}{dt} = -\frac{4\pi^2 \ln \Lambda G^2 M^2 \rho}{V^3} \left[ \text{erf}(X) - \frac{2X}{\sqrt{\pi}} e^{-X^2} \right], \quad (4.3)$$

where  $\rho$  is the background density,  $X = V/(\sqrt{2}\sigma)$  is the ratio of the velocity of the massive body and the velocity dispersion and erf is the error function. However, it should be noted that Chandrasekhar's formula makes some vastly simplifying assumptions, most notably the assumption of an infinite, isotropic and homogeneous background. Realistic galactic environments violate these assumptions since the background density is not homogeneous and isotropic, and the velocity distribution is not Maxwellian and isotropic (Arca-Sedda and Capuzzo-Dolcetta, 2014). Additionally,  $\Lambda$  can significantly vary with the distance from the galactic center (Just et al., 2011) and additional semi-analytical models may need to be employed to properly model dynamical friction in rotating disks (Bonetti et al., 2020a, 2021) Despite these limitations, this formula has been proven to work remarkably well in a variety of different astrophysical contexts and is therefore widely used to estimate inspiral timescales of massive bodies such as black holes and satellite galaxies due to dynamical friction.

### Dynamical friction in galaxy mergers

During a galaxy merger the SMBHs which reside in the centers are embedded within the central cusp of each galaxy. At first the effect of dynamical friction on an SMBH is amplified due to the massive cusps surrounding it, which interacts with the surrounding matter as a single massive entity. Over time, the central cusp is stripped away by tidal forces, leaving isolated, wandering SMBHs. When this happens, the effect of dynamical friction diminishes and the inspiral slows down, since the drag force is proportional to the squared mass of the inspiraling body (Eq. 4.3). Nevertheless, eventually their separation will sufficiently decrease for the SMBHs to become bound and form a Keplerian binary system. This happens at separations comparable to the influence radius of the black holes  $r \sim r_{\text{infl}}$ , defined as:

$$r_{\text{infl}} = \frac{GM_{\text{BH}}}{\sigma^2}, \quad (4.4)$$

where  $M_{\text{BH}}$  is the combined mass of the two black holes and  $\sigma$  is the one-dimensional velocity dispersion of the surrounding stars. An alternative definition of the influence radius, which I adopt throughout the thesis, is the radius at which the enclosed mass of stars is equal to twice the combined mass of the black holes:

$$M_*(r < r_{\text{infl}}) = 2M_{\text{BH}}. \quad (4.5)$$

At this point the first phase of the SMBH binary evolution ends, and the newly-formed binary is often referred to as a *soft* binary since its binding energy per unit mass is still smaller than  $\sim \sigma^2$ .

The timescale of the dynamical friction inspiral of the SMBHs depends on their mass, velocities and the properties of the system. In minor mergers such as mergers with satellite galaxies with galaxy mass ratios 1 : 10, the individual cusp of the smaller galaxy will be tidally disrupted much faster, leaving behind an exposed SMBH and prolonging the inspiral timescale. However, if the satellite galaxy has a very compact central cusp, it can resist the tidal disruption and as a result amplify the effect of dynamical friction on the SMBH. If there is a significant fraction of gas present, it can be funneled towards the center and trigger a burst of star formation, increasing the density of the core which can resist the tidal forces (Callegari et al., 2009, 2011), resulting in successful pairing of the black holes. The presence of galactic bars makes the evolution more stochastic, and can result in either a faster decay, or a complete ejection of the SMBH (Bortolas et al., 2020, 2021). If the central remnant has a core with a mostly flat density profile, the core becomes harmonically stable and the effect of dynamical friction essentially drops to zero (Read et al., 2006) and the black hole will stall at separations comparable to the core radius (Antonini and Merritt, 2012). This can then result in damped oscillatory motion of the SMBH and the density center, where the timescale for the damping of the oscillations may exceed Hubble time (Gualandris and Merritt, 2008). Studies of cosmological simulations have also found that the fraction of stalled binaries may be as high as 40% (Kelley et al., 2017a; Kulier et al., 2015). Bortolas et al. (2020) suggested that at higher redshift, dynamical friction may not be the main driver of SMBH pairing, but rather global gravitational torques. In any case, the higher than expected number of wandering SMBHs in galaxies could then be observed as luminous X-ray sources, offset from the center of the galaxy (McWilliams et al., 2014).

### 4.2.2 Stellar hardening

The newly formed SMBH binary formed at the end of the previous phase can now be characterized in terms of some well-known Keplerian properties. Let us assume the binary consists of SMBHs with masses  $M_1$  and  $M_2$ , where  $M_1$  is the more massive SMBH,  $M_1 > M_2$ . The mass ratio of the binary is then defined as  $q = M_2/M_1 \leq 1$ . As above, we denote with  $M_{\text{BH}} = M_1 + M_2$  the total mass of the binary, and  $\mu = M_1 M_2 / M_{\text{BH}}$  represents the reduced mass. The orbital energy of the binary can then be expressed in terms of its semi-major axis (Binney and Tremaine, 1987):

$$E_b = -\frac{GM_1 M_2}{2a} = -\frac{G\mu M_{\text{BH}}}{2a} < 0. \quad (4.6)$$

Since the binary is bound, the binary orbital energy must be negative. The orbital angular momentum then takes the form of (Merritt, 2013a):

$$L = \mu [GM_{\text{BH}} a (1 - e^2)], \quad (4.7)$$

where  $e$  is the orbital eccentricity. The energy and angular momentum are often expressed in terms of the specific energy and angular momentum:

$$\epsilon_b = \frac{E_b}{\mu}, \quad l = \frac{L}{\mu}. \quad (4.8)$$

For a circular binary, when  $e = 0$  the relative velocity of the two SMBHs takes the form of the circular velocity:

$$V_{\text{circ}} = \sqrt{\frac{GM_{\text{BH}}}{a}}. \quad (4.9)$$

If the binary is eccentric,  $e > 0$ , the closest and farthest approaches of the binary are defined by the apocenter and pericenter, respectively:

$$r_a = a(1 + e), \quad r_p = a(1 - e). \quad (4.10)$$

At this point in time, dynamical friction continues to drive the SMBH inspiral, although it becomes less and less effective. Instead, the dominant mechanism of energy loss becomes close three-body interactions with individual stars. Namely, it can also happen that individual stars, of mass  $m_*$ , cross the binary orbit, resulting in a three-body scattering event. Three body interactions are complex and chaotic interactions, which will most likely result in the ejection of the incoming star. Then the encounter can go in two different ways:

- The incoming star with velocity  $v_i$  can extract orbital energy from the binary, and as a result, get a boost in its own kinetic energy so that  $v_f > v_i$  and is then scattered out to spatial infinity. As a result of the exchange, the orbital energy of the binary further decreases  $E_{b,f} < E_{b,i}$  and the binary semi-major axis shrinks. This effect is known as the gravitational slingshot effect, often used in the context of artificial satellites.
- The incoming star loses some kinetic energy, so that  $v_i > v_f$ . As a result, the binary increases its orbital energy  $E_{b,i} < E_{b,f}$ , and the binary orbit widens. After the exchange, if the total energy of the star is higher than the binary orbital energy, it will still be ejected away, despite losing energy in the interaction.

While it is possible that a three-body encounter results in an exchange, so that body  $M_2$  is

ejected, and a new binary with bodies  $M_1$  and  $m_*$  is formed, in the context of SMBH binaries, this is not expected since it usually happens when  $M_2 < m < M_1$ , which is not true in our case.

The type of interaction according to the above two distinctions depends on the *hardness* of the binary, namely the ratio of its orbital velocity  $V$  to the one-dimensional velocity dispersion of the stars  $\sigma$ . In this regard, we can distinguish between *hard* and *soft* binaries. A binary is then called hard when:

$$-E_b \geq \frac{1}{2}m\sigma^2. \quad (4.11)$$

In turn, a binary is called soft if the above relation is not fulfilled. When a binary is soft, its two components still largely interact with surrounding stars as individual bodies, and not as a single entity (Merritt, 2013a). Heggie's law states that averaged over a large number of interactions, soft binaries tend to become softer, meaning that they tend to gain energy during three-body interactions. Similarly, hard binaries tend to become harder, meaning that they tend to lose energy during three-body interactions (Heggie, 1975). Another, more robust definition of hard binaries is often used, where the binary can be considered hard if the semi-major axis satisfies the relation (Quinlan, 1996):

$$a \leq a_h = \frac{GM}{4\sigma^2}. \quad (4.12)$$

In the soft binary regime, when  $a_h < a < r_{\text{infl}}$  both dynamical friction and three-body interactions play a role in the SMBH binary energy loss, therefore this can be seen as an additional, intermediate phase of SMBH binary evolution. When  $a \leq a_h$ , however, dynamical friction becomes no longer effective and the dominant mechanism of energy loss for the binary is solely through the three-body gravitational slingshot effect, referred to as *stellar hardening*.

Stars that come within several  $a$  can interact strongly with the binary, since those stars will feel the gravitational interaction from both of the SMBHs, and not just as a single massive body. Even if the interaction results in the decrease in energy of the star, the star would likely remain in the binary surroundings, where it would come back for subsequent interactions before being ejected, extracting energy from the binary (Sesana et al., 2008). An example of this interaction is shown on Figure 4.1. Typically, a star will primarily interact with the less massive SMBH,  $M_2$ , since the more massive black hole acts as a fixed potential. After the energy exchange, the change in the specific energy of the star is given as (Merritt, 2013a):

$$\Delta\epsilon_* \approx \left(\frac{M_2}{M}\right)V_{\text{circ}}^2, \quad (4.13)$$

under the assumption of a circular binary. Then, a dimensionless coefficient can be defined which denotes the energy change of the binary (Hills, 1983):

$$C = \frac{M}{2m_*} \frac{\Delta\epsilon_b}{\epsilon_b} = \frac{a\Delta\epsilon_*}{G\mu}. \quad (4.14)$$

Scattering experiments of isolated three-body interactions have been crucial to constraining the value of  $C$  for different binary configurations, finding that the value of  $C$  is on the order of unity (Quinlan, 1996; Sesana et al., 2006). After the interaction the star gets a velocity kick comparable to the binary orbital velocity. For hard binaries, this kick is likely sufficient to eject the star beyond the influence radius of the binary, making it unlikely that the star would return for a repeated interaction.

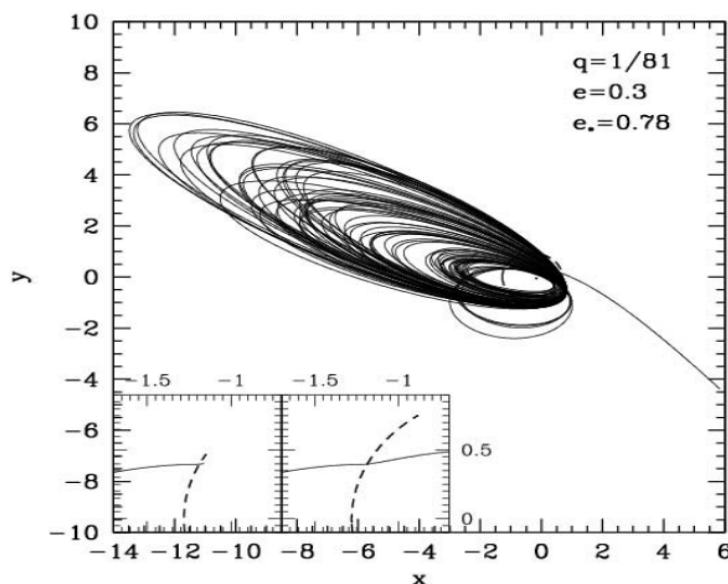


**Figure 4.1:** An example of a multiple interaction and subsequent ejection of stellar particle obtained in a scattering experiment. The mass ratio  $q$  and binary eccentricity  $e$  are denoted in the top right corner. The initial eccentricity of the star is denoted by  $e_*$ . The binary orbit is denoted by dashed lines, and the position of the more massive black hole is denoted by a dot. The zoom-ins at the lower-left corner show the moment of scattering of the star. Image credit: [Sesana et al. \(2008\)](#).

The secular changes in the binary semi-major axis due to many three-body encounters can then be defined as the dimensionless *binary hardening rate*:

$$H = \frac{\sigma}{G\rho} \frac{d}{dt} \left( \frac{1}{a} \right), \quad (4.15)$$

where  $\rho$  is the stellar density and  $\sigma$  the one-dimensional velocity dispersion. In N-body studies, the hardening rate is often expressed as  $s = da/dt$  due to ease of computation of the parameter. The hardening rate of a binary is roughly constant, and only weakly depends on the mass ratio of the black holes ([Quinlan, 1996](#)).

Two more dimensionless parameters can be introduced to characterize the binary evolution. These are the rate of mass ejection  $J$  and rate of eccentricity change  $K$ :

$$J = \frac{1}{M_{\text{BH}}} \frac{dM_{\text{ej}}}{d\ln(1/a)} \quad \text{and} \quad K = \frac{de}{d\ln(1/a)}, \quad (4.16)$$

where  $M_{\text{ej}}$  is the total mass of ejected stars.

The changes in the binary eccentricity denoted by the parameter  $K$  are a consequence of the change in the angular momentum of the binary, or more specifically, the amplitude of its angular momentum. The positive or negative change in eccentricity depends on whether the incoming orbits are prograde or retrograde with respect to the binary. While the population of prograde and retrograde orbits depends on the degree of rotation in the system, in most cases, evolution results in an increase in eccentricity, when  $K \geq 0$ . For equal mass binaries with  $e = 0.75$ , the value of  $K$  grows as the binary hardens, reaching  $K \approx 0.2$ . However, when  $e = 0$  and  $e = 1$ , the value of  $K$  falls to zero ([Merritt, 2013a](#)).

The three dimensionless parameters  $H, J$  and  $K$  are constrained by fits performed using scattering experiments (Quinlan, 1996; Sesana et al., 2006, 2008, 2011; Rasskazov and Merritt, 2017; Rasskazov and Kocsis, 2019; Bonetti et al., 2020b). However, scattering experiments often assume an infinite supply of closely interacting stars, which may not be the case in realistic nuclei, which will be further discussed in the next section.

#### 4.2.3 Gravitational wave inspiral

Once the separation of the black holes decreases to about  $a \sim 0.001 - 0.01$  pc, either by stellar hardening or some other process, the GW emission becomes the dominant mechanism of energy loss. The GW emission proceeds according to the analytical formulas described in the previous chapter (Eqs 3.18 and 3.33) and the binary is quickly brought to coalescence on a Peters timescale (Peters, 1964):

$$T_{\text{GW}} = \frac{5}{256} \frac{c^5 a_0^4}{G^3 M_1 M_2 M_{\text{BH}} f(e_0)}, \quad (4.17)$$

where  $a_0$  is the initial semi-major axis and  $f(e_0)$  is expressed as:

$$f(e) = \left(1 + \frac{73}{24}e^2 + \frac{37}{96}e^4\right)(1 - e^2)^{-7/2}. \quad (4.18)$$

This timescale can be rewritten in a simpler form, under the assumption of a circular binary (Gualandris et al., 2017):

$$T_{\text{GW}} \approx 5.8 \times 10^8 \left(\frac{a}{10^{-3} \text{ pc}}\right)^4 \left(\frac{10^6 M_{\odot}}{M_{\text{BH}}}\right)^3 \text{ yr}. \quad (4.19)$$

While the standard Peters timescale has remained in widespread use, recent studies introduced PN1 perturbation and eccentricity evolution correction factors to the Peters timescale, with the full expression given as (Zwick et al., 2020, 2021):

$$T'_{\text{GW}} = T_{\text{GW}} 8^{1-\sqrt{1-e_0}} \exp\left(\frac{2.5 r_{\text{sch}}}{a_0(1-e_0)}\right), \quad (4.20)$$

where  $r_{\text{sch}}$  is the effective Schwarzschild radius of the binary.

The merger itself will form a new SMBH, which will receive a velocity recoil kick ranging up to 5000 km/s (Campanelli et al., 2007; Lousto and Zlochower, 2007; Lousto et al., 2012; Nasim et al., 2020). These kicks can result in the SMBH being ejected out of its core region, leading to oscillatory motion through the central region which will be slowly damped by dynamical friction (Gualandris and Merritt, 2008).

### 4.3 FINAL PARSEC PROBLEM

During the stellar hardening phase, the black holes will quickly clear the inner region from loss cone stars on radial orbits in an effect known as *core scouring*. The ejected stars will cause a mass redistribution within the inner region, comparable to  $r_{\text{infl}}$ . As a result, the stellar density within the inner region will decrease, and the density profile will flatten, resulting in a core rather than a cusp profile. This effect is supported by observational evidence in massive elliptical galaxies, which demonstrate flat inner regions in their light profiles (e.g. Rusli et al., 2013; Dullo

et al., 2017). The radius of the core is correlated with the mass of the black hole and is typically  $r_c \sim 50 - 500 \text{ pc}$ , but can range up to kpc scales (Rantala et al., 2018). The ejected stars within the inner  $\sim r_{\text{infl}}$  correspond to the low angular momentum stars and their ejection will leave a gap in the phase space structure of the galaxy. As discussed in section 2.5.2, in equilibrium spherical systems the only mechanism of loss cone refilling is via two-body relaxation effects. The time required for refilling the loss cone can range up to  $10^{10} \text{ yr}$  in bright elliptical galaxies (Merritt and Wang, 2005). With the loss cone section of phase space largely empty at a given time, the SMBH binary will harden in this empty-loss cone regime, leading to stalling at parsec separations. In this regime, GW emission is not significant enough to efficiently extract energy from the binary leading to merger timescales of the SMBH binary times longer than the Hubble time. This issue is widely known in the literature as the *Final Parsec Problem*.

The FPP arose as a theoretical bottleneck at the start of the 21<sup>st</sup> century as a result of numerical studies that investigated loss cone refilling mechanisms. Under the assumption of collisional loss cone refilling mechanisms in spherical galaxies, the hardening rate of the binary, and therefore the loss cone refilling rate should scale with the number of particles in the simulation  $T_{\text{rel}} \sim N$ . However, in order to achieve this, a sufficiently high number of particles needs to be used so that the relaxation time is much longer than the dynamical time of the system (Vasiliev, 2016). Early studies, such as Milosavljević and Merritt (2001) reported hardening rates independent of the number of particles  $N$ , pointing to the full loss cone hardening regime. However, Milosavljević and Merritt (2003a) reported that this was due to insufficient particle numbers employed, and that particle numbers on the order of  $N \lesssim 10^6$  are required to avoid artificial effects originating from low particle numbers. Berczik et al. (2005) utilized the parallel computation ability of GRAPE cards (see description in Ch. 5) to generate Plummer models of  $N \sim 0.5 \times 10^6$  particles. They found that the hardening rate strongly depends on  $N$ , as expected from collisional loss cone repopulation (see Fig. 4.2). The binaries were found to be in the empty loss cone regime, suggesting that it is unlikely that SMBH binaries would merge within a Hubble time in gas-poor mergers.

The prospect of stalling SMBH binaries would pose a problem for models of efficient SMBH growth through mergers, as well as future GW searches from these systems. Furthermore, observational evidence suggests short coalescence times when compared to the Hubble time, due to the proportionally low number of detected periodic motions of the binary in galactic nuclei.

#### 4.4 SOLUTIONS TO THE FINAL PARSEC PROBLEM

Today, the FPP is usually thought of as a relic of the past, and a consequence of idealized approximations that do not necessarily reflect realistic galaxies. In recent years a number of physical effects have been discussed as potential solutions to the FPP. Here, I will discuss the main processes which can effectively resolve the FPP and lead to effective SMBH hardening up to the GW-dominated regime.

##### 4.4.1 Collisionless loss cone refilling

One mechanism of resolving the FPP is through collisionless loss cone refilling, which is explored in more detail in Ch. 7 of this thesis. In spherical nuclei, the only way to repopulate the loss cone is through collisional relaxation effects. However, as discussed in Sec. 2.5.3

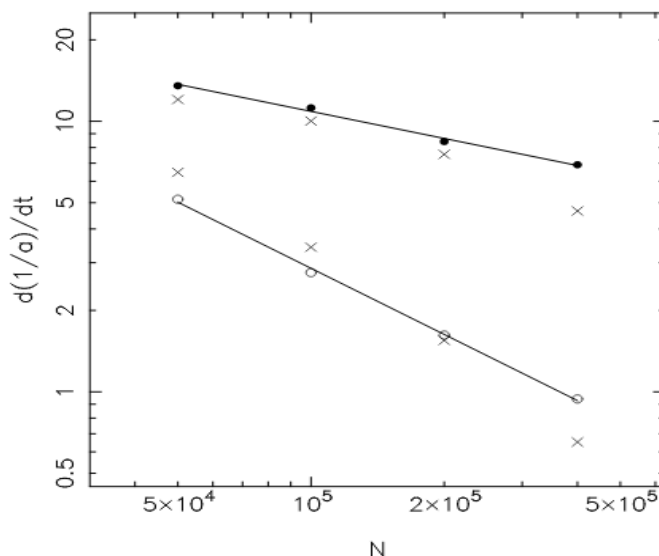


**Figure 4.2:** Mean binary hardening rates as a function of particle number in idealized, spherical Plummer models. Crosses show the theoretical predictions, while circles correspond to results from simulations (open circles correspond to a more massive binary, while filled circles represent a low mass binary). The lines are obtained as least square fits to the data. Image credit: [Berczik et al. \(2005\)](#).

the situation is quite different in axisymmetric or triaxial nuclei, when the notion of spherical symmetry is abandoned. Giant elliptical galaxies are largely thought to be triaxial in shape, and galactic mergers can drastically change the shape of the remnant, even if the original host galaxies were spherical. Therefore, there is no physical justification for restricting the problem to only spherical cases.

[Merritt and Poon \(2004\)](#) constructed self-consistent triaxial models with a central SMBH to investigate collisionless loss cone refilling rates. They found that presence of centrophilic chaotic orbits coming from outside of the influence radius resulted in feeding rates of the SMBH consistent with the full loss cone regime. As a result, they estimated that chaotic orbits corresponding to only a few percent of galaxy's mass were sufficient to overcome the FPP and lead to coalescence of an SMBH binary. [Berczik et al. \(2006\)](#) were the first to perform full direct N-body simulations in rotating, non-axisymmetric galaxy models. They found no dependence on  $N$  in the hardening rates, pointing to collisionless loss cone repopulation. This suggested that the stalling of the binaries observed in previous studies was a consequence of idealized models assuming spherical symmetry, and that more realistic galaxy models provide a natural way to repopulate the loss cone via purely dynamical means. [Preto et al. \(2011\)](#) and [Khan et al. \(2011\)](#) started from spherical galaxy models, but found that the merger naturally results in a triaxial galaxy merger remnant. They found that even a mild amount of triaxiality was sufficient to bypass the FPP, showing higher hardening rates with respect to purely spherical merger remnants. The efficient hardening of the binary suggested that prompt mergers of SMBH binaries might be common, even in the absence of gas torques. Additionally, [Vasiliev et al. \(2015\)](#) used a Monte Carlo method and [Gualandris et al. \(2017\)](#) used the fast multipole code GRIFFIN to investigate collisionless loss cone repopulation. Both studies found that even a slight deviation from axisymmetry is sufficient to resolve the FPP. In the case of axisymmetric galaxies however, the picture is less clear. A solution to the FPP was reported in the axisymmetric case for galaxies

in equilibrium (Khan et al., 2013), as well in rotating galaxies (Khan et al., 2020; Mirza et al., 2017; Holley-Bockelmann and Khan, 2015). On the other hand, Vasiliev et al. (2014) finds that axisymmetry alone is not enough, but that even small deviations from axisymmetry can lead to coalescence. Finally, Kh16, used cosmological simulation data as initial conditions for direct N-body simulations of the entire evolution of an SMBH binary, from formation until coalescence. They report a coalescence timescale on the order of  $\sim 10$  Myr, suggesting fast coalescence in gas-poor mergers. The system and results of this study are given in more detail at the end of this chapter.

#### 4.4.2 Gas and accretion

So far the discussion has been restricted to purely dynamical SMBH binary hardening mechanisms. However, the presence of gas can impact the evolution of the binary in crucial ways. Following galaxy mergers, gas inflows can bring large quantities of gas to the very central region of the remnant (Mayer et al., 2007). This can lead to the formation of massive circumnuclear gaseous disks with radius of  $\sim 100$  pc and thickness of  $\sim 10$  pc. As the binary hardens, the large amount of background gas in the circumnuclear disk can exert gravitational torques on the SMBH binary, accelerating its coalescence. Escala et al. (2005) found that the effect of the torques was sufficient to bring the binaries to coalescence for different model parameters within a  $\sim 10^7$  yr timescale. On smaller, sub-pc scales, gas inflows can form a common circumbinary accretion disk around the black holes. The gravitational torque from the motion of the SMBHs will open a cavity within the innermost region. Accretion onto the SMBHs is then driven by streams, from the circumbinary disk, onto each SMBH, forming a mini-disk around it (Roedig and Sesana, 2014). As the black holes accrete, they can episodically eject clumps of gas outward, injecting angular momentum into the circumbinary disk. Due to its dissipative nature, gas is very efficient in angular momentum transport, which is then transported outward throughout the disk, leading to the shrinking of the binary orbit. Cuadra et al. (2009) found that the circumbinary disk can dominate the dynamics of the binary at sub-pc scales. As the binary separation decreases, the torque the binary exerts on the disk will be stronger, resulting in more efficient transfer of angular momentum. They found that this mechanism is sufficient to coalesce the black holes within a Hubble time if the mass of the binary is  $M \leq 10^7 M_{\odot}$ . Roedig and Sesana (2014) investigated the impact of a retrograde self-gravitating circumbinary disk on the binary orbital parameters. They found no effect on the disks being prograde or retrograde on the evolution of the binary semi-major axis. They also found that the gas flows ejected back into the disk followed the dynamics of three-body scattering.

It can occur that gas clumps can detach from the circumnuclear gaseous disk and infall radially towards the center, potentially forming molecular clouds along the way. This can result in incoherent, episodic infall of the gas towards the binary from arbitrary directions. The infalling gas clumps can boost the binary accretion rate, as well as affect the binary dynamics. Goicovic et al. (2017) simulated the infall of a single molecular cloud towards the binary. They found that the shrinking of the hardening rate of the binary depends on initial orbital configurations with the molecular cloud, as well as with the fraction of total mass accreted. Goicovic et al. (2018) explored the issue further, by simulating a larger number of stochastic infall events of gas clumps. They found mass accretion is significantly enhanced following the infall and that the gravitational torques are efficient in transporting outward the angular momentum lost by the binary by slingshots of gaseous streams following the infall. This makes this mechanism a

viable option to circumventing the FPP. Finally, [Souza Lima et al. \(2020\)](#) followed the evolution of the binary over scales of hundreds of parsecs, from the large circumnuclear disk scales, down to the circumbinary scales. They found the decay of the binary to be rather stochastic, and dependent on various model parameters. Nevertheless, they identified three distinct phases during the decay, resulting in efficient hardening down to scales where GW emission becomes dominant.

#### 4.4.3 *Massive stellar perturbers*

[Perets and Alexander \(2007\)](#) showed that the presence of massive perturbers, such as giant molecular clouds or stellar clusters in galactic nuclei can significantly shorten the relaxation timescale in the inner region, driving stars onto loss cone orbits and resulting in binary merger timescales within a Hubble time. [Bortolas et al. \(2018b\)](#) investigated the effect of a massive stellar cluster infalling on a SMBH binary with parsec scale separations. They placed the stellar cluster on radial and eccentric orbits, and in orbits perpendicular and coplanar with respect to the SMBH binary orbital plane. They found that clusters placed on eccentric orbits do not measurably increase the hardening rate, while clusters on radial orbits can result in effective refilling of the loss cone when the cluster becomes tidally stripped. Similarly, [Arca Sedda et al. \(2019\)](#) explored repeated interactions of a globular cluster with an SMBH binary. They found that the interactions with a cluster on a retrograde orbit can significantly impact the orbital parameters of the binary, such as a rise in eccentricity, resulting in shorter merger timescales. The disruption of the cluster repopulated the loss cone phase space, and repeated interactions with the cluster would cause the binary to coalesce within a Hubble time in the case of when the total mass of the binary is  $M = 10^7 M_{\odot}$ . While the disruption of stellar clusters is not expected to be a common occurrence, this mechanism does provide a way to boost SMBH hardening in a system where it would otherwise stall.

#### 4.4.4 *Triple systems*

When a binary stalls within a merger remnant, it is reasonable to assume that during the binary lifetime, the galaxy would experience another merger which would bring in a third massive black hole into the system, forming a massive black hole triplet. The evolution of such a three-body system would be highly chaotic and dependent on initial conditions. In all but some special cases, the triple system would be unstable and would result in the ejection in one of the black holes (usually the ejected black hole would be the least massive one), leaving behind a two-body Keplerian binary. The single-binary interactions before the ejection of the third body could then increase the orbital eccentricity of the surviving binary, thus significantly shortening the GW inspiral timescale, since GW emission is much more effective for higher eccentricities. When combined with other hardening mechanisms, such as stellar hardening or gas torques, this could lead to the coalescence of the surviving binary within a Hubble time.

Another method of increasing the eccentricity is via Kozai-Lidov oscillations ([Kozai, 1962](#); [Lidov, 1962](#)). Namely, in the case when the black holes form a hierarchical triple system, with a well-defined inner binary and an outer black hole, Kozai-Lidov resonances can induce periodic variations in the orbital elements of the inner binary, including the eccentricity. Similar to the previous mechanism, the growth in eccentricity can significantly shorten GW-induced merger timescales.

[Iwasawa et al. \(2006\)](#) placed three SMBH particles in a single galaxy model and inves-

tigated their subsequent evolution. They found that if the triple orbits are coplanar, the inner binary hardens through binary-single interactions, while in the non-coplanar case, Kozai-Lidov oscillations of eccentricity drive the hardening rate. They found that in most cases the inner binary merges before the ejection of the third black hole, providing a potential solution of the FPP. However, they found also a significant number of ejected SMBHs, which could potentially be detected as wandering black holes. [Hoffman and Loeb \(2007\)](#) investigated mergers between massive ellipticals at high redshift. They also found a high fraction of merging SMBHs supporting triplets as a valid solution to the FPP, but for smaller mass black holes an ejection is more likely leaving behind an uncoalesced binary. On the other hand, [Tanikawa and Umemura \(2011\)](#) found that including precession effects arising from the PN1 correction to the equations of motion destroys the Kozai-Lidov resonances, making this mechanism ineffective in increasing the binary eccentricity. However, the single-binary interactions could still bring the binary to coalescence. Finally, [Bonetti et al. \(2018\)](#) used a three-body PN-corrected integrator ([Bonetti et al., 2016](#)) to investigate triplet evolution for a variety of mass ratios and for black hole masses of  $10^5 M_{\odot} \leq M \leq 10^{10} M_{\odot}$ , giving a comprehensive overview of the parameter space. They found the merger fraction to be 30%, with the vast majority of mergers induced during the single-binary interaction, while 1/5 of mergers were delayed following the ejection of the third black hole. They investigated the importance of Kozai-Lidov oscillations and found they are successful at inducing the merger, except for low mass ratios between the inner and outer binary, when the resonances are destroyed by the 1PN term, resulting in a failure of the binary to merge. The above mentioned results solidify triple interactions as a viable solution to the FPP, especially when combined with other mechanisms.

#### 4.4.5 Other effects

Along with above described solutions to the FPP, several other approaches have been put forth that may influence the SMBH binary orbital evolution. Brownian motion of the SMBH binary can result in additional diffusion of stars in the loss cone ([Bortolas et al., 2016](#)). Additionally, the presence of a rotating stellar cusp can affect the SMBH binary properties, as well as its interactions with incoming stars ([Rasskazov and Merritt, 2017](#); [Wang et al., 2014](#); [Li et al., 2012](#)). Most recently, [Ogiya et al. \(2020\)](#) showed that tidal effects from merging nuclear star clusters can also significantly shorten the SMBH merger timescale. Additionally, the development of a galactic bar can significantly accelerate the inspiral ([Bortolas et al., 2020](#)). As a result from efficient collisionless loss cone refilling, as well as other effects listed above, merger timescales are now estimated to be  $t_{\text{merger}} \lesssim 1 \text{ Gyr}$  ([Biava et al., 2019](#); [Khan et al., 2018b,c](#); [Rantala et al., 2017](#)).

#### 4.5 KHAN ET AL. (2016)

Much of the work done in this thesis uses the system from [Kh16](#) as a starting point, specifically chapters 5, 6 and 7. Therefore, in this section I will describe the results of the study and properties of the system in more detail. In that work, a massive galaxy merger at redshift  $z \sim 3.5$  was identified and followed using the Argo cosmological simulation (see Fig. 4.3, [Feldmann and Mayer, 2015](#); [Fiacconi et al., 2015](#)). At a time which we will refer to as the initial time  $t_{\text{ini}}$  throughout the text, a static particle splitting procedure was performed in order to increase the particle number and two SMBH particles, with masses  $M_{\text{BH1}} = 3 \times 10^8 M_{\odot}$ ,  $M_{\text{BH2}} = 8 \times 10^7 M_{\odot}$ , were introduced at the local minima of the gravitational potential of the galactic cores.

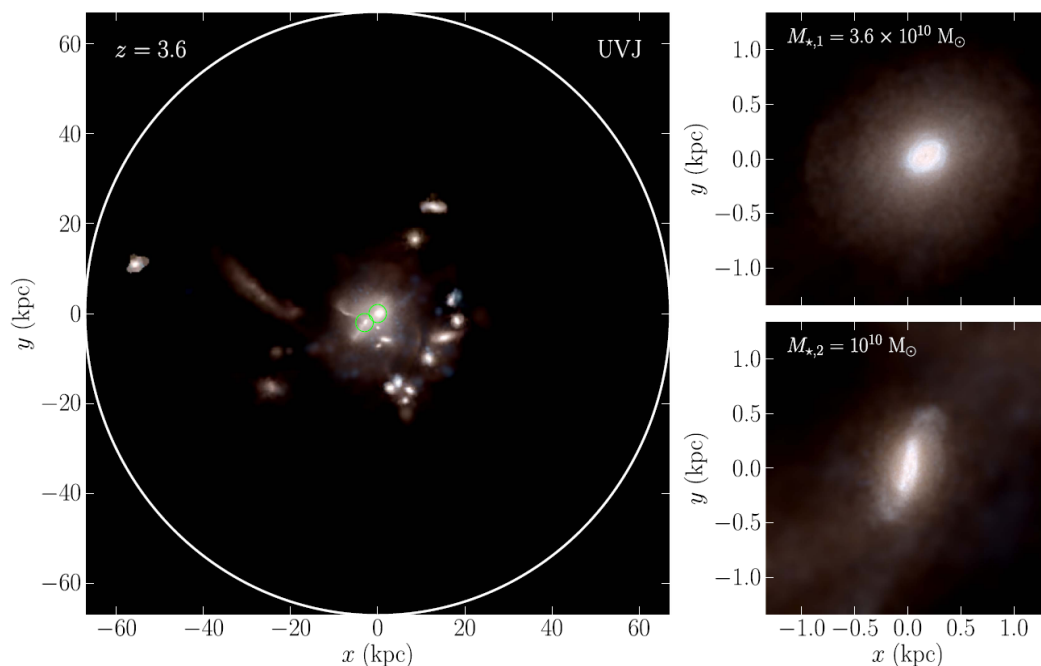


**Figure 4.3:** Mock photometric image of the galaxy group in the Argo cosmological simulation at  $z = 3.6$ . The white circle marks the virial radius of the group halo and the green circles show the merging galaxies of interest. Panels on the right show the central galaxy of the group (top), and its merger companion (bottom). Image credit: [Khan et al. \(2016\)](#).

The system was evolved further using the GASOLINE code ([Wadsley et al., 2004](#)) and during the final stages of the merger, the galaxy merger remnant had a gas fraction of only 5%. At time  $t_{PN} = t_{ini} + 21.5$  Myr the remaining gas particles were turned into star particles, a spherical region of 5 kpc around the most massive SMBH was extracted, the softening was further reduced and the PN terms were turned on. At this stage, the separation between the black holes was  $\sim 300$  pc. The final particle number after these procedures was  $N \sim 6 \times 10^6$  particles, consisting of  $N \sim 6 \times 10^6$  particles, consisting of 2 SMBH particles, 414,414 dark matter particles, and 5,511,152 star particles. The entire system has a mass of  $9.18 \times 10^{10} M_{\odot}$ , while the dark matter and typical stellar particle mass is  $1 \times 10^5 M_{\odot}$ ,  $9.1 \times 10^3 M_{\odot}$ , respectively. This system was then further evolved using the direct N-body code  $\phi$ -GPU ([Berczik et al., 2011](#)). For more details on the simulation setup, I refer the reader to [Kh16](#).

After the start of the direct N-body run, dynamical friction is efficient in bringing the black holes close enough to form a Keplerian binary within 2 Myr. A hard binary is subsequently formed within a Myr, and then the evolution of the binary is dominated by stellar interactions. The hardening phase continues for 8 Myr, after which the GW emission becomes important. Integration was continued until the merger of the SMBH particles 2 Myr later, induced by the PN corrections (up to order 3.5) in the equations of motion. On left panel of Fig. 4.4, the binary separation is shown as a function of time. The fast coalescence of the binary was attributed to a large population of stars on centrophilic orbits, since the merger remnant remained slightly triaxial throughout the run (see Fig. 4.4, middle panel). The evolution of the binary from its formation until coalescence was 10 Myr. This was the first study in the literature to model the entire evolution of a SMBH binary, starting from cosmological initial conditions, down to the Post-Newtonian plunge of the black holes.

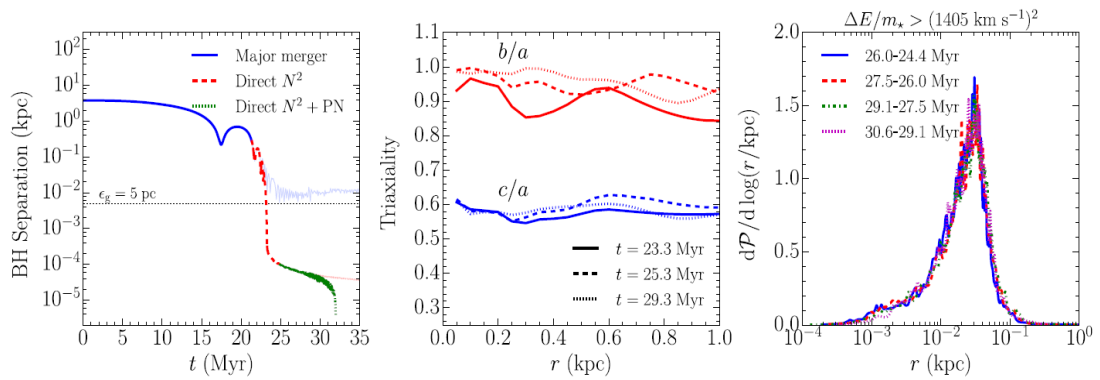


**Figure 4.4:** Left: separation of the SMBH binary as a function of time. The different colored lines represent the hydrodynamical run (blue) and the direct N-body run without (red) and with PN corrections (green). Faded versions of the same lines represent the continuation of those respective runs. The horizontal line denotes the value of the softening in the hydrodynamical run. Middle: Ratios of the principal axes of the moment of inertia tensor as a function of radial distance. The different line styles correspond to different times. Right: Probability density function of the radial distance of stars with large energy changes. Different colors correspond to different times throughout the run. Image credit: [Khan et al. \(2016\)](#).

---

 NUMERICAL DESCRIPTION
 

---

The gravitational force dominates the distribution and evolution of all matter in the Cosmos across all but the smallest of scales. Under the influence of gravity, stars are brought together to form large-scale systems such as galaxies, clusters and planetary systems. To study these systems, we can think of them as collections of  $N$  massive bodies (or particles), where one such body moves under the influence of all the collective gravitational interactions coming from the other  $N-1$  massive bodies. This is known as the  $N$ -body problem, where the gravitational force exerted on body  $i$  from body  $j$  takes the form (Binney and Tremaine, 1987):

$$\vec{F}_{i,j} = -\frac{Gm_i m_j (\vec{x}_i - \vec{x}_j)}{|\vec{x}_i - \vec{x}_j|^3}, \quad (5.1)$$

where  $G$  is the gravitational constant,  $m_i$  and  $m_j$  are the masses and  $\vec{x}_i, \vec{x}_j$  are the position vectors of bodies  $i$  and  $j$ , respectively. Then, we can write the collective gravitational force felt by body  $i$  as the following sum:

$$\vec{F}_i = \sum_{\substack{j \neq i \\ j=1}}^{N-1} \vec{F}_{i,j} = -\sum_{\substack{j \neq i \\ j=1}}^{N-1} \frac{Gm_i m_j (\vec{x}_i - \vec{x}_j)}{|\vec{x}_i - \vec{x}_j|^3}. \quad (5.2)$$

In order to solve the problem, at each time we need to calculate the sum in Eq. 5.2 for particles  $i = 1, \dots, N$ .

Since we can relate the acceleration with the force with  $\frac{\partial^2 \vec{r}_i}{\partial t^2} = \vec{F}_i / m_i$ , it is evident that the problem is a set of  $N$  coupled, non-linear second order differential equations. These equations are not possible to solve by analytic means for  $N > 2$ , and require numerical integration in order to find a solution. Additionally, special care must be taken to ensure accuracy as well as efficiency of the calculation, since at distances that approach zero the gravitational force diverges, leading to singularities as well as increasingly worse performances due to more frequent time integration required by close interactions. Therefore, in order to ensure physical results, commonly an additional parameter is introduced, termed the *gravitational softening* parameter,  $\epsilon$ . The softening represents the minimum relative distance the particles can reach in

the simulation, and therefore modifies the gravitational interaction in the following way:

$$\vec{F}_i = - \sum_{\substack{j=1 \\ j \neq i}}^{N-1} \frac{Gm_i m_j (\vec{x}_i - \vec{x}_j)}{(|\vec{x}_i - \vec{x}_j|^2 + \epsilon^2)^{3/2}}. \quad (5.3)$$

As such, the softening length is a standard and crucial parameter in N-body modeling, and when appropriately chosen, can improve performance by preventing bottlenecks resulting from the formation of tight binary systems, without greatly sacrificing accuracy of the calculation.

In this chapter, I will detail three main force calculation approaches that are commonly used today in order to resolve the above described equations. Then, I will proceed by describing all of the different N-body codes which have been used in the research carried out for this thesis. This will serve as an introduction to the final part of the chapter, where I will present a series of numerical tests and benchmarks that I have performed using the novel N-body code  $\phi$ -GRAPE-hybrid. I will give an overview of the optimal numerical parameters for use of  $\phi$ -GRAPE-hybrid in galactic simulations. More specifically, I will discuss different maximum orders in the multiple expansion series, our analysis of optimal compilers, benchmarks and investigations of optimal numerical parameters for simulations of galactic nuclei, such as the softening, integration timestep and centering strategy.

## 5.1 FORCE CALCULATION

### 5.1.1 Direct N-body

The most straight-forward approach to solve the N-body problem is via direct N-body simulations. In a direct N-body simulation, Eq. 5.3 is simply solved directly for each particle at a certain time determined by the individual block-timestep of the particle (described in Sec. 5.2.1) and the system is then integrated forward in time using a numerical integration scheme. While highly accurate, this method comes at a very high computational cost since the number of operations required at each time is on the order of  $O(N^2)$ .

The history of direct N-body simulations began with the pioneering work by (Holmberg, 1941), who followed the evolution of a stellar system consisting of 37 particles using lightbulbs as individual stars, where the amount of light was proportional to stellar mass. Naturally, the invention of computers has caused a revolution in N-body studies, with the first computational N-body simulation performed by von Hoerner (1960) with 16 particles, followed by Aarseth (1963) with up to 100 particles. The subsequent fast development of hardware was closely followed by improved direct integration methods, such as regularization techniques invented for the purpose of accurate treatment of binaries and bound systems (e.g. Kustaanheimo-Steifel (KS) regularization, Kustaanheimo and Stiefel 1965 and the chain regularization method, Mikkola et al. 1990). Furthermore, the appearance of dedicated hardware such as GRAPEs (GRAvity PipE, Ito et al. 1990), optimized specifically for computation of gravitational interactions as well as the emergence of parallel computing (OpenMP and MPI (Message Passing Interface)) have enabled direct N-body studies to reach  $N \sim 10^6$  particles with  $\sim$  Tflop (i.e. one Trillion FLoating Point OPerations per second) performance (Harfst et al., 2007). Finally, performing computations on GPUs (Graphics Processing Unit) instead of CPUs (Central Processing Unit), such as those using NVIDIA's CUDA architecture (Compute Unified Device Architecture, Hamada and Iitaka 2007; Nyland et al. 2007; Belleman et al. 2008) has resulted in very

significant acceleration of the simulations, making GPU-accelerated direct N-body studies the norm today.

Today, direct N-body methods have successfully reached the particle numbers and efficiency necessary to construct realistic simulations of large stellar systems such as globular clusters (Wang et al., 2016). However, in larger systems such as galaxies with typical numbers of stars on the order of  $\sim 10^{10}$ , individual encounters between the particles do not contribute measurably to the evolution of the system as a whole. This is due to the fact that the relaxation timescale of such systems (i.e. the time needed for two-body particle interactions to considerably change a particle's velocity) is larger than the Hubble time. Therefore, these systems unlike stellar clusters, are referred to as *collisionless* (see Sec. 2.5.2) and are usually treated with other, indirect (collisionless) N-body methods. We will describe below two examples of such methods.

### 5.1.2 Self-consistent field method

Since a galaxy can be considered a collisionless system for timescales longer than the Hubble time, the motion of individual stars in the galaxy will not be governed by direct interaction with other bodies, but rather by the mean, collective gravitational potential generated by all of the other bodies (except in the centers of galaxies where two-body relaxation effects become non-negligible). This means that a star moves in a smooth gravitational field, unperturbed by individual interactions. Therefore, the idea behind multipole expansion methods, and specifically the below-described self-consistent field method (SCF) is that instead of computing all individual interactions, one can simply compute the mean gravitational field from a collection of particles, thereby reducing the computational cost significantly.

This can be accomplished by solving the Poisson equation:

$$\Delta\Phi(\vec{r}) = 4\pi G\rho(\vec{r}). \quad (5.4)$$

While the Poisson equation can in principle be reduced to Eq. 5.3, the difference with the direct N-body approach comes from the fact that instead of discretizing  $\rho(\vec{r})$  as a collection of individual massive bodies, we can expand the potential and density as a set of basis functions. If the zeroth order basis functions are chosen carefully, the entire expansion series can be safely truncated at some pre-determined low order without significant loss of precision.

The first implementation of what is now known as the SCF method was by Clutton-Brock (1972) who constructed a set of bi-orthogonal pairs of basis functions which could be used for the calculation of gravitational fields of flat galaxies. This method was then expanded for three-dimensional mass distributions in Clutton-Brock (1973). The first modern implementation was by Hernquist and Ostriker (1992), who also coined the term: *self-consistent field method*. We below detail the SCF method as described in Hernquist and Ostriker (1992).

In many cases galaxies can be considered spherical or spheroidal in shape. Even in the case of highly flattened galaxies, there is a spherical dark halo component to a galactic system. Therefore, it is most appropriate to choose a spherical model as the zeroth order term for the subsequent multipole expansion. While different spherical models can be chosen for this purpose, similar to Hernquist and Ostriker (1992) we will expand the potential-density pair around the Hernquist density profile (Hernquist, 1990):

$$\rho(r) = \frac{M}{2\pi} \frac{a}{r} \frac{1}{(r+a)^3}, \quad (5.5)$$

$$\Phi(r) = -\frac{GM}{r+a}, \quad (5.6)$$

where  $M$  is the total mass of the model and  $a$  is the scale radius. Then, we can assume the existence of two bi-orthogonal basis sets and express the quantities in the form of a multipole expansion:

$$\rho(r) = \sum_n \sum_l \sum_{m=-l}^{+l} A_{nlm} \rho_{nlm}, \quad (5.7)$$

$$\Phi(r) = \sum_n \sum_l \sum_{m=-l}^{+l} A_{nlm} \Phi_{nlm}, \quad (5.8)$$

where  $A_{nlm}$  are the coefficients of the expansion and  $\rho_{nlm}$  and  $\Phi_{nlm}$  are the basis functions of the density and potential which are pre-determined and must also satisfy the Poisson equation  $\Delta\Phi_{nlm} = 4\pi G\rho_{nlm}$ . The three integers  $(n, l, m)$  in the equation above correspond to the radial expansion number in the case of  $n$  and the angular expansion numbers in the cases of  $l$  and  $m$ . Since two of the sums are infinite, they need to be cut off at some order of  $(n_{max}, l_{max})$ . Naturally, higher orders in  $(n_{max}, l_{max})$  provide greater accuracy at the cost of sacrificing performance. The standard choice for these values is  $(10, 6)$  (Meiron et al., 2014).

The zeroth order functions  $\rho_{000}$  and  $\Phi_{000}$  (when  $n = l = m = 0$ ) then correspond to Eqs. 5.5-5.6 and higher orders in  $n$  and  $l$  correspond to further deviations from spherical symmetry. The angular part of the basis functions, determined by expansion numbers  $(l, m)$  in the case of  $n = 0$  can be easily computed using spherical harmonics:

$$\Phi_{0lm} = -\frac{r^l}{(1+r)^{2l+1}} \sqrt{4\pi} Y_{lm}(\theta, \varphi), \quad (5.9)$$

where  $Y_{lm}$  are the standard spherical harmonics and  $\theta$  and  $\varphi$  are the polar and azimuthal angle in spherical coordinates, respectively. The  $\rho_{0lm}$  term is found correspondingly from the Poisson equation.

In the case of  $n \neq 0$  however, we need to adopt a radial basis. The choice of the radial basis is not unique and a basis can be constructed using various orthogonal polynomials. For our purpose we will adopt Gegenbauer (ultraspherical) polynomials (Szego, 1975):

$$\Phi_{nlm} = -\frac{r^l}{(1+r)^{2l+1}} C_n^{2l+3/2}(r) \sqrt{4\pi} Y_{lm}(\theta, \varphi), \quad (5.10)$$

where  $C_n^{(\alpha)}(r)$  are the Gegenbauer polynomials.

With the basis set now known, the potential of the system is only dependent on the coefficients  $A_{nlm}$ , while the basis functions are calculated beforehand. Therefore, in order to solve Eq. 5.4, it is only needed to compute  $A_{nlm}$  using the mass density of the matter distribution and the bi-orthogonality of the basis functions:

$$A_{nlm} = \frac{1}{I_{nl}} \int \rho(\vec{r}) [\Phi_{nlm}]^*, \quad (5.11)$$

where  $I_{nl}$  is a normalization factor and  $[\Phi_{nlm}]^*$  is the complex conjugate of the potential basis functions.

For a more detailed derivation of the above expressions I refer the reader to [Hernquist and Ostriker \(1992\)](#). The above description demonstrates the increased efficiency of the SCF method with respect to direct N-body. Since the basis functions are calculated only once, the only calculation needed for the computation of the potential is that of the coefficients  $A_{nlm}$ , therefore reducing the scaling of calculations required at each timestep from  $O(N^2)$  to  $O(N)$ . This has a tremendous impact on the performance, making the SCF method ideal for simulations of collisionless systems.

### 5.1.3 Tree algorithm

The most commonly used method in galactic simulations is the tree algorithm. This technique has two main parts and revolves around organizing the particle distribution into a tree structure. The first main part of the algorithm is the construction of the tree itself. This is accomplished by partitioning the entire simulation space into subsequently smaller subvolumes (cells) that correspond to *nodes* of the tree. Each node contains a collection of particles. If a node has no particles, it is not memorized. The hierarchical subdivision of each node into smaller child nodes continues until each node contains exactly one particle, which represents the *leaf* of the tree. While a variety of tree-building algorithms have been developed, the two most commonly used are the bi-tree ([Appel et al., 1985](#)) and the oct-tree ([Barnes and Hut, 1986](#)). In an oct-tree, the tree is constructed in a top-down fashion, where each cube of the volume is further divided into eight sub-volume cubes. This procedure proceeds until the *leaf* level is reached.

The second main part of the algorithm consists of walking the tree and calculating the gravitational interactions between the nodes. Instead of calculating the interactions between all particles individually, only a single interaction is computed between our particle of interest and a node of the tree, where one node typically contains a set of particles. The idea is that if a node is far enough from the particle we are interested in, the gravitational force of all of the particles in the node can be approximated by the gravitational force of the summed total mass of all particles in the node. The criterion of whether or not a node is considered "far enough" is determined by the following condition which is employed while walking the tree:

$$\frac{l}{d} < \theta, \quad (5.12)$$

Where  $l$  is the length of the node,  $d$  is the distance between the node and our particle of interest and  $\theta$  is a numerical parameter termed the *opening angle*. If condition 5.12 is satisfied, the node is deemed far enough, and the interaction with the node is computed using the multipole expansion to a pre-defined order, where the mass of the node is taken as the summed mass of all particles within. On the other hand, if the condition 5.12 is not satisfied, the node is "opened", and the same condition is evaluated for the eight child nodes that are within. The whole procedure is repeated until condition 5.12 is satisfied, or a leaf of the tree is reached. Naturally, the smaller the opening angle  $\theta$  is set, the force calculation will be significantly more accurate, but at the cost of greatly sacrificing performance, since more nodes will need to be

"opened" each time.

Using the tree algorithm, the number of operations needed to be performed in order to calculate the accelerations of all particles scales as  $O(N \log N)$ , a significant decrease compared to the  $O(N^2)$  scaling of direct N-body.

## 5.2 NUMERICAL CODES

In this section I will briefly describe the different numerical codes used throughout this thesis for the study of evolution of massive black hole binaries in galactic nuclei. All of the below described codes are N-body codes which employ different methodologies and have considerably different uses and limitations. Additionally, all of the codes I describe use at least one of three force calculation methods I have described above. However, the majority of the research I describe in this thesis was performed using the N-body code  $\varphi$ -GRAPE-hybrid.

### 5.2.1 $\varphi$ -GRAPE and $\varphi$ -GPU

#### $\varphi$ -GRAPE

$\varphi$ -GRAPE is a direct N-body code, first described in [Harfst et al. \(2007\)](#). As its name suggests, it was made specifically for use on the GRAPE special-purpose-computers ([Makino et al., 1998](#)). The  $\varphi$ -GRAPE uses an individual block-timestep scheme and utilizes a 4<sup>th</sup> order Hermite integration scheme for time integration. The Hermite integration scheme ([Makino, 1991](#)) is a PEC (predictor-evaluator-corrector) integration scheme which has become a standard in direct N-body codes. I now briefly summarize it, as described in [Makino and Aarseth \(1992\)](#). In the integration scheme, a particle  $i$  has its own time ( $t_i$ ), timestep ( $\Delta t_i$ ) position ( $\vec{r}_i$ ), velocity ( $\vec{v}_i$ ), acceleration ( $\vec{a}_i$ ) and jerk ( $\dot{\vec{a}}_i$ ). The minimum value of  $t_i + \Delta t_i$  is found, which becomes the new global time. Then, all particles  $i$  are selected, whose individual time matches the new global time. These particles are called the active particles. Then, the subsequent positions and velocities of all active particles are predicted using the following relations:

$$\vec{r}_{p,j} = \vec{r}_j + \vec{v}_j \Delta t + \vec{a}_j \frac{\Delta t^2}{2} + \dot{\vec{a}}_j \frac{\Delta t^3}{6}, \quad (5.13)$$

$$\vec{v}_{p,j} = \vec{v}_j + \vec{a}_j \Delta t + \dot{\vec{a}}_j \frac{\Delta t^2}{2}, \quad (5.14)$$

where  $j \in 1..N$ , including particle  $i$ . Then proceeds the second step in the PEC scheme, the evaluation of the acceleration and jerk of particle  $i$  using the predicted positions and velocities:

$$\vec{a}_i = \sum_{\substack{j \neq i \\ j=1}} \frac{G m_j \vec{r}_{ij}}{(r_{ij}^2 + \epsilon^2)^{3/2}}, \quad (5.15)$$

$$\dot{\vec{a}}_i = \sum_{\substack{j \neq i \\ j=1}} \left[ \frac{\vec{v}_{ij}}{(r_{ij}^2 + \epsilon^2)^{3/2}} + \frac{3(\vec{v}_{ij} \cdot \vec{r}_{ij}) \vec{r}_{ij}}{(r_{ij}^2 + \epsilon^2)^{5/2}} \right], \quad (5.16)$$

where  $\epsilon$  is the grav. softening,  $\vec{r}_{ij} = \vec{r}_{p,j} - \vec{r}_{p,i}$  and  $\vec{v}_{ij} = \vec{v}_{p,j} - \vec{v}_{p,i}$ .

Then, we use the newly evaluated acceleration and jerk to calculate the higher order derivatives of the acceleration:

$$\ddot{\vec{a}}_{0,i} = \frac{-6(\vec{a}_{0,i} - \vec{a}_{1,i}) - \Delta t_i(4\dot{\vec{a}}_{0,i} + 2\dot{\vec{a}}_{1,i})}{\Delta t_i^2}, \quad (5.17)$$

$$\dddot{\vec{a}}_{0,i} = \frac{-12(\vec{a}_{0,i} - \vec{a}_{1,i}) + 6\Delta t_i(\dot{\vec{a}}_{0,i} + \dot{\vec{a}}_{1,i})}{\Delta t_i^3}, \quad (5.18)$$

where  $\vec{a}_{0,i}$  is the acceleration at time  $t_i$ , while  $\vec{a}_{1,i}$  is the acceleration at time  $t_i + \Delta t_i$ .

Finally, in the corrector part of the integration scheme, we use the higher derivatives of the acceleration to calculate the correct positions and velocities of all of the active particles:

$$\vec{r}_i(t_i + \Delta t_i) = \vec{r}_{p,i} + \frac{\Delta t_i^4}{24} \ddot{\vec{a}}_{0,i} + \frac{\Delta t_i^5}{120} \dddot{\vec{a}}_{0,i}, \quad (5.19)$$

$$\vec{v}_i(t_i + \Delta t_i) = \vec{v}_{p,i} + \frac{\Delta t_i^3}{6} \ddot{\vec{a}}_{0,i} + \frac{\Delta t_i^4}{24} \dddot{\vec{a}}_{0,i}. \quad (5.20)$$

After the positions and velocities have been updated at time  $t_i$ , the new timesteps  $\Delta t_i$  are determined using the standard formula (Aarseth, 1985; Makino and Aarseth, 1992):

$$\Delta t_{i,1} = \sqrt{\eta \frac{|\vec{a}_{i,1}| |\ddot{\vec{a}}_{i,1}| + |\dot{\vec{a}}_{i,1}|^2}{|\dot{\vec{a}}_{i,1}| |\ddot{\vec{a}}_{i,1}| + |\ddot{\vec{a}}_{i,1}|^2}}, \quad (5.21)$$

where  $\eta$  is a parameter that controls the accuracy, typically set as 0.02 or 0.01 (Nitadori and Makino, 2008). However, in order to make the timesteps efficient for parallelization, the individual timesteps  $\Delta t_i$  are then grouped and replaced with a block timestep, expressed in terms of powers of 2:  $\Delta t_{i,b} = (1/2)^n$ . After the computation of the new timesteps, the code once again searches for the minimum timestep and then selects the new active particles.

The  $\varphi$ -GRAPE is fully parallelized through MPI and remains in use today. Even though it was originally intended for use on the GRAPE machines, today it can be used on modern GPU computer clusters through the use of special libraries which emulate the GRAPE machines on GPUs, such as the yebisu (Nitadori, 2009) and sapporo libraries (Gaburov et al., 2009). These libraries are responsible for computing the force of every particle on the GPUs, while the  $\varphi$ -GRAPE itself is responsible for integrating the particles using the Hermite scheme, on the CPU level.

### $\varphi$ -GPU

$\varphi$ -GPU is a direct N-body code which can be seen in many ways as an evolution of  $\varphi$ -GRAPE. It features many of the same characteristics as  $\varphi$ -GRAPE, but is rewritten from scratch in c++ using the NVIDIA CUDA architecture (Berczik et al., 2011). It is based on an earlier CPU serialized N-body code (Nitadori and Makino, 2008) and therefore introduces time integration with 4<sup>th</sup>, 6<sup>th</sup> and 8<sup>th</sup> order Hermite schemes. The MPI parallelization is done in a similar way as in  $\varphi$ -GRAPE, dividing particles into active ("i") particles and non-active ("j") particles, with only the "i" particles integrated at a given time. An important distinction of the

$\varphi$ -GPU is its individual softening procedure, allowing the user to specify different values of the softening per particle type. Since the presence of dark matter particles can result in unwanted relaxation effects due to their typically larger mass, this feature gives an important advantage for galactic-scale simulations. Unlike the  $\varphi$ -GRAPE, it requires no external emulation libraries, since it was written specifically for use on GPU systems.

### 5.2.2 AR-CHAIN

#### Regularization

In a general N-body system, close encounters between particles can be very problematic for the integration. This is evident especially in the case of the formation of tight binary systems or pericenter passages of highly eccentric binaries. These cases not only cause significant slowdown of the calculation, due to the much smaller timesteps required for the integration, but can also introduce large errors in the calculation. While these problems can be somewhat diminished with the appropriate choice of the gravitational softening and individual timestep schemes, to truly remove them one needs to adopt a regularization method for the treatment of close encounters. The basic idea behind the concept of regularization is the introduction of different coordinate transformations in the equations of motion which result in a more suitable form of the equations for numerical calculations.

This can be demonstrated most effectively in the simplest toy example of the perturbed two-body problem, as described in [Aarseth \(2003\)](#). Let us examine the relative equation of motion of a tight binary, with component masses  $m_1$  and  $m_2$ :

$$\ddot{\vec{R}} = -(m_1 + m_2) \frac{\vec{R}}{R^3} + \vec{F}_{ext}, \quad (5.22)$$

where  $\vec{F}_{ext}$  is the external force (perturbation) exerted by the other  $N - 2$  bodies. Out of the two force terms on the right side of the above equation, let us assume the two-body motion is the dominant term. Then, the main culprit for the numerical problems in the integration will be the first term in the above expression. This is because the term becomes singular for close approaches  $R \rightarrow 0$ , leading to divergences in the expression.

We can then introduce a time coordinate transformation in the form of:

$$dt = R^n d\tau, \quad (5.23)$$

where  $n$  depends on the choice of the temporal transformation. It is easy to show that then the derivatives are :

$$\frac{d}{dt} = \frac{1}{R^n} \frac{d}{d\tau}, \quad (5.24)$$

$$\frac{d^2}{dt^2} = \frac{1}{R^{2n}} \frac{d^2}{d\tau^2} - n \frac{R'}{R^{2n+1}} \frac{d}{d\tau}, \quad (5.25)$$

where we denote with primes derivatives with respect to the new time variable  $\tau$ . Then, we can

substitute the second order derivative in Eq. 5.22:

$$\vec{R}'' = \frac{nR'\vec{R}'}{R} - \frac{(m1+m2)\vec{R}}{R^{3-2n}} + R^{2n}\vec{F}_{ext}. \quad (5.26)$$

If we substitute  $n = 1$ , we see that the singularity  $1/R^2$  in Eq. 5.22 has been replaced with  $\vec{R}/R$ , which significantly improves the behavior when  $R \rightarrow 0$ .

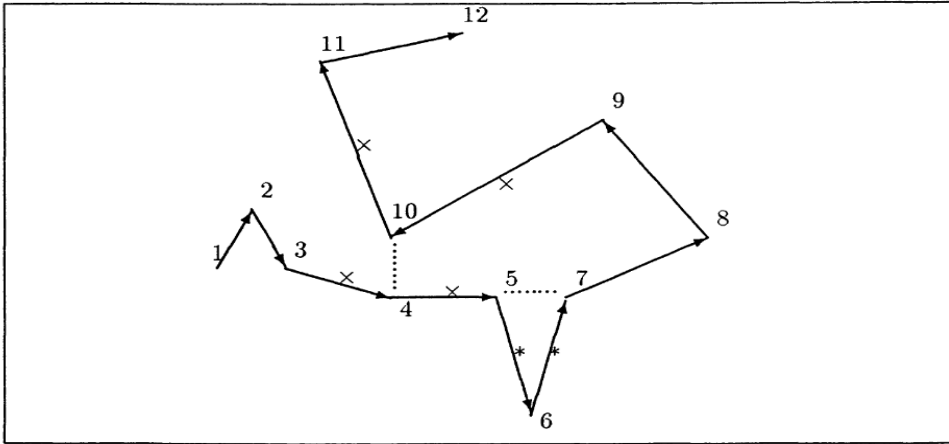


**Figure 5.1:** Example of a chain structure with 12 bodies. In this example in order to update the chain the interparticle distance between bodies 5 and 7 is compared with the distances marked with \*. The distance between bodies 4 and 10 is similarly compared with distances marked with  $\times$ . Image credit: [Mikkola and Aarseth \(1993\)](#).

While the above described example employs transformation of the time coordinate, true regularization requires the transformation of both time and the three spatial coordinates. This was achieved for the first time by [Kustaanheimo and Stiefel \(1965\)](#) in a method now well known as the KS-regularization method. KS regularization has since proven to be very successful in the treatment of close binary interactions. However, the limitation of two-bodies of the method meant that situations such as close approaches by a third perturber or close interactions between two binary systems could not be treated in a regularized way. The next big step forward came with the introduction of the chain regularization method, which was at first limited to  $N = 3$  systems ([Mikkola et al., 1990](#)), but was later expanded for generalized systems of  $N$  bodies ([Mikkola and Aarseth, 1993](#)). The chain method enables regularization of  $N$ -bodies by structuring all particles in a single uninterrupted chain structure. The construction of the chain starts by finding the shortest distance between two particles which becomes the first chain element. Then, the chain is further expanded by finding the particle closest to either end of the chain and adding it to the structure. In order to update the chain, interparticle distances are checked at every timestep. If a distance between two non-chained particles is shorter than the existing chained distances of either of the two particles, the chain is switched. The chain structure and the switching condition evaluation is given on Fig. 5.1. After the chain is constructed, pairwise interactions between chain elements are then treated with the KS regularization formalism.

KS regularization was finally outclassed with the introduction of algorithmic regularization (AR, [Mikkola and Merritt, 2006](#)). Unlike KS, AR did not encounter problems with very large mass ratios and included perturbations from velocity-dependent forces. It employed the time-transformed leapfrog method ([Mikkola and Aarseth, 2002](#)) which was then finally combined

with the chain method to result in the AR-CHAIN code (Mikkola and Merritt, 2008).

Until recently, the AR-CHAIN code was the state-of-the-art in few body regularization. It also includes the PN corrections to the equations of motion up to order PN2.5, for treatment of relativistic systems. While the code is not limited in terms of the number of bodies that are regularized, if more than a few bodies are employed in the regularization scheme the resulting loss in computational speed is very significant and quickly grows with  $N$ . We use the AR-CHAIN code for our high resolution study of three-body encounters with a massive black hole binary, as described in Chapter 6. A new approach, termed MSTAR, promises to significantly increase the number of regularized particles without sacrificing performance (Rantala et al., 2020).

### 5.2.3 *Bonsai*

*Bonsai* and its continuation, *bonsai2* (Bédorf et al., 2012a,b) are N-body codes which utilize the hierarchical oct-tree code algorithm introduced by Barnes and Hut (1986). The implementation of *bonsai* is executed completely on GPUs, enabling fully MPI parallelized runs on dedicated GPU clusters with the use of NVIDIA CUDA architecture. As with other tree codes, the value of the opening angle  $\theta$  represents the trade-off between performance and accuracy in the force calculation. In order to fully take advantage of GPU parallelization and block timestep schemes, the tree traversal is done in a breadth-first fashion, and not depth-first like many other tree codes. The unopened nodes of the tree are treated with the multipole expansion for force calculation up to the quadrupole order. While the code proper has a global softening scheme, for the work done in this thesis, I use a custom made version of *bonsai2* which adopts an individual softening scheme.

### 5.2.4 *ETICS*

*ETICS* (Expansion Techniques in Collisionless Systems, Meiron et al., 2014) is an N-body code that uses collisionless expansion methods for the force and potential calculation. Like other codes described in the thesis, it is parallelized for use on GPUs, using NVIDIA CUDA architecture. It features two different expansion methods, the SCF method, described above in detail, and the multipole expansion method (MEX, also known in the literature as the Spherical Harmonics method). While these two methods are essentially different, they both utilize multipole expansion to expand the potential as a series of terms. The difference comes from the way the expansion is done. Within the SCF method, the density is expanded in a Fourier-like fashion, includes expansion of the radial part and performs the calculation by calculating coefficients within a set of pre-defined basis vectors. On the other hand, MEX revolves around locally expanding the Green function in a Taylor-like series. Since the expansion is done locally, the coefficients are known in advance, while the calculation revolves around calculating the local matter distribution. The maximum order of the expansion terms ( $(n_{max}, l_{max})$  in the case of SCF,  $l_{max}$  in the case of MEX) represents the trade-off between accuracy and performance of the code, but this choice also depends on the degree of deviation from sphericity of the system.

As such, *ETICS* is not well suited for highly flattened systems, or systems where two-body relaxation effects are expected to be measurable. As a collisionless code, *ETICS* is best used for systems with a well defined center and where the potential does not change drastically, such as the study of the secular evolution of near-equilibrium systems.

5.2.5  $\varphi$ -GRAPE-hybrid

The  $\varphi$ -GRAPE-hybrid code (which we will throughout the text refer to as simply "the hybrid") represents a marriage between  $\varphi$ -GRAPE and ETICS and will be detailed in an upcoming publication (Meiron et al., 2021). The code represents an important next step in the N-body approach and is termed as hybrid since it boasts *both* collisionless and collisional force calculation methods, which are employed in parallel with each other on different subsets of particles. In principle, the collisionless part of the hybrid, which utilizes the SCF method for force calculation, can be performed not only by ETICS, but also any other collisionless code, but usage so far has been restricted to ETICS. The code is available in *c* using the original  $\varphi$ -GRAPE code, but  $\varphi$ -GRAPE has also been streamlined and rewritten in *c++*, specifically for its use as a hybrid. The approach adopted in the hybrid bears many similarities with the EuroStar code (Hemsendorf et al., 2002), a hybrid N-body code that combined the SCF method with the collisional code NBODY6++ (Spurzem, 1999).

The hybrid code utilizes a special GRAPE-emulating library called GRAPite which serves as an intermediary between  $\varphi$ -GRAPE and ETICS. This enables the direct code itself to remain unmodified and it can still be used in a purely direct way by turning off the hybrid function, if the user so desires. The code still requires the use of a standard GRAPE-emulating library such as yebisu (Nitadori, 2009) and sapporo libraries (Gaburov et al., 2009). The primary function of GRAPite is to divide particles based on pre-determined tags into particles which are treated with the SCF force, and particles which are treated directly. Then, GRAPite forwards the information for particles treated with the SCF force to ETICS, and the information of particles treated in a direct way to the GRAPE-emulating library. After the force calculation is complete, the data is sent back into GRAPite, which combines the forces of all particles calculated using both ETICS and the GRAPE library, and feeds the information further back to  $\varphi$ -GRAPE for the Hermite time integration, performed on the CPU. This setup is demonstrated in Fig. 5.2.

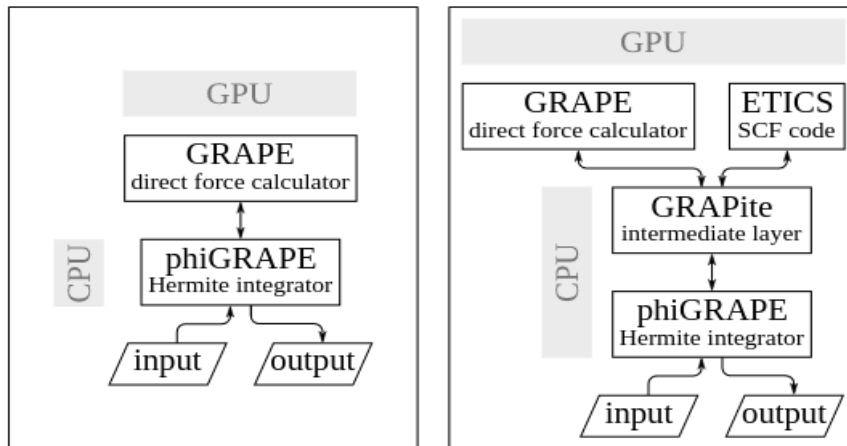


**Figure 5.2:** Left: Schematic representation of the workflow of the standard version of  $\varphi$ -GRAPE. Right: Schematic representation of the workflow in  $\varphi$ -GRAPE-hybrid. Image credit: Yohai Meiron.

The hybridization is performed by dividing particles into three distinct classes: *core* particles, *halo* particles and *black holes*. Despite the nomenclature, these classes are not necessarily related to the cores or halos of galaxies. Rather, *core* particles is the collective name of all of the particles whose forces are calculated in a direct way, while *halo* particles is the collective name for particles which are treated with the SCF force through ETICS. This

means that *core* particles have direct interactions among themselves, while *halo* particles interact among themselves, as well as with the *core* particles, through the SCF force. *Black holes* belong to a special particle type, and always have mutual direct interactions with all particles. The *core-halo* particle division is determined only once by the user at the start of the run, and the criterion by which the division is performed can be freely defined with respect to the goal of the research. This means that the code requires a certain level of pre-existing insight by the user on the expected behavior of the system before the start of the run, since the code still does not support adaptive adjustment of *core-halo* particles throughout the run. Therefore, the importance of the selection of *core-halo* particles at the start of the run should not be underestimated, since it can significantly impact the results.

The main benefit of the hybrid approach is the very large amount of computational time that is saved by reducing the number of interactions which need to be computed directly. The scaling of the force calculation with the number of particles is of the order  $\mathcal{O}(N_{\text{core}}^2) + \mathcal{O}(N_{\text{halo}})$ , assuming that the number of black hole particles is of order unity. If there is only a small fraction of *core* particles, the speed-up obtained over the direct-only approach is very significant. Similar to ETICS itself, it is ideally suited for near-equilibrium systems where the majority of particles have very long relaxation timescales and the shape and center of the system itself is well defined.

### 5.3 NUMERICAL TESTS AND BENCHMARKS OF THE $\varphi$ -GRAPE-HYBRID CODE FOR GALACTIC SIMULATIONS

In this section I will present a series of numerical tests, benchmarks and parameter investigations I performed using the  $\varphi$ -GRAPE-hybrid. The goal of the investigations was twofold. The first goal was to test the effectiveness of the hybrid on different computation systems, make comparisons with direct-only N-body codes and to detect and remove bugs that might appear using different software or hardware configurations. The second goal of the investigations was to explore the necessary parameter values needed for effective usage of the code for studying the evolution of massive black holes in galaxies. These parameters include the value of the gravitational softening, centering strategies, minimum integration timesteps and others. While the hybrid has already been used once in an astrophysical scenario (Perets et al., 2018), numerical tests such as the ones I describe here have not yet been published in the literature. I start by noting that the  $\varphi$ -GRAPE-hybrid code remains a code in active development. Therefore, the results presented below have been made using different versions of the code over a period of several years and they may or may not reflect the results based on the final version of the code which will be published in the upcoming publication (Meiron et al., 2021). The code itself has gone through several major revisions over the years and therefore the results presented below can be seen more as an evolution of the code performance throughout its development.

I performed the numerical tests on a host of different computer clusters (JUWELS in Jülich, Kepler & Kepler2 in Heidelberg, binAC in Tübingen, Germany, "hansolo" and "chewbacca" in Beijing, China). Additional testing has been performed by our collaborators on computer clusters in China, Ukraine and Canada. The galactic models I used for the tests come in two different flavours. The first is a series of simple, equilibrium, spherical Plummer models with variable particle numbers which I use for debugging, testing of compilers and benchmarking. The second flavour is a system more suitable for large-scale galactic simulations, and for this purpose I use the same system of Kh16, described in Section 4.5. I now present below the main

findings of the testing procedure.

### 5.3.1 Benchmarks

One of the most important aspects of a modern N-body code is its computational efficiency. Due to the difficulty of obtaining large amounts of computational time on large computing clusters, one of the most important features of the hybrid code is in its promise of greatly reducing computational cost when compared to the pure direct N-body approach. This is easier said than done however, since the hybrid combines multiple codes and libraries and requires constant communication between them. This communication between different aspects of the code needs to be optimized well, in order to avoid bottlenecks in the computation that might result in the loss of the computational advantage gained by the hybrid approach. Therefore, proper benchmarking represents an important aspect of testing the hybrid code and it is still in progress at the time of writing. Most notably, due to the nature of the hybrid method, it is important to demonstrate how the hybrid performs with respect to the purely direct version.

### Scaling

The scaling behavior of an N-body code is a term used to denote how a code performs when run on an increasing number of GPU or CPU devices. The benefit of a larger number of devices is apparent. With a larger device number, a smaller number of particles will be assigned to each device, resulting in a smaller number of calculations performed at each time and therefore reducing computational time. However, in real applications, bigger is not always better. Firstly, more devices means a bigger drain on computational resources, which might be limited. Secondly, these devices need to communicate information to each other through MPI. If the number of devices is too large, the time taken for the MPI communication of the devices can even exceed the computation time of the gravitational interactions themselves, in which case the code becomes ineffective and wastes computational resources. Therefore, the scaling of an N-body code represents the efficiency of parallelization and gives insight into the ideal number of devices the code should be run on to achieve maximum efficiency.

Since the scaling tests of the current version of the hybrid are still a work in progress at the time of writing, I present on Fig. 5.3 the results of scaling tests done with an early and now outdated version of the hybrid. These runs show that in this early version, runs with up to 1 million particles are best suited for 4 or 8 GPU runs (1 or 2 nodes, each with 4 Nvidia Volta V100 GPU cards). For higher numbers of devices, we can see that the code had become ineffective, showing no measurable speed-up and even occasionally an increase in the total computational time. Current tests show that this behavior is improved on significantly in the new version.

### Timing

The speed of the hybrid code is affected by many different parameters. Some are dependent on the hardware (speed of CPUs and GPUs, slow network communication on computer clusters), while some are dependent on the model being simulated, such as the number of core and halo particles, integration accuracy and the maximum orders in the SCF force calculation, denoted by  $(n_{max}, l_{max})$  parameters. This makes it difficult to make robust predictions of the performance, since they will inevitably differ and depend on the type of the system being simulated and the properties of the computer cluster. However, we can estimate which parameters affect the

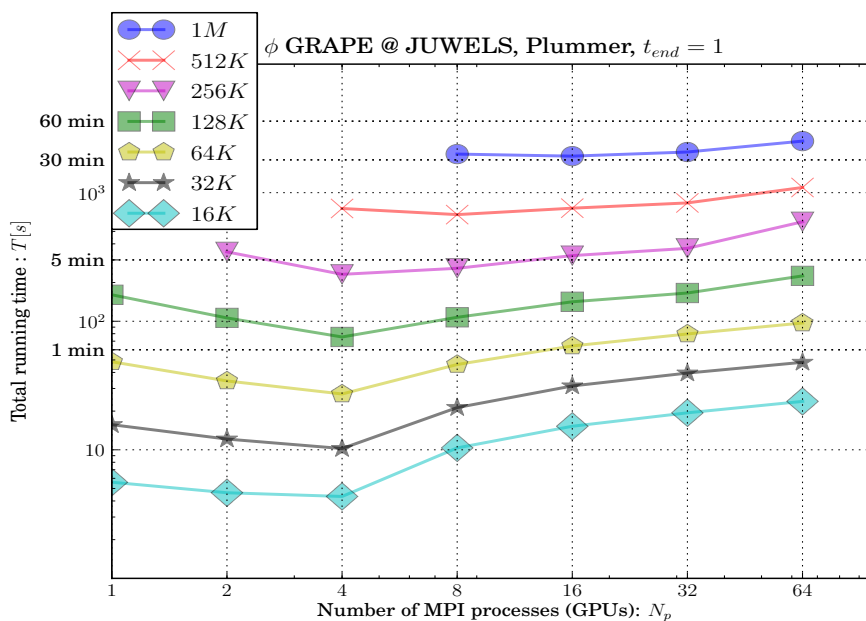


**Figure 5.3:** Scaling plot using an early build of  $\phi$ -GRAPE-hybrid (2018 version). The runs were performed for one N-body time unit on the JUWELS cluster in Jülich using a Plummer spherical galaxy model with variable particle number, corresponding to different symbols on the plot. The y-axis represents the total wallclock running time, while the x-axis represents the number of GPU devices used (Nvidia Volta V100 GPUs).

performance the most. For that purpose I show on Fig. 5.4 timing results of a set of runs using different maximum orders in the angular multipole expansion  $l_{max}$  and with and without core particles. The runs were performed on the system from Kh16, with the core run using 3.3% of all particles (excluding black holes) as core. We can immediately notice that the presence of core particles, even a small percentage like in our case, has a much bigger impact on the performance than the maximum expansion order  $l_{max}$ . This points to the fact that the fraction of collisional particles has the most significant effect on the performance. For high collisional fractions, the resulting overhead can make the run even slower than a pure direct N-body code.

In direct N-body codes, the vast majority of the computational time is spent on the gravity calculation of the particles. Since most of the gravity calculation in the hybrid is performed by the SCF force, this may no longer be the case. For this purpose, I present on Fig. 5.5 the pie chart distribution of different code routines, performed using the Kh16 data with 3.3% core particles on the binAC cluster, using the early 2020 version of the hybrid. We notice that in all of the runs the timing is dominated not by the gravity calculation, but by the active particle search. The reason for this is that the active particle search is performed on the CPU, while the gravity calculation is performed on multiple GPUs in parallel. Therefore, the active particle search presents a bottleneck. For this reason, in the published version of the hybrid the active particle search will also be performed by the GPUs, to maximize efficiency.

Finally, we can investigate how the code performs with a varying number of core particles. Therefore, I present on Fig. 5.6 a benchmark of the code performed on 2 x GeForce RTX 2080 Ti devices on the Chinese computer "han". We can see that all runs show a very significant speedup of the hybrid code when compared to the direct-only version, denoted by the red line. The speed-up for  $N = 2 \times 10^6$  particles ranges from 2.5 for the 50% core particle case, to an

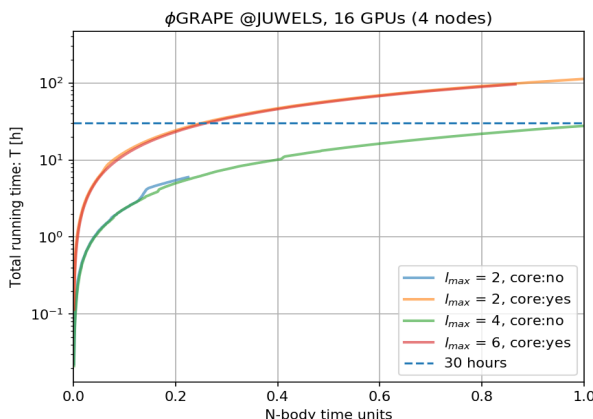


**Figure 5.4:** Representation of the total running time of the code (y-axis) with the total time integrated, given in N-body units. The different lines correspond to different maximum orders in the multipole expansion, denoted by  $l_{max}$  and whether or not core particles are present. The total particle number was  $N = 6 \times 10^6$ , and the fraction of core particles used for the orange and red lines was 3.3%. All runs were performed on 16 Nvidia Volta V100 cards.

impressive factor of 28 speed-up when using only 1% core particles. Since most applications would have a few percent of particles treated as core, we estimate that for most uses the speed-up would be between 7 and 28 times faster than the direct code, based on the timing from the blue and green lines on the plot, respectively.

### Compilers and GRAPE libraries

In order to obtain a good estimate of the code benchmarks, I have also tested how the `c++` version of the code performs using different software. Most notable, I wanted to see if the choice of the compiler, as well as the GRAPE emulation library, affects the performance. For this purpose I used the JUWELS cluster, which features two families of compilers: The Intel `c++` compiler (ICC, version 19.1.2.254) and the GNU `c++` compiler (GCC, version 9.3.0). In terms of the GRAPE libraries, I use the previously mentioned `yebisu` (Nitadori, 2009) and `sapporo` libraries (Gaburov et al., 2009).

To perform the test I used a  $N = 256k$  particle Plummer model and the direct-only version of  $\phi$ -GRAPE (100% core particles). I limited the runs to 1 GPU node, and varied the number of GPU devices from 1 to 4 (Nvidia Volta V100 GPU devices).

On Fig. 5.7 we can see that both the Intel and GNU compiler perform very similarly when using the `yebisu` GRAPE emulation library, therefore we can conclude that the choice of the compiler should not have a significant effect on the performance. On the other hand, the GPU device scaling of the `sapporo` run points to an underlying issue with the current version of the code. Namely, there is no visible performance boost gained from using multiple GPU devices, suggesting that there is a problem with how the code in combination with `sapporo` distributes particles over multiple GPUs. Since then, this issue has been resolved and the code can be used in combination with `sapporo` as well.

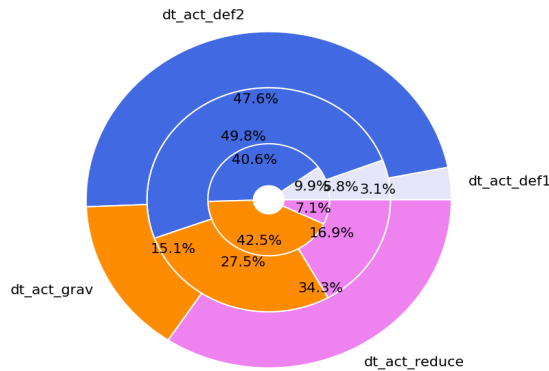


**Figure 5.5:** Pie chart of the fraction of time taken by different parts of the code, performed on the binAC cluster. The three donuts correspond to 1, 2 and 4 nodes, respectively (each with 2 Nvidia Tesla K80 GPUs) The presented code procedures correspond to: dt\_act\_def1 signifies the time spent searching for the minimum integration timestep, dt\_act\_def2 represents the time spent creating the active particle list, dt\_act\_grav represents the time spent on the gravity calculation of all particles and finally dt\_act\_reduce represents the time needed for the communication time needed for the particle information to be collected from different devices. The other timing components correspond to less than 2% and thus were not included.

### 5.3.2 Orders in the multiple expansion

Moving on from purely numerical benchmarks, we now want to investigate how different parameters of the code affect astrophysical applications of the code. Specifically, I will focus further testing on a setup that involves a hard SMBH binary system embedded in a triaxial galactic nucleus. For this reason, I will use the system from [Kh16](#) for all further tests, and I will compare the results to the ones in that study, as a consistency check. This is done in preparation for scientific runs of the same system using the  $\varphi$ -GRAPE-hybrid, described in Chapter 7.

The hybrid code by definition relies on the SCF force calculation for the treatment of the majority of its particles. Therefore, it is important to have a good understanding of how well the SCF force approximates the real potential of the system and which orders  $(n_{max}, l_{max})$  in the two infinite series in Eq. 5.7 are necessary to achieve the needed precision. Since the zero order terms  $(n_{max}, l_{max}) = (0, 0)$  correspond to the spherically-symmetric Hernquist profile seen in Eq. 5.5, it is reasonable to assume that nearly spherical systems would be represented to a high degree of accuracy. However, for axisymmetric or triaxial systems it is not clear if a SCF treatment would be justified. Therefore, for this purpose I investigate the treatment of the potential in the galaxy merger remnant of [Kh16](#). As seen on figure 4.4, the system is significantly flattened, and slightly triaxial. The flattening is large enough to present a significant deviation from spherical symmetry, and in principle this deviation should be accounted for by the angular part of the SCF potential expansion, denoted by the expansion number  $l$ .

For this purpose I present on figure 5.8 a comparison of the potential of the system obtained in a direct way, with the potential calculated using different orders in the multipole expansion. While the simulation itself was performed with  $(n_{max}, l_{max}) = (10, 6)$ , we use the coefficient output option in the hybrid code which allows us to save the coefficients  $A_{nlm}$  from Eq. 5.11 at each snapshot of the integration. These lists of coefficients then allow us to reconstruct the SCF force and potential, up to a desired order. In the figure we immediately notice that the

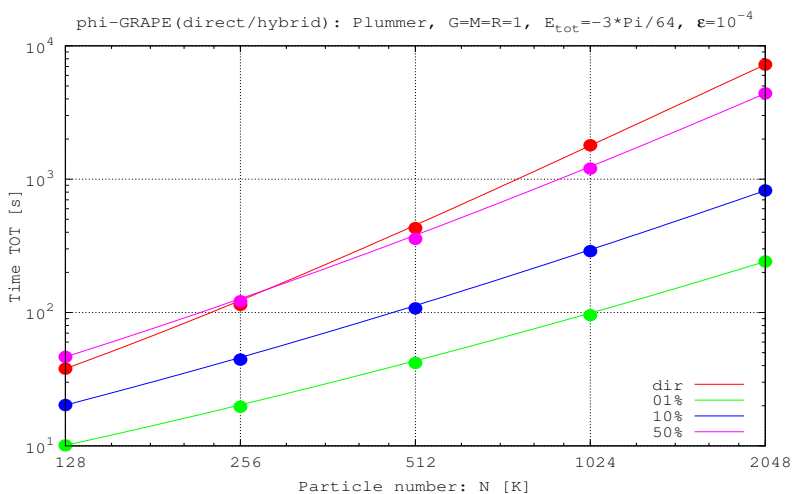


**Figure 5.6:** Benchmark of the hybrid code performed on the Beijing computer "han" using a Plummer galactic model. The x-axis corresponds to the particle number, given in thousands. The y-axis corresponds to the total running time of 1 N-body time unit. The different lines correspond to varying fractions of core particles, from 1% to 50%, while the red line corresponds to the direct-only version (100% core particles). Image credit: Peter Berczik.

assumption of spherical symmetry (corresponding to the line denoted by  $l = 0$ ) results in the biggest deviation from the actual measured potential. On the other hand, higher orders ( $l_{max} > 0$ ) all peak at the relative error on the order of  $-3$  and there seem to be no significant differences between the cases of  $l \leq 2, l \leq 4, l \leq 6$ .

The differences between the different orders of the expansion can be further highlighted by Figure 5.9. Here I have presented the potential calculated from the SCF coefficients within logarithmic-spaced spherical shells. We can see both in the  $\varphi$  and  $\theta$  distributions that near the center when  $r$  is small, the higher order contributions ( $l > 2$ ) do not play a significant role since they are several orders of magnitude smaller than the  $l = 2$  term. However, in the farther regions  $r > 0.1$  kpc, we notice that the  $l > 2$  contributions become more significant, and comparable to the  $l = 2$  term. Therefore, for outer regions of the galaxy where the angular anisotropy is more noticeable, the higher order terms become more relevant and should be included in the multipole expansion.

From the analysis we can conclude that despite the non-negligible flattening of the system, the SCF force does a great job of representing the potential, with respect to the one obtained with direct integration.

### 5.3.3 Gravitational softening

N-body studies need to take special care when choosing the value of the gravitational softening, since a larger value of the softening will result in the closest encounters being unresolved, but a smaller value of the softening would result in a higher likelihood that a close stellar binary would form, causing a bottleneck in the integration, or increase the likelihood that dark matter particles (which are typically non-physically massive) introduce spurious relaxation effects by

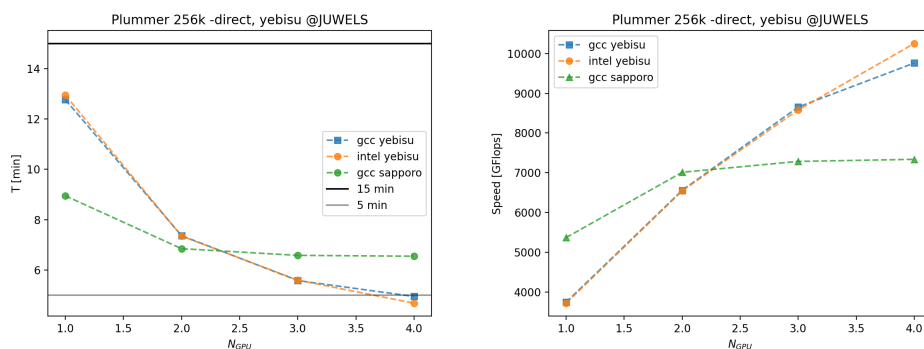


**Figure 5.7:** Left: Total running time for 1 N-body time unit of a direct-only run on the JUWELS supercomputer, as a function of GPU number. I used a Plummer model with 256k particles to perform the test. The different lines correspond to different combinations of compilers and GRAPE emulation libraries. Right: Computational speed expressed in GFlops as a function of number of GPUs. Other elements are the same as on the left figure.

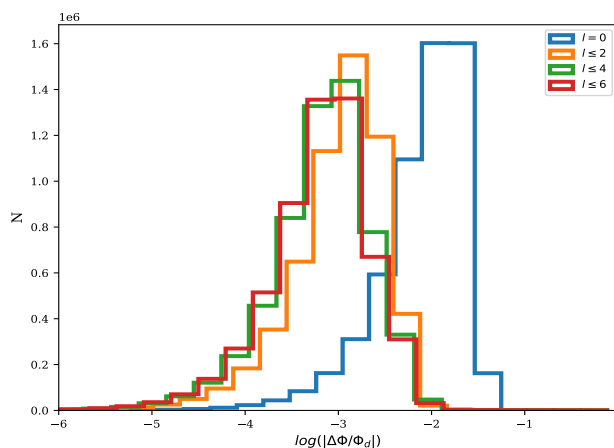


**Figure 5.8:** Histograms showing the relative error in the potential calculation  $|\Delta\Phi/\Phi_d| = |(\Phi - \Phi_d)|/\Phi_d$ , where  $\Phi_d$  is the potential obtained using the direct-only version of phi-GRAPE. Different colors correspond to different maximum orders in the multipole expansion.

closely interacting with the other particles. The second issue can be resolved by adopting an individual softening procedure, where each particle type has its own value of the softening. However, large, computationally expensive runs, might not be able to properly investigate the ideal parameter selection due to the inability to do extensive pilot runs and testing because of limited computational resources. This makes the softening an extremely important numerical parameter, since an inappropriately chosen value can affect the evolution of the system and result in spurious effects. This is especially true for studies of SMBH binaries in galactic nuclei, where exceedingly close approaches of stars to the binary play a crucial role in the evolution of the system. Therefore, in this section I present an investigation into the appropriate value of the softening for such systems.

As described in section 5.2.1, one of the differences between  $\varphi$ -GPU and  $\varphi$ -GRAPE is the fact that  $\varphi$ -GPU features an individual softening procedure, where each particle type is assigned their own individual softening. Then, the softening for individual interactions is calculated

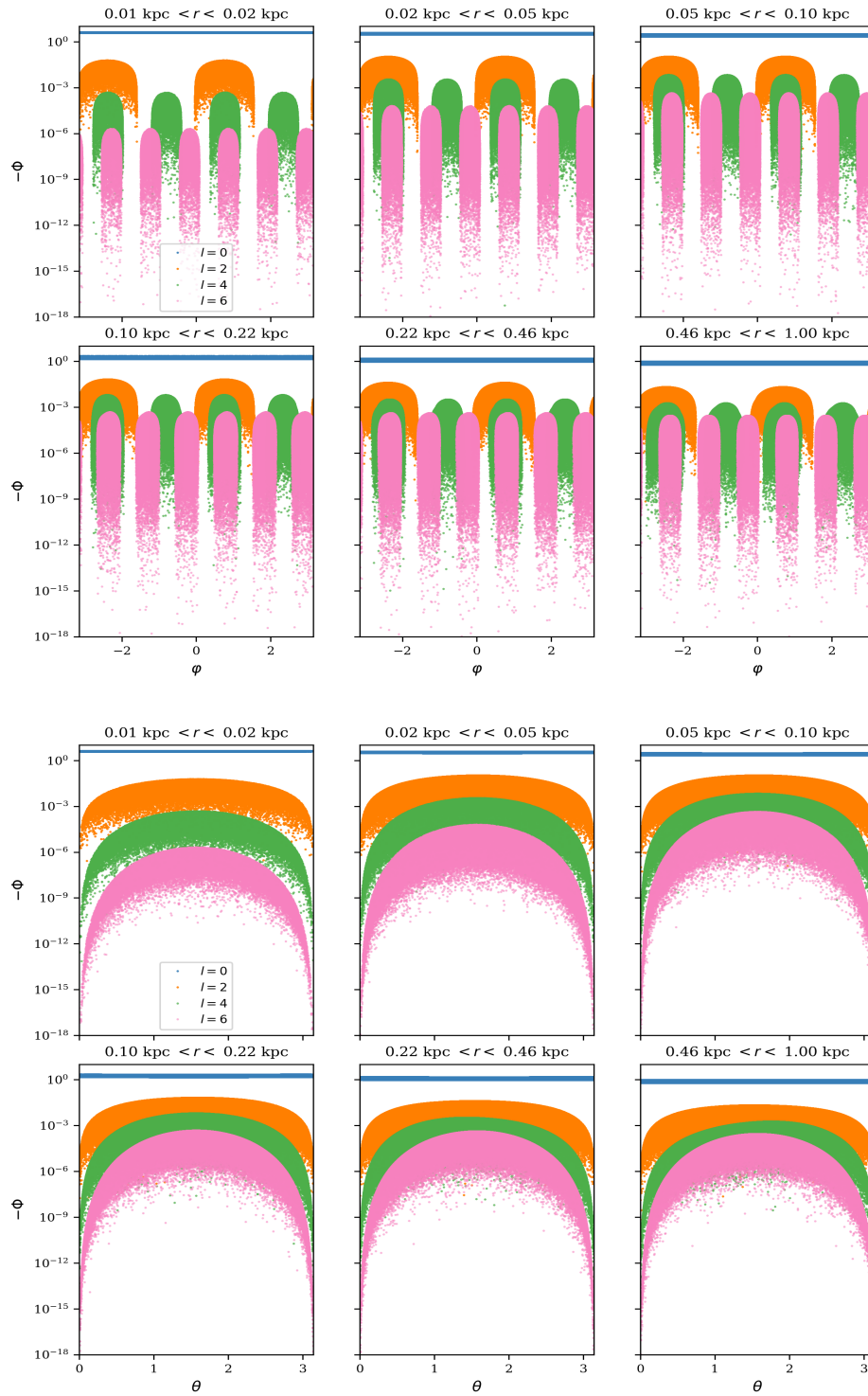


**Figure 5.9:** Top six figures: The contribution of different orders in the multiple expansion to the potential as a function of the spherical coordinate  $\varphi$ . The six different figures correspond to particles within log-spaced spherical shells, up to  $r = 1$  kpc. Bottom six figures: The contribution of different orders in the multiple expansion to the potential as a function of the spherical coordinate  $\theta$ . The six different figures correspond to particles within log-spaced spherical shells, up to  $r = 1$  kpc.

according to the following formula:

$$\epsilon_{i,j}^2 = \epsilon_c \frac{(\epsilon_i^2 + \epsilon_j^2)}{2}, \quad (5.27)$$

where  $i, j$  correspond to different particle types (stars, black holes or dark matter) and  $\epsilon_c$  is the softening correction factor. However,  $\varphi$ -GRAPE, and by extension  $\varphi$ -GRAPE-hybrid, have no such feature and instead utilize one global softening parameter for all particle types  $\epsilon_{glob}$  (except the black holes which have zero softening in interactions with each other). This can make comparisons of the impact of the softening between the codes inherently difficult, simply due to the different ways the codes were designed. The original  $\varphi$ -GPU run featured in [Kh16](#) used  $\epsilon_{BH} = 0$  for the black holes,  $\epsilon_{st} = 0.1$  pc for stars and  $\epsilon_{dm} = 125$  pc for the dark matter. The softening correction factor in Eq. 5.27 was only used for star-black hole interactions, otherwise it was ignored. With the value of  $\epsilon_c = 0.01$ , the black hole-stellar softening results in  $\epsilon_{BH-st} = 0.007$  pc, corresponding to  $\epsilon_{BH-st} = 7 \times 10^{-6}$  in N-body units. The description of N-body units is given in Table 6.1. The correction factor is implemented in order to allow close interactions of stars with the binary to properly account for stellar hardening. Keeping the value of the softening in orders of 10, the closest corresponding global value of the softening for  $\varphi$ -GRAPE would then be  $\epsilon_{glob} = 0.01$  pc, corresponding to  $10^{-5}$  in N-body units.

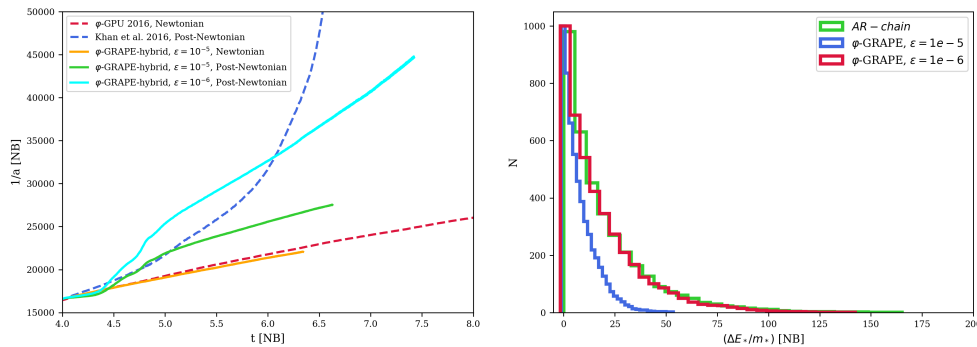


**Figure 5.10:** Left: Time evolution of the inverse of the SMBH binary semi-major axis, given as a measure of black hole hardening. The blue dashed line corresponds to the Post-Newtonian corrected run used in [Kh16](#), while the red dashed line corresponds to the Newtonian run done with the same code. The full lines correspond to lines done with the hybrid code which features global softening. Right: Histogram of the specific energy changes of the stars as a result of 3-body scattering experiments, performed using the AR-chain code (green line) and the phi-GRAPE using different softening (blue and red lines). All units on the plots are given in N-body units.

However, on the left plot of Fig. 5.10 we can see that this value of the softening fails to reproduce the 2016 data in the Post-Newtonian case. While lowering the softening to  $10^{-6}$  somewhat reduces the deviation, the original 2016 data still show a much faster evolution of the binary, resulting in a merger already at  $t \approx 6.5$ . However, this discrepancy is caused by another parameter, detailed in the following section, while here we only focus on the effect of the softening. Namely, the mismatch between the lines corresponding to softening of  $\epsilon = 10^{-6}$  and  $\epsilon = 10^{-5}$  demonstrates that the hardening rate is dependent on the value of the softening. Since the hardening rate is caused by the collective effect of a larger number of close stellar approaches, this suggests that in runs with a larger value of the softening, the closest stellar encounters remain unresolved which results in overall lower hardening rates. This is further

demonstrated by the right plot on the same Figure, where we present the results of a series of 3-body scattering experiments I performed to investigate the effect of the softening on strong stellar interactions. I compare the results obtained in 3-body runs using  $\varphi$ -GRAPE, starting at initial time  $t = 5$ , with the results of the scattering experiments obtained using the AR-chain code, which are detailed in Chapter 6. Since the AR-chain features zero softening, its results are not affected by this numerical parameter, enabling accurate comparisons with  $\varphi$ -GRAPE. The 3-body runs show that at least the value of  $\epsilon = 10^{-6} = 10^{-3}$  pc is necessary to properly account for all of the energetic changes of the stars at this phase of the SMBH binary evolution, and likely even smaller values of the softening are required for later phases of the merger, when the semi-major axis of the binary is much smaller.

Finally, I want to underline that this issue is not exclusive to  $\varphi$ -GRAPE, since similar behavior is observed using the current version of  $\varphi$ -GPU. Testing runs using the current version of  $\varphi$ -GPU, performed by Peter Berczik, are presented on Fig. 5.11. The figure clearly shows that the softening correction factor of  $\epsilon_c = 0.01$ , which was used in the original run is not sufficient to properly account for the obtained stellar hardening. The plot shows us that the hardening converges only for values of  $\epsilon_c = 10^{-8}$ , which according to formula 5.27 corresponds to a global softening value of  $\epsilon \approx 10^{-7} = 10^{-4}$  pc in the case of  $\varphi$ -GRAPE. Therefore, we can conclude that regardless of the code used, in order to resolve all of the energetic interactions which result in black hole hardening, the value of the softening for stellar-black hole interactions should be constrained by the following relation:

$$\epsilon_{BH-star} \lesssim 10^{-4} \text{ pc.} \quad (5.28)$$

However, in reality this value depends on the binary semi-major axis.

The full run of the system using the hybrid, described in Chapter 7, showed that the semi-major axis in the hardening phase, before the GW-driven inspiral, takes the values  $0.06 \text{ pc} \leq a_{BH} \leq 0.01 \text{ pc}$ . This suggests that the value of the softening for stellar-black hole interactions should be two orders of magnitude smaller than the value of the semi-major axis at the start of the GW-dominated regime, in order to properly resolve all of the strong stellar interactions. This value is much lower than many past studies of close black hole binaries, and can have important implications for future studies of such systems.

#### 5.3.4 Black hole integration timestep

Another aspect that can significantly affect the evolution of a close SMBH binary is the black hole integration timestep. As of the time of writing, the code does not feature regularization for the black holes. Instead, the value of the black hole integration timestep is determined primarily by two numerical parameters: the minimum integration timestep  $\Delta t_{min}$  and the  $\eta_{BH}$  parameter which originates from the  $\eta$  accuracy parameter in Eq. 5.21. While  $\eta$  is specified globally,  $\eta_{BH}$  can be set separately so it is only used in interactions of particles with the black holes. This has the benefit of increased accuracy in the black hole integration without significant loss of computational time. On the other hand,  $\Delta t_{min}$ , usually given as a power of 2, represents the minimum possible timestep any particle can have that is allowed by the code. Therefore, when the individual timestep of a particle  $\Delta t_i$  is calculated according to Eq. 5.21, if it is smaller than the minimum integration timestep so that  $\Delta t_i < \Delta t_{min}$ ,  $\Delta t_i$  will take the value of  $\Delta t_i = \Delta t_{min}$  instead. This is done in order to avoid computational bottlenecks that would appear if  $\Delta t_i$  is too small, as well as to avoid larger errors in the calculation that would arise from calculations

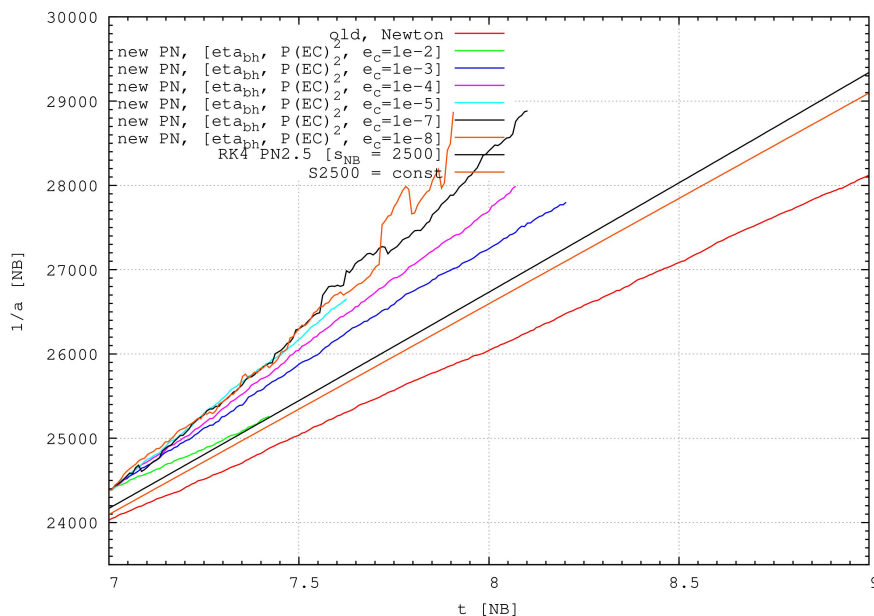


**Figure 5.11:** Time evolution of the inverse semi-major axis of the binary, for different values of the softening correction parameter  $e_c$  performed using the current version of  $\varphi$ -GPU. The red line corresponds to the Newtonian run performed using the 2016 version of the code. Plot credit: Peter Berczik.

of extremely small timesteps that could reach the precision limits of floating point operations. However, if the  $\Delta t_{min}$  parameter is chosen too large, the timestep of particles experiencing close encounters will constantly be artificially limited by  $\Delta t_{min}$  causing large errors in the integration and making the orbits and dynamics of those particles unreliable.

The minimum integration timestep becomes especially relevant when the softening is drastically reduced (which we found was necessary in the previous section), since smaller values of the softening would result in closer approaches between particles, which in turn demand lower integration timesteps in the pericenter of the approach to properly account for the dynamics of the system. Therefore, it becomes extremely important to explore how the calculation of the black hole integration timestep affects the evolution and hardening of the system.

The original 2016 run performed by  $\varphi$ -GPU utilized  $\Delta t_{min} = 2^{-30}$  and did not include the option to specify the  $\eta_{BH}$  parameter. Instead, a single global  $\eta$  was utilized for all particles. One caveat of further reducing the black hole integration timestep is that it increases the likelihood that the minimum integration timestep will be reached. However, the current versions of the codes have an additional feature which enables the user to receive warnings when the minimum possible timestep  $\Delta t_{min}$  is reached for any particles. These warnings enabled me to verify that, as suspected, reducing the black hole timestep via the  $\eta_{BH}$  correction requires further reducing the minimum integration timestep by many orders of magnitude. In fact, I found that at least the minimum integration timestep with the value of  $\Delta t_{min} = 2^{-36}$  is required in the time period between  $4.0 < t < 7.0$ , corresponding to the semi-major axis range  $6.03 \times 10^{-2} \text{ pc} > a_{BH} > 2.55 \times 10^{-2} \text{ pc}$ . to avoid the appearance of the warnings and therefore the artificial limitation

of the black hole integration timestep. However, at  $t \approx 7$  the code again enters an inaccurate regime, and the black hole integration is once more limited by  $\Delta t_{min}$ . Therefore, I found that the value of  $\Delta t_{min} = 2^{-44}$  is required to avoid the warnings in the later part of the SMBH evolution. However, great care should be taken, since further reducing this parameter may result in loss of precision, due to the calculation entering a regime where double floating point operations are no longer reliable ( $2^{-44} = 5 \times 10^{-14}$  and double values have 16 significant digits). For this reason, the value of  $\Delta t_{min} = 2^{-44}$  presents the lower limit of possibility for this present configuration and should not be reduced further.

In Fig. 5.12 we can see if the  $\eta_{BH}$  correction has an effect on the SMBH binary evolution. We notice that employing a smaller timestep criterion for black holes e.g.  $\eta_{BH} = \eta/4$  has a very significant effect on the hardening, as well as the merger timescale. This effect is found only in the Post-Newtonian runs, while the Newtonian runs match very well with the old data. This seems to suggest that in the case when the Post-Newtonian corrections are implemented, additional accuracy in the black hole integration is required. Otherwise, the larger timestep used for the black hole integration may result in a slight over-estimation of the PN terms, causing slightly higher hardening rates. However, this will then cause a "snowball" effect of sorts, where this slight over-estimation will cause even larger hardening rates, ultimately causing a premature PN-induced plunge of the SMBH binary. The fact that a premature PN plunge was observed is further shown by the right plot on Fig. 5.12. Namely the dependence of the hardening rate  $s$  with the inverse of the semi-major axis is uniquely determined in the GW regime by the formulae given in Eq. 3.33, given a constant stellar hardening rate. In light of this, using a standard Runge-Kutta 4th order numerical integrator, I plotted on the figure in dash-dotted lines the expected hardening of the binary for different values of the stellar hardening rate  $s$ . We can immediately notice that the original 2016 run does not follow the expected evolution at all, instead showing a premature plunge. The orange line, corresponding to the hybrid run with  $\Delta t_{min} = 2^{-36}$  and  $\eta_{BH} = \eta/4$  does a good job of following the expected behavior in the beginning, but afterwards also drifts away from the Runge-Kutta estimates. The blue line, corresponding to the hybrid run with  $\Delta t_{min} = 2^{-44}$  and  $\eta_{BH} = \eta/8$  also shows some small deviation in the final stages, but overall does the best job of following the expected evolution.

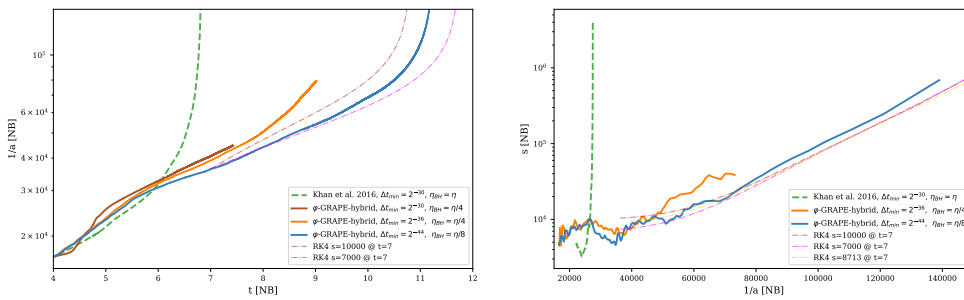


**Figure 5.12:** Left: Time evolution of the inverse of the SMBH binary semi-major axis, given as a measure of black hole hardening. The green dashed line corresponds to the PN corrected run used in [Kh16](#), while the full lines correspond to runs of the hybrid code with different values of the minimum integration timestep and the black hole accuracy parameter  $\eta_{BH}$ . The dash-dotted lines correspond to analytical estimates of the SMBH binary evolution using a constant hardening rate and the orbital formulae in [Peters and Mathews \(1963\)](#). Right: The hardening rate  $s$  of the SMBH binary as a function of the inverse of the semi-major axis. Other elements are the same as on the left plot.

Therefore, we can conclude that the black hole integration timestep, determined by numerical parameters  $\eta_{BH}$  and  $\Delta t_{min}$ , is a very significant parameter that can drastically alter the evolution of the binary in the PN regime. However, drastically reducing it to the values shown here results in a very significant slowdown of the code, even with the hybrid approach. For example, reducing the minimum integration timestep from  $\Delta t_{min} = 2^{-30}$  to  $\Delta t_{min} = 2^{-36}$  resulted in a 500% slowdown of the code. Despite this, I showed that such drastic reduction is absolutely necessary to avoid numerical errors significantly influencing the value of the merger timescale.

### 5.3.5 Centering strategy

When using the hybrid code, one needs to carefully consider the appropriate centering strategy. This is due to the fact that by definition, the expansion of the SCF collisionless force is computed in the origin of the reference frame of the simulation. If the origin is not aligned with the stellar density center to a high degree of accuracy, the overall particle distribution as seen by ETICS will not be symmetric, but rather skewed in some preferred direction. This asymmetry will then result in a non-physical bias in the SCF force calculation. This aspect may seem relatively straight-forward to implement in systems with a well-defined and stationary density center, but in real astrophysical scenarios this may not be the case.

In our system hosting a hard SMBH binary, the stellar density center does not align with the overall center of mass of the system, but rather with the center of mass of the black holes, since the black holes are surrounded by a dense, inner stellar cusp. The black holes themselves have their own accelerated, proper motion with respect to the overall center of mass of the system, and therefore the SMBH binary center of mass represents a non-inertial reference frame. A non-inertial reference frame is not an acceptable choice for the origin of the simulation, since this would then introduce fictitious (inertial) forces acting on all bodies. Newtonian mechanics teaches us that this would result in Newton's second law of motion no longer being valid in this non-inertial reference frame, disrupting the global angular momentum and energy conservation.

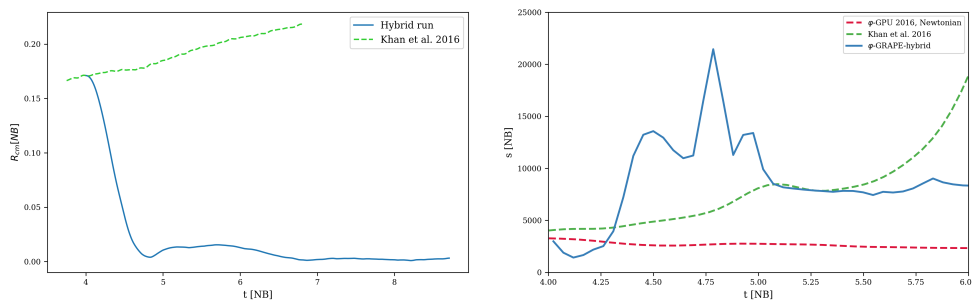


**Figure 5.13:** Left: Distance of the SMBH binary center of mass with respect to the origin of the simulation, as a function of time. The blue line corresponds to an early hybrid run, while the orange line represents the data from [Kh16](#). Right: The hardening rate  $s$  of the SMBH binary as a function of time. The same data is featured as on the left plot, with the addition of the red line which corresponds to the  $\phi$ -GPU 2016 Newtonian run.

On [Fig. 5.13](#) I present the result of one of my early hybrid runs, when the origin of the reference frame is positioned on the stationary, global center of mass of the system (at the time of the start of the simulation). We can notice on the figure that quickly after the start of the run, the SMBH binary sinks towards the origin, due to the bias in the SCF force. This unphysical

sinking of the binary is then also reflected on the right plot, showing the binary hardening rate. The plot demonstrates that an improper centering strategy results in artificial spikes in the hardening rates, as the black holes interact with stars during their sinking towards the center. As a result, neither the global center of mass nor the density center (which aligns with the black hole binary center of mass) are appropriate choices for the origin of the reference frame in our system.

In order to resolve the issue, I decided to switch to an inertial reference frame that is comoving with the binary. Specifically, instead of aligning it exactly with the density center, I assign a constant velocity to the origin that would follow the general, mean motion of the black holes throughout the run. The general idea of this strategy is that small deviations from the actual density center would not be significant enough to introduce a bias in the SCF force, while keeping the simulation origin in an inertial reference frame. For this purpose, I use the original 2016 data to find the mean direction and amplitude of the velocity of the binary center of mass over a period of several Myr. Then, I perform the following coordinate transformation on all particles. This transformation is performed only once at the start of the hybrid run:

$$\vec{r}' = \vec{r} - \vec{r}_{com}, \quad \vec{v}' = \vec{v} - \langle \vec{v}_{com} \rangle, \quad (5.29)$$

where  $\vec{r}_{com}$  is the position of the SMBH binary center of mass at the start of the run and  $\langle \vec{v}_{com} \rangle$  is the mean velocity of the SMBH binary center of mass in the original 2016 run (starting from  $t = 4$  until the SMBH merger).

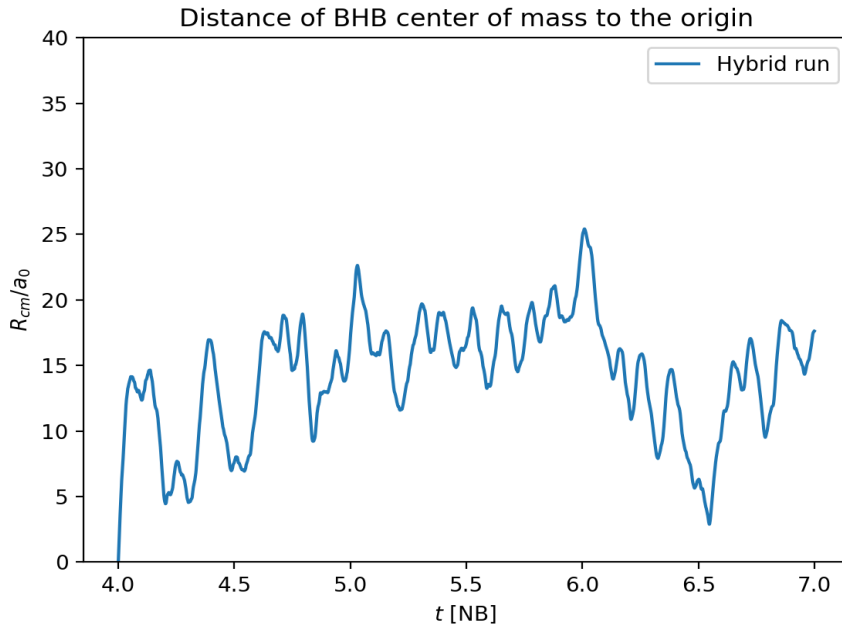


**Figure 5.14:** Deviation between the binary SMBH center of mass with our comoving, inertial reference frame throughout the run. The position of the center of mass is given in units of the binary semi-major axis at the start of the run  $a_{BH,0} = 6.02 \times 10^{-5}$ .

Since this correction is only applied at the start of the run, it may happen that during the

evolution the SMBH binary drifts away from our comoving, inertial reference frame. Therefore, I check the movement of the binary with respect to the origin throughout the run, shown on Fig. 5.14. As seen on the plot, the deviation of the actual binary center of mass (and therefore also stellar density center) with respect to the origin does not exceed more than  $25a_{BH,0} \approx 1.5$  pc. This drift is too small to introduce a bias in the SCF force calculation, therefore resolving the above described issue successfully. In this section, I demonstrated how an improper centering strategy can significantly impact the evolution of the system with the hybrid code. For this reason, the hybrid is best used for stationary systems with well defined density centers. For more complex applications, one needs to adopt a special centering strategy, such as the one presented here, with the comoving, inertial reference frame.

### 5.3.6 Summary and conclusions

In this chapter, I showed an overview of the most relevant numerical parameters of the  $\varphi$ -GRAPE-hybrid code for astrophysical applications. I present results obtained using idealized, spherical Plummer stellar distributions for the purposes of benchmarking, as well as in the case of a more complex and realistic system, for which I utilized the slightly triaxial, rotating galaxy merger remnant system which hosts a hard, SMBH binary system, as described in Kh16. While my investigation was focused on the use of the hybrid for galactic-scale simulations of close SMBH binary systems, the results and conclusions presented here can be of great use for any future use of the  $\varphi$ -GRAPE-hybrid.

In the first part of the chapter, I presented the results from a series of benchmarking runs, where I aimed to give a comprehensive overview of the different aspects of the hybrid that can affect its computational speed. However it should be noted that the benchmarks presented here were based on different versions of the code throughout its development. For more conclusive benchmarks, I refer the reader to the upcoming publication Meiron et al. 2021. Benchmarks showed that out of all the parameters, the greatest effect on the performance by far is the fraction of core particles. While this fraction depends on the type of system the code is being applied to, low fractions of core particles ( $\lesssim 10\%$ ) should be kept in order to fully utilize the gain in computational speed of the hybrid. The core-halo fraction of particles also affects the performance with respect to the direct-only approach. Benchmarks showed that an impressive 28 factor of the speed-up is obtained when using only 1% of core particles, but this value decreases to 2.5 when using 50% of core particles. On the other hand, I found that the maximum order in the multipole expansion  $l_{max}$  does not impact the performance significantly. At the time of writing, the hybrid code can be used in combination with both the yebbisu GRAPE-emulation library (Nitadori, 2009) and the sapporo GRAPE emulation library (Gaburov et al., 2009).

In the second part of the chapter, I presented an overview of the most important numerical parameters of the hybrid and how they can affect the scientific results if not chosen carefully. While this analysis focused on the use of the hybrid for the study of close SMBH binaries in galactic nuclei, many of the results presented here are applicable for studies of binary SMBH systems using other codes and methods as well, especially the results concerning the softening and black hole integration timestep. Most notably, Fig. 5.6 shows a similar analysis of the appropriate softening, performed by Peter Berczik using the  $\varphi$ -GPU, showing that the results are relevant for studies of such systems in general.

The combined analysis using both  $\varphi$ -GRAPE-hybrid and  $\varphi$ -GPU demonstrates the dependence of the hardening rate on the value of the gravitational softening if a larger than necessary

value of the softening is used. This results in some energetic stellar interactions being softened, thereby artificially reducing the hardening rate. In order to avoid this, a significantly lower value of the softening is required,  $\epsilon \sim 10^{-4}$  pc in order to properly resolve all of the interactions. This value is two orders of magnitude smaller than the binary semi-major axis at the onset of the GW-dominated phase. Most N-body studies so far used values of the softening larger by at least an order of magnitude (Nasim et al., 2020; Khan et al., 2016; Gualandris et al., 2017; Khan et al., 2011; Preto et al., 2011, and others), suggesting that the hardening rate may have been somewhat underestimated in these studies. The best results would without a doubt be obtained when using zero softening for the stellar-black hole interactions, provided the code supports chain regularization for particles around the SMBH, like in the case of Rantala et al. (2017) and Vasiliev et al. (2014). However, the use of chain regularization comes with a caveat, since only a very limited number of stars may be regularized at a time using the AR-chain method. However, new algorithmic regularization techniques should drastically improve this (Rantala et al., 2020).

I demonstrated the importance of the black hole integration timestep, and how insufficient accuracy in the black hole integration in combination with the PN terms in the equations of motion can lead to a premature GW-driven plunge and the underestimation of merger timescales of the system. Out of all the parameters presented, the results show that this one is the one that impacts the evolution of the SMBH binary the most. In the case of Kh16, this led to a premature SMBH merger, with the actual expected merger timescale being a factor of 2 larger. I demonstrated that a good way to avoid this issue is by looking at the evolution of the hardening rate  $s$  with respect to  $1/a$  and comparing this with the expected values using constant hardening rates and analytical formulae of GW emission (Peters and Mathews, 1963). If there is a large discrepancy present, this can be evidence of insufficient accuracy in the black hole integration.

In the last section, I underlined the importance of a proper centering strategy when using the  $\varphi$ -GRAPE-hybrid code. Unlike many other N-body codes which can specify an arbitrary origin of the reference frame, by definition, the hybrid needs to be centered on the density center of the system. Otherwise, the resulting bias in the SCF force will result in non-physical results. In more complex systems, however, using the density center as the origin while remaining in an inertial frame of reference may be easier said than done. For this purpose, I present an example of a solution for such cases, so that the origin is centered very near the density center, while remaining in an inertial frame.

The biggest advantage of  $\varphi$ -GRAPE-hybrid by far is the great gain in computational speed over purely direct approaches, while retaining accuracy of direct integration for a subset of particles of interest. However, one should also be aware of the limitations of the code, since it is only meant to be used for well-centered, equilibrium systems, with a relatively low fraction of core particles. As such, it is only applicable in these very specific scenarios.

---

## NUMERICAL INVESTIGATION OF THREE-BODY SCATTERING EVENTS WITH A SMBH BINARY IN THE POST-NEWTONIAN REGIME

---

In this chapter, I perform a series of high-resolution 3-body scattering experiments to investigate the Post-Newtonian corrected energy balance of a hard SMBH binary during strong interactions with incoming stars. The simulations were performed at the Kepler computer cluster, at the University of Heidelberg.

### 6.1 INTRODUCTION

During the hardening phase of a SMBH binary merger, described in Chapter 4, the main mechanism of energy loss for the binary is via energetic stellar interactions, during which incoming stars on radial orbits are able to extract energy from the binary with the gravitational slingshot effect. In order for the energy extracted from the binary to be significant enough to measurably contribute to the hardening, the star needs to experience very close interactions with the binary (with the closest approach distance on the order of the binary semi-major axis,  $r_p \lesssim 3a_{bh}$ ). The proper treatment of this physical process is of crucial importance since this is the primary method of bringing the black holes close enough in order to reach coalescence. However, it may be problematic and cumbersome to include in galactic scale simulations, due to the very high spatial resolution which is necessary to properly resolve all of the close interactions (compared to galactic scales which are orders of magnitude larger). Therefore, direct treatment of these interactions might be out of reach for studies that do not have access to large and efficient computational resources. Instead, they may use semi-analytical estimates of hardening rates which can then be used to model the evolution of SMBH binaries without actually resolving the encounters themselves (e.g. [Sesana and Khan, 2015](#)).

On the other hand, direct N-body codes are able to calculate forces during the encounters up to a high degree of accuracy, but are often unable to accurately analyze the individual encounters between the stellar and BH particles, due to resolution constraints and exceptionally high computational cost. Therefore, they are usually unable to give precise estimates of the specific energy changes in a single encounter, instead focusing on cumulative effects from many interactions.

Instead, 3-body scattering experiments provide a computationally efficient way to study the nature of these interactions in a multitude of different configurations and scenarios and to investigate these effects for different masses of the binary members and orbital configurations (see Sec. 4.2.2). They can be especially useful as a precursor to N-body runs, as a way to gain insight into the cumulative, as well as average energy changes from stellar encounters, without the presence of other physical effects from the galactic environment which may affect the result, such as gravitational torques from overdensities in the distribution, two-body relaxation effects and the gravitational impact of the system itself.

In particular, in the [Kh16](#) study, there was a mismatch between the overall SMBH binary energy change and the cumulative energy changes of the stars ([Ikape, 2016](#)), pointing to the presence of either spurious numerical effects, or other physical hardening processes which were not accounted for. For example, it was not fully understood if the introduction of Post-Newtonian terms in the equations of motion will affect the star-binary energy exchange, and if so, if the effect would be measurable. This is especially interesting to consider during the phase of the merger when gravitational wave emission becomes comparable to the binding energy gained from stellar interactions. During this transitional period, both stellar hardening and PN terms induce secular, as well as periodic changes in the orbital motion of the binary and the interplay between these two effects in N-body studies has not yet been thoroughly explored in the literature.

Therefore, in this chapter I will present the results of a number of three-body scattering experiments, performed using the state-of-the-art AR-chain integration method ([Mikkola and Merritt, 2006, 2008](#)). The goal of these experiments was to provide valuable insight into the energy exchange at a time when the PN effects are non-negligible, enabling an overview of dominant terms in the energy balance, as well as a useful check in order to see if the mismatch between stellar hardening and the total energy change of the binary can be reproduced ([Ikape, 2016](#)).

Additionally, the simulation run in [Kh16](#) was unable to evaluate the complexity and nature of the interaction, including the closest approach of the star to the binary, the number of stars which would directly plunge into one of the black holes, and whether or not a star experiences multiple interactions before ejection. Therefore, I will present a distribution of the evaluated pericenter distance of the interacting stars, as well as an estimate of the fraction of direct plunges of stars into black hole, termed the merger rate throughout the chapter.

The chapter is structured as follows. In Section 6.2 I describe the simulations parameters and describe the initial setup of the code. In Section 6.3 I present the derivation of the condition employed for the initial velocity of the stellar particles. In Section 6.4.1 I briefly describe the merger rate detected in the runs. In Section 6.4.2 I analyze the pericenter distances of the stellar encounters and discuss their connection to the energy change of the star. In Section 6.4.3 I discuss the energy balance of the system and identify the energy discrepancies within. Section 6.4.4 contains the main result, where PN corrections are introduced to the energy balance and a full description of the energy balance within a scattering event is given. Finally, Section 6.5 contains the conclusions and the discussion of the results.

## 6.2 INITIAL CONDITIONS AND SETUP

In the following, I describe the numerical setup employed for the investigation of the three-body encounters in the hardening regime of an SMBH binary. Each simulation run consists of three particles in total, two SMBH particles, situated near the centre of mass of the system and a stellar particle, acting as a distant third body. For the initialization of the SMBH binary I use the original data from [Kh16](#), at different times throughout the run. The black hole particles are part of a hard Keplerian binary system, with equations of motion corrected for PN effects up to order PN 2.5 (leading radiation-reaction term). It is important to note that all of the units in this chapter do not reflect physical units and are given in N-body units, defined by setting the speed of light as  $c = 477.12$ . For the sake of clarity, I present the N-body units with respect to their physical unit equivalents in [Table 6.1](#).

M.U. [ $M_{\odot}$ ]	T.U. [Myr]	L.U. [kpc]	V.U. [km/s]	E.U. [ $M_{\odot} (\text{km/s})^2$ ]
$9.18 \times 10^{11}$	1.55	1	628.3	$3.62 \times 10^{16}$

**Table 6.1:** Table of N-body units with respect to physical units, used throughout the chapter. The columns correspond to: mass unit, time unit, length unit, velocity unit and energy unit, respectively.

The stellar particle is assigned a mass several orders of magnitude smaller than the mass of the less massive black hole (see [Table 6.2](#)), and is positioned at a significant initial distance from the binary system  $D_0 = 0.1$ . Every stellar particle is assigned the same mass value of  $m_* = 10^{-6}$ , which corresponds to  $91,800 M_{\odot}$ . One advantage of the AR-chain integration method is that implementing the softening is optional, since the interactions between the particles are regularized to avoid singularities when  $R \rightarrow 0$ . Therefore, in the code the softening between the star and the black holes, as well as between the black holes themselves is zero, allowing for arbitrarily close approaches.

Two different sets of scattering experiments were performed, corresponding to different times of the original N-body run. The first set of runs is initialized when the binary semi-major axis is  $a_0 = 4.6 \times 10^{-5}$ , corresponding to time  $t_0 = 5$  of the original run. At this point in time, we expect the gravitational wave emission to be measurable, but not dominant with respect to stellar hardening. The second set of runs is initialized when the binary semi-major axis is  $a_0 = 3.15 \times 10^{-5}$ , corresponding to time  $t_0 = 6$  in the original run. At this point in time we expect gravitational wave emission to be dominant with respect to stellar hardening.

A simulation run is ended if the stellar particle becomes unbound. A stellar particle is considered unbound if its total energy becomes positive,  $E_* > 0$ , and if it is at a distance  $D > 2D_0$  from the center of mass. Both of these conditions need to be met in order to stop the run. Otherwise, a run is stopped if the star does not experience large energy changes over a sufficiently large timescale  $t > t_f = 10$ , or if there is a merger event between the star particle and the black hole binary. After each encounter, the system is reset, the binary is given the same initial conditions and orbital parameters as before, and the next stellar particle is generated.

The initial conditions for stellar particles are calculated in such a way so that the stellar particles are isotropically distributed around the SMBH binary. Using standard random number generation, stars are distributed evenly on a spherical shell surrounding the binary with a radius  $R = D_0$ . The Cartesian coordinates of each star particle were then calculated in the following

way:

$$x_i = r_i \cos(\phi_i), \quad (6.1)$$

$$y_i = r_i \sin(\phi_i), \quad (6.2)$$

$$z_i = D_0 \cdot R_1, \quad (6.3)$$

where  $R_1 \in [-1, +1]$  is a randomly generated number. The coordinates  $r_i$  and  $\phi_i$  were calculated using:

$$\phi_i = 2\pi R_2, \quad (6.4)$$

$$r_i = \sqrt{D_0^2 - z_i^2}, \quad (6.5)$$

where  $R_2 \in [0, +1]$  is another randomly generated number. The initial velocity conditions are covered in detail in the next subsection.

The first set of runs, corresponding to initial time  $t_0 = 5$ , consisted of 1000 scattering experiments with output generated at the timestep of  $\Delta t = 10^{-3}$ . The second set of runs consisted of 2000 encounters in total, and the output frequency was lowered since snapshots were generated at the timestep of  $\Delta t = 10^{-2}$ . The sample size for the second set of runs was increased by a factor of 2 in order to investigate if the results are affected by the low number statistics. It is important to note that the output frequency for both sets of runs is several orders of magnitude lower than the output frequency needed to actually resolve the orbit of the binary. This can be easily verified with Kepler's third law of motion, which we can use to calculate the orbital period of the binary, which we find to be  $T \sim 10^{-5}$ . This means that while the time resolution is significantly increased with respect to the full N-body run, it is still insufficient to resolve the energetic encounter itself.

$N$	$\Delta t$	$t_0$	$t_{max}$	$m_{BH,1}$	$m_{BH,2}$	$m_*$	$D_0$	$a_0$	$e_0$	$T_0$	PN terms
1000	$10^{-3}$	5	10	$3.3 \times 10^{-3}$	$8.7 \times 10^{-4}$	$10^{-6}$	0.1	$4.6 \times 10^{-5}$	0.13	$3.21 \times 10^{-5}$	1+2+2.5
2000	$10^{-2}$	6	10	$3.3 \times 10^{-3}$	$8.7 \times 10^{-4}$	$10^{-6}$	0.1	$3.15 \times 10^{-5}$	0.15	$1.73 \times 10^{-5}$	1+2+2.5

**Table 6.2:** In this table we present the initial conditions and parameters of the runs. All units are in N-body units. The columns represent in left-to-right order: number of runs per simulation set, output frequency of run, initial time of run expressed in the original data timing scheme, maximum possible time of run, major black hole mass, minor black hole mass, stellar mass, initial stellar distance from the binary center of mass, initial semi-major axis of binary, initial orbital eccentricity of binary, initial orbital period of binary, order of PN terms included.

The numerical values of the parameters described so far are given in Table 6.2.

### 6.3 INITIAL VELOCITY CONDITION

The closest approach of the stellar particle to the binary (its pericenter distance  $r_p$ ) depends on its initial velocity amplitude  $V_i$ . Therefore, in order to make sure that our encounters experience strong interactions with the black hole binary, we need to carefully choose the initial velocity of the stellar particles. We are interested in the particles which have closest approaches comparable

to the initial semi-major axis of the binary:

$$r_p < 2a_0. \quad (6.6)$$

Using a standard equilibrium velocity distribution, e.g. the Plummer distribution is not appropriate in this case, since we would expect that the stars to come beyond the influence radius on highly radial, centrophilic orbits. Therefore, in this section I derive a relation that determines the initial stellar velocity in the following way:

Since the system is an isolated 3-body system, the total energy and angular momentum of the stellar particle does not change until the energy exchange with the SMBH binary. Therefore, the initial energy of the stellar particle is equal to its energy at the point of closest approach to the binary (before energy exchange). The same can be said for the angular momentum of the particle, so we can write:

$$E_*|_{t_i} = \frac{1}{2}\mu V_i^2 + \frac{GM\mu}{r_i} = \frac{1}{2}\mu V_f^2 + \frac{GM\mu}{r_f} = E_*|_{t_f}, \quad (6.7)$$

$$L_*|_{t_i} = |\mu\vec{r}_i \times \vec{v}_i| = |\mu\vec{r}_f \times \vec{v}_f| = L_*|_{t_f} \quad (6.8)$$

where  $t_i$  denotes the initial time,  $t_f$  denotes the time of closest approach to the binary,  $\mu$  is the relative mass in the star-binary two-body Keplerian approximation and  $M$  is the total mass of the system. Here I assume that we can approximate the black hole binary as a point mass with a total mass of  $m_{BH} = m_{BH,1} + m_{BH,2}$ , in order to reduce the system to a standard 2-body Kepler problem. Substituting the quantities for our system we get:

$$E_*|_{t_i} = \frac{1}{2} \frac{m_* m_{BH}}{m_{BH} + m_*} V_i^2 - \frac{m_*(m_{BH})}{D_0} = \frac{1}{2} \frac{m_* m_{BH}}{m_{BH} + m_*} V_f^2 - \frac{m_* m_{BH}}{r_p} E_*|_{t_f}, \quad (6.9)$$

$$L_*|_{t_i} = V_i D_0 \sin \alpha = r_p V_f = L_*|_{t_f} \quad (6.10)$$

where  $\alpha$  is the initial angle between vectors  $\vec{v}$  and  $\vec{r}$ . The gravitational constant  $G$  is taken as  $G = 1$ , as is standard for N-body units. Here I also assume that  $D_0 \gg a_0$ . By definition, at pericenter the velocity is orthogonal to the position vector, so the amplitude of the angular momentum at that time is simply the product of the amplitudes of the position and velocity vectors. Combining equations 6.9 and 6.10 by eliminating  $V_f$ , we can rewrite condition 6.6 as:

$$r_p = \frac{\sqrt{1 + \frac{2V_i^2 D_0^2 \sin^2 \alpha}{m_{tot}} \left( \frac{V_i^2}{2m_{tot}} - \frac{1}{D_0} \right)}}{2 \left( \frac{V_i^2}{2m_{tot}} - \frac{1}{D_0} \right)} - 1 \leq 2a_0, \quad (6.11)$$

where  $m_{tot}$  is the total mass of the 3-body system  $m_{tot} = m_{BH} + m_*$ . This allows us to easily get a condition for the initial velocity amplitude, with only one unknown variable, the angle  $\alpha$ :

$$V_i^2 \leq \frac{4a_0(D_0 - 2a_0)m_{tot}}{D_0(D_0^2 \sin^2 \alpha - 4a_0^2)}, \quad (6.12)$$

$$\rightarrow \left( \frac{V_i}{V_{esc}} \right)^2 \leq \frac{2a_0(D_0 - 2a_0)}{D_0^2 \sin^2 \alpha - 4a_0^2}, \quad (6.13)$$

where we have expressed velocity in terms of the escape velocity needed for the star to be ejected from the system,  $V_e = \sqrt{\frac{2m_{BH}}{D_0}}$ .

The angle between two vectors is independent of their amplitude. Therefore, in order to calculate the angle  $\alpha$ , we first generate a randomly oriented normalized velocity vector  $\hat{v}_i$ , using a similar approach as the one in Eqs. 6.1 to find the cartesian components:

$$v_{x,i} = v_{t,i} \cos(\phi'_i), \quad (6.14)$$

$$v_{y,i} = v_{t,i} \sin(\phi'_i), \quad (6.15)$$

$$v_{z,i} = R_3, \quad (6.16)$$

where  $R_3 \in [-1, +1]$  is a randomly generated number. The quantities  $v_{t,i}$  and  $\phi'_i$  were calculated using

$$\phi'_i = 2\pi R_4, \quad (6.17)$$

$$v_{t,i} = \sqrt{1 - v_{z,i}^2}, \quad (6.18)$$

where  $R_4 \in [0, +1]$ .

With the normalized velocity vector calculated, we can find the angle  $\alpha$  using the standard scalar product:

$$\cos \alpha = \frac{\vec{r}_i}{\|\vec{r}_i\|} \cdot \hat{v}_i = \frac{(x_i v_{x,i} + y_i v_{y,i} + z_i v_{z,i})}{D_0}. \quad (6.19)$$

With the angle  $\alpha$  calculated, we can substitute the above relation in Eq. 6.13 in order to finally obtain our initial velocity amplitude condition. Then, we simply multiply the obtained velocity amplitude with the already generated unit velocity vector  $\hat{v}_i$ :

$$v_i = V_i \hat{v}_i. \quad (6.20)$$

On Fig. 6.1, the distribution of initial velocities obtained with this method is shown. As seen on the figure, most of the encounters are slow with respect to the local escape velocity.

## 6.4 RESULTS

### 6.4.1 Merger rate

Previously described parameter values are set up in such a way that is expected to be ideal for highly effective energy exchange between the stellar and SMBH particles. This is in large part due to the fact that the initial velocity condition given by Eq. 6.13 guarantees close approaches

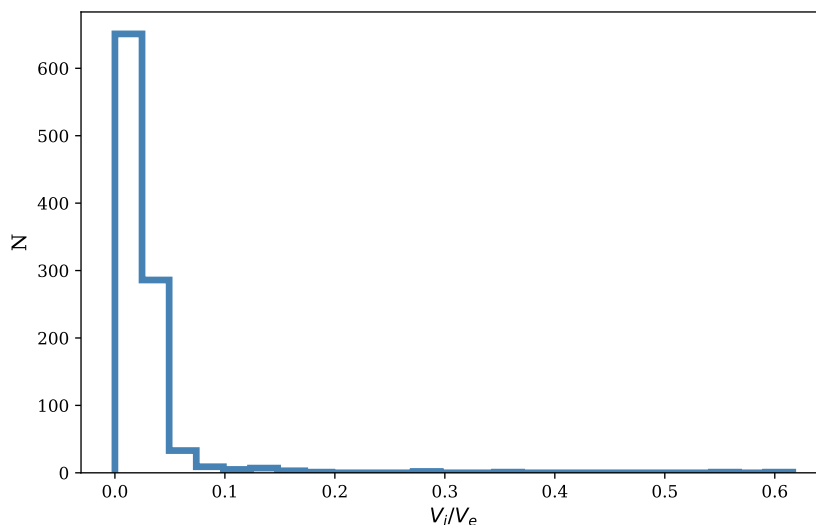


**Figure 6.1:** Histogram of the initial velocity amplitude normalized to the escape velocity  $V_e$  at radius  $D_0$  for the simulation set with  $t_0 = 5$ .

to the binary. Normally, the value of the softening determines the closest possible approach between the particles. Since the softening in the AR-chain is set to zero for all particles, this artificial limit is not present and allows for arbitrarily close interactions between all particles. However, this can also lead to merger events, which should be excluded from any energy exchange analysis. A merger between a stellar and black hole particle is registered as the moment when their separation becomes smaller than, or equal to  $\leq 4R_{sch}$ , where  $R_{sch}$  is the Schwarzschild radius of the black hole involved in the interaction. The merger rates obtained from the simulations for the cases of  $t_0 = 5$  and  $t_0 = 6$ , respectively are 2.01% and 2%, and these events are therefore excluded from further analysis, since in reality they would result in direct plunges of stars into the black hole.

#### 6.4.2 Pericenter distribution

Large, galactic-scale N-body simulations require set values of the gravitational softening parameter  $\epsilon$  for interactions between the particles (i.e star-star, star-black hole). If the value of the softening parameter is not chosen carefully, it can result in under- or over-estimating the hardening rate of the binary, which in turn determines the merger timescale (see the discussion in Ch. 5). Therefore, it is relevant to estimate the pericenter distribution of the incoming stars, which would give insight into the appropriate value of the softening parameter to be used. The pericenter distance of the star particle is calculated according to Eq. 6.11. However, as previously mentioned, this equation approximates the black hole binary as a single point mass, and calculates the pericenter in the two-body star-black hole binary system. While we use the two-body pericenter as a measure of the closest approach, during the actual three-body interaction the closest approach of the star does not coincide with the Keplerian two-body pericenter. Therefore, we check if the derived initial  $r_p$  with respect to the SMBH binary center of mass corresponds to the actual resolved closest approach of the star from the simulation and we find very good agreement.

The resulting pericenter distribution for the  $t_0 = 5$  set of runs is given in Figure 6.2, where  $\Delta E_*/m_*$  is the specific total energy change of the stellar particle. The initial pericenter

distributions for runs with initial time  $t_0 = 6$  show the same behavior, and therefore are not given here.

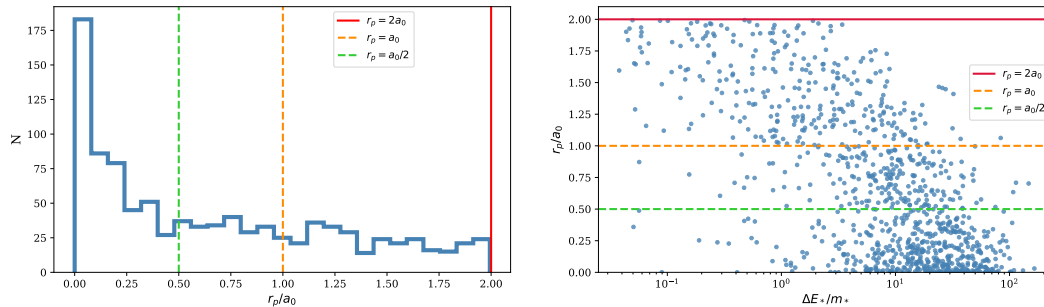


**Figure 6.2:** Left: Histogram of the initial pericenter distance in units of initial binary semi-major axis  $r_p/a_0$ . Right: Scatter plot of the pericenter distance  $r_p/a_0$  as a function of  $\Delta E_*/m_*$ ,

Using the left plot on Figure 6.2 we can evaluate the pericenter distribution within the radius of  $2a_0$  from the binary. It is clear that, out of 1000 total encounters, the vast majority of encounters (around  $\sim 300$ ) comes as close as  $0.25a_0$  to the binary, likely crossing the orbit of the binary.

On the other hand, the right panel of Figure 6.2 tells us how energetic each encounter is, represented by the specific energy change of the particle  $\Delta E_*/m_*$ . The most energetic encounters fall on the right side of the plot, while the less energetic ones are represented in the far left side. In reality, most of the encounters (those which satisfy  $\Delta E_*/m_* < 1$ ) do not contribute significantly to the hardening rate of the binary, as their specific energy changes are too low. However, the high-energy tail, even when it only contains a fraction of the total population of encounters, can significantly increase the hardening rate. Therefore, regarding large-scale N-body runs, it is important to understand which properties of the star particles result in the most energetic exchanges which would fall in the high-energy tail (in this consideration taken to be  $\Delta E_*/m_* \geq 1$ ). We can see from the plot that even though there is a clear tendency for more energetic encounters to come close to the black hole binary ( $r_p < a_0$ ), there are a few energetic outliers that do not follow the trend. These outliers are also the most energetic encounters obtained from these 1000 runs, hinting that the most significant encounters for the hardening rate may have complex interactions with the binary, with multiple orbits, resulting in a large energy increase, which would not be reflected in the initial pericenter distance  $r_p < a_0/2$ . However, as seen on the figure, these cases are rare.

### 6.4.3 Energy balance

In this section, I will analyze in detail the energy balance of the system by examining the different energy terms which constitute the total energy of the three-body system for each run.

The equations of motion of the two black hole particles have been corrected for Post-Newtonian effects up to order PN 2.5, according to the formulas found in [Blanchet and Iyer \(2003\)](#). However, it is important to note that the treatment of stellar particles remains strictly Newtonian. The only dissipative term in the equations of motion of the black holes is the PN 2.5 term, corresponding to the GW radiation-reaction term ([Peters, 1964](#)), while the other PN terms (namely PN 1 and 2) terms are conservative and maintain the conservation of energy of the SMBH binary. The simulation employs black holes without spin, so the PN 1.5 term is equal

to zero. Because of this, we expect the PN 2.5 term to be the only one to effectively take away net energy from the system.

The relative energy error of our simulation runs  $\delta E/U$  is in the range of  $10^{-13}$ – $10^{-9}$ , several orders of magnitude smaller than the values of the energy components of the system. Therefore, we expect that when corrected for the PN 2.5 term, the total energy of the simulated 3-body system is conserved to a high degree, and the energy exchange is well resolved. Let us now provide a simplified overview of all the energy components. We will assume the binary center of mass is at rest at the origin and treat the binary as a single massive body when computing the potential exerted by the binary on the star. This is a justified approximation since the initial ( $D_0$ ) and final distance of the star ( $> 2D_0$ ) is much larger than the binary orbital separation. Additionally, at this point in the analysis, we will only consider the Newtonian expression for the binary orbital energy.

The binding energy of the black hole binary is then given by the standard orbital energy formula (Binney and Tremaine, 1987):

$$E_{BE} = \frac{Gm_1m_2}{2a}. \quad (6.21)$$

Before the interaction the total energy of the system can be written as:

$$E = E_{BH} + E_*, \quad (6.22)$$

where  $E_{BH} = -E_{BE} < 0$  is the total orbital energy of the black hole binary, and  $E_* = E_{*,kin} + U < 0$ , is the total energy of the star, with  $E_{*,kin}$  designating kinetic energy and  $U$  designating potential energy. After the interaction and energy exchange, corresponding to the end of our simulation run, the energy of the system can be written as:

$$E' = E'_{BH} + E'_* + E_{GW}, \quad (6.23)$$

where  $E_{GW}$  is the energy emitted by gravitational radiation during the simulation. Since energy is conserved to a high order, we can equate these two expressions to get:

$$E_{BH} + E_* = E'_{BH} + E'_* + E_{GW}, \quad (6.24)$$

$$\rightarrow -(E'_{BH} - E_{bh}) = E'_* - E_* + E_{GW}, \quad (6.25)$$

$$\rightarrow -\Delta E_{BH} = \Delta E_{BE} = \Delta E_* + E_{GW}, \quad (6.26)$$

where the SMBH binary energy change  $\Delta E_{BH}$  is given by:

$$\Delta E_{BH} = -\frac{Gm_1m_2}{2} \cdot \Delta\left(\frac{1}{a}\right) < 0. \quad (6.27)$$

Equation 6.26 tells us that we expect that the binding energy change of the binary corresponds to a high degree of accuracy to the sum of the energy change of the star particle and the energy emitted by gravitational radiation. Additionally, the total energy change of the star can

be calculated easily from the data using:

$$\Delta E_* = (E'_{*,kin} + U') - (E_{*,kin} + U) \quad (6.28)$$

$$= \frac{m_*}{2} (v'^2 - v^2) - m_* G (m_1 + m_2) \left( \frac{1}{D} - \frac{1}{D_0} \right). \quad (6.29)$$

The energy emitted via gravitational waves  $E_{GW}$  is calculated using the radiation-reaction term from Eq. 3.14, and cross-checked with the orbit-averaged formulas (see Eq. 3.33):

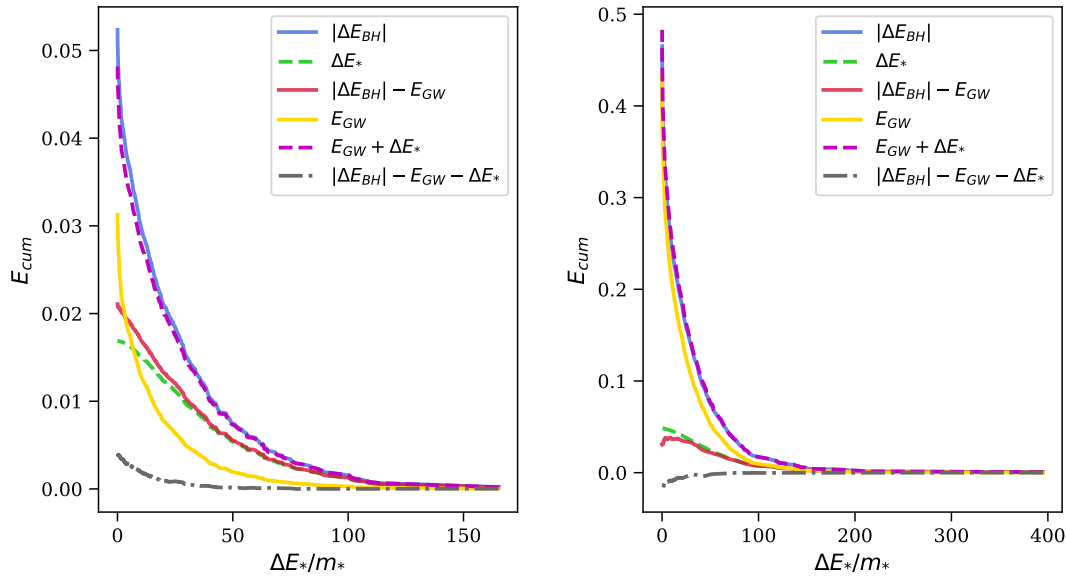


**Figure 6.3:** Cumulatively summed energy terms as a function of specific energy change for the simulation set with initial time  $t_0 = 5$  (left) and  $t_0 = 6$  (right). The different colors correspond to different combinations of terms from Eq. 6.26. The energy discrepancy not accounted for in the energy balance equation is shown as a dash-dotted gray line. In the absence of energy discrepancy, the blue and purple lines should match, as well as the red and green lines, according to Eq. 6.26.

An overview of the cumulatively summed different energy terms for both sets of simulation runs can be seen on Figure 6.3, as a function of specific energy change. If Eq. 6.26 is satisfied, the blue and dashed magenta line, as well as the red and dashed green lines should match to a very high degree. Then, we would expect that the energy difference between all terms (gray dash-dotted line) remains at zero at all energies. However, we notice from the figure that this is not the case. In both simulation sets, there is a non-negligible energy discrepancy denoted by the gray dash-dotted line, which represents energy not accounted for by the energy balance equation. In the case of  $t_0 = 5$ , the cumulative sum of the energy discrepancies is positive, while when  $t_0 = 6$  the summed energy discrepancies are negative. This energy discrepancy is at the same order of magnitude as the other energy terms. As previously noted, the energy error of the simulation is a few orders of magnitude smaller than any value of the energy terms, and therefore cannot be responsible for the energy discrepancy.

#### 6.4.4 PN energy correction terms

In order to resolve the energy discrepancy problem, we need to carefully look at the assumptions and energy terms used in Eq. 6.26. In that analysis, we have used strictly Newtonian definitions

of the binary orbital energy, except for the GW emission term. However, at this point of the SMBH binary evolution, when the separation between the black holes is comparable to their Schwarzschild radii, Post-Newtonian corrections must also be added to the total energy calculation, since standard Newtonian notions of energy no longer apply.

Let us remind ourselves of the considerations made in Ch. 3.3.3. We previously mentioned that the even PN terms are non-dissipative and we did not previously include them in the equation denoting the energy changes (Eq. 6.26). Nevertheless, I will now show that they must still be included in order to properly account for all energy changes. These terms, while not effectively carrying away energy from the system, can cause instabilities and oscillations with respect to the Newtonian total energy. These instabilities, which can be neglected over long timescales and a large number of interactions, do however play a role in the energy balance of an individual encounter. We can perhaps, illustrate this better using the following analysis:

If we omit the odd PN2.5 radiation reaction term (Eq. 3.14), the total PN-corrected energy of the black hole binary  $E_{BH}$  is fully described by Eq. 3.12. We can separate this energy into a Newtonian term and the PN correction term:

$$E_{BH} = E_{Newt} + E_{PN}, \quad (6.30)$$

where the Newtonian part is given by:

$$E_{Newt} = \frac{\mu v^2}{2} - \frac{\mu(m)}{r}. \quad (6.31)$$

The Post-Newtonian term corresponds to the effect of the even PN terms:

$$E_{PN} = E_{PN1} + E_{PN2} + \dots \quad (6.32)$$

The leading correction term is repeated here for the sake of clarity (Blanchet and Iyer, 2003):

$$E_{PN1} = \frac{\mu}{c^2} \left\{ \frac{3v^4}{8} - \frac{9m_1 m_2 v^4}{8m^2} + \frac{m}{r} \left( \frac{m_1 m_2 (\vec{n} \cdot \vec{v})^2}{2m^2} + \frac{3v^2}{2} + \frac{m_1 m_2 v^2}{2m^2} \right) + \frac{m^2}{2r^2} \right\}. \quad (6.33)$$

If the equations of motion are corrected up to the 2PN term, the energy of the binary  $E_{BH}$  is fully conserved. However, since the equations of motion also include the dissipative 2.5PN term, this energy is conserved only in the sense that its time derivative computed through the fully PN-corrected equations of motion is exactly equal to the effect of the PN2.5 term (Blanchet and Iyer, 2003). Then, in the absence of stellar interactions, the total change in the binary energy can be expressed as:

$$|\Delta E_{BH}| = |\Delta E_{Newt} + \Delta E_{PN}| = \Delta E_{GW}. \quad (6.34)$$

When a star extracts energy from the binary, this additional term can be added to the right side of the above equation:

$$|\Delta E_{Newt} + \Delta E_{PN}| = \Delta E_* + E_{GW}. \quad (6.35)$$

The important distinction here with respect to Eq. 6.26 is the addition of the  $\Delta E_{PN}$  term, which

was previously neglected. This leads to the final expression for stellar energy change:

$$\Delta E_* = |(\Delta E_{Newt} + \Delta E_{PN})| - E_{GW}. \quad (6.36)$$

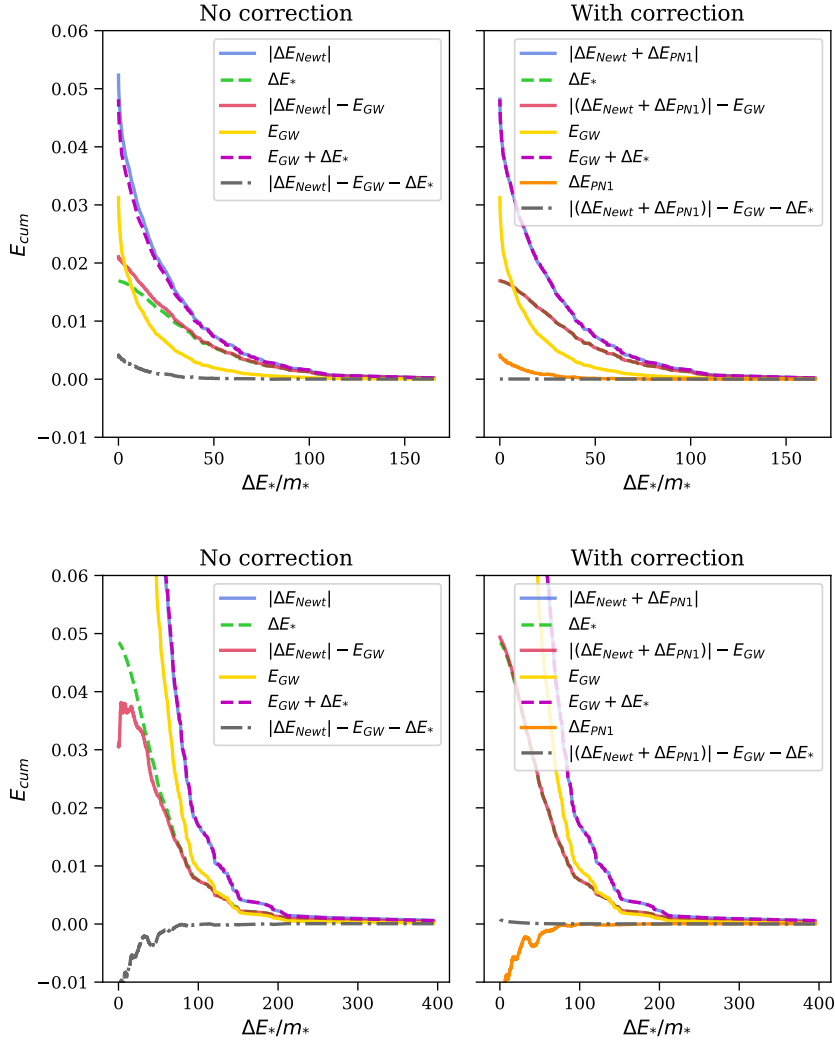


**Figure 6.4:** Top: Cumulative energy terms as a function of specific energy change, for the simulation set at initial time  $t_0 = 5$ , without (left) and with (right) the  $E_{PN1}$  correction term. Bottom: Cumulative energy terms as a function of specific energy change, for for the simulation set at initial time  $t_0 = 6$ , without (left) and with (right) the  $E_{PN1}$  correction term. Other elements are the same as Fig. 6.3.

In Fig. 6.4 we can see the updated cumulative energy term plots. The figures on the left are the same as in Fig. 6.3. The figures on the right include the correction for the leading order PN 1 energy term to the energy balance. This first order correction is clearly sufficient to successfully resolve the energy discrepancy that was obtained earlier. This is shown by the gray dash-dotted line which is now consistently at zero for all encounters, proving that Eq. 6.35 is sufficient to properly account for all of the energy changes in the runs.

This is also illustrated in Fig. 6.5, where we can see on the left side the value of the energy discrepancy for each individual run, as shown by the vertical distance of the points from the black line. The black line corresponds to an ideal situation with no energy losses, when the

energy change of the binary is exactly equal to the stellar energy changes. The color coding corresponds to Newtonian orbital eccentricity changes of the SMBH binary, calculated using the Runge-Lenz vector. The color coding shows that the value of the energy discrepancy is correlated to the eccentricity change of the binary. Positive values of the the discrepancy result in largely negative changes in eccentricity, and vice versa. The right side of the plot shows that the energy discrepancies seen in the left side of the plot come from the  $E_{PN1}$  correction term, and after the correction we obtain much better energy conservation, with all points falling almost exactly on the black line. We can conclude that the energy discrepancy is resolved simply by the inclusion of the leading PN1 correction to the energy of the binary.

### 6.5 SUMMARY AND CONCLUSIONS

In this chapter I have described two sets of three-body simulations that were performed using the highly accurate AR chain regularization integration method (Mikkola and Merritt, 2006,

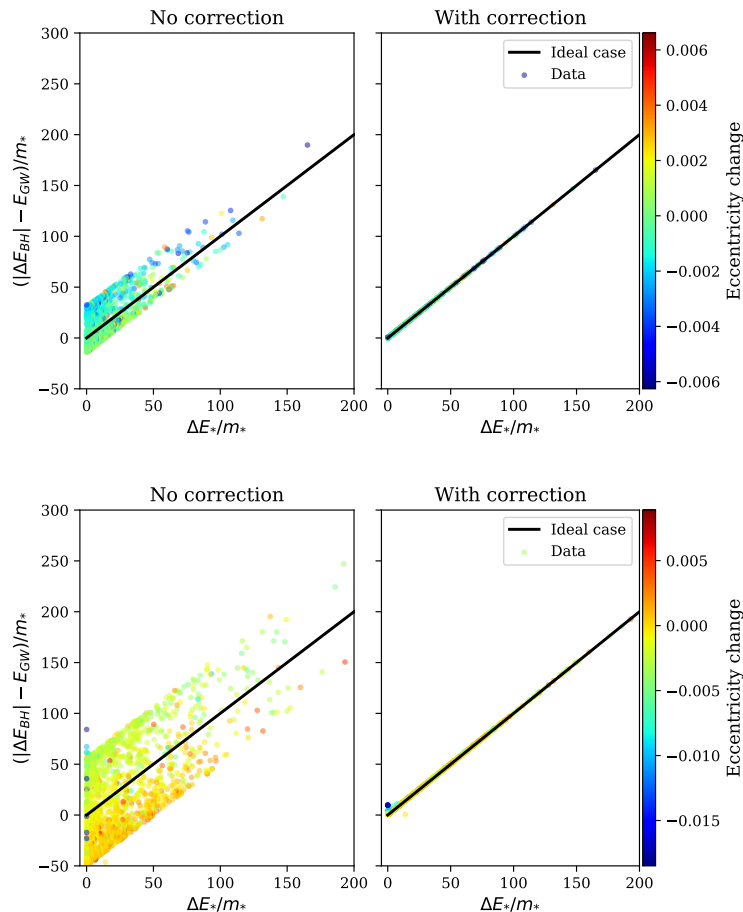


**Figure 6.5:** Top: Specific binary orbital energy change, corrected for GW emission, as a function of specific energy change of the star, for initial time  $t_0 = 5$ , without (left) and with (right) the  $E_{PN1}$  correction term. Each point corresponds to one scattering experiment. The black line shows the ideal case when the quantity on the y-axis is identical to the quantity on the x-axis, corresponding to no energy losses of any kind. Bottom: Binding energy change, corrected for GW emission, as a function of specific energy change of the star, for initial time  $t_0 = 6$ , without (left) and with (right) the  $E_{PN1}$  correction term. Other elements are the same as in the top plots.

2008). The goal of the simulations was to explore the interaction and study the energy exchange between a stellar particle and a SMBH binary in the final phase of the merger with the star acting as an incoming third body. More specifically, I aimed to analyze the energy balance of individual interactions and provide insight into the mismatch between the energy change of the binary and the stars, found in previous work (Ikape, 2016). The scattering experiments were done in preparation for future full N-body runs of the system, described in the next chapter.

The initial conditions for the SMBH binary system were obtained from earlier, large-scale simulations which are detailed in Kh16. The equations of motion of the binary were corrected for PN effects up to term 2.5, corresponding to the leading radiation-reaction term. This provided insight into the close encounters between the binary and stars from the loss cone, at a time when Post-Newtonian effects are already significantly contributing to the orbital decay. Two different sets of runs were performed, depending on the initial times  $t_0 \in \{5, 6\}$ . The first set of runs had more frequent output interval and consisted of 1000 total scattering experiments, while the second set of runs was characterized by greater number statistics, consisting of 2000 runs in total, but with lower output frequency compared to the first set. The stellar particle distribution was generated isotropically on a spherical shell at a distance of  $D_0 = 1$  kpc from the binary center of mass. The initial conditions were set up in such a way that was ideal for close and energetic encounters between the stellar and black hole particles. The goal was to get an estimate of the parameters and properties of the high-energy tail which consists of stellar particles that experience large energy boosts during their interaction with the binary, thus increasing the SMBH binding energy. This was done by deriving an initial velocity condition, given by Eq. 6.13, that guarantees very close approaches between the star and black hole particles.

While the closest approach of the star is not resolved, the velocity condition allowed for an estimate of the Keplerian pericenter distribution of the stellar particles, in the approximation where the SMBH binary acts as a single massive body on a star at the distance of  $R = D_0$  from the binary. The obtained pericenter distribution is given in Figure 6.2, as a histogram (left) and as a function of spec. energy change of the star (right). The estimation of the initial pericenter suggests that the vast majority of the encounters crosses the SMBH binary orbit during the interaction. While the general trend shows that smaller initial pericenter typically results in higher specific energy changes after the interaction, there is also a non-negligible number of energetic events at  $a_0/2 < r_p < 2a_0$ . These results should be taken in consideration when setting the value of the softening parameter for future runs of galaxy mergers. While the number statistics of encounters is not particularly high, the results point to the fact that with a much larger particle number, the majority of strong encounters would take place significantly close to the binary and suggesting that the value of the softening employed should not be higher than  $\epsilon = 0.2a_0$ , and ideally several orders of magnitude lower than that. Additionally, using our sample we estimated the merger rate for this set of initial parameters, finding it to be  $\approx 2\%$ .

The energy balance analysis showed that there is a significant error in the energy balance of the system when the Newtonian definition of binary orbital energy is used. The detected energy discrepancy was comparable to the other energy changes of the system and was orders of magnitude larger than the energy error of the code. The introduction of the PN1 term to the energy definition has proven sufficient to account for all energy discrepancies. For this reason, the orbital energy of the binary must be modified by at least the leading PN order in order to properly account for all energy changes in the system. The Newtonian approximation is shown to fail even in the regime when GW emission is not the dominant effect driving the binary evolution. Alternatively, a quasi-Keplerian definition of orbital elements can be used to avoid

the issue (see Sec. 3.3.4). The PN1 term - Eq. 6.33, while not effectively carrying away energy from the system, does produce variations in the energy and the binary orbital parameters. Fig. 6.5 shows that the sign of the PN1 energy term is correlated with the Newtonian eccentricity change of the SMBH binary orbit. This is likely correlated to the fact that while PN dynamics admit the conservation of angular momentum, the magnitude of the vector  $\vec{r} \times \vec{v}$  is no longer conserved (Will, 2011), resulting in the observed changes in the eccentricity.

---

## PROPERTIES OF LOSS CONE STARS IN A COSMOLOGICAL MERGER REMNANT

---

In this chapter, I present the results of an N-body simulation of a close SMBH binary embedded in a slightly triaxial, rotating galactic merger remnant. I study in detail individual stellar hardening interactions with a hard SMBH binary and investigate properties of loss cone stars. This chapter has been adapted from the publication [Avramov et al. \(2021\)](#), which has been published in *Astronomy & Astrophysics*. B. Avramov performed the below described simulations, analyzed the data, wrote the text and performed all of the calculations. A. Acharya contributed by performing the fitting described in Eq.7.3, and the other co-authors contributed with numerical support, ideas, discussions and comments.

### 7.1 INTRODUCTION

Cosmological context and a cosmological environment can be crucial factors that affect galaxy morphology and dynamics in a merger and therefore determine the orbital nature of loss cone stars and the evolution of the SMBH binary system. Recently, several studies have explored the conditions for the formation of an SMBH pair in a cosmological context ([Bortolas et al., 2020](#); [Pfister et al., 2019](#); [Tremmel et al., 2018a,b](#)), showing that along with dynamical friction, additional more complex effects might be in play in the early evolution of an SMBH binary. Nevertheless, [Kh16](#) was the first example in the literature to model the entire evolution of an SMBH binary, starting from a cosmologically-formed galaxy merger, down to the PN plunge of the black holes themselves. This study was therefore in a unique position to explore the properties of the orbits of the stars which contributed to the binary hardening and to investigate loss cone refilling mechanisms originating from a robust, cosmological environment. However, like many direct N-body studies that came before, this study fell short of exploring this aspect.

The reason for this lies in the nature of the standard N-body approach. Along with high computational cost, one of the main drawbacks of N-body is that since the number of particles that can be simulated is significantly smaller than a realistic galaxy, non-physically massive particles may cause artificially enhanced two-body relaxation effects, thus unintentionally increasing the effect of collisional hardening processes and making it inherently difficult to consistently study mechanisms of loss cone refilling. It should also be noted that in a similar fashion, Brownian motion of a binary in an N-body system can be enhanced because of

insufficient particle numbers and can artificially increase the hardening rate (Milosavljević and Merritt, 2003a), but this effect is not expected to be significant in simulations with  $N > 10^6$  particles (Bortolas et al., 2016). Therefore, to circumvent the issue, a sort of hybrid approach is needed, which would retain the accuracy of direct summation for particles interacting with the SMBH binary, but would be able to use collisionless expansion techniques (or sufficiently large particle numbers) to accurately model the outer regions of the system. Recently, several similar approaches using different methodologies have been proposed in the literature. Mannerkoski et al. (2019) and Rantala et al. (2018) utilize a hybrid-tree code (Rantala et al., 2017), combining GADGET-3 (Springel, 2005) with algorithmic regularization (Mikkola and Merritt, 2008) to investigate SMBH merger timescales. Lezhnin and Vasiliev (2019) used a Monte-Carlo approach (Vasiliev et al., 2015) to investigate tidal disruption rates and ejection of stars from the loss cone. Finally, Nasim et al. (2020); Gualandris et al. (2017) used a Fast Multiple Method code combined with direct summation to simulate SMBH binary evolution.

## 7.2 INITIAL CONDITIONS

The data was obtained by resimulating the final stages of the merger in the *Kh16* system, for which I utilize the  $\phi$ -GRAPE-hybrid code. In this way, sufficient integration accuracy is ensured for particles of interest, while avoiding the high computational cost and enhanced relaxation effects that typically plague pure direct N-body approaches. I include Post-Newtonian effects in the equations of motion up to order 2.5 (Blanchet, 2014), in order to account for GW emission.

In order to resimulate the final stages of the merger, we initialize our simulations at  $t_0 = t_{\text{ini}} + 27.7 \text{ Myr} = t_{\text{PN}} + 6.2 \text{ Myr} = 4 [\text{NB}]$ , which we will refer to as the resimulation time. At this time the SMBH binary is well into the hardening phase of the merger with no measureable PN effects and the binary semi-major axis is  $a_{\text{bh}} \sim 0.06 \text{ pc} \sim 1650 R_{\text{sch}}$ , where  $R_{\text{sch}} = 3.6 \times 10^{-5} \text{ pc}$  is the Schwarzschild radius of the combined mass of the binary. The particle number and mass resolution was the same as in the original study, described in Sec. 4.5.

The particles which are treated in a direct way (*core* particles) need to be selected before the initialization of the run. In our system, while relaxation effects are negligible in the outer regions of the system, they become important in the central region. We therefore choose *core* particles to reflect that. In order to estimate the region of influence of the SMBH binary, we use the cumulative radial mass profile of the GMR. Namely, we define the influence radius of the SMBH binary, as the radius at which the following condition is satisfied:

$$M_{\text{cum}}(R_{\text{infl}}) = 2M_{\text{BH}}, \quad (7.1)$$

where  $M_{\text{cum}}(r)$  is the cumulative mass of all of the particles (excluding the SMBHs) within the sphere of radius  $r$  and  $M_{\text{BH}}$  is the total mass of the SMBH binary  $M_{\text{BH}} = M_{\text{BH1}} + M_{\text{BH2}}$ . This corresponds to the radius of  $R_{\text{infl}} = 13.15 \text{ pc}$ . In order to ensure that we select particles which have the potential to interact strongly with the binary, we determine stellar particles to be *core* if they fulfill *at least* one of the following criteria:

$$r_{\text{p}} < 0.5R_{\text{infl}} \quad \text{or} \quad r < R_{\text{infl}}, \quad (7.2)$$

where  $r_{\text{p}}$  is the pericenter distance in the two-body Keplerian approximation of a star-BH binary system and  $r$  is the radial distance of the particle at the start of the resimulation. This

selection is performed only with stellar particles and only once at the start of the run. Using this condition, we obtain  $2 \times 10^5$  *core* particles which will be calculated in a direct way. This corresponds to 3.3% of our total particle number  $N = 6 \times 10^6$ . We note however that as a result of the complex phase space structure of the GMR, there is a fraction of *halo* stars which will enter the inner region at a later time, and possibly even become centrophilic. This fraction of stars is low ( $\approx 18\%$  of all stars in the inner region are *halo* at the end of the simulation) and has only a minor effect on the shape of the potential deep within the influence radius. These stars still have direct interaction with the black holes, and therefore can contribute to the overall hardening rate.

The criterion in Eq. 7.2 helps us to ensure that we represent the potential correctly at the time of resimulation in the transition between the Kepler-potential dominated region inside  $R_{\text{infl}}$  and the outer region where the potential is dominated by the contribution of the GMR. Within the Kepler region, the potential of the system can be approximated to a high degree of accuracy by the analytical expression:

$$\Phi(r < R_{\text{infl}}) = -\frac{GM_{\text{BH}}}{R_{\text{BH}}} + C, \quad (7.3)$$

where  $C = \text{const.}$  approximates the contribution of the surrounding galactic system to the total potential within the Kepler region and  $R_{\text{BH}}$  is the distance to the SMBH binary center of mass. In order to estimate  $C$ , our collaborator A. Acharya performed a fitting procedure on the radial profile of the potential in the centre of mass of the black holes reference frame. The fitting is performed at resimulation time  $t_0$  using the least squares method, over a radial range of  $R = [0.119, 2.9]$  pc, with the zero-point of the potential being at infinity. We obtain the value of  $C = -1.983 \times 10^6 \text{ km}^2 \text{ s}^{-2}$  which corresponds to the minima of the residual of the fitting parameter. We find that within  $0.3R_{\text{infl}}$ , Eq. 7.3 does a good job of approximating the potential. Additionally, we do not observe measureable deviations in the potential over time.

In order to be able to identify and study the strong interactions the stars experience with the SMBH binary, at every integration timestep we monitor each time a star enters and exits a sphere of radius  $r = 10a_{\text{bh}}$  around the black holes, where  $a_{\text{bh}}$  is the SMBH binary semi-major axis. This is done with additional, more frequent output of the black hole and interacting star parameters. The time frequency of the additional output is 1,500 years, while the full snapshots are obtained every 12,000 years, a factor of 8 larger. This allows us to identify stars from the loss cone, by analyzing the energy and orbital changes of the stellar particle before and after interaction, while eliminating any other effects that could cause such significant energy changes. At this radius, the escape velocity is  $V_{\text{esc}} = 3063 \text{ km s}^{-1}$ , corresponding to the potential of  $\phi = -4.692 \times 10^6 \text{ km}^2 \text{ s}^{-2}$ . The SMBH binary gravitational pull constitutes about 58% of this value, while the effect of the GMR is represented by the remaining 42%.

### 7.2.1 Numerical parameters and performance

Because of the inherent difference between codes, as well as for increased accuracy, we change several simulation parameters from the setup used in Kh16. The numerical setup described here is based on the results of numerical tests, described in Ch. 5. Most notably, we employed a global softening parameter of  $\epsilon = 2 \times 10^{-4}$  pc, while the original simulation had an individual softening approach, depending on particle type. The smallest value of the softening was  $\epsilon = 0.007$  pc, used for the black hole-star interactions. Our value is considerably smaller than the ones used in

the original simulation, since we found that larger values of the softening parameter affected the hardening rate of the SMBH binary, resulting in artificially lower hardening rates. Additionally, we considerably decrease the minimum black hole integration timestep in order to get better accuracy in the Post-Newtonian terms calculation. The minimum integration timestep has been decreased from  $\Delta t_{\min} = 10^{-3}$  yr in the original run, to  $\Delta t_{\min} = 10^{-5}$  yr in our resimulation. This level of accuracy was previously unreachable for direct-only N-body approaches due to the already extremely high computational cost for a system with particle numbers  $N > 10^6$ . The relative energy error throughout our run is typically  $\Delta E/E \approx 10^{-5}$ . However we record higher errors upon each restart of the run (roughly every 0.8 Myr), reaching up  $\Delta E/E = 4.7 \times 10^{-3}$ . Therefore, for best results, frequent restarts should be avoided.

Finally, our pilot runs showed that the choice of the origin of the reference frame can significantly affect the results and produce non-physical hardening of the binary. This results from the fact that by design the SCF force is calculated at the origin of the reference frame. If the origin does not match with the density center of the system, the spatial asymmetry will introduce a bias in the SCF force, causing artificial sinking of the black holes towards the origin. For this reason, the comoving inertial reference frame, described in Ch. 5, was adopted as the reference frame of the simulation. Throughout the chapter, the results in the figures are centered to the SMBH binary center of mass, unless specified otherwise.

We find that changes to the numerical parameters listed in this section affect the overall evolution of the SMBH binary, which we discuss in Section 7.3.1.

Our benchmarks have shown that  $\varphi$ -GRAPE-hybrid has a speed-up of a factor of 16 over the direct-only version. This will be discussed in detail in an upcoming publication (Meiron et al. 2021, in prep). Our case in particular is very well suited for a hybrid approach due to the very large range of scales that need to be resolved in order to obtain the proper physics of the system. These scales range from 1 mpc for the close interactions, to 10 kpc for the outer ranges of the system. An even bigger performance issue is the range of timescales that are present in our system. The SMBH binary orbital period is on the order of  $\sim 1$  yr, however the average crossing time of the system is on the order of  $\sim 1$  Myr. Therefore, the time resolution needs to be high enough in order to properly resolve the 3-body interactions with incoming stars, which happen on the SMBH binary orbital timescale, while also evolving the surrounding system for several crossing times in order to allow for proper refilling of the loss cone. This obstacle comes at a great computational cost, even with the hybrid approach. However, despite this, the comparatively small percentage of particles calculated in a direct way and efficiency of the hybrid code enabled us to maintain sufficient speed on 4 computational nodes, each equipped with 4 Nvidia V100 GPU devices.

## 7.3 RESULTS

### 7.3.1 SMBH binary properties

In this section we present the orbital evolution of the SMBH binary and compare our results to the ones obtained in [Kh16](#). We start the resimulation at  $t = t_0$  when the binary is hard and dynamical friction is no longer effective. At this point, the PN effects on the hardening are still insignificant, and the primary mechanism of energy loss for the binary is via the interactions with the stars from the loss cone. On [Figure 7.1](#) we present the orbital evolution of the SMBH binary, compared to the original run (see left panel of [Figure 4.4](#)). The hardening rate of the

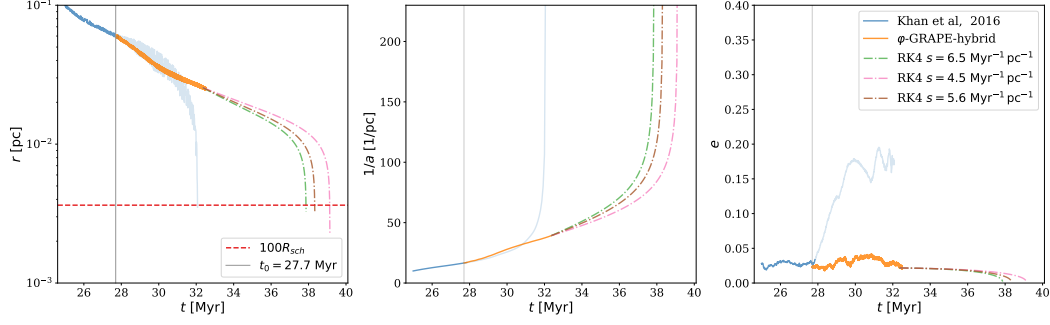


**Figure 7.1:** Left: Separation of the black holes, as a function of time since  $t_{\text{ini}}$  (since the particle splitting procedure). The blue line corresponds to the original run in [Kh16](#), while the orange line corresponds to our run. The light version of the blue line refers to the continuation of the original simulation data. The three dashed-dotted lines starting at 33.35 Myr correspond to analytical estimates of the merger time in the Post-Newtonian dominated regime using constant values of hardening rate. The vertical line marks the initial time of our run,  $t_0$ . The horizontal dashed line marks the separation of  $100R_{\text{Sch}}$ , where the  $R_{\text{Sch}}$  is the Schwarzschild radius of the combined mass of both black holes. Middle: Inverse of the binary semi-major axis, used as a measure of hardening rate. Plot elements are the same as on the left plot. Right: Eccentricity evolution of the SMBH binary. Plot elements are the same as on the left plot.

binary, defined as:

$$s = \frac{d(1/a)}{dt} \quad (7.4)$$

is approximately constant, which can be seen from the linear behaviour of  $1/a$  in the middle panel of [Figure 7.1](#). In the same figure, in the left panel we see the black hole separation as a function of time since  $t_{\text{ini}}$ . The separation of the SMBH particles during our run is on the order of  $\sim 1000R_{\text{Sch}}$ . Up to resimulation time  $t_0$ , we plot the data obtained with the  $\phi$ -GPU code in [Kh16](#). The period between  $t_0 < t < 32.35$  Myr corresponds to the time period of our resimulation of the system using  $\phi$ -GRAPE-hybrid.

From  $t = 32.35$  Myr and onwards, we plot the analytical estimates of the hardening driven by stellar interactions and GW emission, using well known formulae in [Peters and Mathews \(1963\)](#) and a constant value of hardening rate  $s = \text{const}$ . The estimates were performed using standard Runge-Kutta 4th order integration, for 3 different values of hardening rates:  $s = 4.5, 5.56, 6.4 \text{ Myr}^{-1} \text{ pc}^{-1}$ , where the middle value corresponds to the hardening rate that we measure at the end of the run (see [Fig. 7.7](#), middle panel). From this, we estimate the SMBH merger timescale at  $38.3 \pm 0.8$  Myr since  $t_{\text{ini}}$ , or  $16.8 \pm 0.8$  Myr since  $t_{\text{PN}}$ . This value is a factor of two larger than the value reported in [Kh16](#), who reported a merger timescale of under 10 Myr.

During our pilot runs presented in [Ch. 5](#), we investigated different combinations of numerical parameter values to test how they affect the hardening rate. We found that the gravitational softening value and the minimum black hole integration timestep affected the hardening rate most significantly, resulting in the discrepancy between our merger timescale and the one in the original study. The value of the merger time in [Kh16](#) might be underestimated primarily as a result of insufficient time resolution of the binary, determined by the minimum black hole integration timestep. This would have led to an overestimation of the PN terms in the equations of motion and a premature PN plunge. This is also visible in the eccentricity evolution, where we interpret the rise in eccentricity after  $t = t_0$  in the original data as evidence of numerical

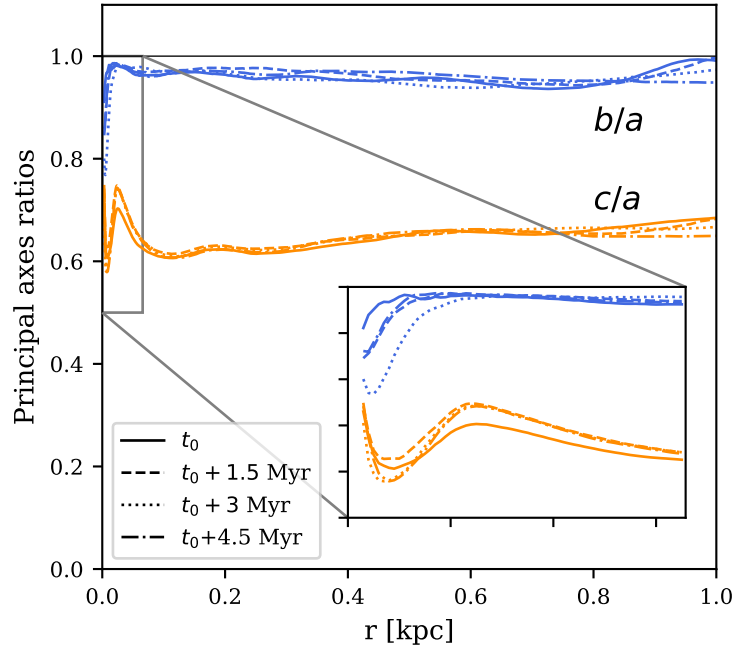


**Figure 7.2:** Ratios of the principal axes of the system up to 1 kpc, shown for different times. The figure in the bottom-right corner shows a zoomed-in region, ranging from 0.5 to 1 in the y-direction, and from 0 to  $5R_{\text{infl}} = 66$  pc in the x-direction, where  $R_{\text{infl}}$  is the SMBH binary influence radius.

artifacts. The decrease of the black hole minimum integration timestep reduced the effect of overestimation of the PN terms, and the hardening rate is now in agreement with analytical formulae of GW emission [Peters and Mathews \(1963\)](#), demonstrated by the dash-dotted lines on Figure 7.1.

Additionally, we performed convergence tests in an effort to see if further decreasing the value of the softening from the original run affects the hardening rate. These tests showed a dependence of the hardening rate on the value of gravitational softening both using the  $\varphi$ -GRAPE-hybrid code, as well as the  $\varphi$ -GPU, which adopts an individual softening procedure and was used in the original study. We found that the hardening rate converged using both codes when the softening value for star-black hole interactions was set to  $\epsilon \leq 2 \times 10^{-4}$  pc, which is why we adopted this value for our run. This suggests that the limited spatial resolution of the original run somewhat underestimated<sup>1</sup> the hardening rate during close pericenter passages of stars.

### 7.3.2 Merger remnant properties

In this section we will present properties of the GMR. Our goal is to demonstrate the stationarity of the system, in terms of its shape and orientation. This is done to make sure that the stellar parameters we analyze are not affected by changes in the galactic system and that the system does not measurably change its properties at the time of resimulation. In this way, our results would not be affected by the sudden change in the gravitational potential of the system as a result of the switching of the codes, and therefore, the force calculation method.

<sup>1</sup>It is important to note that despite the underestimation of the hardening rate due to the softening, the insufficient time resolution of the binary which overestimated the hardening rate was the dominant numerical effect that we believe resulted in the premature plunge driven by PN effects.

In the classical loss cone regime inside of spherical nuclei, stars in the loss cone would interact with the SMBH binary on a crossing time timescale, after which the loss cone would be largely empty and the binary would stall (Milosavljević and Merritt, 2003b). The refilling of the loss cone by two-body relaxation effects would happen on a relaxation timescale  $t_{\text{relax}}$  which may be larger than the Hubble time (Berczik et al., 2005). Therefore, collisionless refilling of the loss cone by stars on centrophilic orbits, originating from triaxial, or possibly axisymmetric orbits is necessary for efficient loss cone refilling and a constant hardening rate.

It is important to note that for the analysis of strong stellar interactions with the binary, we do not consider the first 1.8 average crossing times (1.55 Myr, which corresponds to 1 N-body time unit) and we only use the last 3.1 Myr of data for the analysis of energetic interactions. The reason for this is that, while the overall properties of the GMR do not change significantly at the moment we start the resimulation, owing to the potential switch, it is possible that some stars would artificially be perturbed and put on centrophilic orbits. Therefore, during the first 1.55 Myr we allow the system to relax and adjust to the new potential, in order to ensure that all of the encounters we obtain are physical.

In Fig. 7.2, we present a time evolution of the ratios of the principal axes of the system,  $b/a$  and  $c/a$  respectively, within a radius of 1 kpc, as well as the inner-most region  $5R_{\text{infl}}$  ( $\approx 66$  pc, zoomed-in region). The principal axes were obtained from the eigenvalues of the following tensor<sup>2</sup>:

$$I_{jk} = \int \rho x_j x_k d^3 x. \quad (7.5)$$

We find the axis ratios in cumulative spheres in the range of  $3 \text{ pc} < r < 5R_{\text{infl}}$  for the main figure and in the range of  $3 \text{ pc} < r < 1 \text{ kpc}$  for the zoomed-in figure. The axes of the system were computed in the reference frame that is comoving with the SMBH binary (described in Section 7.2.1). Looking at the ratios of the medium and major axis we can see that the galaxy merger remnant is slightly triaxial at all times ( $b/a < 1$ ). It is precisely this slight triaxiality that we expect to efficiently refill the loss cone, pointing to the fact that we should expect a roughly constant supply of stars in the SMBH binary vicinity, and therefore a constant hardening rate of the black holes as well. This is in agreement with the findings of Kh16, so we can conclude that there is no change in the shape of the system at the time of resimulation. Fig. 7.2 also shows us that the GMR is significantly flattened at all values of  $r$  with  $\epsilon \approx 0.4$ . We calculate the flattening in the standard form  $\epsilon = 1 - c/a$ , where  $c/a$  is the ratio of the minor and major axis.

In order to investigate the orientation of the system, we first for each snapshot rotate the data so that the  $z$ -axis is aligned with the minor axis of the ellipsoid at  $t_0$ . We then look at the orientation of the orbital angular momentum vector of the SMBH binary, as well as the cumulative angular momentum of the GMR system. To define the cumulative angular momentum of the system, we sum the contribution of all particles which are contained within a sphere of a radius  $r < 5R_{\text{infl}}$ , excluding the black holes. We find that during the time period of 3 Myr used for the analysis of energetic interactions, the overall angular momentum vector of the system, and the smallest axis of the GMR ellipsoid match exceedingly well (the misalignment is always within  $1^\circ$ ). This means that there is no misaligned rotation of the system, since the rotation of the GMR is aligned with the flattened shape and that the three-body encounters are

<sup>2</sup>The  $I_{jk}$  tensor is sometimes referred to as the moment of inertia tensor, but this name is often reserved for the  $I'_{jk}$  tensor, where  $I'_{jk} = \text{Tr}(I)\delta_{jk} - I_{jk}$  (Binney and Tremaine, 1987).

not scattered in a preferred direction because of this.

Additionally, the orientation of the SMBH binary orbit does not show significant changes during this period. The orientation of the SMBH orbit is misaligned to the overall system by  $\theta \approx 15^\circ$  throughout the run. It is expected that the SMBH binary orbital plane would realign according to the rotation axis of the system (Rasskazov and Merritt, 2017; Wang et al., 2014; Li et al., 2017) on a timescale of several hundred orbital periods (Gualandris et al., 2012). This realignment is caused by the angular momentum exchange and interaction with stars in a rotating cusp. Unlike these studies, we do not measure visible changes in the SMBH binary orbital plane. However, we argue that this is due to the already significant alignment with the system, and full realignment is not necessarily expected (Gualandris et al., 2012). Additionally, the slight triaxiality and present rotation of our system might significantly reduce the alignment effect (Cui and Yu, 2014).

In order to properly characterize the orbits of stars from the loss cone, first we need to explore the properties of the overall system and understand the motion of stars within. Since the GMR is only slightly triaxial, we will assume axisymmetry for this part of the analysis. In the comoving reference frame, we switch to cylindrical coordinates, given by  $(R, \varphi, z)$  and explore properties in the  $(R, z)$  (meridional) plane.

In an oblate elliptical galaxy, the motions of the stars can be distinguished between a net streaming motion around the minor axis (rotation) and a random dispersion of velocities with respect to that streaming motion. The prevalence of one or the other motion type can give important clues to the orbital structure of the galaxy. With this in mind, we start with a reference frame centered on the SMBH binary center of mass at time  $t = t_0$  (i.e., the comoving inertial reference frame described in Sec. 7.2.1). We then rotate the frame of reference according to the three axes of the ellipsoid, so that the minor axis is aligned with the overall angular momentum in direction  $z$ . Then, within  $5R_{\text{infl}}$  we divide the  $(R, z)$  plane in a  $10 \times 10$  grid of cylindric rings and find average values of kinematic properties of all particles in each ring. In our reference frame, the streaming motion corresponds to the rotation around the  $z$ -axis, denoted by the tangential component of the velocity  $V_\varphi$ . The random motion is characterized by the velocity dispersion along each axis:  $\sigma_R$ ,  $\sigma_\varphi$  and  $\sigma_z$ . On Fig. 7.3, we can see the ratio of rotational to mean random motion in the meridional plane, where  $\sigma = \sqrt{(\sigma_R^2 + \sigma_\varphi^2 + \sigma_z^2)}/3$ . We find that there is considerable rotation throughout the meridional plane, especially towards the equatorial plane. Our analysis shows us that after the galactic merger and throughout our run the GMR remnant retains a well-defined rotation axis that coincides with the minor axis of the remnant. This is also reflected in the motion of stars in the inner region, with a prevalence of ordered to random motion in the direction parallel to the equatorial plane.

The strong rotation of the GMR undoubtedly plays a part in the significant flattening of the system that we measure, as shown on Fig. 7.2. In the past, rotation along the minor axis was considered the dominant contribution to the flattening of an axisymmetric system, however the discovery of giant elliptical galaxies not flattened by rotation showed that is not necessarily the case (Binney, 2005; Bertola and Capaccioli, 1977; Illingworth, 1977). In reality, the flattening of an elliptic galaxy can be supported by rotation, significant velocity anisotropy or a combination of both of those mechanisms (Mo et al., 2010). The prevalence of one or the other is often characterized by the anisotropy diagram, which relates the ratio of ordered and random motion ( $V/\sigma$ ) to the ellipticity of a galaxy. The tensor virial theorem, in the formalism of Binney and Tremaine (1987) gives us a relation between  $(V/\sigma)$  and the flattening ( $\epsilon$ ) for an axisymmetric

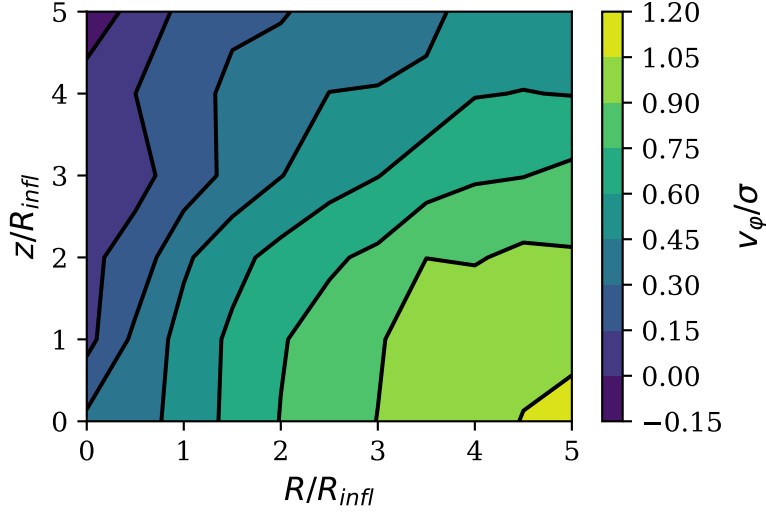


**Figure 7.3:** Contour density plot of the tangential to random motion ratio  $v_\phi/\sigma$  in the meridional plane at the time of resimulation.

elliptical system that rotates about its symmetry axis ( $z$ -axis). This is accomplished with the  $e'$  parameter<sup>3</sup> which only depends on ellipticity:

$$e' = \sqrt{(1 - (1 - \epsilon)^2)}. \quad (7.6)$$

Then, the  $(V/\sigma)$  relation takes the form (Binney and Tremaine, 1987):

$$(V/\sigma)^2 = 2(1 - \delta)\Omega(e') - 2, \quad (7.7)$$

where  $\delta < 1$  and  $\Omega(e)$  in the oblate approximation takes the form of (Cappellari et al., 2007):

$$\Omega(e') = \frac{0.5(\arcsin e' - e'\sqrt{1 - e'^2})}{e'\sqrt{1 - e'^2} - (1 - e'^2)\arcsin e'}. \quad (7.8)$$

The  $\delta$  in Eq. 7.7 is a dimensionless global anisotropy parameter which quantifies the anisotropy between the symmetry axis and any direction orthogonal to it in an axisymmetric system (Binney and Tremaine, 1987).

Relation 7.7 enables us to see where our system falls on the anisotropy diagram, and to which extent is the flattening we observe supported by rotation around the minor axis (Fig. 7.4). We use the values of  $\bar{v}_\phi/\bar{\sigma}$  and  $\epsilon$  at  $R = 5R_{\text{infl}}$  and  $z = 0$  as local analogs of the global values  $V/\sigma$  and  $\epsilon$ . We can see that our system falls near the  $\delta = 0.2$  line in the plot, suggesting that while the flattening in our system is partially rotationally supported, rotation alone is not significant enough to solely account for the flattening. Therefore, there is also a non-negligible degree of anisotropy-supported flattening present.

Additional insight of an axisymmetric galaxy's flattening mechanism can be gained with the  $\gamma$  anisotropy parameter (Thomas et al., 2009), which we adopt from Cappellari et al. (2007), along with the formula for  $\delta$ :

<sup>3</sup>This parameter should not be confused with orbital eccentricity  $e$  which is used throughout the text.

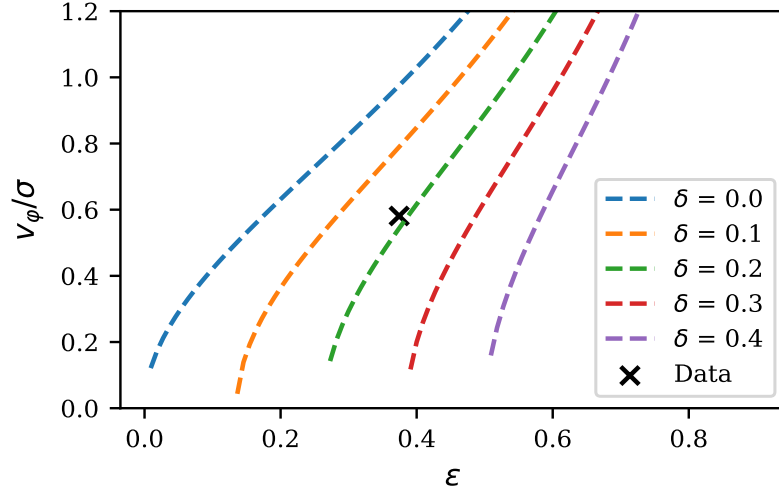


**Figure 7.4:**  $(V/\sigma, \epsilon)$  relation from the tensor virial theorem. The lines correspond to different levels of anisotropy  $\delta$ . Our system is denoted by the black cross.

$$\delta = 1 - \frac{2\sigma_z^2}{(\sigma_R^2 + \sigma_\phi^2)} \quad \text{and} \quad \gamma = 1 - \frac{\sigma_\phi^2}{\sigma_R^2}. \quad (7.9)$$

Using this formula for  $\delta$ , we obtain  $\delta = 0.205$  at  $z = 0$  for  $R = 5R_{\text{infl}}$ , in very good agreement with the value estimated in Fig. 7.4.

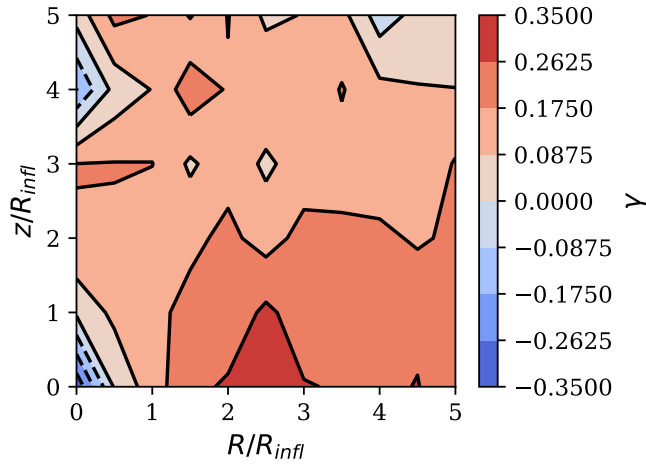


**Figure 7.5:** Contour density plot of the  $\gamma$  anisotropy parameter, in the meridional plane at the time of resimulation.

We present on Figure 7.5 the anisotropy profile of the  $\gamma$  parameter in the meridional plane, at the time of resimulation  $t_0$ . We immediately notice that  $\gamma > 0$  throughout the meridional plane, suggesting a flattening supported in part by radial anisotropy. This is expected in merger remnants (Thomas et al., 2007) because of a large population of central box orbits which cause the centres of the merger remnants to become triaxial (Thomas et al., 2009). Surrounding the SMBH binary, we see a prevalence of tangential orbits ( $\gamma < 0$ ), a clear sign that strongly radial orbits in the region have been scattered out and suggesting that the higher flattening up to

$R_{\text{infl}}$  (Figure 7.2, zoomed-in section) is supported by tangential anisotropy. The abundance of tangential orbits near the SMBH binary is in agreement with other studies that found the vicinity of the SMBH binary to have measurable tangential anisotropy (Meiron and Laor, 2013, 2010; Milosavljević and Merritt, 2001) with a large fraction of counter-rotating orbits with respect to the SMBH binary.

### 7.3.3 Properties of centrophilic stars

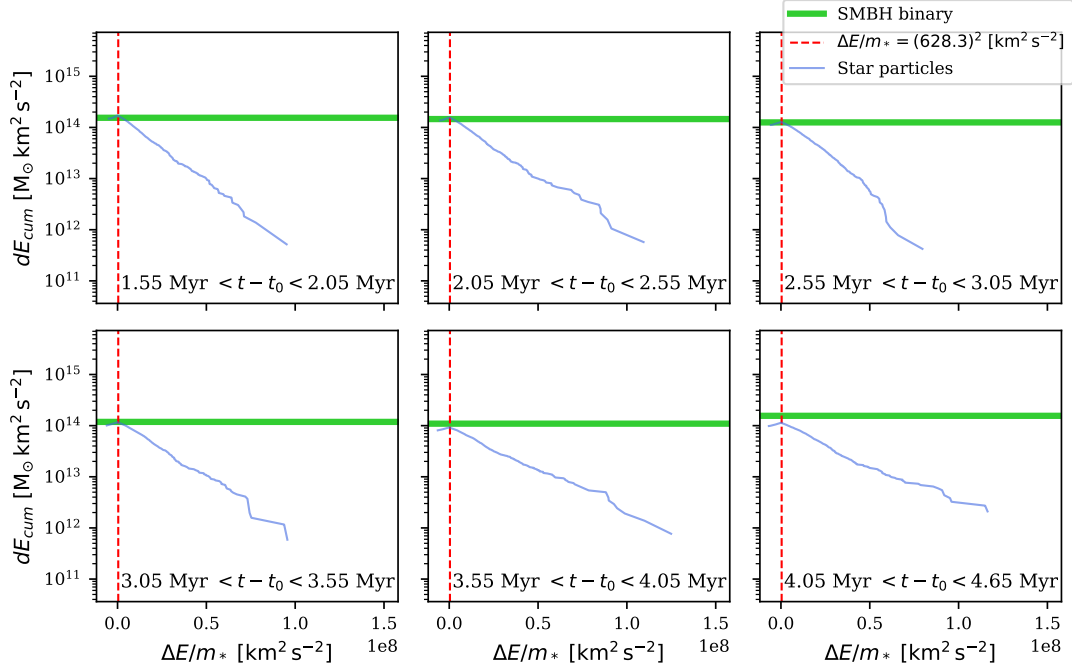


**Figure 7.6:** Energy balance plots showing the SMBH binary orbital energy changes compared to the cumulative energy changes of stellar particles for different times. The blue lines represent the cumulative energy changes of all stars that come within  $10a_{\text{bh}}$  of the SMBH binary during the specified time period. The green, thick line corresponds to the total SMBH binary orbital energy change for the same time period. The red dashed line corresponds to the cutoff value we use to define the high-energy tail.

In this section we will present our main findings and focus on exploring the parameters of the stars interacting strongly with the SMBH binary. During a strong interaction, the star experiences significant kinetic energy change, as it receives a strong velocity kick. Therefore, we only consider interactions where a star particle experiences large enough specific energy changes, which we refer to as the high-energy tail. We define the high-energy tail by finding stars with specific energy changes  $\Delta E_*/m_* > (628.3)^2 \text{ km}^2 \text{ s}^{-2}$  during a single interaction. This value is about 3% of the total energy of the binary at resimulation time and is equal to 1 in N-body units. It was chosen since other effects produced from the overall evolution of the system could not reproduce such large energy changes. While relaxation effects could create changes of this value under certain conditions, in our simulation the vast majority of particles is treated with the SCF force, and the rest of the interactions are softened.

To identify the interactions, we register passages within a sphere of  $10a_{\text{bh}}$  around the SMBH binary and monitor the energy changes. In this way, we identify a total of 13383 strong interactions during a period of 3.1 Myr. We make sure that these strong interactions correspond to star particles and that dark matter particles do not contribute to the SMBH hardening in a

measurable way. While most of the strongly interacting stars experience the potential in a direct way, we find that 20% of these stars are *halo* particles, and therefore the force they feel from other particles is calculated with the SCF method (except the force from the black holes which is always calculated directly). This fraction is in agreement with the  $\approx 18\%$  of halo particles we found in the inner region at the end of the run, as described earlier in the chapter. We acknowledge that the presence of these *halo* stars in the inner region is a consequence of the assumption of spherical symmetry in our *core-halo* criterion (Eq. 7.2), however we argue that this does not affect our results in a measurable way. The interactions with the black holes are unaffected by the *core-halo* division and we find no statistical differences in the properties of strong interactions between *core* and *halo* stars. We find that a star typically experiences multiple passages through the  $10a_{\text{bh}}$  sphere that result in small-angle and low-energy scatterings before finally experiencing a highly energetic interaction. With this in mind, we only consider the most energetic interaction per star for our analysis, unless explicitly stated otherwise.

Fig. 7.6 shows the cumulative energy changes of stellar particles during each passage through the  $10a_{\text{bh}}$  sphere around the binary, including non-energetic interactions. The different plots correspond to different time intervals during the run, given in 0.5 Myr increments. We compare all the cumulative energy changes of stars in the high-energy tail (to the right of the red dashed line) to the total SMBH binary orbital energy change during the same time period in order to make sure we are correctly identifying the stellar interactions that contribute to the binary hardening. As we can see on the figure, the interactions we identify as the high-energy tail match incredibly well with the total orbital energy change of the SMBH binary at all times. Only in the final plot, just before we stop the run, we notice a measureable gap in the energy balance, likely as a result of insufficient accuracy in the black hole integration, caused by the minimum integration timestep (see Section 4.3 for further discussion). We calculate the GW energy emission for these time intervals using the formulae from Peters and Mathews (1963) and we find that while measurable, the energy change from GW emission is several orders of magnitude smaller than the cumulative stellar hardening energy and the GW emission alone cannot account for the gap on the plot. Overall, the total SMBH binary orbital energy change over the entire period of 3.1 Myr is  $\Delta E_{\text{BH}} = \Delta(-GM_{\text{BH1}}M_{\text{BH2}}/2a_{\text{bh}}) = 4.07 \times 10^{14} \text{ M}_{\odot} \text{ km}^2 \text{ s}^{-2}$ , while the summed energy changes of stars in the high-energy tail is  $E_{\text{cum}} = \sum_{i=1}^{13383} \Delta E_{\text{max}} = 3.701 \times 10^{14} \text{ M}_{\odot} \text{ km}^2 \text{ s}^{-2}$ , where  $\Delta E_{\text{max}}$  corresponds to the energy extracted during their most energetic interaction. Therefore, we can conclude that our setup enables us to define the population of stars which contribute to the SMBH orbital energy changes with a very high degree of certainty. While additional effects could contribute to the overall binary energy evolution, e.g., gravitational torques from overdensities in the mass distribution (Souza Lima et al., 2020), the good match between the energy extracted by interacting stars and the energy change of the binary show that stellar interactions can be considered the most important drivers of the binary hardening in the presented configuration, and other sources of energy change can be neglected.

The distribution of the amount of energy the star particle extracts during a single encounter peaks at about  $5 \times 10^6 \text{ km}^2 \text{ s}^{-2}$ , which corresponds to  $\Delta V = 2238 \text{ km s}^{-1}$  in terms of velocity kicks (Figure 7.7, top panel). This is slightly higher than the median velocity of the major SMBH,  $\langle V_{\text{BH1}} \rangle = 1519 \text{ km s}^{-1}$  and corresponds to 31% of the median velocity of the minor SMBH  $\langle V_{\text{BH2}} \rangle = 5700 \text{ km s}^{-1}$ . The typical specific energy changes of a star are given in dash-dotted lines for different times on the same figure and are determined by the relation (Merritt, 2013b):

$$\Delta E_{\text{typ}} = (M_{\text{BH2}}/M_{\text{BH}}) * \langle V_{\text{rel}} \rangle, \quad (7.10)$$

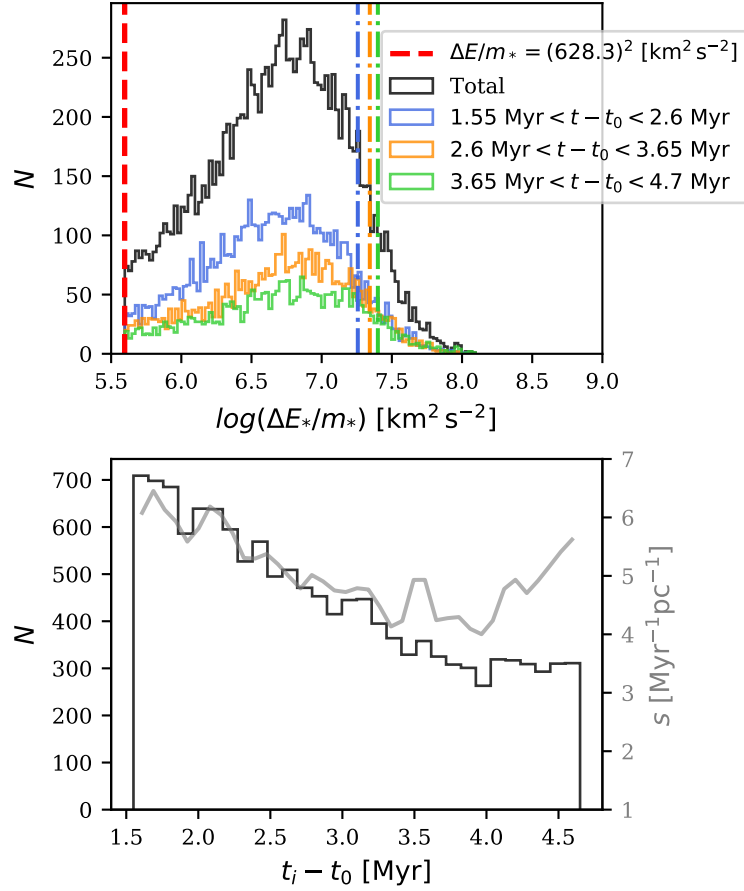


**Figure 7.7:** Top panel: In full lines, we present the distribution of specific energy changes of the interacting stars, where the colors correspond to different times throughout the run. The dash-dotted lines represent the expected typical specific energy changes of a star ejected by the binary at each time interval, given by Eq. 7.10. The red dashed line corresponds to the cutoff value we use to define the high-energy tail. Bottom panel: Time distribution of the most energetic interactions for each interacting star, given in Myr since  $t_0$ . In gray, the hardening rate ( $s$ ) is given, as a measure of energy extracted from the binary by the interaction. We notice that while the number of encounters decreases, the hardening rate remains largely constant.

where  $M_{\text{BH}2}$  is the mass of the less massive black hole,  $M_{\text{BH}}$  is the total mass of the binary and  $\langle V_{\text{rel}} \rangle$ , is the median relative velocity of the binary during that time interval. The bottom panel shows that the overall number of interactions decreases with time. However, as the binary semi-major axis shrinks with time, the energy per encounter increases, leading to a roughly constant hardening rate, as demonstrated by the gray line on the same plot.

We can estimate the incoming inclination of interacting stars entering the  $10a_{\text{bh}}$  sphere with respect to the SMBH binary orbital plane from the orientation of their respective angular momentum vectors (top plot on Fig. 7.8). We find that there is a preference for prograde rotating stars with respect to the SMBH binary ( $\cos(i) \geq 0$ ), compared to the population of stars with retrograde rotation ( $\cos(i) < 0$ ). While there are no significant changes in orientation just before the first and final interaction (green and blue lines in top panel of Fig. 7.8), we do notice that there are a number of retrograde stars that experience an angular momentum sign-flip change during their energetic interaction, resulting in them becoming prograde (orange line in the same

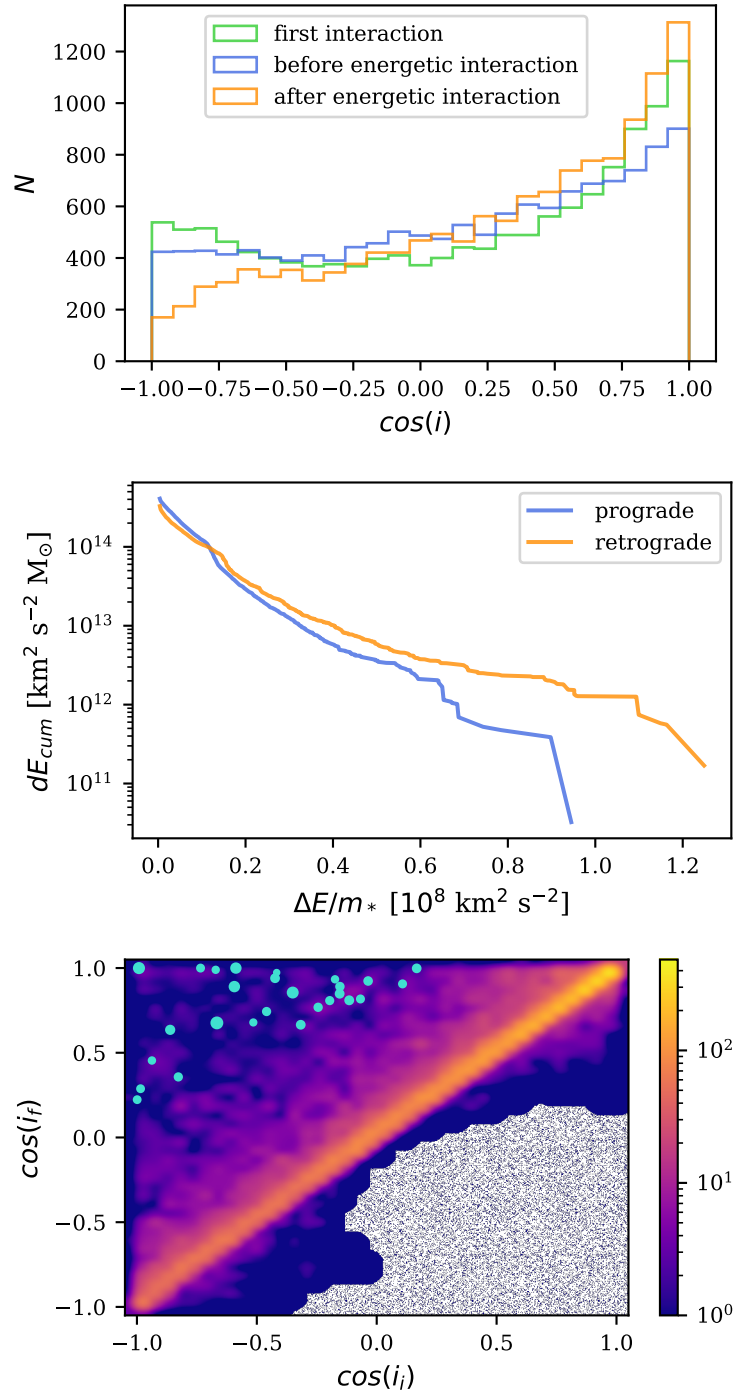


**Figure 7.8:** Top: Distributions of orbital inclination of the encounters, with respect to the black hole binary, at first passage (green), as well as before and after the energetic interaction (blue and orange lines, respectively). Middle: Cumulatively summed maximum energy changes of prograde (blue) and retrograde (orange) orbits as a function of specific energy change. Bottom: Two-dimensional histogram of the initial (x-axis) and final inclination (y-axis). The green points correspond to the 27 most energetic encounters (with  $\Delta E/m_* > 7.9 \times 10^7 \text{ [km}^2 \text{s}^{-2}]$ ). The size of points is correlated with the total energy extracted.

plot).

However, let us focus our attention on the middle part of the same figure, which shows the cumulative energy change of prograde ( $\cos(i_i) \geq 0$ ) and retrograde ( $\cos(i_i) < 0$ ) interactions as a function of specific energy change. While the prograde interactions are much larger in number, they account for only slightly more in the cumulative energy change than the retrograde group. This is because of the fact that the retrograde interactions dominate the high-energy tail of the distribution, as evidenced by the right side of the plot. Therefore, retrograde interactions, while lower in number, account for the highest energy changes. This is evident in the bottom panel of Fig. 7.8, where the 27 most energetic encounters are given as green points. Most interactions do not experience any visible changes in their inclination and therefore, fall on the diagonal on the plot. The most energetic interactions are almost all initially retrograde, and experience the largest inclination changes, orienting according to the SMBH binary orbital plane. This is due to the fact that the energy change of a star during the encounter is proportional to its change in angular momentum parallel to the SMBH binary orientation (Eq. 63 in [Rasskazov and Merritt, 2017](#)).

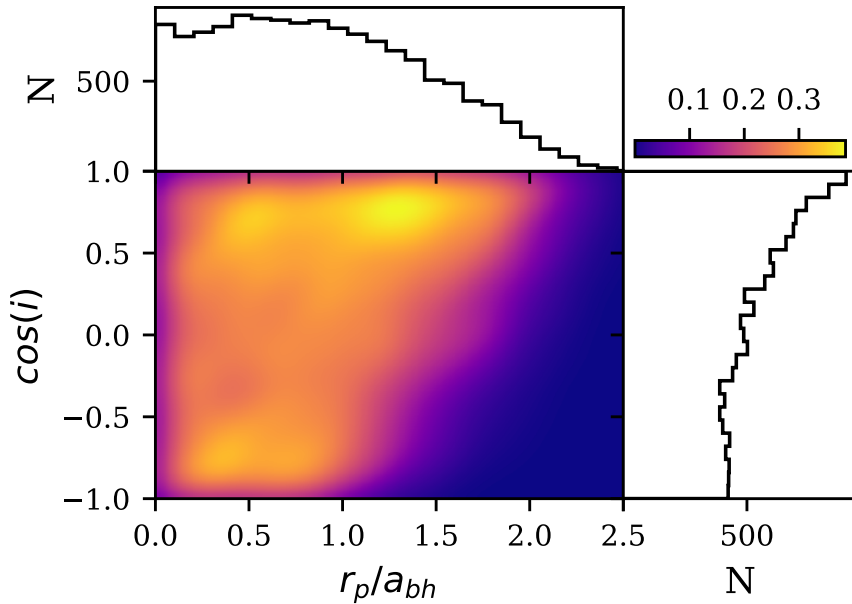


**Figure 7.9:** Density distribution of the inclination of the stellar orbit passage with respect to the SMBH binary orbital plane (y-axis) and the Keplerian pericenter (x-axis) at the time of the energetic interaction, normalized to the binary semi-major axis value. The distribution was smoothed using a Gaussian kernel density estimation.

The pericenter distance of a stellar orbit is a significant parameter that facilitates strong energy exchange. In order to experience a sufficiently strong energetic interaction it is expected that the star should come within several  $a_{bh}$  of the SMBH binary. We can confirm this by looking at Fig. 7.9, where we see that for all of the energetic interactions the stars come within  $3a_{bh}$  of the binary. Generally, the closer the encounter is to the binary, the more energetic it will be. It is then no surprise to see that the retrograde interactions have much lower pericenter values. In fact, we find that unlike the prograde group, almost all of the retrograde interactions cross the binary orbit  $r_p < a_{bh}$ . Additionally, we obtain no highly energetic interactions with  $r_p > 3a_{bh}$ . Therefore, we find this value to be a hard boundary for the pericenter of the energetic interactions in our run. We note however, that the pericenter shown here is calculated from a Keplerian approximation which ignores the binarity of the SMBH system, and is meant only

as a proxy to estimate the shape and size of the stellar orbit from a distance of  $10a_{\text{bh}}$  from the binary. The actual three-body interaction is far more complex and depends on the orbital phase of the binary.

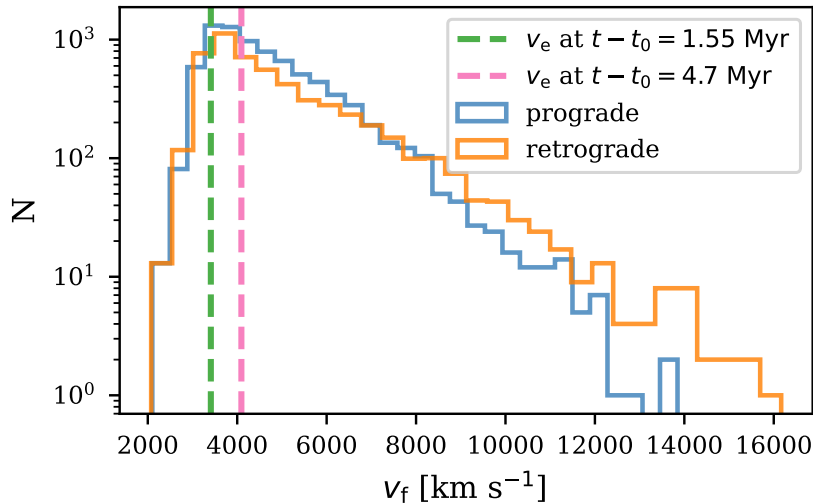


**Figure 7.10:** Ejection velocity distribution of the interacting stars with respect to the SMBH binary. Blue and orange lines correspond to stars on prograde and retrograde orbits with respect to the binary orbital plane, respectively. The dashed lines represent the escape velocity from the overall galactic system at radius of  $10a_{\text{bh}}$  from the binary center of mass, at the start and at the end of the run.

Similarly, we can look at the ejection velocity distributions of the prograde and retrograde interactions (Figure 7.10). The ejection velocities for both populations are peaked just beyond the escape velocity (with respect to the galactic system) at  $r = 10a_{\text{bh}}$  from the binary, which ranges from  $V_e = 3410 \text{ km s}^{-1}$  at the beginning of the analysis ( $t - t_0 = 1.55 \text{ Myr}$ ) to  $V_e = 4093 \text{ km s}^{-1}$  at the end of the run. We find that the prograde distribution is narrower and that the retrograde distribution extends up to  $16,000 \text{ km s}^{-1}$ . This behaviour is in agreement with our results so far and the velocity distribution presented in [Arca Sedda et al. \(2019\)](#), although we obtain significantly higher velocities than in that study, likely as a result of our simulation having more massive SMBH particles with lower separation.

Loss cone orbits are defined in terms of their position in phase space, rather than in physical space. This is because even stars well outside the SMBH binary region of influence can be part of the loss cone if their angular momentum is low enough. However, it is still not clear out to which radii in physical distance can a potential loss cone orbit extend. In order to investigate this, we estimate the apocenter of the stellar orbits by assuming that energy is conserved along the orbit. This is a justified approximation since the orbits are highly eccentric and the kinetic energy at apocenter is negligible. We estimate the apocenter by finding the maximum radius a particle with that energy can have in the potential of the system, assuming spherical symmetry for the potential. In this way, our approximation of the apocenter is only dependant on the energy of the stellar particle, unlike our pericenter approximation which took into account both energy and angular momentum of the orbit. We present the estimates of the apocenters of the star at the time of the first (not necessarily energetic) interaction (y-axis) and at the time just before the most energetic interaction (x-axis) in Fig. 7.11, top panel. In the 2-D histogram we notice three distinct populations, which are also evident on the top and right histograms. The two populations on the diagonal line (hereafter Populations I and II, from left to

	$N$	$\langle \Delta E/m \rangle$ [ $\text{km}^2 \text{s}^{-2}$ ]	$\langle dt \rangle$ [yr]	$dE_{\text{cum}}$ [ $M_{\odot} \text{km}^2 \text{s}^{-2}$ ]
<i>Total</i>	13383	$5.11 \times 10^6$	153.73	$7.36 \times 10^{14}$
<i>Population 1</i>	2816	$4.51 \times 10^6$	177.57	$1.77 \times 10^{14}$
<i>Population 2</i>	6680	$4.79 \times 10^6$	138.95	$3.33 \times 10^{14}$
<i>Population 3</i>	3465	$5.93 \times 10^6$	166.94	$1.95 \times 10^{14}$

**Table 7.1:** General properties of stellar encounters of Populations I-III. The columns represent, from left to right: number of stars in the population, median specific energy change per encounter, median duration of most energetic encounter and cumulative energy change of the population. The values of the three rightmost quantities are calculated only from the most energetic interaction of each star.

right) consist of encounters where there is no visible change in the apocenter before the energetic interaction, either as a result of multiple low-energy interactions that do not change the orbital parameters significantly (Pop. I) or because they consist of single, energetic interactions (Pop. II). The gap between these populations shows us that the loss cone is essentially empty within  $R_{\text{infl}}$ , except for the population very close to the SMBH binary. The population outside of the diagonal (hereafter Population III) initially comes from within  $R_{\text{infl}} < r_{\text{ap}} < 5R_{\text{infl}}$  and changes its orbital properties in a number of weak 3-body encounters, decreasing the energy, and as a result also the apocenter, until the pericenter falls below  $3a_{\text{bh}}$  and it experiences an energetic interaction. While there are some outliers, we can see that almost all of the interactions come from a region within  $5R_{\text{infl}}$ , or 66 pc in physical units and after this point the distribution drops quite sharply.

After the interaction, the stars get a kick in their orbital velocity and some gain enough energy to leave the system as a HVS. We find that a total of 72% of interacting stars have a positive total energy after the interaction  $E_{\text{tot}} > 0$ , and thus can be ejected from the system completely. The remaining 28%, or 3649 stars ( $\approx 1000$  in each population), still gain a significant velocity kick, and we estimate their new apocenters to investigate the nature of their orbits. On Fig. 7.11, in the bottom panel we see that the maximum of the distribution lies just beyond  $5R_{\text{infl}}$ . Since the vast majority of our interactions are contained within the region of  $5R_{\text{infl}}$  at initial apocenter, we do not expect this population to be able to return and interact strongly with the binary another time. However, the population contained within  $r_{\text{ap}} < 5R_{\text{infl}}$  still has that possibility, since the radial orbital timescale at  $R = 5R_{\text{infl}}$  is  $\sim 5 \times 10^4$  yr. Some stars, while still bound, are put on exceedingly extended orbits, with apocenters going up to 23 kpc in the high  $r$  tail of the distribution.

In Table 7.1 we present the general characteristics of stellar encounters in the apocenter populations I-III. The 422 stars which do not belong to any population from Figure 7.11 (top panel) were not considered here because of their low number statistics and negligible contribution to the binary hardening. In the table we notice that Pop. II is the most populous, with 6680 stars. It also has the shortest median duration of the most energetic encounter. This population contributes most significantly to the hardening, with 45% of the overall energy exchange. Population III, while smaller in number, has the highest median specific energy change, suggesting more energetic interactions. On the other hand, Population I is the least populous, has the lowest median specific energy change per encounter and therefore contributes the least to the overall binary hardening.

The populations can be characterized by taking a look at their phase space distributions.

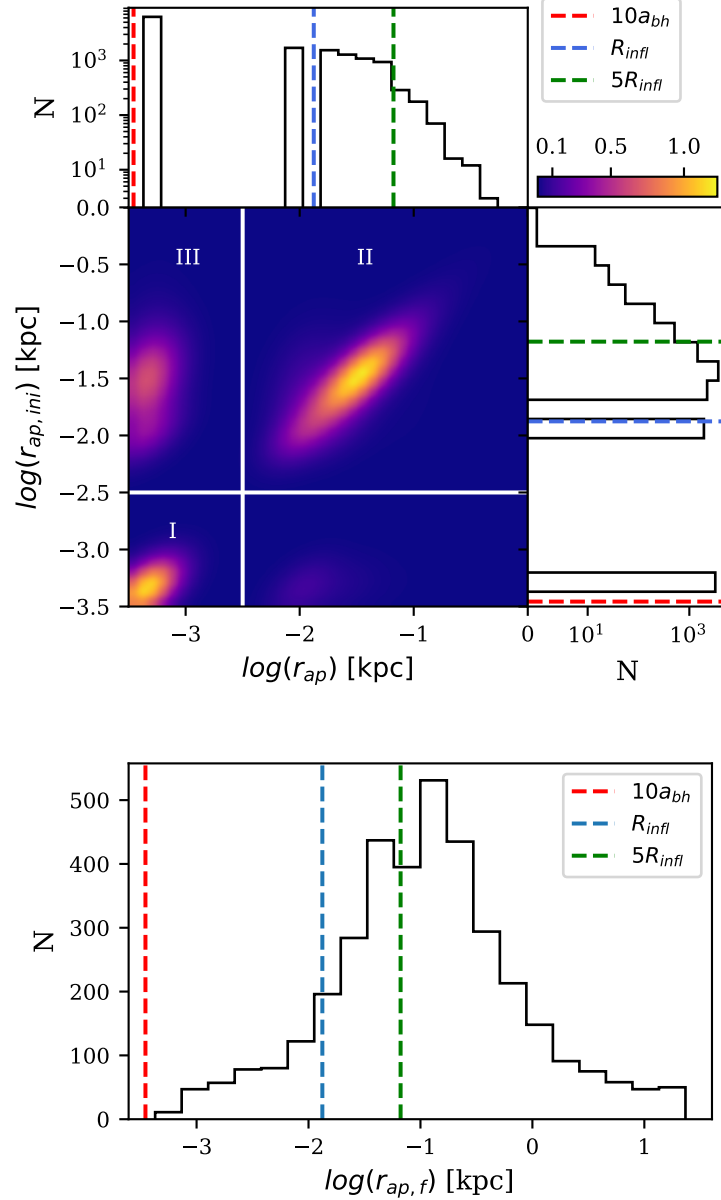


**Figure 7.11:** Top: Apocenter distribution of stellar orbits just before the first interaction (y-axis) and just before the most energetic interaction (x-axis), in log-spaced bins. The distribution was smoothed using a Gaussian kernel density estimation. Bottom: Apocenter distribution of stars still bound to the galactic system after the most energetic interaction with the SMBH binary.

Namely, the classical loss cone of an SMBH binary is typically characterized as the region populated by low angular momentum stars, which follow the condition (Yu, 2002):

$$L \leq L_{\text{crit}} = \sqrt{(\eta 2GM_{\text{BH}} a_{\text{BH}})}, \quad (7.11)$$

where  $\eta$  is a dimensionless factor on the order of unity and assuming spherical geometry. However, in non-spherical nuclei, there is an extended region in phase space, consisting of stars which, while not originally in the loss cone, may be driven into the classical loss cone by non-spherical torques. This region has previously been called the loss region (Vasiliev et al., 2014). We plot the distribution of the three apocenter populations (Pop. I-III) in the  $(L, L_z)$  plane on Fig. 7.12, at the time of their first passage, taking the value  $\eta = 3$  (which agrees with our pericenter investigations). The  $z$  in  $L_z$  corresponds to the minor axis of the GMR. We immediately notice that in all three cases, there is a large region of parameter space populated by stellar orbits, which are not yet in the classical loss cone at the time of their first passage (denoted by the bottom dashed square at  $L/L_{\text{crit}} < 1$  and  $-1 < L_z/L_{\text{crit}} < 1$ ). These correspond to the stars which interact with the binary several times before their energetic interaction and consequent ejection. We find that at the time of their most energetic interaction, all of them satisfy condition 7.11, with  $\eta = 3$ .

The first population, situated close to the SMBH binary, shows significant positive rotation around the  $z$ -axis, corotating with the binary, as well as the system, during their first encounter. Interestingly, we see no visible difference in the phase space properties of the Pops. II and III, both of which have initial apocenters  $\log(r_{\text{ap,ini}}) > -2.5$  [kpc]. Both populations are skewed towards positive  $L_z$ , suggesting a preference for corotating stars, in agreement with Fig. 7.8. However, unlike the first population, most of the stars have sufficiently low angular momentum to be considered proper loss cone stars. It is therefore puzzling, why only the second population will be promptly ejected at this time, while the third one will be captured by the binary. The answer to this lies in their energies with respect to the SMBH binary. We can see in the middle panels of Fig. 7.12 that the second population is almost completely unbound to the binary, and therefore represents a population of fast, parabolic and hyperbolic encounters. On the other hand, population three is captured by the binary during its first passage, most likely by chance due to the incoming orbital phase with respect to the binary, and the stars are put on eccentric orbits before their ejection, despite having the same phase space properties as Pop. II.

The bottom panels of Fig. 7.12 can give insight into which stars experience several interactions and which interact only once. For this purpose, we show histograms of the total interaction time per stellar particle, including all non-energetic interactions with the binary. Namely, the duration of the majority of single interactions would be quick slingshots with small pericenters, which should correspond to crossing times of stars on parabolic orbits, denoted by dashed lines on the figure. We see that Pops. I and III have typically long interaction times, ranging up to the entire duration of the run ( $\sim 10^6$  Myr) and suggesting that they have many multiple passages before experiencing a strong interaction. Pop. II on the other hand, shows the strongest peak at shortest interaction times, making this population characterized by single interactions, however there is also a second peak at  $dt \sim 1$  Myr. Unlike the other two populations, there is a prominent gap between the two peaks, which might signify that this group consists of stars which have already experienced a strong interaction, and have returned to interact once more, after a few crossing times of the system ( $t_{\text{cross}} \sim 1$  Myr).

On Fig. 7.13 we present the spatial angular distributions of stars in an equal area projection,

of incoming stars at initial passage (top panels), and after the most energetic interaction (bottom panels), centered on the SMBH binary center of mass. We immediately notice that Pop. I is highly anisotropic in the azimuthal angle, both before and after interaction. Our investigations show that this is the result of the Brownian motion of the black holes around the centre of our comoving reference frame. Namely, we observe that the black holes experience a Brownian motion around the center of the system (in the comoving reference frame) with an amplitude of  $\approx 1$  pc. Unlike [Khan et al. \(2020\)](#), we do not observe Brownian motion in a rotational fashion despite the rotation of our system. Instead, the Brownian motion we measure is in the form of a random walk. The stars in Pop. I belong to an inner, rotating stellar cusp. Stellar hardening is known to erode the central stellar cusp, leaving lower densities in the very center ([Khan et al., 2012b](#)). As a result, as the black holes move around the center in a random walk, they preferentially disrupt and capture the population that surrounds this inner region, which will be in the opposite direction from the origin, when viewed from the perspective of the black holes (Fig. 7.13, top-left panel). We therefore conclude that the presence of this population in the loss cone is the combined result of very high central densities of our system and the Brownian motion of the black holes.

In contrast, we find that Populations II and III are more isotropically distributed. These are the stars that come from outer regions on centrophilic orbits, and therefore the effect of random motion of the black holes does not play a role, like it does in the case of Pop. I. We notice that the third and especially second population show a prevalence of ejections along the SMBH binary orbital plane. This is in agreement with previous studies which find that HVS are primarily ejected near the SMBH binary orbital plane, e.g., [Sesana et al. \(2006\)](#), [Wang et al. \(2014\)](#); [Zhong et al. \(2014\)](#), when their SMBH orbital plane is aligned with the rotational plane of the system, and more recently [Lezhnin and Vasiliev \(2019\)](#) and [Rasskazov and Kocsis \(2019\)](#). Our findings show that not all of our three populations are uniformly distributed in azimuthal direction. While there is some disagreement in the literature on the existence of a preferential ejection direction in eccentric binaries ([Rasskazov and Kocsis, 2019](#)), in the case of a circular SMBH binary like ours, previous studies report uniform distribution of ejected stars in the orbital plane ([Rasskazov and Kocsis, 2019](#); [Lezhnin and Vasiliev, 2019](#); [Sesana et al., 2006](#)). We argue that the motion of black holes around the center can result in anisotropic ejections for the central population of stars (Pop. I), while stars originating from outside of the SMBH binary influence sphere are uniformly distributed (Pop. II and III).

From the apocenter distribution on Fig. 7.11, we conclude that Populations II and III correspond to stars on centrophilic orbits that are responsible for repopulating the loss cone. Depending on the shape and the degree of non-sphericity of the nuclei (e.g., axisymmetric or triaxial), different orbital families may fulfil this role ([Merritt, 2013b](#)). We can distinguish between the different orbital families if we look at their angular momentum at a time significantly before the interaction. Namely, because of the symmetries of different geometries, we can distinguish between *spherical*, *axisymmetric* and *triaxial* orbits. Spherical orbits have conserved angular momentum, and in order to satisfy Eq. 7.11, are necessarily contained at all times within the bottom dashed square region of Fig. 7.12, top panel. Axisymmetric orbits, such as the saucer and tube orbits, in turn have conservation of the z-component of angular momentum and are therefore necessarily contained in the  $|L_z/L_{\text{crit}}| < 1$  region of phase space, denoted by vertical dashed lines on the same figures. And finally, triaxial orbits (pyramids, boxes or chaotic orbits) can have arbitrarily small or large values in the  $(L, L_z)$  plane as a result of a lack of an integral of motion in that plane. This simple classification scheme is inspired by Fig. 6 of [Vasiliev](#)

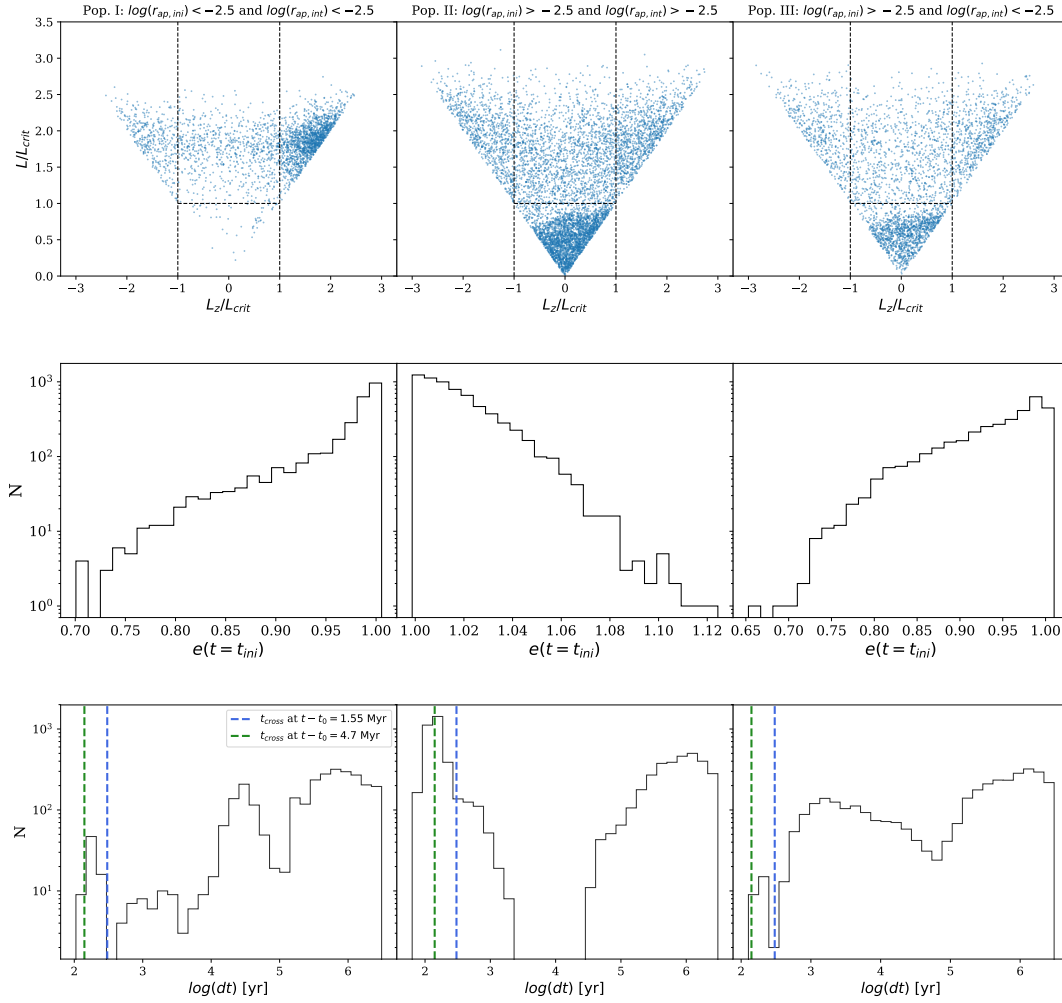


**Figure 7.12:** Top: Phase space properties of Populations I-III at the time of their first interaction with the SMBH binary. The bottom rectangular region bounded by dashed lines of  $L = L_{crit}$  corresponds to the classic loss cone, when  $\eta = 3$ . Middle: Eccentricity distributions in the Keplerian star-SMBH binary approximation at the time of first interaction. Bottom panel: Total duration of all of the interactions per particle (including non-energetic interactions), given in years and calculated as the amount of time between the first registered entrance and final exit from the sphere of radius  $r = 10a_{bh}$  around the black hole binary. The dashed lines correspond to the central crossing time of a star on a parabolic orbit for different times.

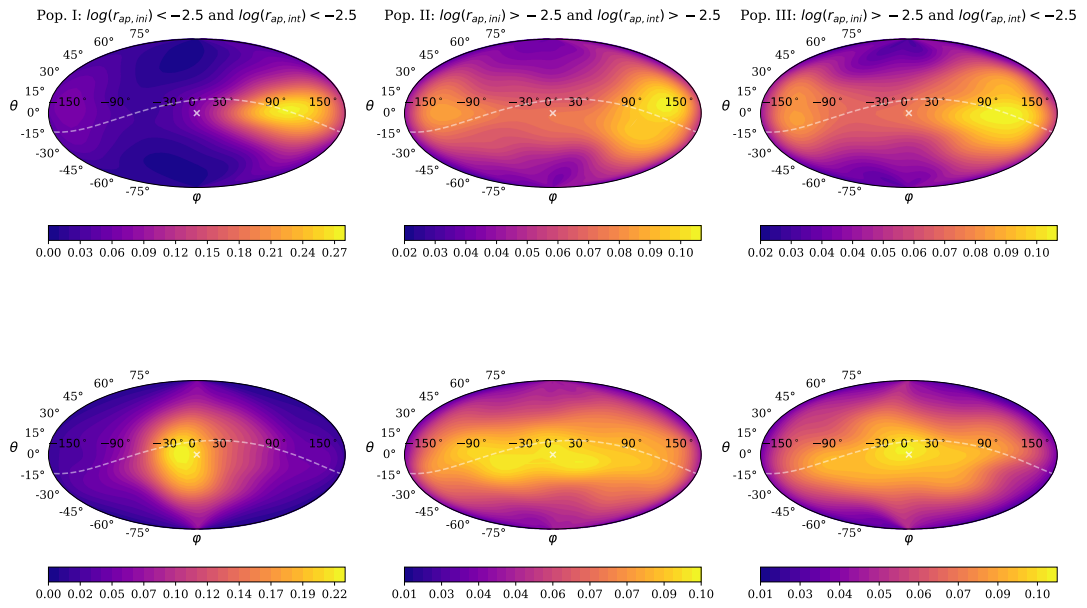


**Figure 7.13:** Top: Angular ejection distribution of Populations I-III at the time of initial interaction with the binary. The figures are centered on the SMBH binary center of mass, with the gray line representing the projection of the SMBH binary orbit. The white cross corresponds to the direction of the origin of our comoving reference frame, where the potential is evaluated. The  $\theta = 0$  plane corresponds to the equatorial plane of the system. Bottom: Angular ejection distribution after the most energetic interaction. Other elements are same as above.

Potential type	Fraction of encounters (%)
<i>Spherical</i>	0.0
<i>Axisymmetric</i>	23.8
<i>Triaxial</i>	76.2

**Table 7.2:** Fraction of orbital families of centrophilic stars depending on the shape of the potential. The classification is performed based on angular momentum changes of the stars throughout our run. Only stars in Populations II and III were considered.

et al. (2015), and we refer the reader to that study for more details. We can therefore estimate orbital type fractions of Populations II and III using these criteria by looking at their total and  $z$ -component of angular momentum at previous times throughout the run. We present these fractions in Table 7.2. We find that more than 76.2% of Pop. II-III orbits can only originate in triaxial nuclei, since only 23.8% show consistent conservation of  $L_z$  so that  $|L_z/L_{\text{crit}}| < 1$  is fulfilled throughout the run. This clearly shows that our centrophilic orbits are dominated by triaxial orbits by a factor of 3, despite only a small deviation from axisymmetry of our system (Fig. 7.2).

## 7.4 DISCUSSION

### 7.4.1 *Inclination of loss cone stars*

We found an overabundance of stars on prograde (co-rotating) orbits interacting strongly with the SMBH binary. This is expected, since stars on prograde orbits have a higher chance of capture by the binary because of the larger orbital phase they have compared to the retrograde cases (Wang et al., 2014; Milosavljević and Merritt, 2001). This preference naturally results in an overabundance of counter-rotating orbits within close vicinity of the SMBH binary, as discovered by previous studies (Meiron and Laor, 2010, 2013). We have shown that retrograde orbits have a possibility of experiencing a sign flip change in angular momentum during the interaction, in agreement with Wang et al. (2014). These cases are also the most energetic events we measure, in agreement with Rasskazov and Merritt (2017) who assert that total energy change of the star is proportional to its change in the component of angular momentum parallel to the binary.

### 7.4.2 *Hybrid integration approach*

Our results have demonstrated that the hybrid integration approach is very well suited for systems like our own. The combination of the SCF force calculation for the outer regions with direct summation for inner particles of interest successfully resolves two of the biggest issues that typically plague N-body approaches. The first issue being, the artificial enhancement of two-body relaxation effects that originates from insufficient mass resolution of N-body codes when compared to real galaxies. This issue has always pervaded N-body simulations and has previously cast doubt on measured hardening rates in N-body (Vasiliev et al., 2015). The second issue resolved by the hybrid approach is the exceptionally high computational cost for simulations with  $N \gtrsim 10^6$ . The proportionally small fraction of particles integrated in a direct way results in a factor of 16 speed-up over the pure N-body approach and enables simulations of multi-million particle systems easily attainable even by smaller computing clusters with only a few computation nodes.

### 7.4.3 Merger timescale and numerical parameters

We noted that the merging time of the SMBH binary reported in [Kh16](#) was underestimated by a factor of two as a result of numerical artifacts. Namely, we found that the rise in eccentricity of the binary in the original study was not due to stellar interactions, but a sign of insufficient integration accuracy in the black hole equations of motion, leading to an overestimation of the contribution of the PN terms and a premature PN plunge. We believe that this happened primarily because of two numerical parameters, insufficient spatial resolution (gravitational softening) and the minimum black hole integration timestep. Our convergence tests showed that at least the values of  $\epsilon = 2 \times 10^{-4}$  pc for the softening and the minimum timestep of  $\Delta t_{\min} = 10^{-5}$  yr are necessary to accurately integrate the SMBH binary evolution in this phase of the merger. Similarly, we found that this value of  $\Delta t_{\min}$  becomes insufficient for the later part of the merger, when  $t - t_0 > 4.65$  Myr, which is why we stop the run at this point. Therefore, this study focused only on the phase of the merger when no PN effects are measurably present, since even greater numerical accuracy would be necessary to accurately integrate the later phase of the merger when PN hardening becomes comparable to stellar hardening. This would result in a slowdown which would contribute to the already present and significant slowdown of the code in the PN regime. Because of this, accurate investigation of loss cone stars in this regime is inherently difficult and computationally intensive, even with the hybrid approach. Nevertheless, we plan to explore this regime in an upcoming publication.

We estimate the new merger timescale to be on the order of  $\approx 20$  Myr, which is still two orders of magnitude smaller than the Hubble time, thus avoiding the FPP. However, we note that the same limitations and uncertainties may apply as those that were discussed in [Kh16](#).

Finally, we also note that our simulation does not take into account the possibility of direct plunges of stars into the black hole horizon. Since many of our stars are able to come exceedingly close to the binary ( $< a_{\text{bh}}$ ), it is natural to assume that some of them would be lost in this way. This investigation is however beyond the scope of this study. Instead, we refer the reader to a few recent studies on tidal disruption events: [Li et al. \(2019\)](#); [Lezhnin and Vasiliev \(2019\)](#); [Darbha et al. \(2018\)](#)

## 7.5 SUMMARY AND CONCLUSIONS

In this chapter, we have presented an N-body simulation of an unequal-mass SMBH binary system embedded in a dense, slightly triaxial, rotating stellar cusp. Our system originated from a high-redshift major galactic merger in an *ab initio* cosmological simulation, as described in [Kh16](#). With a particle number of  $6 \times 10^6$ , we have simulated the hardening phase of the SMBH binary merger and explored in detail the properties of the stellar particles which experience energetic interactions with the black holes. We utilize the  $\varphi$ -GRAPE-hybrid code, which combines direct integration with the collisionless SCF integration method to considerably reduce computational cost and spurious relaxation effects and enables exploration of the orbital parameters of stars in the loss cone with high accuracy. We now summarize our main conclusions:

- To a very high degree of accuracy, we are able to identify the exact stars that contribute to the SMBH binary hardening. Our energy balance plots (see [Fig. 7.6](#)) show that throughout the run, the cumulative energy changes of stars within the high-energy tail correspond almost exactly to the overall SMBH binary orbital energy change for the same time intervals. This demonstrates beyond any doubt that stellar hardening is the main driver

of SMBH binary energy loss in our system, and that other possible effects of energy loss can be neglected. This further implies that in gas-poor systems, proper treatment of stellar scattering interactions, either via simple analytic recipes derived on scattering experiments (e.g., [Sesana and Khan, 2015](#); [Sesana, 2010](#)) or via direct summation, can be sufficient to properly characterize the evolution of SMBH binaries.

- We distinguish three populations of stellar encounters based on their apocenter distributions (see Fig. 7.11). Population I originates close to the binary, contributes to hardening the least and is a consequence of the Brownian random motion of the SMBH binary around the center. Population II originates from outside the influence radius, with apocenters  $r_{\text{ap}} \approx 5R_{\text{infl}}$  and is characterized by fast, single hyperbolic and parabolic interactions. This population has the highest effect on the SMBH hardening by far, since it is the most populous. Population III has similar properties as Pop. II, but becomes bound to the binary and is put on eccentric orbits.
- We identify Pops. II and III as the centrophilic orbits responsible for refilling the loss cone. We analyze their angular momentum changes and estimate that 76.2% of these orbits can originate only in a triaxial potential, cementing the fact that even slight triaxiality is crucial for the efficient hardening of the SMBH binary that we measure, in agreement with [Vasiliev et al. \(2014\)](#); [Bortolas et al. \(2018a\)](#); [Khan et al. \(2018c\)](#).
- Most of the energetic interactions show prograde rotation with the SMBH binary, as well as the overall system. However, the retrograde interactions correspond to the most energetic interactions that we measure and can result in a sign-flip change in angular momentum. Because of this, we find that despite being significantly lower in number, retrograde orbits make up for 45% of the total energy exchange.

---

## DYNAMICAL EVOLUTION OF MASSIVE BLACK HOLE TRIPLETS IN ILLUSTRISTNG

---

In this chapter, I present the results of a series of numerical zoom-in simulations of the cosmological, hydrodynamical simulation IllustrisTNG. The simulations presented here focus on the formation and evolution of massive black hole triplets following subsequent galactic mergers.

### 8.1 INTRODUCTION

According to the standard  $\Lambda$ CDM (Lambda Cold Dark Matter) cosmological model, dark energy is the dominant energy component in Universe, driving its accelerated expansion. The matter distribution on the other hand, is dominated by dark matter, which contributes 84.2% to the total matter content. The baryonic part of matter, consisting of all observable structures in the Universe, in turn corresponds to only 15.8% of the total matter content ([Aghanim et al., 2020](#)).

Cosmological simulations are large N-body simulations, with particle numbers as high as  $N \sim 10^{10}$ , that follow the growth and evolution of structures over a wide range of scales and across all of cosmic time within an expanding Universe. Relying on the  $\Lambda$ CDM cosmological model, these simulations utilize dark matter as the crucial component for early structure formation, since structures like galaxies and galaxy clusters form at the centers of dark matter overdensities, known as dark matter halos. The dark matter behaves in a collisionless way, only interacting through gravitational interactions. Baryonic matter, on the other hand, needs to be treated in a collisional way through hydrodynamics, and incorporates much more complex processes such as gas and radiative cooling, star formation and evolution, magnetic hydrodynamics and supernova and AGN feedback, among others. Due to the incredibly large range of scales these simulations entail, these complex effects must often be incorporated with additional, sub-grid physical models to account for all of the necessary physics that represents the evolution of cosmic structures in a realistic manner.

Within the last few decades, these cosmological simulations of structure and galaxy formation have been crucial in providing insight into galaxy formation and evolution and can now reproduce many properties of observed galaxies. Today, the state-of-the-art simulations have simulation box sizes on the scale of several hundred Mpc, resulting in tens of thousands of simulated galaxies. These include the EAGLE simulation ([Schaye et al., 2015](#)), Illustris

Vogelsberger et al. (2014), IllustrisTNG (Springel et al., 2018) and Horizon-AGN (Dubois et al., 2014), among others. A comprehensive review of cosmological simulations can be found in (Vogelsberger et al., 2020). The resulting galaxy populations represent a diverse sample of a variety of different galactic features and histories. These virtual "galaxy zoos" present a unique opportunity to investigate effects that are otherwise difficult and cumbersome to observe, such as star formation histories and metal enrichment. Furthermore, these galaxies are not subject to simplifying or non-physical assumptions that can arise from theoretical models of isolated objects, but rather have formed in a self-consistent way, taking into account the effect of their surrounding cosmological environment.

The processes that determine the evolution of massive black holes in cosmological simulations, such as black hole growth, formation of massive seeds and feedback, happen on scales orders of magnitude smaller than the spatial resolution of the most modern cosmological simulations. As a result, these features are implemented using sub-grid models which differ between simulations and can produce different results. Nevertheless, the existing black hole populations have been used previously to investigate scaling relations between the black hole and the host galaxy (Habouzit et al., 2020), massive black hole seed formation (Degraf and Sijacki, 2020) and to investigate massive black hole merger timescales and prospects for GW detections (Kelley et al., 2017a,b; Katz et al., 2020). Additionally, in recent years an increasing number of studies have been using cosmological simulation data as a starting point for higher-resolution zoom-in simulations of individual SMBH binary systems (Khan et al., 2016; Tremmel et al., 2018b,a; Pfister et al., 2019; Bortolas et al., 2020), including Ch. 7 of this thesis.

However, the investigation of triple SMBH systems and their dynamical evolution has so far been limited to simulations of triplets embedded in an external, fixed stellar background (Hoffman and Loeb, 2007; Bonetti et al., 2016, 2018) or with the use of semi-analytical models (Bonetti et al., 2019). In this chapter, I present the results of a number of high-resolution zoom-in simulations of possible SMBH triplets using data obtained from the cosmological simulation IllustrisTNG. The simulations were performed on the high-performance JUWELS computation cluster in Jülich (Germany) as part of the computation project *smbhdynamics*. The galactic mergers themselves were simulated with the GPU tree code *bonsai2* (Bédorf et al., 2012a,b). Additional comparison simulations were simulated using the direct N-body code  $\phi$ -GPU (Berczik et al., 2011). During the writing of this thesis, a similar approach has been introduced in the literature which performed a cosmological zoom-in simulation of an SMBH triplet system (Mannerkoski et al., 2021).

The chapter is structured as follows. In section 8.2 I present a short overview of the IllustrisTNG (commonly abbreviated as TNG) simulation suite and describe the selection parameters used to identify possible SMBH triple candidates in section 8.3. In section 8.4, I describe the galaxy modeling and fitting procedure used to construct initial conditions for higher-resolution N-body runs. In section 8.5 I describe the results obtained, focusing on the evolution of the massive black holes. Finally, in section 8.7 I present a summary of the results and discuss the main conclusions.

## 8.2 ILLUSTRIS-TNG

TNG (The Next Generation, Springel et al., 2018; Pillepich et al., 2018a; Marinacci et al., 2018; Nelson et al., 2018; Naiman et al., 2018) is a suite of cosmological, gravo-magnetohydrodynamical simulations and a successor of the original Illustris simulations (Vogelsberger et al., 2014). Sim-

ilar to Illustris, TNG utilises the moving-mesh hydrodynamic code AREPO (Springel, 2010). The gravitational forces in AREPO are calculated using a combination of the tree and particle-mesh integration schemes (TPM, Xu, 1995), where close-range forces are calculated using the oct-tree method, while long-range forces are calculated using the particle-mesh. TNG improves on the original Illustris by adopting a new galaxy formation model, new black hole feedback models as well as including treatment of cosmic magnetic fields.

The simulations are split into three main flagship runs (TNG300, TNG100, TNG50), with simulation box lengths of 300 Mpc, 100 Mpc and 50 Mpc, respectively. The flagship runs themselves are split into dark-matter-only (gravity only) runs, as well as baryonic (gravohydrodynamic) runs, and each of these is split into multiple runs with different mass resolution and particle numbers, for a total of 20 simulation runs. The data from all three flagship runs are publicly available (Nelson et al., 2019).

The selection of the box size depends on the needs of the user. TNG300 features the largest available cosmological box, and thereby boasts the largest galaxy sample size and enables investigation of rare systems and galaxy clusters at the cost of lower mass resolution. TNG50, on the other hand, features vastly improved mass resolution (a factor of 16 compared to TNG100), enabling the investigation of small-scale phenomena and individual galaxy features, at the cost of smaller galaxy sample size. TNG100 is a middle-ground between the previous two sets, featuring a considerable sample size without significantly sacrificing mass resolution. For the work performed in this thesis, I used data from the simulation TNG100-1, and all subsequent discussion refers to this simulation. The mass resolution is then  $M_b = 1.4 \times 10^6 M_\odot$  for the baryonic mass and  $M_{\text{dm}} = 7.5 \times 10^6 M_\odot$  for the mass of dark matter particles, with dark matter particle number  $N \sim 6 \times 10^9$ .

The simulation is initialized at  $z = 127$  and run until  $z = 0$ . To simulate an evolution within an expanding universe of bounds much larger than the box size, comoving coordinates are used in combination with periodic boundary conditions. The gravitational softening employed for dark matter and stellar particles is  $\epsilon = 1 \text{ ckpc}/h$  at redshifts  $z \geq 1$ , where ckpc signifies comoving kiloparsec and  $h$  is the value of the Hubble parameter in units of 100 km/s/Mpc at  $z = 0$ , taken as  $h = 0.6774$ . When  $z < 1$ , the value of the softening is fixed to the value at  $z = 1$ . For identifying structure, the simulations utilize the Friends-of-Friends (FoF) algorithm which divides the dark matter particles into *halos* (sometimes referred to as *groups* or *FoF groups*) and assigns baryonic particle types to their halo of their closest dark matter particle. Then, each halo is divided by the Subfind algorithm (Springel et al., 2001) into *subhalos* (also known as *subgroups* or *Subfind groups*), which can be thought of as the equivalent of galaxies. Each halo is then assigned a primary subhalo (the most massive one) and the other subhalos are treated as satellite subhalos. In this chapter, the terms subhalos and galaxies are used interchangeably.

The black holes are treated as massive and collisionless sink particles. Since the mass resolution is insufficient to account for formation of SMBH particles, and since these formation mechanisms are still not well constrained, the black holes are seeded automatically by the algorithm in FoF halos with masses  $M_{\text{fof}} \geq 7.38 \times 10^{10} M_\odot$  that have no black hole particles. The black hole seed mass is  $M_{\text{BH}} = 1.18 \times 10^6 M_\odot$  and the particle is placed at the center of the halo (Weinberger et al., 2018). Since the black hole mass is comparable, or even smaller than the masses of the other particles, perturbations from other particles would cause the black hole to wander and potentially leave its host subhalo. Therefore, to avoid these effects, the black holes are artificially fixed to the center of their host subhalos at all times. For this reason, the

velocities of the black holes in the simulation hold no relevant physical meaning. The growth of black holes is prescribed through accretion and mergers. The black holes grow dominantly through accretion, and the accretion rate is determined by the Eddington-limited Bondi accretion rate (Weinberger et al., 2018). The mergers between black holes are treated in an instantaneous fashion. Whenever two black hole particles come within a smoothing particle length from each other, they are immediately merged and the surviving black hole gains the mass of the other black hole (not including the mass deficit as a result of GW emission). This separation is typically on the order of a kiloparsec (Kelley et al., 2017a). This prompt merger of the black holes is unphysical, since in reality coalescence would take place on a timescale  $t \lesssim 1$  Gyr. Due to this, the evolution and formation of black hole pairs and the various processes that contribute to their coalescence on this timescale are unresolved.

### 8.3 SELECTION CRITERIA

In this section, I describe the selection procedure used to extract possible SMBH triple candidates from the TNG100-1 dataset. While TNG provides ready-to-use data of black hole mergers, in the case of TNG100, the data is incomplete at certain redshifts. Therefore, in order to perform a comprehensive analysis, the selection procedure was instead performed with the Sublink merger tree (Rodríguez-Gomez et al., 2015) which enables the user to traverse the history of each subhalo backwards in time. The selection was performed using the Illustris-TNG JupyterLab interface. At each snapshot, for a given subhalo, the merger tree allows the user to identify all subhalos in the previous snapshot which have common particles with the subhalo in question. These subhalos are termed progenitors, and the subhalo in question is referred to as their descendant. If the number of progenitors for a subhalo is higher than one, a merger event between subhalos has taken place. The selection was performed by following the merger trees of all subhalos at  $z = 0$ .

There are cases of subhalos which are not cosmological in origin but rather may have formed as clumps from various instabilities of nearby subhalos, such as disk instabilities. Nevertheless, they are identified as separate objects by the Subfind algorithm and can introduce spurious results. These objects are identified with the SubhaloFlag parameter provided in the TNG group catalog and are excluded from this analysis (see [www.tng-project.org](http://www.tng-project.org) for a full description of the parameter). Additionally, the vast majority of subhalos are very small in mass, with very low particle numbers ( $N \sim 10 - 100$ ), just above the threshold of 20 particles required for a particle formation to be identified as a subhalo. Many of these cases have no histories in the merger trees and are unsuitable for our analysis. Therefore, only subhalos with stellar particle number higher than  $N_{\text{st}} > 100$  were selected at  $z = 0$ , resulting in a total of 48,974 subhalos whose histories were investigated within the merger tree.

In order to identify mergers of galaxies containing black holes at every snapshot the primary progenitor of the subhalo candidate was identified, as well as all other progenitors. If both the main progenitor and another progenitor contained at least one black hole particle and the mass ratio between the masses of the black holes was higher than  $q > 0.3$ , it was registered as a merger. The mass ratio condition was adopted to identify black hole mergers of comparable mass, which are expected to have much higher successful merger fractions (Bonetti et al., 2018). The lookback time at each merger event was calculated using the same set of cosmological parameters as in the TNG simulations, consistent with Planck 2015 results (Ade et al., 2016). We calculated the timespan between each merger, and if a subhalo experienced multiple of

the above described merger events within a timespan of 1 Gyr, it was marked as a candidate, otherwise it was omitted from further selection. Furthermore, we restricted the selection to candidates where the redshift of both merger events was  $z < 6$  and the surviving black hole after each merger was in the mass range of  $10^7 M_{\odot} < M_{\text{BH}} < 10^8 M_{\odot}$ , since these parameters are optimal for high signal-to-noise ratio detection with LISA (Amaro-Seoane et al., 2017), while also allowing for black hole mergers in the higher mass range, which could be detectable by PTAs (Nguyen et al., 2020). The above selection criteria resulted in twenty candidates.

In order to verify which candidates are suitable for individual N-body runs, we look at the mass histories and particle numbers of all of the candidates in the snapshots before the mergers. One notable issue that can be seen in the mass histories is the subhalo switching problem (Poole et al., 2017). Namely, during close approaches, such as mergers for example, the Subfind algorithm can have issues detecting the primary subhalo of the group. Since the primary subhalo by construction gets attributed the surrounding particles which do not belong to any subhalo (i.e. the *particle fuzz*), it is also the most massive. This can result in the algorithm attributing different subhalos as the primary one at each subsequent snapshot, causing large, non-physical jumps in mass in both subhalos. Even without the switching issue, the division of particles into separate subhalos during mergers is unreliable, and typically results in one subhalo being attributed most of the particles, while the other is very small in mass. The subhalo switching issue can be resolved by averaging the masses of the galaxies over a certain number of snapshots (Peschken et al., 2020) or by disregarding the masses of each subhalo at the time of the merger and instead taking the maximum past mass (in all previous snapshots) of each subhalo as the mass parameters during the merger (this method is suggested in the TNG documentation).

Another consequence of this issue is that it can result in false detections in our triple selection criteria. For example, during a merger a particle distribution can be detected as a new, separate subhalo. If this new subhalo is sufficiently massive, a black hole will be automatically seeded at the center by the algorithm, and be promptly merged with one of the other two black holes. When this happens, the above described setup detects the event as a triple black hole merger, while in reality the newly formed subhalo and its black hole do not have unique cosmological histories, and their formation is just a consequence of the original, binary merger. Looking at the mass history of each individual candidate is therefore the best way to detect these false triple systems, since they would not show any history before the merger event. On Fig. 8.1, the mass history and particle numbers for one of the candidates is shown as a function of redshift as an example. The large dips in mass and particle number of galaxies one and three in the snapshot preceding the merger are clear signs of the subhalo switching issue. All three black holes are formed between  $5 < z < 6$ . Dark matter dominates the masses of the galaxies in all cases.

On Fig. 8.2 the distribution of all twenty triple mergers is shown as a function of redshift and the mass of the surviving black hole after the merger. The candidates are distributed equally in redshift, except around  $z \approx 0.7$  where the concentration of points is much higher. There are three cases in the plot with vertical dashed lines, indicating that the surviving black hole mass is the same for both merger events. This is due to the fact that occasionally the merger tree does not recognize one of the progenitors in the snapshot of the merger, but only in the snapshot before and after. As a result, if two mergers take place in subsequent snapshots, the resulting black hole mass in the snapshot following the merger is the summed mass from all three black holes.

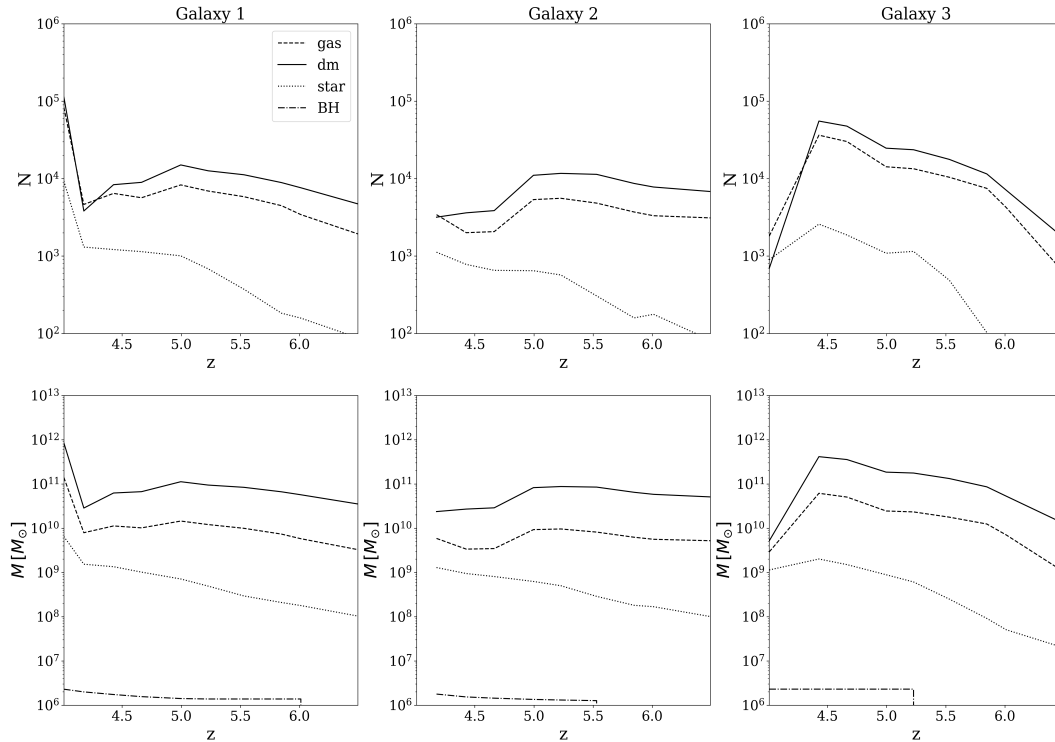


**Figure 8.1:** Top: Particle numbers as a function of redshift of one of the candidate triple systems selected for further N-body runs (subhalo id 179886 at  $z = 0$ ). The first column corresponds to the primary galaxy, while the second and third correspond to the galaxies involved in the first and second merger event, respectively. Different line styles correspond to different particle types. Bottom: Mass of the three galaxies as a function of redshift. Other elements are the same as above.

Using the mass histories, we find that nine out of our twenty candidates include subhalos that have no, or very short histories ( $\approx 2$  snapshots) preceding the original merger event, and we exclude them from the selection, leaving 11 candidates. Additionally, several candidates include subhalos with very low stellar particle numbers,  $N_{st} \sim 10$ , in snapshots preceding the merger. These cases would be unreliable for the construction of full galaxy models due to extremely low number statistics, and are also excluded. As a result, for the final selection only candidates with stellar particle number  $N_{st} > 1000$ , featuring subhalos with individual, cosmological histories before the merger, and black holes that were formed at least five snapshots before the first merger event. With these criteria, six out of the original twenty candidates were selected for construction of the galaxy models (Fig. 8.2). The six selected systems are designated throughout the text by letters A, B, C, D, E & F.

## 8.4 NUMERICAL SETUP AND INITIAL CONDITIONS

### 8.4.1 Data extraction

In this section, I will describe the procedure utilized to extract the data of the triple galactic merger for each of the six candidates from TNG snapshots. This data will then be used as a starting point for galaxy fitting and construction of full galaxy models. The simulation has a box size length of  $l = 75 \text{ cMpc}/h \approx 110 \text{ Mpc}$ , with coordinates in the range  $r_i \in (0, l)$ , where  $i$  denotes one of the cartesian coordinates. Due to the periodicity of the boundaries, it can happen

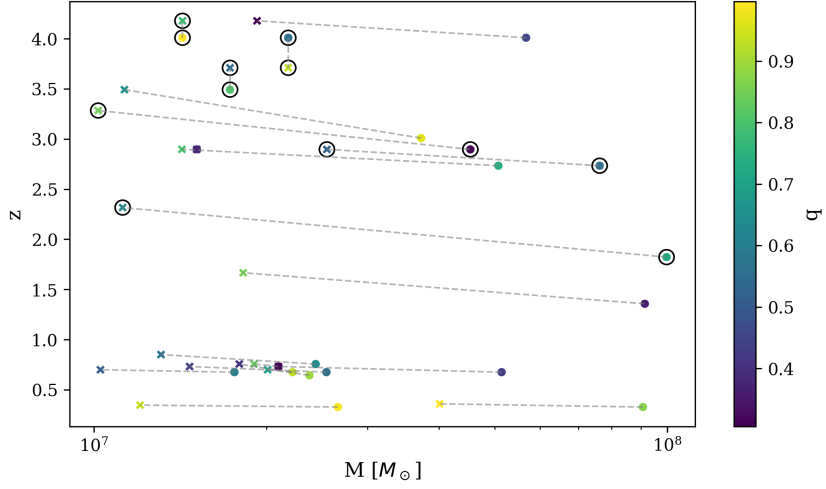


**Figure 8.2:** The distribution of the twenty triple merger candidates as a function of redshift of the merger (y-axis) and the mass of the resulting black hole (x-axis). Each point corresponds to one merger event involving two black holes. The crosses correspond to the first merger, the round points correspond to the second merger and the dashed lines show which mergers involve the same systems. The color coding corresponds to the mass ratio between the two black holes in the merger. The black circles around certain points show the six systems which were selected for N-body runs.

that a subhalo is split on the edges of the simulation box, with a portion of particles at  $r_i \approx 0$ , and another portion at  $r_i \approx 75 \text{ kpc}/h$ , which should be corrected. Therefore, all of the data was converted from comoving to physical coordinates and corrected for the periodic boundary conditions of TNG. This can be done by centering the center of the subhalo to the center of the cosmological box:

$$\Delta r_i = \frac{l}{2} - r_{c,i}, \quad (8.1)$$

where  $\vec{r}_{c,i}$  is the position of the center of the subhalo in direction  $i$  at a certain snapshot. Then, all of the particles of the subhalo can be translated to this position:

$$r'_i = r_i + \Delta r_i. \quad (8.2)$$

If the new position  $r'_i$  is outside of the cosmological box, with  $r'_i < 0$  or  $r'_i > l$ , then the box size  $l$  is either added or subtracted to the position:

$$r'' = \begin{cases} r'_i + l, & \text{for } r'_i < 0, \\ r'_i - l, & \text{for } r'_i > l, \\ r'_i, & \text{for } 0 \leq r'_i \leq l. \end{cases} \quad (8.3)$$

Finally, since the positions are now centered to  $l/2$ , this value is subtracted from all particles in order to center the data to the center of the subhalo.

The next step is to estimate the parameters of the galaxies in the snapshots before the merger, which would allow for the construction of equilibrium galaxy models. We extract the data at redshift  $z_0$ , corresponding to four snapshots before the first merger (the time period between four snapshots is equivalent to roughly  $0.4 \text{ Gyr}$  at  $z \approx 4$ ), since at this time the stellar

components of all three galaxies are well-separated and distinct from one-another. While this is necessary in order to isolate the individual galaxies, it comes with a caveat since at this time, the black holes did not yet have a chance to grow considerably via accretion and their masses are considerably smaller, with values on the order  $M_{\text{BH}} \sim 10^6 M_{\odot}$ , similar to their seed mass values. Even though the stellar components are spatially separated at this time, the same can not be said for the dark matter and gas distribution which are already in the process of merging.

In order to account for all of the particles in the surroundings of the system, we load all of the particles in the halos which contain the three subhalos. In order to divide the particles between the three galaxies, we perform a radial cut by attributing all of the particles within  $2r_{hm,j}$ , where  $r_{hm,j}$  is the half-mass radius of subhalo  $j$ . The half-mass radii of the subhalos were obtained by traversing the merger tree. Namely, in the absence of mergers and the subhalo switching issue, the total mass of any given subhalo is expected to be monotonically increasing with time. We therefore identify for each subhalo a previous snapshot where the centers of each subhalo are separated by at least 100 kpc and the total mass difference between subsequent snapshots is negative:

$$\Delta m_{tot} = m_{tot}(n) - m_{tot}(n-1) < 0, \quad (8.4)$$

where  $n$  is the snapshot number increasing with time. This condition enables us then to identify the previous snapshot where the mass starts to decrease due to the merger and when the subhalos are sufficiently separated. Then, the half-mass radius is measured at this snapshot, and this value is used for the radial cut at redshift  $z_0$ . The particles that are not within the  $2r_{hm}$  limit of any subhalo are then attributed to their closest subhalo. On Fig. 8.3, the spatial distribution of the particles after the radial cut selection is given for one system.

#### 8.4.2 Galaxy modeling

Using the extracted data, we now construct radial cumulative mass and density profiles for all of the matter components and galaxies. Due to resolution constraints of the original simulation, the profiles show low particle number statistics in the inner region, making the densities uncertain within the inner kpc. In order to get accurate estimates of the densities in the inner region, we perform a bezier spline smoothing procedure on the data before the fitting of the density profiles.

The stellar component was fitted with the Dehnen family of density profiles (Dehnen, 1993), according to the distribution:

$$\rho(r) = \frac{(3-\gamma)M}{4\pi} \frac{a}{r^\gamma(r+a)^{4-\gamma}}, \quad (8.5)$$

where the  $\gamma$  parameter is in the range  $\gamma \in [0, 3)$ ,  $a$  is the scale radius and  $M$  is the total mass of the stellar component. These three quantities were used as free parameters during the fitting procedure. For initial values of the fits, we used  $\gamma = 1$ ,  $a = 1$  kpc and the total mass of the stellar component in the TNG data for the fitting parameter  $M$ .

On the other hand, the gas and dark matter components were fitted with the Hernquist density profile (Hernquist, 1990), which corresponds to the Dehnen profile when  $\gamma = 1$ :

$$\rho(r) = \frac{M}{2\pi} \frac{a}{r(r+a)^3}. \quad (8.6)$$

The fitting was performed with two free parameters in this case,  $a$  and  $M$ . The initial value of  $M$

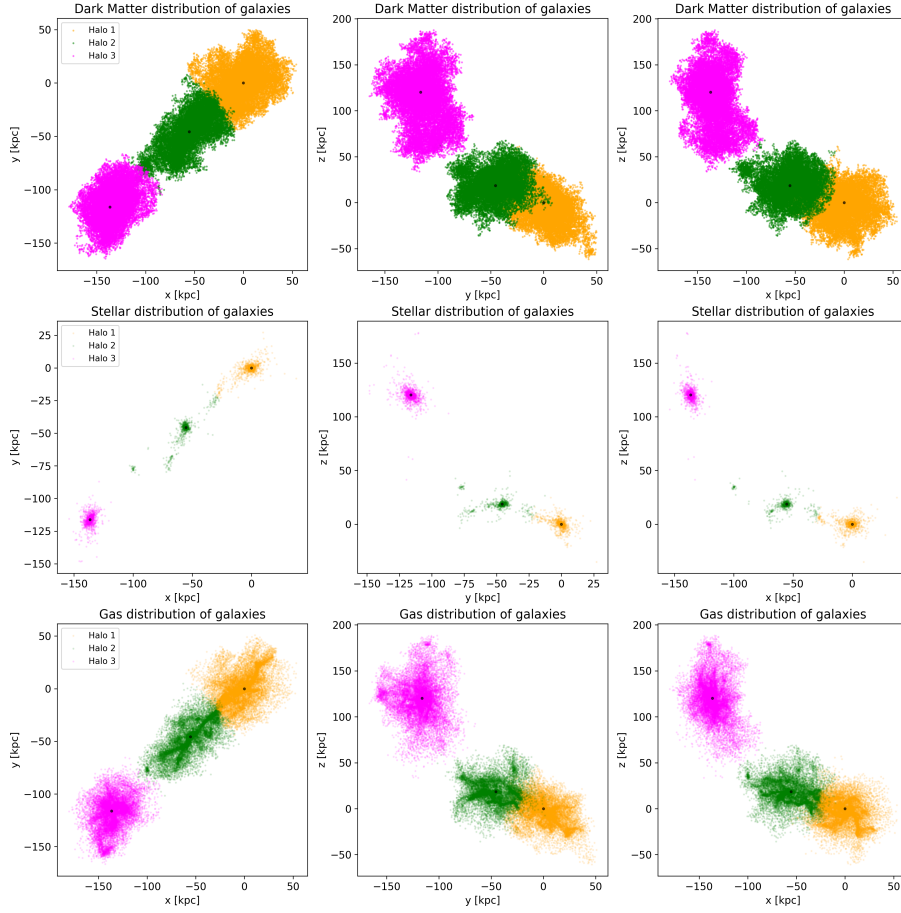


**Figure 8.3:** Spatial particle distribution of system C, showing the three galaxies after the radial cut. The rows from top to bottom correspond to the distribution of dark matter, stars and gas, respectively. The different columns correspond to different projections in Cartesian directions. The different colors designate the affiliation of the particles with respect to the three galaxies after the selection.

was the total mass of that component as obtained from TNG, while the initial value of  $a$  was:

$$a_0 = r_{\text{hm}}(\sqrt{2} - 1). \quad (8.7)$$

In order to avoid spurious effects due to the spatial resolution of TNG in the inner region, only data with central radial distance  $r > 4\epsilon$  was used for the fitting, where  $\epsilon$  is the spatial resolution of TNG. The spatial resolution is  $\epsilon = 1 \text{ ckpc}/h$  for  $z > 1$ , corresponding to  $\epsilon = 0.21 - 0.33 \text{ kpc}$  for all six systems. The fits were performed with the open-access python `lmfit` library (Newville et al., 2014), which utilizes non-linear least squares minimization. In Fig. 8.4, the radial density profiles of all systems and their respective density fits are presented. The exact values of the fitted parameters, as well as black hole masses and redshifts are given in Table 8.1.

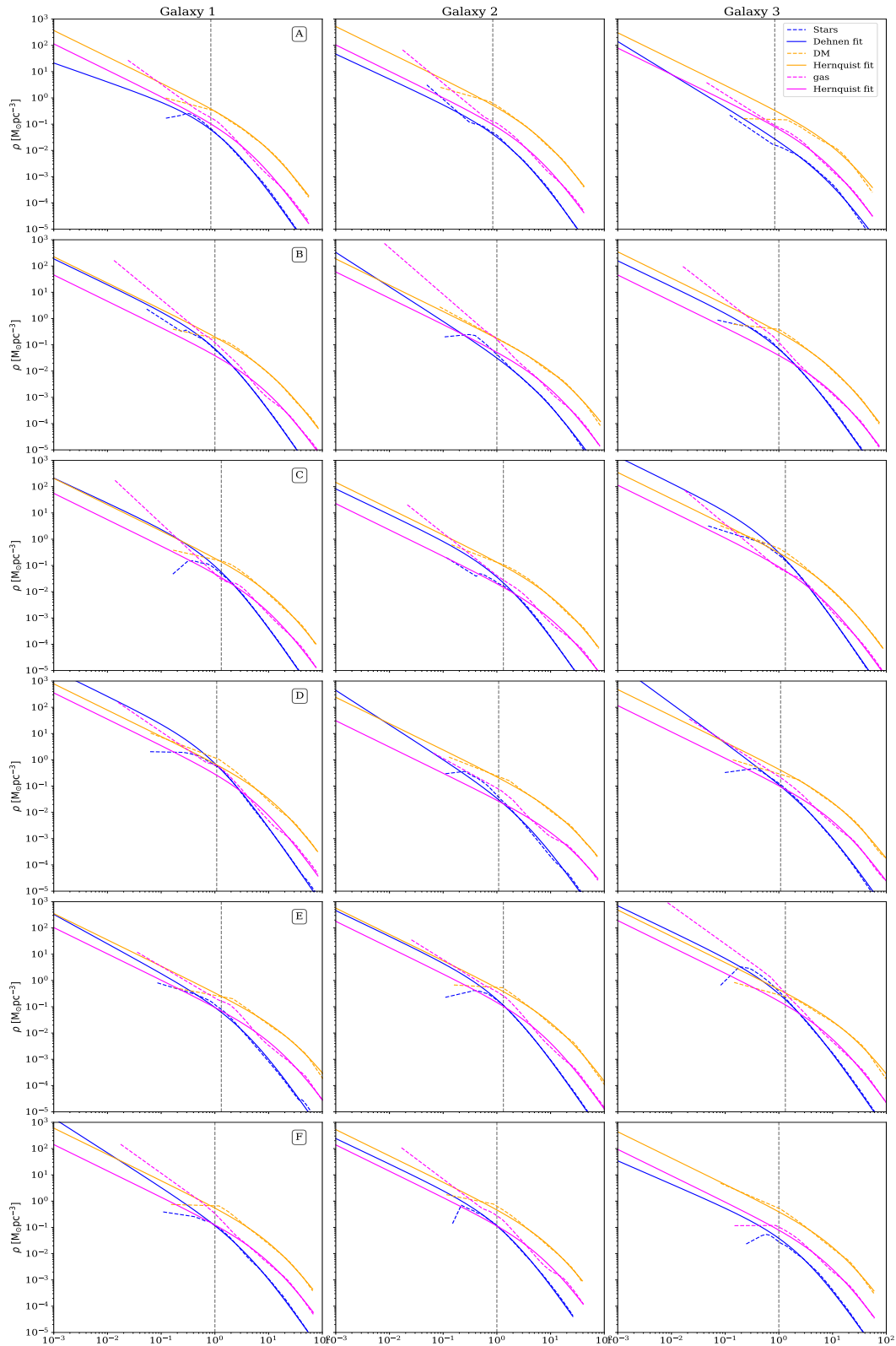


**Figure 8.4:** Radial density profiles (dashed line) with density fits (full line), given for each matter component. The blue, orange and pink lines correspond to stars, dark matter and gas, respectively. The three columns correspond to the three galaxies in each system, while different rows denote the system being plotted, designated in the top right corner of the leftmost plot. The vertical dashed line corresponds to the value of  $r = 4\epsilon$ , and only data with higher radial distances than this value was used for the fitting.

id	$j$	$z_0$	$M_{\text{bh}}$ [ $10^6 M_{\odot}$ ]	$M_{\text{st}}$ [ $10^9 M_{\odot}$ ]	$\gamma_{\text{st}}$	$a_{\text{st}}$ [kpc]	$M_{\text{dm}}$ [ $10^{11} M_{\odot}$ ]	$a_{\text{dm}}$ [kpc]	$M_{\text{g}}$ [ $10^{10} M_{\odot}$ ]	$a_{\text{g}}$ [kpc]
A	1	5.23	1.37	1.54	0.71	1.47	1.98	11.31	1.45	5.5
A	2	5.23	1.31	1.61	0.95	2.36	2.04	9.66	1.71	6.27
A	3	5.23	2.3	6.2	1.25	10.27	5.06	19.99	3.1	9.67
B	1	4.18	1.45	1.71	0.98	1.39	2.27	15.51	2.58	11.6
B	2	4.18	1.55	4.89	1.31	7.52	5.21	25.78	4.59	13.56
B	3	4.18	1.53	1.91	0.98	1.55	2.63	13.46	3.36	13.27
C	1	2.9	1.9	2.15	0.95	1.29	2.97	18.49	3.25	11.81
C	2	2.9	2.13	1.03	0.98	1.58	2.42	19.9	2.71	16.92
C	3	2.9	2.8	4.55	1.00	0.89	2.53	13.18	2.70	7.54
D	1	4.7	1.7	13.32	1.00	1.09	11.17	18.46	10.99	8.6
D	2	4.7	1.29	2.05	1.31	3.82	6.78	25.96	10.56	28.53
D	3	4.7	1.64	8.67	1.49	5.88	11.27	23.82	13.87	16.88
E	1	3.71	1.69	7.81	1.12	3.88	25.41	41.49	17.65	20.17
E	2	3.71	1.35	5.02	0.98	1.49	8.61	19.01	6.43	9.26
E	3	3.71	1.6	9.10	0.98	1.61	20.23	31.64	11.92	12.21
F	1	5.00	1.65	7.91	1.31	4.20	8.91	18.79	11.04	13.60
F	2	5.00	1.62	3.38	0.97	1.63	4.25	13.85	5.04	9.32
F	3	5.00	1.79	2.51	0.89	2.67	5.48	17.32	4.68	10.94

**Table 8.1:** Properties of six triple candidates including the fitted density parameters. The columns represent from left to right: name of the triple system (A-F), index of the galaxy (1 – 3), redshift at which simulations are initialized, black hole mass, total stellar mass, dimensionless Dehnen density parameter of stars, stellar scale radius, total mass of dark matter, scale radius of dark matter, total gas mass and scale radius of the gas distribution.

id	$j$	$N_{tot}$ [ $\times 10^6$ ]	$m_{st}$ [ $M_{\odot}$ ]	$N_{st}$ [ $\times 10^6$ ]	$m_{dm}$ [ $M_{\odot}$ ]	$N_{dm}$ [ $\times 10^6$ ]	$m_g$ [ $M_{\odot}$ ]	$N_g$ [ $\times 10^6$ ]
A	1	7.0105	1030	1.5048	41,200	4.8032	20,600	0.7025
A	2	7.3415	1030	1.5596	41,200	4.9507	20,600	0.8312
A	3	19.809	1030	6.0153	41,200	12.290	20,600	1.5037
B	1	8.4419	1030	1.6613	41,200	5.5283	20,600	1.2623
B	2	19.625	1030	4.7512	41,200	12.645	20,600	2.2287
B	3	9.883	1030	1.8574	41,200	6.3952	20,600	1.6304
C	1	10.867	1030	2.0911	41,200	7.1986	20,600	1.5778
C	2	8.1909	1030	1.0016	41,200	5.8717	20,600	1.3176
C	3	11.865	1030	4.4162	41,200	6.1357	20,600	1.3128
D	1	13.226	2060	6.4680	206,000	5.4233	82,400	1.3343
D	2	5.5686	2060	0.9935	206,000	3.2939	82,400	1.2812
D	3	11.364	2060	4.2079	206,000	5.4721	82,400	1.6839
E	1	18.266	2060	3.7905	206,000	12.334	82,400	2.1417
E	2	7.3996	2060	2.4386	206,000	4.1806	82,400	0.7805
E	3	15.687	2060	4.4170	206,000	9.8231	82,400	1.4471
F	1	9.5089	2060	3.8419	206,000	4.3273	82,400	1.3396
F	2	4.3166	2060	1.6404	206,000	2.0647	82,400	0.6115
F	3	4.4472	2060	1.218	206,000	2.6612	82,400	0.5681

**Table 8.2:** Particle numbers and mass resolution of all matter components for the generated N-body models. The columns correspond, from left to right: id of the triple system (A-F), index of the galaxy (1 – 3), total particle number, stellar particle mass, stellar particle number, dark matter particle mass, dark matter particle number, gas particle mass and gas particle number.

#### 8.4.3 Initialization of N-body runs

Using the fitted parameters, full galaxy models were generated with the publicly available AGAMA software library (Vasiliev, 2019). AGAMA enables construction of equilibrium multi-component galaxy models with a central black hole. Each component was modeled under the assumption of spherical symmetry, using a spherical and isotropic distribution function for the given density profile under the influence of the combined gravitational potential of all of the components. The mass resolution of stars was initially chosen to be  $m_{st} = 1030 M_{\odot}$ , since then each galaxy has at least  $\approx 10^6$  star particles. The values of gas and dark matter particle mass are then  $20m_{st}$  and  $40m_{st}$ , respectively. However, three of the candidate systems (D, E, F) have significantly higher masses and the mass resolution was changed for these three systems in order to reduce the computational burden caused by exceedingly high particle numbers. Therefore, for these three systems the mass of stars was increased to  $m_{st} = 2060 M_{\odot}$  and the gas and dark matter particle mass was  $40m_{st}$  and  $100m_{st}$ , respectively. With this setup, the mass of the most massive matter component (dark matter) is still at least an order of magnitude smaller than the mass of the smallest black hole, in order to avoid strong interactions between the black hole and dark matter particles which could cause non-physical changes in the black hole orbital evolution due to insufficient mass resolution. The particle numbers and particle masses for each system are given in full in Table 8.2.

A black hole particle of appropriate mass was then added at the center of each galaxy and all particles of the galaxy were assigned the initial positions and velocities of the subhalo in the

TNG dataset (parameters 'SubhaloPos' and 'SubhaloVel', respectively). The six triple systems were then simulated with the GPU tree code `bonsai2` (Bédorf et al., 2012a,b) on the JUWELS computer cluster in Jülich. In order to avoid very large box sizes due to few particles at large distances, we performed a radial cut at a distance  $r = 450 \text{ kpc}$  from the center of mass of all particles, disregarding the few particles that were beyond this radius. The same radial cut was applied periodically throughout the runs, since some particles may be ejected to large distances during the galactic mergers. It is important to note that the simulations only take into account stellar dynamics. The code does not feature hydrodynamical treatment of gas, and instead gas was treated as a collisionless component made up of discrete, massive particles, similar to dark matter. Black holes were treated as constant mass particles, since accretion was not taken into account.

One of the most significant numerical parameters in tree codes is the value of the opening angle  $\theta$  that determines whether or not a node in the tree is deemed "far" enough to be opened (see Section 5.1.3). In order to maximize accuracy  $\theta$  was set to  $\theta = 0.5$ . In order to reduce the effect of dark matter and gas on the evolution of the black holes, these particle types were assigned higher softening values, with  $\epsilon_{\text{DM}} = \epsilon_{\text{g}} = 10 \text{ pc}$ . The stellar particles, on the other hand, were assigned a softening of  $\epsilon_{\text{st}} = 0.1 \text{ pc}$ . Black holes were assigned the smallest value of the softening, with  $\epsilon_{\text{BH}} = 10^{-3} \text{ pc}$ . The integration timestep was  $dt = 10^{-2} \text{ Myr}$ . For system C, in parallel, we also ran comparison runs with lower integration timestep  $dt = 10^{-3} \text{ Myr}$ , and different combinations of the softening and the opening angle and we obtained similar results, demonstrating that the choice of these parameters does not affect the result. Due to the large particle number, a significant portion of computational time is dedicated to the reading and writing of the output. For this reason, we limit the snapshot output timestep to every 10 Myr.

## 8.5 RESULTS

The three galaxies in all of the six systems merge within 2 Gyr. On Fig. 8.5 we show the density distribution of stars of system C over time. Within one Gyr the first galactic merger takes place (between galaxies 1 and 2), and the third galaxy comes in for a close approach. Initially both black holes are surrounded by their own stellar cusps, and dynamical friction effects exerted by the background stars, dark matter and gas brings the black holes closer together. During the period of  $1 \text{ Gyr} < t < 2 \text{ Gyr}$ , the stellar cusp around BH2 is steadily stripped away, leaving a "naked", wandering black hole, while BH1 remains at the density center of the galaxy merger remnant. At  $\approx 2 \text{ Gyr}$ , galaxy 3 approaches and the second galactic merger takes place. By  $t = 2.5 \text{ Gyr}$ , the system has settled into a new equilibrium state, with BH3 having replaced BH1 at the density center. None of the black holes have formed binary systems with each other. Instead, BH1 and BH2 are oscillating around the center at  $\sim \text{kpc}$  distances on highly radial, eccentric orbits that cross the density center. This can also be seen on Fig. 8.6, where the trajectories of the black holes over a period of 100 Myr is shown. BH3, positioned at the density center, shows ordered, secular motion while BH1 oscillates around it with an apocenter of  $\approx 2 \text{ kpc}$ . BH2 shows similar behaviour as BH1, but with an apocenter of  $\approx 10 \text{ kpc}$ . Further runs have shown that these oscillations are stable over the next 3 Gyr with no noticeable signs of decreasing amplitude of the oscillations. It is evident that dynamical friction is inefficient and the black hole evolution stalls.

Simulations of the other systems revealed that the case described above is not unique. On Fig. 8.7, we show the separation between the black holes as a function of time, for all six

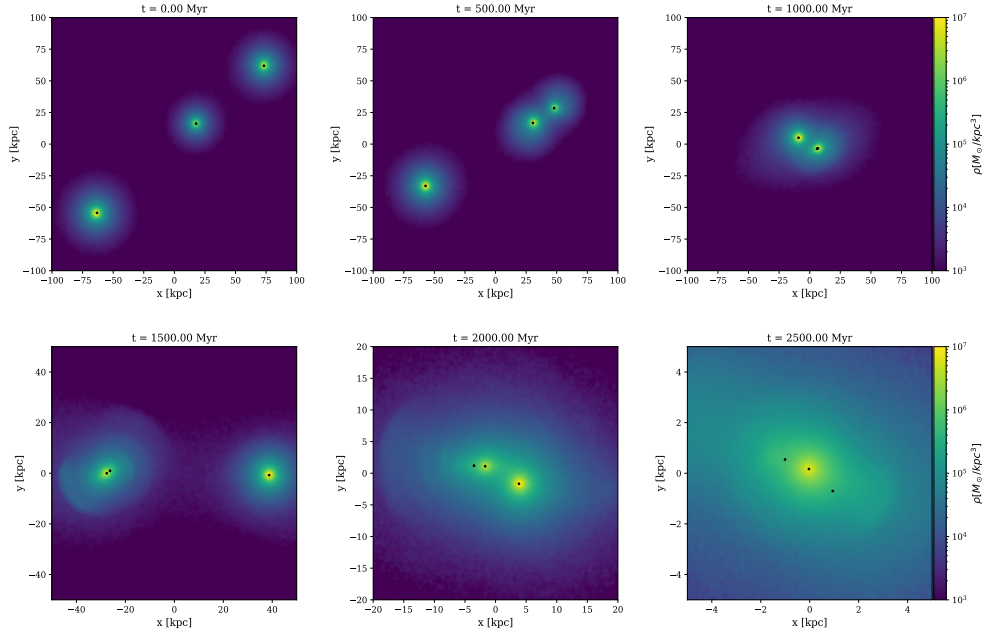


**Figure 8.5:** Density distribution of the stellar component of the triple system C. Panels show the x-y projection of the mass density, averaged over the z-axis. The figures show the density distribution in 500 Myr intervals. The black holes are denoted by black circles. Note the changed axis limits in the bottom three plots.

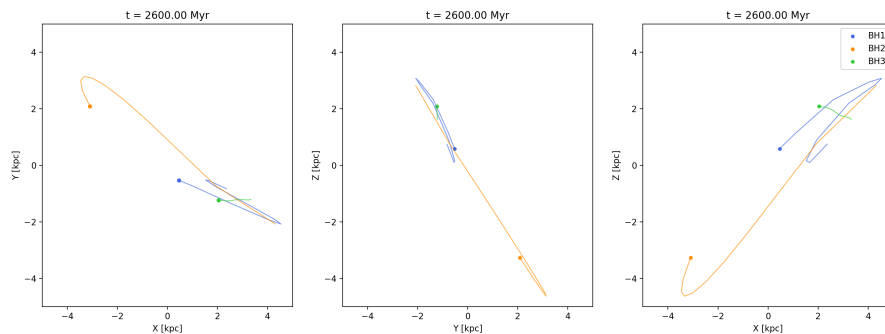


**Figure 8.6:** Spatial distribution of the three black holes at  $t = 2.6$  Gyr of system C, in the center of mass reference frame of the three black holes. The positions of the black holes are designed by the different colored points. The lines behind the points show the positions of the black holes during the last 100 Myr.

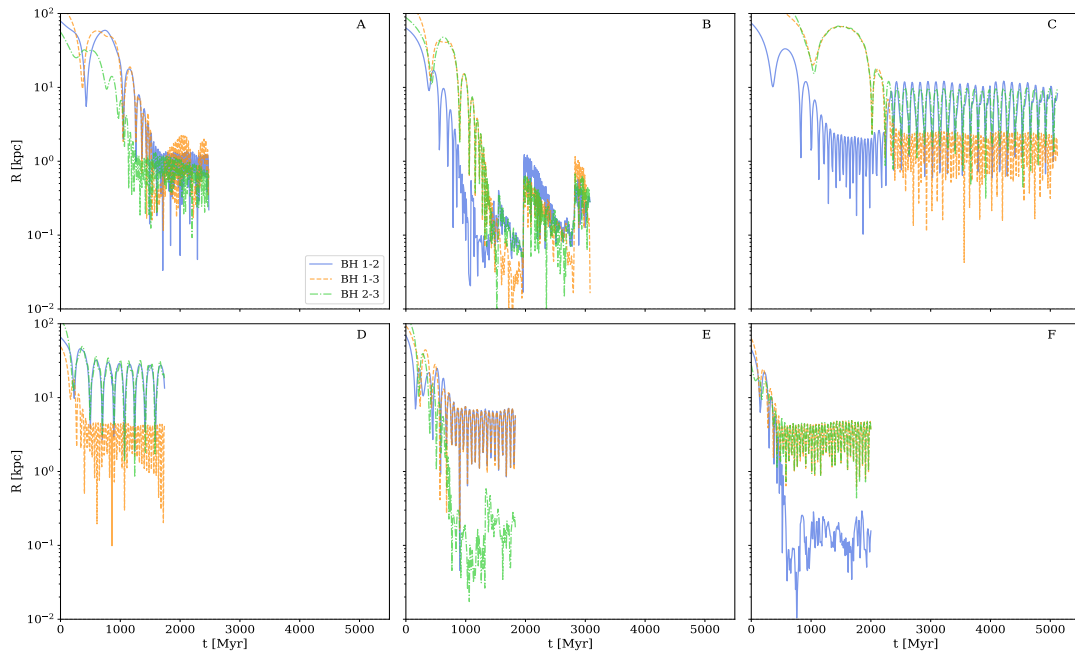


**Figure 8.7:** Relative separation of black holes as a function of time. Each plot corresponds to one system, designated by the system identifier (A-E). For each system the relative separation between each of the black holes is shown by different line styles and colors.

systems. System C was studied most extensively, while the other simulations were performed up to  $\approx 2$  Gyr due to computational time constraints. Almost all systems show similar behavior, with at least one of the black holes stalling at  $\sim$  kpc scales. Systems C, D, E and F show similar evolution, where a stable, hierarchical configuration of the black holes is formed. This configuration is designated with an outer black hole on a radial orbit with apocenter of  $\sim 10$  kpc from the density center, while another, inner black hole oscillates with higher frequency with apocenter of  $\sim 1$  kpc (in the case of systems C and D), or an apocenter of  $\sim 0.1$  kpc (in the case of systems E and F). Due to the large speed of the black holes when crossing the density center, their pericenter approach is unresolved. Looking at system A, after the second galactic merger, the three black holes form a chaotic triple system, with BH2 (the least massive black hole) at the center, while the other two black holes oscillate at similar separation from BH2. Dynamical friction is significantly more effective in system B. This is the only case where a stable SMBH binary is formed with a lifetime of more than 100 Myr (between black holes BH 1-3 at  $t \approx 1700$  Myr). However, after only a few hundred Myr, the close presence of BH2 disrupts the binary, and both black holes BH2 and BH3 are ejected out to  $\sim$  kpc separations at  $t \approx 2000$  Myr, forming a chaotic triple system, similar to system A.

In order to ensure that the observed black hole stalling is physical and not originating from numerical issues, our collaborator Peter Berczik performed a comparison run of system C with the tree code *ber-gal0* (Zinchenko et al., 2015). The code uses leap-frog integration with expansion for force computation up to monopole order. The same value of the opening angle was used ( $\theta = 0.5$ ), with global softening of  $\epsilon = 1$  pc and integration timestep of  $dt \approx 7.8 \times 10^{-2}$  Myr. Only galaxies 1 and 2 were used in the comparison run, in order to reduce the particle number to  $N \sim 15 \times 10^6$ . Additionally, we performed higher-resolution comparison runs of systems A, B and C using the direct  $\phi$ -GPU code (Berczik et al., 2011) with an individual block-timestep

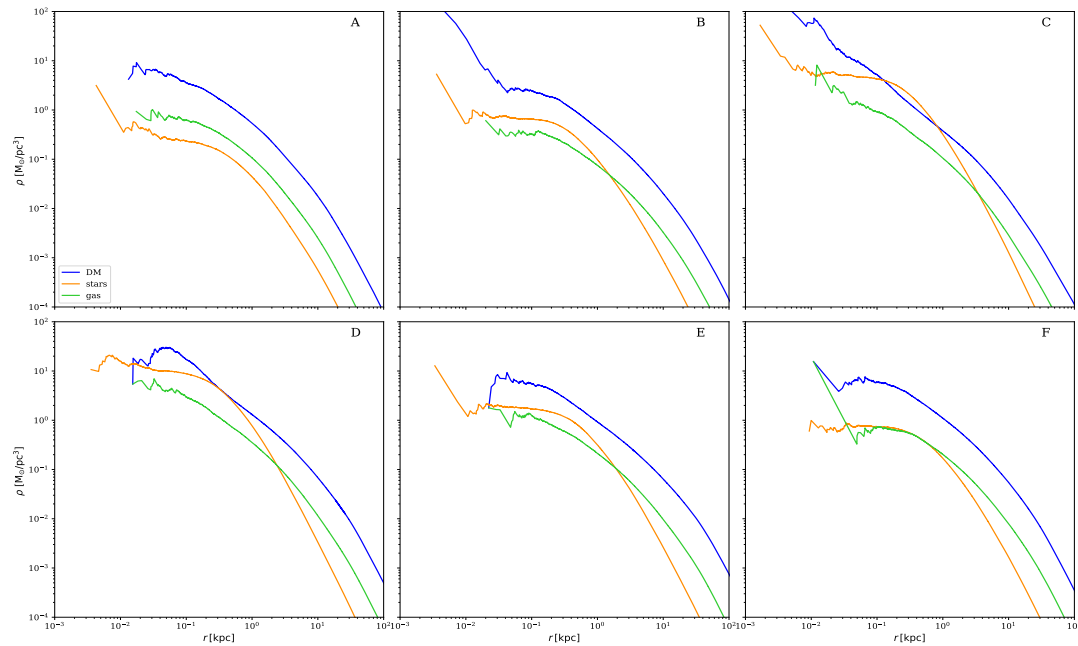


**Figure 8.8:** Radial density profiles of all six systems at the end of their respective simulation runs. Different colors correspond to different matter components. The profiles are centered on the stellar density center of the system.

scheme. The  $\varphi$ -GPU runs were initialized after the merger of all three stellar cusps, and a radial particle cut at  $r = 10\text{kpc}$  was performed in order to reduce the particle number to  $N \sim 7 \times 10^6$ , since the code does not support significantly larger particle numbers.

One possible effect that can impact the results is the fact that the masses of the black holes used in the simulations are smaller than the black hole masses in IllustrisTNG at the time of the black hole mergers. This is because we do not take into account the black hole mass growth during the period between data extraction and at the time the black hole mergers take place in TNG. For this reason, we perform comparison runs of systems D, E and F with increased masses of the black holes, taken as the masses at the time of the mergers in IllustrisTNG. All of the above described comparison runs showed very similar results to the main runs obtained with `bonsai2`, confirming that the results are not affected by the choice of the code, the choice of numerical parameters or lack of treatment of black hole growth.

Chandrasekhar’s well known formula for dynamical friction describes the force exerted on a massive body (in this case a black hole) embedded in a homogenous background density field  $\rho$  consisting of particles with isotropic velocities (Binney and Tremaine, 1987):

$$\dot{V}_{df} = \frac{-4\pi G^2 \rho M_{BH}}{V_{BH}^2} \xi \ln \Lambda, \quad (8.8)$$

where  $\ln \Lambda$  is the Coulomb logarithm,  $M_{BH}$  and  $V_{BH}$  are the black hole mass and velocity and  $\xi$  is the fraction of particles with velocities smaller than the black hole. We can then estimate the

dynamical friction inspiral timescale, based on Chandrasekhar’s description:

$$t_{df} = -\frac{V_{BH}^3}{4\pi G^2 \rho M_{BH} \xi \ln \Lambda}. \quad (8.9)$$

Following [Just et al. \(2011\)](#), we estimate the Coulumb logarithm as:

$$\ln \Lambda = \ln \left( \frac{b_{max}}{b_{min}} \right), \quad (8.10)$$

where  $b_{max}$  is the maximum impact parameter, taken as the amplitude of the black hole oscillations and  $b_{min}$  is the minimum impact parameter, determined by the largest value of the gravitational softening  $b_{min} = 1.5\epsilon_{DM}$ . Assuming  $\xi = 0.3$ , we find that the dynamical friction timescale is  $t_{df} \approx 1$  Gyr. However, our results show that the actual black hole energy losses due to dynamical friction are much smaller than predictions of Chandrasekhar’s formula. While this is present to a degree in every system, this is most noticeable in system C.

Previous studies have found that in the presence of harmonic, constant density galaxy cores, dynamical friction becomes ineffective (or even completely absent), leading to stalled black holes at distances comparable with the core radius ([Read et al., 2006](#); [Gualandris and Merritt, 2008](#); [Antonini and Merritt, 2012](#)). We therefore determine the stellar density center of each system, and then calculate the radial density profiles of each matter component at the end of the simulation run of each system, given on [Fig. 8.8](#). The figure shows that, throughout the runs, all of the systems develop largely constant stellar density cores, in agreement with the above mentioned studies. Our results match particularly well with the findings of [Gualandris and Merritt \(2008\)](#), who examine the infall of recoiled black holes in galaxy centers and find damped oscillations of the SMBH with respect to the density center, leading to infall timescales much longer than those predicted by Chandrasekhar’s description. However, unlike in that study, we find that the oscillations are undamped over timescales of  $\sim$  Gyr, with no signs of decreasing amplitude.

## 8.6 DISCUSSION

We now discuss several possible explanations for the black hole stalling we find in all of our simulated systems. We estimate that likely a combination of below described effects have contributed to the observed black hole stalling.

1. **Radial orbits:** All of our simulated systems result in black holes on radial, highly eccentric orbits. The value of the Coulumb logarithm for radial orbits is considerably smaller than for circular or slightly eccentric orbits ([Gualandris and Merritt, 2008](#)). As the massive body moves through the background density, it deflects particles in its path, forming a trailing overdensity of particles behind it, called the gravitational wake. The gravitational wake then exerts a drag force on the massive body, in the direction opposite to its movement. For bodies on circular orbits, the gravitational wake is formed on a timescale compared to a galaxy crossing time. However, massive bodies on highly radial orbits experience large changes in its velocity over a single orbital period, preventing the formation of a stable gravitational wake that would exert a drag force on the massive body over multiple passages.
2. **Constant stellar density cores:** Harmonic, constant density cores have been shown to

result in little or none at all energy loss due to dynamical friction. This happens since in the special case of these harmonic potentials, particles move on epicycles around the infalling massive body, resulting in a stable configuration (Read et al., 2006). Our results have shown that throughout the run, after the merger of the individual stellar cusps, all systems form constant density stellar cores, leading to stalling of the black holes at separations comparable to the radius of the core. While it is not clear exactly why these constant density cores form in all of our systems, our comparison runs using both other tree and direct N-body codes rule out the possibility of contamination of the results due to numerical issues.

3. **Gas as a collisionless component:** The largest caveat of our method is the lack of proper treatment of collisional phenomena such as star formation, accretion and feedback. In particular, our treatment of gas as a collisionless, purely dynamical galaxy component undoubtedly plays a role in the observed stalling of the black holes. The undamped oscillations of the black holes start only after the stellar cusp around the black hole is completely stripped away by tidal forces. In reality, during the merger gas would be funneled towards the center of the infalling galaxies, causing strong bursts of star formation that would increase the central stellar density, allowing the stellar cusp to resist tidal effects. If the black hole is surrounded by its own stellar cusp, the effect of dynamical friction is much stronger (by a factor 2 – 3), since the background particles see the stellar cusp and its black hole as a single, effective mass that spirals towards the center. With the premature tidal stripping of the cusp due to the lack of star formation, the effect of dynamical friction on the "naked" black hole becomes negligible and the black hole is left wandering at separations comparable to the core radius with inspiral timescales on the order of a Hubble time. For this reason, gas is considered a key component that is responsible for pairing the black holes in gas-rich galaxy mergers (Callegari et al., 2009, 2011; Khan et al., 2012a).
4. **Wandering black hole populations:** Recent studies of galactic mergers in cosmological simulations and observations have suggested that the number of wandering black holes originating from failed SMBH binary pairing or gravitational wave recoil events may be significantly higher than previously thought. Kelley et al. (2017a) characterized SMBH mergers in the entire original Illustris simulation box and found that 65% of all systems resulted in stalled black holes, at separations of  $r \geq 100$  pc. Additionally, Kulier et al. (2015) used a host of cosmological simulations and found that in cluster environments, 40% of black holes are left wandering at kiloparsec separations, approximately 2 black holes per massive galaxy. Furthermore, Ricarte et al., (2021) estimated the population of wandering black holes in the Romulus cosmological simulation and found that halos of Milky Way-mass should contain as many as ten wandering SMBHs at  $z_0$ , and conclude that the wandering black hole population may even dominate AGN emission at higher redshifts. The high fraction of wandering black holes in cosmological simulations could be the consequence of insufficient resolution, raising doubt about the use of cosmological simulation data (including zoom-in simulations) for the study of black hole dynamics (Tamfal et al., 2018). On the other hand, McWilliams et al. (2014) used observational data of massive galactic mergers to construct models on the fate of their central black holes. They found an unexpected increase in the number of wandering black holes that were unable to reach the center due to dynamical friction. If the higher fraction of stalled SMBH mergers is physical, wandering black holes would constitute a sizable fraction of

the whole SMBH population. These wandering black holes could explain the detections of offset AGN systems (Blecha et al., 2011; Barrows et al., 2016; Blecha et al., 2019). Additionally, they could be detected as progenitors of ultra-luminous X-ray sources (Islam et al., 2004).

## 8.7 SUMMARY AND CONCLUSIONS

In this chapter, we used the IllustrisTNG-100-1 cosmological simulation to identify possible SMBH triple systems and investigated their evolution. We found in total twenty SMBH triple candidates, and selected six for further simulations. Using the density profiles from the cosmological simulation, we then constructed spherical multi-component galaxy models using the AGAMA software library, and performed N-body simulations of the triple galactic mergers using the bonsai2 GPU tree code, with particle numbers  $N \sim 30 \times 10^6$  per system. We now summarize our main findings:

- We found that in all of the simulated systems, dynamical friction is unable to efficiently reduce the energy of the black holes and no stable Keplerian binary systems are formed between the black holes. In the one example where dynamical friction does manage to form a binary SMBH system, this system is short-lived and disrupted by the third black hole, resulting in the formation of chaotic triple system with kpc separations.
- Initially during the galactic mergers, the black hole evolution follows the behaviour expected by Chandrasekhar’s prescription of dynamical friction as the black holes spiral towards the center. The stellar cusps surrounding the black holes are gradually stripped away by tidal forces, leaving naked black holes wandering at 100 pc or kpc scales on radial, highly eccentric orbits. After this point, dynamical friction effects become negligible and the black holes demonstrate long-term, stable oscillations around the density center of the system.
- The galactic mergers result in the formation of harmonic galactic cores with constant stellar density. In this special configuration, there is effectively no momentum transfer between the black hole and the background particles causing dynamical friction to cease.
- Our results show that in galaxies with non-negligible gas mass, purely dynamical effects are unable to successfully pair massive black holes, even in the case of SMBH triplets. The high-resolution of our runs makes effects due to insufficient resolution unlikely to explain the SMBH stalling that we observe. Effects like star formation and black hole growth, which are not included in this study, could significantly boost the impact of dynamical friction on the black holes. This points to the fact that proper treatment of gas is a crucial step that could allow for efficient black hole pairing in these systems and possibly, their later coalescence. The observed black hole stalling is in agreement with previous work that found high fractions of wandering and stalled black holes in full cosmological simulation datasets (Kulier et al., 2015; Kelley et al., 2017a; Ricarte et al., 2021).

---

## SUMMARY AND FUTURE OUTLOOK

---

### 9.1 SUMMARY

In this thesis, I have used  $N$ -body simulations as a means of investigating the dynamical evolution of supermassive black holes in merging galaxies. In this chapter, I will summarize and discuss the main findings of the study, and consider future prospects for further research.

In Ch. 5, I presented the results of a testing and benchmarking procedure of the new  $N$ -body code  $\varphi$ -GRAPE-hybrid. The code utilizes the SCF method for force calculation for the majority of particles, while retaining the accuracy of direct  $N$ -body for a chosen subset of particles. This feature makes the code a good choice for the study of massive black hole binaries in galactic environments since it enables direct integration of stars that are driven to the binary vicinity by gravitational torques while avoiding spurious relaxation effects due to insufficient resolution and greatly reducing computational cost. The tests were performed using idealized, spherical Plummer stellar distributions, as well as using initial conditions of a triaxial, rotating system that hosts an SMBH binary, obtained from a previous study (Kh16). While the final benchmarking of the code is still in progress at the time of writing, I have presented preliminary results of the effect of numerical parameters on the performance and accuracy of the calculations. The fraction of particles treated with the direct approach has the highest impact on the performance. Nevertheless, even if this fraction is 50%, the code boasts a speedup over the speedup pure direct  $N$ -body version of a factor of 2.5. However, in order to maximize efficiency, the fraction of direct-only particles should be kept below 10%.

In the case of the system from Kh16, convergence tests of the gravitational softening parameter have shown that a value of the softening of  $\epsilon \sim 10^{-4}$  pc for star-black hole interactions is necessary to properly resolve all of the energetic interactions and obtain the appropriate hardening rate of the binary. This value is two orders of magnitude smaller than the binary semi-major axis in the GW dominated regime. The black hole minimum integration timestep was shown to be a significant numerical parameter that can cause a premature PN plunge of the black holes if chosen improperly. This can lead to an underestimation of the SMBH merger timescales, and it was shown that the merger timescale of the system in Kh16 is a factor of two longer than previously reported. Finally, I have shown how an improper centering strategy can lead to non-physical results and artificial jumps in the binary hardening rate. For this reason,

$\varphi$ -GRAPE-hybrid should only be used in systems with well-defined density centers, and is not suitable for simulations of rapidly changing environments, such as galactic mergers.

I then present the results of a series of three-body scattering experiments, simulating close interactions between stars and a hard SMBH binary. The simulations used the highly accurate AR-chain code (Mikkola and Merritt, 2006, 2008) in order to study energy exchange during a single interaction. The initial conditions for the SMBH binary was taken from the Kh16 data, while the stellar particle positions were generated uniformly on a spherical shell of radius 100pc around the binary. The initial stellar velocities were chosen in such a way so that we ensure close approaches of the stars to the binary, with the two-body Keplerian pericenter of the orbits satisfying  $r_p \leq 2a_0$ , where  $a_0$  is the initial binary semi-major axis. Previous work found a discrepancy between the energy change of the binary and the interacting stars (Ikape, 2016) before and after the interactions. Investigation of the energy balance after each interaction shows that Post-Newtonian corrections (at least up to PN1 order) to the SMBH binary orbital energy need to be taken into account, even in the regime where GW emission is sub-dominant to stellar hardening. Omitting the PN1 correction results in an energy discrepancy comparable to the other energy changes of the system and can lead to a significant mismatch between the total energy changes of interacting stars and the SMBH binary in full  $N$ -body studies.

The full  $N$ -body resimulation of this system is then performed in Ch. 7 using the  $\varphi$ -GRAPE-hybrid. Unlike the original study, this work focused on exploring in detail the properties of loss cone stars that interact and extract energy from the binary. The particle number was kept the same as in Kh16, but only 3% of particles were treated in a direct way, while the force from the remaining particles was calculated using the SCF method. This selection was performed based on two-body Keplerian pericenter distance of the stars at the start of the run. Stars that interact strongly with the binary were identified by monitoring each time a star enters and exits a sphere of radius  $10a_{bh}$  around the black holes, where  $a_{bh}$  corresponds to the time-dependent binary semi-major axis. I first investigated the properties of the system and found that it is slightly triaxial at all times throughout the run. The observed flattening of the system was partly supported by rotation around the minor axis, and partly by significant velocity anisotropy throughout the inner region.

Monitoring individual interactions with the binary, I identified the high-energy tail of stars that experience significant energy changes after their encounter with the binary, with  $\Delta E_*/m_* > (628.3)^2 km^2 s^{-2}$ . A total of 13,383 of these strong interactions were identified. I found that the summed energy changes of these stars match exceedingly well with the overall binary energy changes throughout the run. This result demonstrates that stellar interactions are the primary driver of binary hardening in triaxial, gas-poor systems and all other possible hardening mechanisms are negligible. Therefore, in gas-poor systems, proper treatment of stellar scattering is sufficient to accurately characterize SMBH binary evolution. Three distinct populations of stellar interactions were identified, based on their initial and final apocenter distance. The first population consists of stars that were originally in the vicinity of the SMBH binary, and interact with it as a consequence of Brownian motion of the binary around the center of the system. Populations two and three, on the other hand, consist of stars on centrophilic orbits that are responsible for repopulating the loss cone. Investigation of their angular momentum changes throughout the run demonstrates that the vast majority of these stars can only originate in a triaxial potential, cementing the fact that triaxial systems provide a natural solution to the FPP. Finally, I find that the majority of interacting stars show prograde rotation with respect to the binary. Nevertheless, retrograde interactions, while smaller in number are more energetic

and constitute  $\approx 45\%$  of the overall energy exchange. The most energetic interactions result in a sign-flip change in the angular momentum of the star, showing prograde rotation after the energetic interaction.

Finally, in Ch. 8, I investigate the dynamical evolution of massive black hole triplets using initial conditions from the IllustrisTNG-100-1 cosmological simulation. I identify 20 possible SMBH triple systems in the IllustrisTNG-100-1 cosmological volume and select 6 systems for higher-resolution simulations of the triple galactic mergers with the `bonsai2` (Bédorf et al., 2012a,a) tree GPU code. Using density profiles from the cosmological simulation as a starting point, I construct multi-component, spherical galaxy models using the AGAMA software library (Vasiliev, 2019). Due to lack of treatment of hydrodynamics in the simulations, gas is treated as a collisionless, purely dynamical component, similar to dark matter. In all of the six systems, dynamical friction effects are unable to pair the black holes, and no stable binary systems are formed. Most of the systems form a stable, hierarchical configuration, with an outer black hole at kpc separations, and an inner black hole at 100 pc separations, with both showing radial, highly eccentric and oscillatory orbits around the black hole situated at the density center. Investigation of the density profiles shows that after the initial phase of efficient dynamical friction, the stellar cusps around the black holes are stripped away, greatly reducing the effect of dynamical friction and causing the stalling. In all of the cases, the galaxy merger remnant forms a harmonic stellar core, characterized by constant density. This special configuration results in particles that move on epicyclic orbits around the black holes, further diminishing the effect of dynamical friction on the black holes. The results indicate that in systems with non-negligible gas mass, stellar dynamical effects are insufficient to efficiently pair black hole binaries, even in the case of triplets. As a result, proper treatment of gas and its effects such as star formation and black hole growth seem to be a crucial component that could lead to efficient pairing of these systems.

## 9.2 FUTURE OUTLOOK

The projects presented in this thesis leave ample room for new directions in future research. In Ch. 7 it was shown that a significant fraction of stars experiencing energetic interactions with the SMBH binary originate from the stellar, rotating cusp in the vicinity of the black holes (Population I). As the black holes move around the center in a random walk as a consequence of Brownian motion, the stars in the inner-most region are disrupted from their orbits and interact with the binary, repopulating the loss cone. Brownian motion of the binary as a possible solution to the FPP has already been suggested by previous studies (Quinlan and Hernquist, 1997; Chatterjee et al., 2003). However, Bortolas et al. (2016) reported that in simulations with particle number  $N \geq 10^6$ , the contribution of Brownian motion to the binary hardening is negligible and can be discarded as a possible loss cone-refilling mechanism. This is in disagreement with the results presented in this thesis, possibly due to insufficient spatial resolution of that study. As was shown in Ch. 5, a value of the softening  $\epsilon = 2 \times 10^{-4}$  pc should be employed in order to properly resolve all of the energetic stellar interactions. Our unique ability to identify exact stars which contribute to the binary hardening has shown that  $\approx 25\%$  of the binary hardening in our system is a consequence of the binary Brownian motion. While this fraction is sub-dominant with respect to collisionless loss cone refilling originating from the non-sphericity of the system, it is certainly not negligible. This is especially relevant for simulations of highly-rotating systems, since Khan et al. (2020) reported that in these cases, the center of mass orbit of the binary expands to radii comparable to the binary influence radius, suggesting an even higher effect of Brownian motion in these cases. Therefore, further work is needed to estimate the effect of

Brownian motion-induced hardening in systems with considerable rotation.

In Ch. 8, it was shown that all six simulated SMBH triple systems show a degree of stalling of the black holes in the pairing phase and no stable binary systems were formed. While there is evidence to suggest that wandering black holes as a result of stalled evolution might be more common in cosmological simulations than previously thought (Kulier et al., 2015; Kelley et al., 2017a), it is not clear whether the stalling of systems in Ch. 8 is physical due to our lack of treatment of appropriate gas physics. As discussed in that chapter, gas can play an important role in pairing of massive black holes due to enhanced star formation during galactic mergers, which can increase central stellar densities around the black holes during the inspiral and thereby boosting the effects of dynamical friction on the black holes. For this reason, future simulations that incorporate these effects are needed for these systems in order to accurately investigate their evolution and prospects for coalescence. Purely dynamical codes, such as the ones employed in this thesis, are insufficient for this purpose, and instead codes utilizing smooth particle hydrodynamics (SPH) should be used, such as GADGET-4 (Springel et al., 2020), ChaNGaSPH (Menon et al., 2015) or GASOLINE (Wadsley et al., 2004).

The Post-Newtonian treatment in N-body approaches of massive binaries was so far limited to two-body Post-Newtonian corrections in the equations of motion. However the recent appearance of 3-body Post-Newtonian integrators (Bonetti et al., 2018) has made N-body investigations of fully Post-Newtonian corrected hierarchical SMBH triplets possible. This allows for galactic-scale simulations of SMBH triple systems that take into account the effect of the cosmological environment and that follow the entire evolution of the triplet from the galactic mergers down to GW-dominated scales in a fully consistent way. Additionally, the inclusion of three-body PN treatment would allow for the exploration of relativistic loss cone effects (Stone et al., 2020) between a star and an SMBH binary, an aspect that has been largely unexplored due to the limitation of two-body PN treatment.

Additionally, one important aspect that was omitted from this thesis was the consideration of black hole spins. With the numerous recent detections of black hole binaries by LIGO/Virgo, constraints on the spin parameter of a stellar mass black hole are now better than ever before. However, the same cannot be said for massive black holes, whose spin parameters remain largely unconstrained (Reynolds, 2020). While cosmological simulations have shown the expected evolution of SMBH spins (Bustamante and Springel, 2019) and how it can affect binary coalescence timescales (Sayeb et al., 2021), it is still not clear how individual stellar scatterings in a realistic galactic environment could affect the spin, both in the Newtonian as well as the Post-Newtonian regime, when spin-spin and spin-orbit interactions play a role. Since black hole spins can significantly influence the nature of the emitted GW signal, its proper treatment in future N-body simulations is of paramount importance.

---

## ACKNOWLEDGEMENTS

---

First and foremost, I would like to thank my supervisor and mentor, apl. Prof. Dr. Andreas Just for his support and guidance that made this thesis possible. I am particularly thankful to him for giving me the opportunity to work in this field and for always being available for discussions that contributed significantly to my understanding of the field. I am also thankful for his experienced leadership, which provided crucial direction and helpful feedback, while also enabling me to pursue and develop independent ideas and results, at the same time.

I would also like to acknowledge Dr. Peter Berczik, my closest collaborator, and in many ways, my second supervisor. Much of the computational knowledge I obtained during my studies is thanks to him. I thank him for his patience and willingness to teach me all about numerical simulations and high-performance computing. Our many morning coffee meetings gave me valuable experience and the confidence to freely ask questions on scientific topics.

I would like to warmly acknowledge the support of the International Max Planck Research School for Astronomy and Cosmic Physics at the University of Heidelberg (IMPRS-HD) for organizing my graduate study programme and funding my attendance of schools and conferences. In particular, I would like to thank Christian Fendt, for his support, guidance and advice during my thesis committee meetings. I would also like to acknowledge Rainer Spurzem for his advice during my thesis committee meetings and ARI seminars, as well as for granting me access to the computational resources of the "chhd28" project on the JUWELS computer cluster. I thank Ralf Klessen, for agreeing to referee this thesis, and Björn Malte Schöfer and Sabine Reffert for joining my examination committee.

I would like to thank my collaborators, Manuel Arca Sedda and Yohai Meiron, who were always a pleasure to work with. I am especially thankful to Manuel for numerous discussions and insightful comments on my work and to Yohai for teaching me how to use  $\varphi$ -GRAPE-hybrid, and helping me with numerous numerical issues and problems.

My PhD project was funded by a "Landesgraduiertenstipendium" of the University of Heidelberg. It was also partly funded by the Volkswagen Foundation under the Trilateral Collaboration Scheme (Russia, Ukraine, Germany) project titled ("Accretion Processes in Galactic Nuclei") (funding for personnel and international collaboration exchanges). The Heidelberg Graduate School for Physics receives my gratitude for funding my trips and schools. I also gratefully acknowledge the Gauss Centre for Supercomputing e.V. ([www.gauss-centre.eu](http://www.gauss-centre.eu)) for funding this project by providing computing time through the John von Neumann Institute for Computing (NIC) on the GCS Supercomputer JUWELS at Jülich Supercomputing Centre (JSC) through grants hhd28 and *smbhdynamics*. I acknowledge support by the state of Baden-Württemberg through bwHPC and the grant bw19B001. Part of the research carried out in this thesis was also performed on the Kepler computer cluster in Heidelberg.

A very special acknowledgement goes to those that are closest to me, Marija Harmat, Ana Avramov and Matej Trindić. Their endless encouragement has motivated me to overcome all obstacles and without their support, my successes would not have been possible. Their belief in me was never questioned, and for that they have my sincerest gratitude. For this reason, I dedicate this thesis to them.

I feel very grateful for all of the amazing people I met during my studies, which are too numerous to fit in this paragraph. Matteo, my office mate, thank you for your support, friendship as well as for making our time in the office so fun. I am also thankful for the many other friendships made at the institute, with Bahar, Sebastian, Katja, Bartosz, Kseniia, as well as outside of it, with Giada, Diana, Giulia, Martina, Riccardo(s) and many others. Thank you for all the castle trips, beer festivals, dinner parties and board game evenings. You made these years a truly unforgettable experience. Last but certainly not least, my best friends from back home are always close to me, despite the distance between us. Thank you to Maria, Kristina, Daniel, David and Nebojša for your support and friendship, I miss you very much.

Finally, special thanks goes to Manuel Arca Sedda, Albrecht Kamlah and Matteo Mazzarini for reading and helping me improve this thesis, as well as to Katja Stock for translating the abstract to German.

---

## LIST OF PUBLICATIONS

---

### REFERENCED IN THESIS

- **Avramov, B.**, Arca Sedda, M., Khan, F. M., Berczik, P. & Just, A., Dynamical evolution of massive black hole triplets in IllustrisTNG, *in preparation*.
- Meiron, Y., **Avramov, B.**, Berczik, P. & Spurzem, R.,  $\varphi$ -GRAPE hybrid: A hybrid N-body and self-consistent field approach to galactic dynamics, *in preparation*.
- **Avramov, B.**, Berczik, P., Meiron, Y., Acharya, A. & Just, A., Properties of loss cone stars in a cosmological galaxy merger remnant, 2021, [A&A, 649, A41](#).

### NOT REFERENCED IN THESIS

- Khoperskov, S., Zinchenko, S. , **Avramov, B.**, Khrapov, S., Berczik, P., Saburova, A., Ishchenko, M., Khoperskov, A., Pulsoni, C., Venichenko, Y., Bizyaev, D., Moiseev, A., Extreme kinematic misalignment in IllustrisTNG galaxies: the origin, structure and internal dynamics of galaxies with a large-scale counterrotation, 2021, [MNRAS, 500, 3, pp. 3870-3888](#).
- Mardini, M., Placco, V., Meiron, Y., Ishchenko, M., **Avramov, B.**, Mazzarini, M., Berczik, P., Arca Sedda, M., Beers, T., Frebel, A., Taani, A., Donnari, M., Al-Wardat, M. & G. Zhao, Cosmological Insights into the Early Accretion of r-Process-Enhanced stars. I. A Comprehensive Chemo-dynamical Analysis of LAMOST J1109+0754, 2020, [ApJ, 903, 2, 88, 18](#).

---

## BIBLIOGRAPHY

---

- Aarseth, S. (1963). Dynamical evolution of clusters of galaxies. *MNRAS*, 126:223.
- Aarseth, S. J. (1985). Direct N-body calculations. *IAUS*, 113:251–258.
- Aarseth, S. J. (2003). *Gravitational N-body Simulations*. Cambridge University Press, Cambridge, UK.
- Abbott, B. P., Abbott, R., Abbott, T. D., Abernathy, M. R., Acernese, F., Ackley, K., Adams, C., Adams, T., Addesso, P., Adhikari, R. X., Adya, V. B., Affeldt, C., Agathos, M., Agatsuma, K., Aggarwal, N., Aguiar, O. D., Aiello, L., Ain, A., Ajith, P., Allen, B., Allocca, A., Altin, P. A., Anderson, S. B., Anderson, W. G., Arai, K., Arain, M. A., Araya, M. C., Arceneaux, C. C., Areeda, J. S., Arnaud, N., Arun, K. G., Ascenzi, S., Ashton, G., Ast, M., Aston, S. M., Astone, P., Aufmuth, P., Aulbert, C., Babak, S., Bacon, P., Bader, M. K., Baker, P. T., Baldaccini, F., Ballardín, G., Ballmer, S. W., Barayoga, J. C., Barclay, S. E., Barish, B. C., Barker, D., Barone, F., Barr, B., Barsotti, L., Barsuglia, M., Barta, D., Bartlett, J., Barton, M. A., Bartos, I., Bassiri, R., Basti, A., Batch, J. C., Baune, C., Bavigadda, V., Bazzan, M., Behnke, B., Bejger, M., Belczynski, C., Bell, A. S., Bell, C. J., Berger, B. K., Bergman, J., Bergmann, G., Berry, C. P., Bersanetti, D., Bertolini, A., Betzwieser, J., Bhagwat, S., Bhandare, R., Bilenko, I. A., Billingsley, G., Birch, J., Birney, R., Birnholtz, O., Biscans, S., Bisht, A., Bitossi, M., Biwer, C., Bizouard, M. A., Blackburn, J. K., Blair, C. D., Blair, D. G., Blair, R. M., Bloemen, S., Bock, O., Bodiya, T. P., Boer, M., Bogaert, G., Bogan, C., Bohe, A., Bojtós, P., Bond, C., Bondu, F., Bonnand, R., Boom, B. A., Bork, R., Boschi, V., Bose, S., Bouffanais, Y., Bozzi, A., Bradaschia, C., Brady, P. R., Braginsky, V. B., Branchesi, M., Brau, J. E., Briant, T., Brillet, A., Brinkmann, M., Brisson, V., Brockill, P., Brooks, A. F., Brown, D. A., Brown, D. D., Brown, N. M., Buchanan, C. C., Buikema, A., Bulik, T., Bulten, H. J., Buonanno, A., Buskulic, D., Buy, C., Byer, R. L., Cabero, M., Cadonati, L., Cagnoli, G., Cahillane, C., Bustillo, J. C., Callister, T., Calloni, E., Camp, J. B., Cannon, K. C., Cao, J., Capano, C. D., Capocasa, E., Carbognani, F., Caride, S., Diaz, J. C., Casentini, C., Caudill, S., Cavaglià, M., Cavalier, F., Cavalieri, R., Cella, G., Cepeda, C. B., Baiardi, L. C., Cerretani, G., Cesarini, E., Chakraborty, R., Chalermsoongsak, T., Chamberlin, S. J., Chan, M., Chao, S., Charlton, P., Chassande-Mottin, E., Chen, H. Y., Chen, Y., Cheng, C., Chincarini, A., Chiummo, A., Cho, H. S., Cho, M., Chow, J. H., Christensen, N., Chu, Q., Chua, S., Chung, S., Ciani, G., Clara, F., Clark, J. A., Cleva, F., Coccia, E., Cohadon, P. F., Colla, A., Collette, C. G., Cominsky, L., Constancio, M., Conte, A., Conti, L., Cook, D., Corbitt, T. R., Cornish, N., Corsi, A., Cortese, S., Costa, C. A., Coughlin, M. W., Coughlin, S. B., Coulon, J. P., Countryman, S. T., Couvares, P., Cowan, E. E., Coward, D. M., Cowart, M. J., Coyne, D. C., Coyne, R., Craig, K., Creighton, J. D., Creighton, T. D., Cripe, J., Crowder, S. G., Cruise, A. M., Cumming, A., Cunningham, L., Cuoco, E., Canton, T. D., Danilishin, S. L., D’Antonio, S., Danzmann,

K., Darman, N. S., Da Silva Costa, C. F., Dattilo, V., Dave, I., Daveloza, H. P., Davier, M., Davies, G. S., Daw, E. J., Day, R., De, S., Debra, D., Debreczeni, G., Degallaix, J., De Laurentis, M., Deléglise, S., Del Pozzo, W., Denker, T., Dent, T., Dereli, H., Dergachev, V., Derosa, R. T., De Rosa, R., Desalvo, R., Dhurandhar, S., Díaz, M. C., Di Fiore, L., Di Giovanni, M., Di Lieto, A., Di Pace, S., Di Palma, I., Di Virgilio, A., Dojcinoski, G., Dolique, V., Donovan, F., Dooley, K. L., Doravari, S., Douglas, R., Downes, T. P., Drago, M., Drever, R. W., Driggers, J. C., Du, Z., Ducrot, M., Dwyer, S. E., Edo, T. B., Edwards, M. C., Effler, A., Eggenstein, H. B., Ehrens, P., Eichholz, J., Eikenberry, S. S., Engels, W., Essick, R. C., Etzell, T., Evans, M., Evans, T. M., Everett, R., Factourovich, M., Fafone, V., Fair, H., Fairhurst, S., Fan, X., Fang, Q., Farinon, S., Farr, B., Farr, W. M., Favata, M., Fays, M., Fehrmann, H., Fejer, M. M., Feldbaum, D., Ferrante, I., Ferreira, E. C., Ferrini, F., Fidecaro, F., Finn, L. S., Fiori, I., Fiorucci, D., Fisher, R. P., Flaminio, R., Fletcher, M., Fong, H., Fournier, J. D., Franco, S., Frasca, S., Frasconi, F., Frede, M., Frei, Z., Freise, A., Frey, R., Frey, V., Fricke, T. T., Fritschel, P., Frolov, V. V., Fulda, P., Fyffe, M., Gabbard, H. A., Gair, J. R., Gammaitoni, L., Gaonkar, S. G., Garufi, F., Gatto, A., Gaur, G., Gehrels, N., Gemme, G., Gendre, B., Genin, E., Gennai, A., George, J., Gergely, L., Germain, V., Ghosh, A., Ghosh, A., Ghosh, S., Giaime, J. A., Giardina, K. D., Giazotto, A., Gill, K., Glaefke, A., Gleason, J. R., Goetz, E., Goetz, R., Gondan, L., González, G., Castro, J. M., Gopakumar, A., Gordon, N. A., Gorodetsky, M. L., Gossan, S. E., Gosselin, M., Gouaty, R., Graef, C., Graff, P. B., Granata, M., Grant, A., Gras, S., Gray, C., Greco, G., Green, A. C., Greenhalgh, R. J., Groot, P., Grote, H., Grunewald, S., Guidi, G. M., Guo, X., Gupta, A., Gupta, M. K., Gushwa, K. E., Gustafson, E. K., Gustafson, R., Hacker, J. J., Hall, B. R., Hall, E. D., Hammond, G., Haney, M., Hanke, M. M., Hanks, J., Hanna, C., Hannam, M. D., Hanson, J., Hardwick, T., Harms, J., Harry, G. M., Harry, I. W., Hart, M. J., Hartman, M. T., Haster, C. J., Haughian, K., Healy, J., Heefner, J., Heidmann, A., Heintze, M. C., Heinzl, G., Heitmann, H., Hello, P., Hemming, G., Hendry, M., Heng, I. S., Hennig, J., Heptonstall, A. W., Heurs, M., Hild, S., Hoak, D., Hodge, K. A., Hofman, D., Hollitt, S. E., Holt, K., Holz, D. E., Hopkins, P., Hosken, D. J., Hough, J., Houston, E. A., Howell, E. J., Hu, Y. M., Huang, S., Huerta, E. A., Huet, D., Hughey, B., Husa, S., Huttner, S. H., Huynh-Dinh, T., Idrisy, A., Indik, N., Ingram, D. R., Inta, R., Isa, H. N., Isac, J. M., Isi, M., Islas, G., Isogai, T., Iyer, B. R., Izumi, K., Jacobson, M. B., Jacqmin, T., Jang, H., Jani, K., Jaranowski, P., Jawahar, S., Jiménez-Forteza, F., Johnson, W. W., Johnson-Mcdaniel, N. K., Jones, D. I., Jones, R., Jonker, R. J., Ju, L., Haris, K., Kalaghatgi, C. V., Kalogera, V., Kandhasamy, S., Kang, G., Kanner, J. B., Karki, S., Kasprzack, M., Katsavounidis, E., Katzman, W., Kaufer, S., Kaur, T., Kawabe, K., Kawazoe, F., Kéfélian, F., Kehl, M. S., Keitel, D., Kelley, D. B., Kells, W., Kennedy, R., Keppel, D. G., Key, J. S., Khalaidovski, A., Khalili, F. Y., Khan, I., Khan, S., Khan, Z., Khazanov, E. A., Kijbunchoo, N., Kim, C., Kim, J., Kim, K., Kim, N. G., Kim, N., Kim, Y. M., King, E. J., King, P. J., Kinzel, D. L., Kissel, J. S., Kleybolte, L., Klimentenko, S., Koehlenbeck, S. M., Kokeyama, K., Koley, S., Kondrashov, V., Kontos, A., Koranda, S., Korobko, M., Korth, W. Z., Kowalska, I., Kozak, D. B., Kringel, V., Krishnan, B., Królak, A., Krueger, C., Kuehn, G., Kumar, P., Kumar, R., Kuo, L., Kutynia, A., Kwee, P., Lackey, B. D., Landry, M., Lange, J., Lantz, B., Lasky, P. D., Lazzarini, A., Lazzaro, C., Leaci, P., Leavey, S., Lebigot, E. O., Lee, C. H., Lee, H. K., Lee, H. M., Lee, K., Lenon, A., Leonardi, M., Leong, J. R., Leroy, N., Letendre, N., Levin, Y., Levine, B. M., Li, T. G., Libson, A., Littenberg, T. B., Lockerbie, N. A., Logue, J., Lombardi, A. L., London, L. T., Lord, J. E., Lorenzini, M., Lorette, V., Lormand, M., Losurdo, G., Lough, J. D., Lousto, C. O., Lovelace, G., Lück, H., Lundgren, A. P., Luo, J., Lynch, R., Ma, Y., Macdonald, T., Machenschalk, B., Macinnis, M., Macleod,

D. M., Magaña-Sandoval, F., Magee, R. M., Mageswaran, M., Majorana, E., Maksimovic, I., Malvezzi, V., Man, N., Mandel, I., Mandic, V., Mangano, V., Mansell, G. L., Manske, M., Mantovani, M., Marchesoni, F., Marion, F., Márka, S., Márka, Z., Markosyan, A. S., Maros, E., Martelli, F., Martellini, L., Martin, I. W., Martin, R. M., Martynov, D. V., Marx, J. N., Mason, K., Masserot, A., Massinger, T. J., Masso-Reid, M., Matichard, F., Matone, L., Mavalvala, N., Mazumder, N., Mazzolo, G., McCarthy, R., McClelland, D. E., McCormick, S., McGuire, S. C., McIntyre, G., McIver, J., McManus, D. J., McWilliams, S. T., Meacher, D., Meadors, G. D., Meidam, J., Melatos, A., Mendell, G., Mendoza-Gandara, D., Mercer, R. A., Merilh, E., Merzougui, M., Meshkov, S., Messenger, C., Messick, C., Meyers, P. M., Mezzani, F., Miao, H., Michel, C., Middleton, H., Mikhailov, E. E., Milano, L., Miller, J., Millhouse, M., Minenkov, Y., Ming, J., Mirshekari, S., Mishra, C., Mitra, S., Mitrofanov, V. P., Mitselmakher, G., Mittleman, R., Moggi, A., Mohan, M., Mohapatra, S. R., Montani, M., Moore, B. C., Moore, C. J., Moraru, D., Moreno, G., Morriss, S. R., Mossavi, K., Mours, B., Mow-Lowry, C. M., Mueller, C. L., Mueller, G., Muir, A. W., Mukherjee, A., Mukherjee, D., Mukherjee, S., Mukund, N., Mullavey, A., Munch, J., Murphy, D. J., Murray, P. G., Mytidis, A., Nardecchia, I., Naticchioni, L., Nayak, R. K., Necula, V., Nedkova, K., Nelemans, G., Neri, M., Neunzert, A., Newton, G., Nguyen, T. T., Nielsen, A. B., Nissanke, S., Nitz, A., Nocera, F., Nolting, D., Normandin, M. E., Nuttall, L. K., Oberling, J., Ochsner, E., O'Dell, J., Oelker, E., Ogini, G. H., Oh, J. J., Oh, S. H., Ohme, F., Oliver, M., Oppermann, P., Oram, R. J., O'Reilly, B., O'Shaughnessy, R., Ott, C. D., Ottaway, D. J., Ottens, R. S., Overmier, H., Owen, B. J., Pai, A., Pai, S. A., Palamos, J. R., Palashov, O., Palomba, C., Pal-Singh, A., Pan, H., Pan, Y., Pankow, C., Pannarale, F., Pant, B. C., Paoletti, F., Paoli, A., Papa, M. A., Paris, H. R., Parker, W., Pascucci, D., Pasqualetti, A., Passaquieti, R., Passuello, D., Patricelli, B., Patrick, Z., Pearlstone, B. L., Pedraza, M., Pedurand, R., Pekowsky, L., Pele, A., Penn, S., Perreca, A., Pfeiffer, H. P., Phelps, M., Piccinni, O., Pichot, M., Pickenpack, M., Piergiovanni, F., Pierro, V., Pillant, G., Pinard, L., Pinto, I. M., Pitkin, M., Poeld, J. H., Poggiani, R., Popolizio, P., Post, A., Powell, J., Prasad, J., Predoi, V., Premachandra, S. S., Prestegard, T., Price, L. R., Prijatelj, M., Principe, M., Privitera, S., Prix, R., Prodi, G. A., Prokhorov, L., Puncken, O., Punturo, M., Puppo, P., Pürerer, M., Qi, H., Qin, J., Quetschke, V., Quintero, E. A., Quitzow-James, R., Raab, F. J., Rabeling, D. S., Radkins, H., Raffai, P., Raja, S., Rakhmanov, M., Ramet, C. R., Rapagnani, P., Raymond, V., Razzano, M., Re, V., Read, J., Reed, C. M., Regimbau, T., Rei, L., Reid, S., Reitze, D. H., Rew, H., Reyes, S. D., Ricci, F., Riles, K., Robertson, N. A., Robie, R., Robinet, F., Rocchi, A., Rolland, L., Rollins, J. G., Roma, V. J., Romano, J. D., Romano, R., Romanov, G., Romie, J. H., Rosińska, D., Rowan, S., Rüdiger, A., Ruggi, P., Ryan, K., Sachdev, S., Sadecki, T., Sadeghian, L., Salconi, L., Saleem, M., Salemi, F., Samajdar, A., Sammut, L., Sampson, L. M., Sanchez, E. J., Sandberg, V., Sandeen, B., Sanders, G. H., Sanders, J. R., Sassolas, B., Sathyaprakash, B. S., Saulson, P. R., Sauter, O., Savage, R. L., Sawadsky, A., Schale, P., Schilling, R., Schmidt, J., Schmidt, P., Schnabel, R., Schofield, R. M., Schönbeck, A., Schreiber, E., Schuette, D., Schutz, B. F., Scott, J., Scott, S. M., Sellers, D., Sengupta, A. S., Sentenac, D., Sequino, V., Sergeev, A., Serna, G., Setyawati, Y., Sevigny, A., Shaddock, D. A., Shaffer, T., Shah, S., Shahriar, M. S., Shaltev, M., Shao, Z., Shapiro, B., Shawhan, P., Sheperd, A., Shoemaker, D. H., Shoemaker, D. M., Siellez, K., Siemens, X., Sigg, D., Silva, A. D., Simakov, D., Singer, A., Singer, L. P., Singh, A., Singh, R., Singhal, A., Sintes, A. M., Slagmolen, B. J., Smith, J. R., Smith, M. R., Smith, N. D., Smith, R. J., Son, E. J., Sorazu, B., Sorrentino, F., Souradeep, T., Srivastava, A. K., Staley, A., Steinke, M., Steinlechner, J., Steinlechner, S., Steinmeyer, D., Stephens, B. C., Stevenson, S. P., Stone, R., Strain, K. A., Straniero, N., Stratta, G., Strauss, N. A.,

- Strigin, S., Sturani, R., Stuver, A. L., Summerscales, T. Z., Sun, L., Sutton, P. J., Swinkels, B. L., Szczepańczyk, M. J., Tacca, M., Talukder, D., Tanner, D. B., Tápai, M., Tarabrin, S. P., Taracchini, A., Taylor, R., Theeg, T., Thirugnanasambandam, M. P., Thomas, E. G., Thomas, M., Thomas, P., Thorne, K. A., Thorne, K. S., Thrane, E., Tiwari, S., Tiwari, V., Tokmakov, K. V., Tomlinson, C., Tonelli, M., Torres, C. V., Torrie, C. I., Töyrä, D., Travasso, F., Traylor, G., Trifirò, D., Tringali, M. C., Trozzo, L., Tse, M., Turconi, M., Tuyenbayev, D., Ugolini, D., Unnikrishnan, C. S., Urban, A. L., Usman, S. A., Vahlbruch, H., Vajente, G., Valdes, G., Vallisneri, M., Van Bakel, N., Van Beuzekom, M., Van Den Brand, J. F., Van Den Broeck, C., Vander-Hyde, D. C., Van Der Schaaf, L., Van Heijningen, J. V., Van Veggel, A. A., Vardaro, M., Vass, S., Vasúth, M., Vaulin, R., Vecchio, A., Vedovato, G., Veitch, J., Veitch, P. J., Venkateswara, K., Verkindt, D., Vetrano, F., Viceré, A., Vinciguerra, S., Vine, D. J., Vinet, J. Y., Vitale, S., Vo, T., Vocca, H., Vorvick, C., Voss, D., Vousden, W. D., Vyatchanin, S. P., Wade, A. R., Wade, L. E., Wade, M., Waldman, S. J., Walker, M., Wallace, L., Walsh, S., Wang, G., Wang, H., Wang, M., Wang, X., Wang, Y., Ward, H., Ward, R. L., Warner, J., Was, M., Weaver, B., Wei, L. W., Weinert, M., Weinstein, A. J., Weiss, R., Welborn, T., Wen, L., Weßels, P., Westphal, T., Wette, K., Whelan, J. T., Whitcomb, S. E., White, D. J., Whiting, B. F., Wiesner, K., Wilkinson, C., Willems, P. A., Williams, L., Williams, R. D., Williamson, A. R., Willis, J. L., Willke, B., Wimmer, M. H., Winkelmann, L., Winkler, W., Wipf, C. C., Wiseman, A. G., Wittel, H., Woan, G., Worden, J., Wright, J. L., Wu, G., Yablon, J., Yakushin, I., Yam, W., Yamamoto, H., Yancey, C. C., Yap, M. J., Yu, H., Yvert, M., Zadrożny, A., Zangrando, L., Zanolin, M., Zendri, J. P., Zevin, M., Zhang, F., Zhang, L., Zhang, M., Zhang, Y., Zhao, C., Zhou, M., Zhou, Z., Zhu, X. J., Zucker, M. E., Zuraw, S. E., and Zweizig, J. (2016). Observation of gravitational waves from a binary black hole merger. *Phys. Rev. Lett.*, 116(6):061102.
- Abbott, B. P., Abbott, R., Abbott, T. D., Abraham, S., Acernese, F., Ackley, K., Adams, C., Adhikari, R. X., Adya, V. B., Affeldt, C., Agathos, M., Agatsuma, K., Aggarwal, N., Aguiar, O. D., Aiello, L., Ain, A., Ajith, P., Allen, G., Allocca, A., Aloy, M. A., Altin, P. A., Amato, A., Ananyeva, A., Anderson, S. B., Anderson, W. G., Angelova, S. V., Antier, S., Appert, S., Arai, K., Araya, M. C., Areeda, J. S., Arène, M., Arnaud, N., Arun, K. G., Ascenzi, S., Ashton, G., Aston, S. M., Astone, P., Aubin, F., Aufmuth, P., Aultoneal, K., Austin, C., Avendano, V., Avila-Alvarez, A., Babak, S., Bacon, P., Badaracco, F., Bader, M. K., Bae, S., Baker, P. T., Baldaccini, F., Ballardin, G., Ballmer, S. W., Banagiri, S., Barayoga, J. C., Barclay, S. E., Barish, B. C., Barker, D., Barkett, K., Barnum, S., Barone, F., Barr, B., Barsotti, L., Barsuglia, M., Barta, D., Bartlett, J., Bartos, I., Bassiri, R., Basti, A., Bawaj, M., Bayley, J. C., Bazzan, M., Bécsy, B., Bejger, M., Belahcene, I., Bell, A. S., Beniwal, D., Berger, B. K., Bergmann, G., Bernuzzi, S., Bero, J. J., Berry, C. P., Bersanetti, D., Bertolini, A., Betzwieser, J., Bhandare, R., Bidler, J., Bilenko, I. A., Bilgili, S. A., Billingsley, G., Birch, J., Birney, R., Birnholtz, O., Biscans, S., Biscoveanu, S., Bisht, A., Bitossi, M., Bizouard, M. A., Blackburn, J. K., Blackman, J., Blair, C. D., Blair, D. G., Blair, R. M., Bloemen, S., Bode, N., Boer, M., Boetzel, Y., Bogaert, G., Bondu, F., Bonilla, E., Bonnand, R., Booker, P., Boom, B. A., Booth, C. D., Bork, R., Boschi, V., Bose, S., Bossie, K., Bossilkov, V., Bosveld, J., Bouffanais, Y., Bozzi, A., Bradaschia, C., Brady, P. R., Bramley, A., Branchesi, M., Brau, J. E., Briant, T., Briggs, J. H., Brighenti, F., Brilliet, A., Brinkmann, M., Brisson, V., Brockill, P., Brooks, A. F., Brown, D. D., Brunnett, S., Buikema, A., Bulik, T., Bulten, H. J., Buonanno, A., Buskulic, D., Bustamante Rosell, M. J., Buy, C., Byer, R. L., Cabero, M., Cadonati, L., Cagnoli, G., Cahillane, C., Calderón Bustillo, J., Callister, T. A., Calloni, E., Camp, J. B., Campbell, W. A.,

- Canepa, M., Cannon, K. C., Cao, H., Cao, J., Capocasa, E., Carbognani, F., Caride, S., Carney, M. F., Carullo, G., Casanueva Diaz, J., Casentini, C., Caudill, S., Cavaglià, M., Cavalier, F., Cavalieri, R., Cella, G., Cerdá-Durán, P., Cerretani, G., Cesarini, E., Chaibi, O., Chakravarti, K., Chamberlin, S. J., Chan, M., Chao, S., Charlton, P., Chase, E. A., Chassande-Mottin, E., Chatterjee, D., Chaturvedi, M., Chatziioannou, K., Cheeseboro, B. D., Chen, H. Y., Chen, X., Chen, Y., Cheng, H. P., Cheong, C. K., Chia, H. Y., Chincarini, A., Chiummo, A., Cho, G., Cho, H. S., Cho, M., Christensen, N., Chu, Q., Chua, S., Chung, K. W., Chung, S., Ciani, G., Ciobanu, A. A., Ciolfi, R., Cipriano, F., Cirone, A., Clara, F., Clark, J. A., Clearwater, P., Cleva, F., Cocchieri, C., Coccia, E., Cohadon, P. F., Cohen, D., Colgan, R., Colleoni, M., Collette, C. G., Collins, C., Cominsky, L. R., Constancio, M., Conti, L., Cooper, S. J., Corban, P., Corbitt, T. R., Cordero-Carrión, I., Corley, K. R., Cornish, N., Corsi, A., Cortese, S., Costa, C. A., Cotesta, R., Coughlin, M. W., Coughlin, S. B., Coulon, J. P., Countryman, S. T., Couvares, P., Covas, P. B., Cowan, E. E., Coward, D. M., Cowart, M. J., Coyne, D. C., Coyne, R., Creighton, J. D., Creighton, T. D., Cripe, J., Croquette, M., Crowder, S. G., Cullen, T. J., Cumming, A., Cunningham, L., Cuoco, E., Canton, T. D., Dálya, G., Danilishin, S. L., D'Antonio, S., Danzmann, K., Dasgupta, A., Da Silva Costa, C. F., Datrier, L. E., Dattilo, V., Dave, I., Davier, M., Davis, D., Daw, E. J., Debra, D., Deenadayalan, M., Degallaix, J., De Laurentis, M., Deléglise, S., Del Pozzo, W., Demarchi, L. M., Demos, N., Dent, T., De Pietri, R., Derby, J., De Rosa, R., De Rossi, C., Desalvo, R., De Varona, O., Dhurandhar, S., Díaz, M. C., Dietrich, T., Di Fiore, L., Di Giovanni, M., Di Girolamo, T., Di Lieto, A., Ding, B., Di Pace, S., Di Palma, I., Di Renzo, F., Dmitriev, A., Doctor, Z., Donovan, F., Dooley, K. L., Doravari, S., Dorrington, I., Downes, T. P., Drago, M., Driggers, J. C., Du, Z., Ducoin, J. G., Dupej, P., Dwyer, S. E., Easter, P. J., Edo, T. B., Edwards, M. C., Effler, A., Ehrens, P., Eichholz, J., Eikenberry, S. S., Eisenmann, M., Eisenstein, R. A., Essick, R. C., Estelles, H., Estevez, D., Etienne, Z. B., Etzel, T., Evans, M., Evans, T. M., Fafone, V., Fair, H., Fairhurst, S., Fan, X., Farinon, S., Farr, B., Farr, W. M., Fauchon-Jones, E. J., Favata, M., Fays, M., Fazio, M., Fee, C., Feicht, J., Fejer, M. M., Feng, F., Fernandez-Galiana, A., Ferrante, I., Ferreira, E. C., Ferreira, T. A., Ferrini, F., Fidecaro, F., Fiori, I., Fiorucci, D., Fishbach, M., Fisher, R. P., Fishner, J. M., Fitz-Axen, M., Flaminio, R., Fletcher, M., Flynn, E., Fong, H., Font, J. A., Forsyth, P. W., Fournier, J. D., Frasca, S., Frasconi, F., Frei, Z., Freise, A., Frey, R., Frey, V., Fritschel, P., Frolov, V. V., Fulda, P., Fyffe, M., Gabbard, H. A., Gadre, B. U., Gaebel, S. M., Gair, J. R., Gammaitoni, L., Ganija, M. R., Gaonkar, S. G., Garcia, A., García-Quirós, C., Garufi, F., Gateley, B., Gaudio, S., Gaur, G., Gayathri, V., Gemme, G., Genin, E., Gennai, A., George, D., George, J., Gergely, L., Germain, V., Ghonge, S., Ghosh, A., Ghosh, A., Ghosh, S., Giacomazzo, B., Giaime, J. A., Giardino, K. D., Giazotto, A., Gill, K., Giordano, G., Glover, L., Godwin, P., Goetz, E., Goetz, R., Goncharov, B., González, G., Gonzalez Castro, J. M., Gopakumar, A., Gorodetsky, M. L., Gossan, S. E., Gosselin, M., Gouaty, R., Grado, A., Graef, C., Granata, M., Grant, A., Gras, S., Grassia, P., Gray, C., Gray, R., Greco, G., Green, A. C., Green, R., Gretarsson, E. M., Groot, P., Grote, H., Grunewald, S., Gruning, P., Guidi, G. M., Gulati, H. K., Guo, Y., Gupta, A., Gupta, M. K., Gustafson, E. K., Gustafson, R., Haegel, L., Halim, O., Hall, B. R., Hall, E. D., Hamilton, E. Z., Hammond, G., Haney, M., Hanke, M. M., Hanks, J., Hanna, C., Hannam, M. D., Hannuksela, O. A., Hanson, J., Hardwick, T., Haris, K., Harms, J., Harry, G. M., Harry, I. W., Haster, C. J., Haughian, K., Hayes, F. J., Healy, J., Heidmann, A., Heintze, M. C., Heitmann, H., Hello, P., Hemming, G., Hendry, M., Heng, I. S., Hennig, J., Heptonstall, A. W., Hernandez Vivanco, F., Heurs, M., Hild, S., Hinderer, T., Hoak, D., Hochheim, S., Hofman, D., Holgado, A. M., Holland, N. A., Holt, K., Holz, D. E., Hopkins, P., Horst, C., Hough, J., Howell, E. J., Hoy, C. G.,

Hreibi, A., Huang, Y., Huerta, E. A., Huet, D., Hughey, B., Hulko, M., Husa, S., Huttner, S. H., Huynh-Dinh, T., Idzkowski, B., Iess, A., Ingram, C., Inta, R., Intini, G., Irwin, B., Isa, H. N., Isac, J. M., Isi, M., Iyer, B. R., Izumi, K., Jacqmin, T., Jadhav, S. J., Jani, K., Janthapur, N. N., Jaranowski, P., Jenkins, A. C., Jiang, J., Johnson, D. S., Johnson-Mcdaniel, N. K., Jones, A. W., Jones, D. I., Jones, R., Jonker, R. J., Ju, L., Junker, J., Kalaghatgi, C. V., Kalogera, V., Kamai, B., Kandhasamy, S., Kang, G., Kanner, J. B., Kapadia, S. J., Karki, S., Karvinen, K. S., Kashyap, R., Kasprzack, M., Katsanevas, S., Katsavounidis, E., Katzman, W., Kaufer, S., Kawabe, K., Keerthana, N. V., Kéfélian, F., Keitel, D., Kennedy, R., Key, J. S., Khalili, F. Y., Khan, H., Khan, I., Khan, S., Khan, Z., Khazanov, E. A., Khursheed, M., Kijbunchoo, N., Kim, C., Kim, J. C., Kim, K., Kim, W., Kim, W. S., Kim, Y. M., Kimball, C., King, E. J., King, P. J., Kinley-Hanlon, M., Kirchhoff, R., Kissel, J. S., Kleybolte, L., Klika, J. H., Klimenko, S., Knowles, T. D., Koch, P., Koehlenbeck, S. M., Koekoek, G., Koley, S., Kondrashov, V., Kontos, A., Koper, N., Korobko, M., Korth, W. Z., Kowalska, I., Kozak, D. B., Kringel, V., Krishnendu, N., Królak, A., Kuehn, G., Kumar, A., Kumar, P., Kumar, R., Kumar, S., Kuo, L., Kutynia, A., Kwang, S., Lackey, B. D., Lai, K. H., Lam, T. L., Landry, M., Lane, B. B., Lang, R. N., Lange, J., Lantz, B., Lanza, R. K., Lartaux-Vollard, A., Lasky, P. D., Laxen, M., Lazzarini, A., Lazzaro, C., Leaci, P., Leavey, S., Lecoeuche, Y. K., Lee, C. H., Lee, H. K., Lee, H. M., Lee, H. W., Lee, J., Lee, K., Lehmann, J., Lenon, A., Leroy, N., Letendre, N., Levin, Y., Li, J., Li, K. J., Li, T. G., Li, X., Lin, F., Linde, F., Linker, S. D., Littenberg, T. B., Liu, J., Liu, X., Lo, R. K., Lockerbie, N. A., London, L. T., Longo, A., Lorenzini, M., Lorette, V., Lormand, M., Losurdo, G., Lough, J. D., Lousto, C. O., Lovelace, G., Lower, M. E., Lück, H., Lumaca, D., Lundgren, A. P., Lynch, R., Ma, Y., MacAs, R., MacFoy, S., MacInnis, M., MacLeod, D. M., MacQuet, A., Magaña-Sandoval, F., Magaña Zertuche, L., Magee, R. M., Majorana, E., Maksimovic, I., Malik, A., Man, N., Mandic, V., Mangano, V., Mansell, G. L., Manske, M., Mantovani, M., Marchesoni, F., Marion, F., Márka, S., Márka, Z., Markakis, C., Markosyan, A. S., Markowitz, A., Maros, E., Marquina, A., Marsat, S., Martelli, F., Martin, I. W., Martin, R. M., Martynov, D. V., Mason, K., Massera, E., Masserot, A., Massinger, T. J., Masso-Reid, M., Mastrogiovanni, S., Matas, A., Matichard, F., Matone, L., Mavalvala, N., Mazumder, N., McCann, J. J., McCarthy, R., McClelland, D. E., McCormick, S., McCuller, L., McGuire, S. C., McIver, J., McManus, D. J., McRae, T., McWilliams, S. T., Meacher, D., Meadors, G. D., Mehmet, M., Mehta, A. K., Meidam, J., Melatos, A., Mendell, G., Mercer, R. A., Mereni, L., Merilh, E. L., Merzougui, M., Meshkov, S., Messenger, C., Messick, C., Metzdrorf, R., Meyers, P. M., Miao, H., Michel, C., Middleton, H., Mikhailov, E. E., Milano, L., Miller, A. L., Miller, A., Millhouse, M., Mills, J. C., Milovich-Goff, M. C., Minazzoli, O., Minenkov, Y., Mishkin, A., Mishra, C., Mistry, T., Mitra, S., Mitrofanov, V. P., Mitselmakher, G., Mittleman, R., Mo, G., Moffa, D., Mogushi, K., Mohapatra, S. R., Montani, M., Moore, C. J., Moraru, D., Moreno, G., Morisaki, S., Mours, B., Mow-Lowry, C. M., Mukherjee, A., Mukherjee, D., Mukherjee, S., Mukund, N., Mullavey, A., Munch, J., Muñiz, E. A., Muratore, M., Murray, P. G., Nagar, A., Nardecchia, I., Naticchioni, L., Nayak, R. K., Neilson, J., Nelemans, G., Nelson, T. J., Nery, M., Neunzert, A., Ng, K. Y., Ng, S., Nguyen, P., Nichols, D., Nielsen, A. B., Nissanke, S., Nitz, A., Nocera, F., North, C., Nuttall, L. K., Obergaulinger, M., Oberling, J., O'Brien, B. D., O'Dea, G. D., Ogín, G. H., Oh, J. J., Oh, S. H., Ohme, F., Ohta, H., Okada, M. A., Oliver, M., Oppermann, P., Oram, R. J., O'Reilly, B., Ormiston, R. G., Ortega, L. F., O'Shaughnessy, R., Ossokine, S., Ottaway, D. J., Overmier, H., Owen, B. J., Pace, A. E., Pagano, G., Page, M. A., Pai, A., Pai, S. A., Palamos, J. R., Palashov, O., Palomba, C., Pal-Singh, A., Pan, H. W., Pang, B., Pang, P. T., Pankow, C., Pannarale, F., Pant, B. C., Paoletti, F., Paoli, A., Papa, M. A.,

Parida, A., Parker, W., Pascucci, D., Pasqualetti, A., Passaquieti, R., Passuello, D., Patil, M., Patricelli, B., Pearlstone, B. L., Pedersen, C., Pedraza, M., Pedurand, R., Pele, A., Penn, S., Perego, A., Perez, C. J., Perreca, A., Pfeiffer, H. P., Phelps, M., Phukon, K. S., Piccinni, O. J., Pichot, M., Piergiovanni, F., Pillant, G., Pinard, L., Pirello, M., Pitkin, M., Poggiani, R., Pong, D. Y., Ponrathnam, S., Popolizio, P., Porter, E. K., Powell, J., Prajapati, A. K., Prasad, J., Prasai, K., Prasanna, R., Pratten, G., Prestegard, T., Privitera, S., Prodi, G. A., Prokhorov, L. G., Puncken, O., Punturo, M., Puppo, P., Pürner, M., Qi, H., Quetschke, V., Quinonez, P. J., Quintero, E. A., Quitzow-James, R., Raab, F. J., Radkins, H., Radulescu, N., Raffai, P., Raja, S., Rajan, C., Rajbhandari, B., Rakhmanov, M., Ramirez, K. E., Ramos-Buades, A., Rana, J., Rao, K., Rapagnani, P., Raymond, V., Razzano, M., Read, J., Regimbau, T., Rei, L., Reid, S., Reitze, D. H., Ren, W., Ricci, F., Richardson, C. J., Richardson, J. W., Ricker, P. M., Riemenschneider, G. M., Riles, K., Rizzo, M., Robertson, N. A., Robie, R., Robinet, F., Rocchi, A., Rolland, L., Rollins, J. G., Roma, V. J., Romanelli, M., Romano, R., Romel, C. L., Romie, J. H., Rose, K., Rosińska, D., Rosofsky, S. G., Ross, M. P., Rowan, S., Rüdiger, A., Ruggi, P., Rutins, G., Ryan, K., Sachdev, S., Sadecki, T., Sakellariadou, M., Salafia, O., Salconi, L., Saleem, M., Salemi, F., Samajdar, A., Sammut, L., Sanchez, E. J., Sanchez, L. E., Sanchis-Gual, N., Sandberg, V., Sanders, J. R., Santiago, K. A., Sarin, N., Sassolas, B., Sathyaprakash, B. S., Saulson, P. R., Sauter, O., Savage, R. L., Schale, P., Scheel, M., Scheuer, J., Schmidt, P., Schnabel, R., Schofield, R. M., Schönbeck, A., Schreiber, E., Schulte, B. W., Schutz, B. F., Schwalbe, S. G., Scott, J., Scott, S. M., Seidel, E., Sellers, D., Sengupta, A. S., Sennett, N., Sentenac, D., Sequino, V., Sergeev, A., Setyawati, Y., Shaddock, D. A., Shaffer, T., Shahriar, M. S., Shaner, M. B., Shao, L., Sharma, P., Shawhan, P., Shen, H., Shink, R., Shoemaker, D. H., Shoemaker, D. M., Shyamsundar, S., Siellez, K., Sieniawska, M., Sigg, D., Silva, A. D., Singer, L. P., Singh, N., Singhal, A., Sintès, A. M., Sitmukhambetov, S., Skliris, V., Slagmolen, B. J., Slaven-Blair, T. J., Smith, J. R., Smith, R. J., Somala, S., Son, E. J., Sorazu, B., Sorrentino, F., Souradeep, T., Sowell, E., Spencer, A. P., Srivastava, A. K., Srivastava, V., Staats, K., Stachie, C., Standke, M., Steer, D. A., Steinke, M., Steinlechner, J., Steinlechner, S., Steinmeyer, D., Stevenson, S. P., Stocks, D., Stone, R., Stops, D. J., Strain, K. A., Stratta, G., Strigin, S. E., Strunk, A., Sturani, R., Stuver, A. L., Sudhir, V., Summerscales, T. Z., Sun, L., Sunil, S., Suresh, J., Sutton, P. J., Swinkels, B. L., Szczepańczyk, M. J., Tacca, M., Tait, S. C., Talbot, C., Talukder, D., Tanner, D. B., Tápai, M., Taracchini, A., Tasson, J. D., Taylor, R., Thies, F., Thomas, M., Thomas, P., Thondapu, S. R., Thorne, K. A., Thrane, E., Tiwari, S., Tiwari, S., Tiwari, V., Toland, K., Tonelli, M., Tornasi, Z., Torres-Forné, A., Torrie, C. I., Töyrä, D., Travasso, F., Traylor, G., Tringali, M. C., Trovato, A., Trozzo, L., Trudeau, R., Tsang, K. W., Tse, M., Tso, R., Tsukada, L., Tsuna, D., Tuyenbayev, D., Ueno, K., Ugolini, D., Unnikrishnan, C. S., Urban, A. L., Usman, S. A., Vahlbruch, H., Vajente, G., Valdes, G., Van Bakel, N., Van Beuzekom, M., Van Den Brand, J. F., Van Den Broeck, C., Vander-Hyde, D. C., Van Heijningen, J. V., Van Der Schaaf, L., Van Veggel, A. A., Vardaro, M., Varma, V., Vass, S., Vasúth, M., Vecchio, A., Vedovato, G., Veitch, J., Veitch, P. J., Venkateswara, K., Venugopalan, G., Verkindt, D., Vetrano, F., Viceré, A., Viets, A. D., Vine, D. J., Vinet, J. Y., Vitale, S., Vo, T., Vocca, H., Vorvick, C., Vyatchanin, S. P., Wade, A. R., Wade, L. E., Wade, M., Walet, R., Walker, M., Wallace, L., Walsh, S., Wang, G., Wang, H., Wang, J. Z., Wang, W. H., Wang, Y. F., Ward, R. L., Warden, Z. A., Warner, J., Was, M., Watchi, J., Weaver, B., Wei, L. W., Weinert, M., Weinstein, A. J., Weiss, R., Wellmann, F., Wen, L., Wessel, E. K., Weßels, P., Westhouse, J. W., Wette, K., Whelan, J. T., White, L. V., Whiting, B. F., Whittle, C., Wilken, D. M., Williams, D., Williamson, A. R., Willis, J. L., Willke, B., Wimmer, M. H., Winkler, W., Wipf, C. C., Wittel, H., Woan,

- G., Woehler, J., Wofford, J. K., Worden, J., Wright, J. L., Wu, D. S., Wysocki, D. M., Xiao, L., Yamamoto, H., Yancey, C. C., Yang, L., Yap, M. J., Yazback, M., Yeeles, D. W., Yu, H., Yu, H., Yuen, S. H., Yvert, M., Zadrożny, A. K., Zanolin, M., Zappa, F., Zelenova, T., Zendri, J. P., Zevin, M., Zhang, J., Zhang, L., Zhang, T., Zhao, C., Zhou, M., Zhou, Z., Zhu, X. J., Zimmerman, A. B., Zlochower, Y., Zucker, M. E., and Zweizig, J. (2019). GWTC-1: A Gravitational-Wave Transient Catalog of Compact Binary Mergers Observed by LIGO and Virgo during the First and Second Observing Runs. *Phys. Rev. X*, 9(3):031040.
- Abbott, B. P., Abbott, R., Abbott, T. D., Abraham, S., Acernese, F., Ackley, K., Adams, C., Adya, V. B., Affeldt, C., Agathos, M., Agatsuma, K., Aggarwal, N., Aguiar, O. D., Aiello, L., Ain, A., Ajith, P., Allen, G., Allocca, A., Aloy, M. A., Altin, P. A., Amato, A., Anand, S., Ananyeva, A., Anderson, S. B., Anderson, W. G., Angelova, S. V., Antier, S., Appert, S., Arai, K., Araya, M. C., Areeda, J. S., Arène, M., Arnaud, N., Aronson, S. M., Arun, K. G., Ascenzi, S., Ashton, G., Aston, S. M., Astone, P., Aubin, F., Aufmuth, P., Aultoneal, K., Austin, C., Avendano, V., Avila-Alvarez, A., Babak, S., Bacon, P., Badaracco, F., Bader, M. K., Bae, S., Baird, J., Baker, P. T., Baldaccini, F., Ballardini, G., Ballmer, S. W., Bals, A., Banagiri, S., Barayoga, J. C., Barbieri, C., Barclay, S. E., Barish, B. C., Barker, D., Barkett, K., Barnum, S., Barone, F., Barr, B., Barsotti, L., Barsuglia, M., Barta, D., Bartlett, J., Bartos, I., Bassiri, R., Basti, A., Bawaj, M., Bayley, J. C., Bazzan, M., Bécsy, B., Bejger, M., Belahcene, I., Bell, A. S., Beniwal, D., Benjamin, M. G., Berger, B. K., Bergmann, G., Bernuzzi, S., Berry, C. P., Bersanetti, D., Bertolini, A., Betzwieser, J., Bhandare, R., Bidler, J., Biggs, E., Bilenko, I. A., Bilgili, S. A., Billingsley, G., Birney, R., Birnholtz, O., Biscans, S., Bisch, M., Biscoveanu, S., Bisht, A., Bitossi, M., Bizouard, M. A., Blackburn, J. K., Blackman, J., Blair, C. D., Blair, D. G., Blair, R. M., Bloemen, S., Bobba, F., Bode, N., Boer, M., Boetzel, Y., Bogaert, G., Bondu, F., Bonnand, R., Booker, P., Boom, B. A., Bork, R., Boschi, V., Bose, S., Bossilkov, V., Bosveld, J., Bouffanais, Y., Bozzi, A., Bradaschia, C., Brady, P. R., Bramley, A., Branchesi, M., Brau, J. E., Breschi, M., Briant, T., Briggs, J. H., Brighenti, F., Brilliet, A., Brinkmann, M., Brockill, P., Brooks, A. F., Brooks, J., Brown, D. D., Brunett, S., Buikema, A., Bulik, T., Bulten, H. J., Buonanno, A., Buskulic, D., Buy, C., Byer, R. L., Cabero, M., Cadonati, L., Cagnoli, G., Cahillane, C., Calderón Bustillo, J., Callister, T. A., Calloni, E., Camp, J. B., Campbell, W. A., Canepa, M., Cannon, K. C., Cao, H., Cao, J., Carapella, G., Carbognani, F., Caride, S., Carney, M. F., Carullo, G., Casanueva Diaz, J., Casentini, C., Caudill, S., Cavaglià, M., Cavalier, F., Cavalieri, R., Cella, G., Cerdá-Durán, P., Cesarini, E., Chaibi, O., Chakravarti, K., Chamberlin, S. J., Chan, M., Chao, S., Charlton, P., Chase, E. A., Chassande-Mottin, E., Chatterjee, D., Chaturvedi, M., Chatziioannou, K., Cheeseboro, B. D., Chen, H. Y., Chen, X., Chen, Y., Cheng, H. P., Cheong, C. K., Chia, H. Y., Chiadini, F., Chincarini, A., Chiummo, A., Cho, G., Cho, H. S., Cho, M., Christensen, N., Chu, Q., Chua, S., Chung, K. W., Chung, S., Ciani, G., Cieřlar, M., Ciobanu, A. A., Ciolfi, R., Cipriano, F., Cirone, A., Clara, F., Clark, J. A., Clearwater, P., Cleva, F., Coccia, E., Cohadon, P. F., Cohen, D., Colleoni, M., Collette, C. G., Collins, C., Colpi, M., Cominsky, L. R., Constancio, M., Conti, L., Cooper, S. J., Corban, P., Corbitt, T. R., Cordero-Carrión, I., Corezzi, S., Corley, K. R., Cornish, N., Corre, D., Corsi, A., Cortese, S., Costa, C. A., Cotesta, R., Coughlin, M. W., Coughlin, S. B., Coulon, J. P., Countryman, S. T., Couvares, P., Covas, P. B., Cowan, E. E., Coward, D. M., Cowart, M. J., Coyne, D. C., Coyne, R., Creighton, J. D., Creighton, T. D., Cripe, J., Croquette, M., Crowder, S. G., Cullen, T. J., Cumming, A., Cunningham, L., Cuoco, E., Dal Canton, T., Dálya, G., D'Angelo, B., Danilishin, S. L., D'Antonio, S., Danzmann, K., Dasgupta, A., Da Silva Costa, C. F., Datrier, L. E., Dattilo, V.,

Dave, I., Davier, M., Davis, D., Daw, E. J., Debra, D., Deenadayalan, M., Degallaix, J., De Laurentis, M., Deléglise, S., Del Pozzo, W., Demarchi, L. M., Demos, N., Dent, T., De Pietri, R., De Rosa, R., De Rossi, C., Desalvo, R., De Varona, O., Dhurandhar, S., Díaz, M. C., Dietrich, T., Di Fiore, L., Difronzo, C., Di Giorgio, C., Di Giovanni, F., Di Giovanni, M., Di Girolamo, T., Di Lieto, A., Ding, B., Di Pace, S., Di Palma, I., Di Renzo, F., Divakarla, A. K., Dmitriev, A., Doctor, Z., Donovan, F., Dooley, K. L., Doravari, S., Dorrington, I., Downes, T. P., Drago, M., Driggers, J. C., Du, Z., Ducoin, J. G., Dupej, P., Durante, O., Dwyer, S. E., Easter, P. J., Eddolls, G., Edo, T. B., Effler, A., Ehrens, P., Eichholz, J., Eikenberry, S. S., Eisenmann, M., Eisenstein, R. A., Errico, L., Essick, R. C., Estelles, H., Estevez, D., Etienne, Z. B., Etzel, T., Evans, M., Evans, T. M., Fafone, V., Fairhurst, S., Fan, X., Farinon, S., Farr, B., Farr, W. M., Fauchon-Jones, E. J., Favata, M., Fays, M., Fazio, M., Fee, C., Feicht, J., Fejer, M. M., Feng, F., Fernandez-Galiana, A., Ferrante, I., Ferreira, E. C., Ferreira, T. A., Fidecaro, F., Fiori, I., Fiorucci, D., Fishbach, M., Fisher, R. P., Fishner, J. M., Fittipaldi, R., Fitz-Axen, M., Fiumara, V., Flaminio, R., Fletcher, M., Floden, E., Flynn, E., Fong, H., Font, J. A., Forsyth, P. W., Fournier, J. D., Frasca, S., Frasconi, F., Frei, Z., Freise, A., Frey, R., Frey, V., Fritschel, P., Frolov, V. V., Fronzè, G., Fulda, P., Fyffe, M., Gabbard, H. A., Gadre, B. U., Gaebel, S. M., Gair, J. R., Gammaitoni, L., Gaonkar, S. G., García-Quirós, C., Garufi, F., Gateley, B., Gaudio, S., Gaur, G., Gayathri, V., Gemme, G., Genin, E., Gennai, A., George, D., George, J., Gergely, L., Ghonge, S., Ghosh, A., Ghosh, A., Ghosh, S., Giacomazzo, B., Giaime, J. A., Giardino, K. D., Gibson, D. R., Gill, K., Glover, L., Gniesmer, J., Godwin, P., Goetz, E., Goetz, R., Goncharov, B., González, G., Gonzalez Castro, J. M., Gopakumar, A., Gossan, S. E., Gosselin, M., Gouaty, R., Grace, B., Grado, A., Granata, M., Grant, A., Gras, S., Grassia, P., Gray, C., Gray, R., Greco, G., Green, A. C., Green, R., Gretarsson, E. M., Grimaldi, A., Grimm, S. J., Groot, P., Grote, H., Grunewald, S., Gruning, P., Guidi, G. M., Gulati, H. K., Guo, Y., Gupta, A., Gupta, A., Gupta, P., Gustafson, E. K., Gustafson, R., Haegel, L., Halim, O., Hall, B. R., Hall, E. D., Hamilton, E. Z., Hammond, G., Haney, M., Hanke, M. M., Hanks, J., Hanna, C., Hannam, M. D., Hannuksela, O. A., Hansen, T. J., Hanson, J., Harder, T., Hardwick, T., Haris, K., Harms, J., Harry, G. M., Harry, I. W., Hasskew, R. K., Haster, C. J., Haughian, K., Hayes, F. J., Healy, J., Heidmann, A., Heintze, M. C., Heitmann, H., Hellman, F., Hello, P., Hemming, G., Hendry, M., Heng, I. S., Hennig, J., Hernandez Vivanco, F., Heurs, M., Hild, S., Hinderer, T., Ho, W. C., Hochheim, S., Hofman, D., Holgado, A. M., Holland, N. A., Holt, K., Holz, D. E., Hopkins, P., Horst, C., Hough, J., Howell, E. J., Hoy, C. G., Huang, Y., Hübner, M. T., Huerta, E. A., Huet, D., Hughey, B., Hui, V., Husa, S., Huttner, S. H., Huynh-Dinh, T., Idzkowski, B., Iess, A., Inchauspe, H., Ingram, C., Inta, R., Intini, G., Irwin, B., Isa, H. N., Isac, J. M., Isi, M., Iyer, B. R., Jacqmin, T., Jadhav, S. J., Jani, K., Janthalur, N. N., Jaranowski, P., Jariwala, D., Jenkins, A. C., Jiang, J., Johnson, D. S., Jones, A. W., Jones, D. I., Jones, J. D., Jones, R., Jonker, R. J., Ju, L., Junker, J., Kalaghatgi, C. V., Kalogera, V., Kamai, B., Kandhasamy, S., Kang, G., Kanner, J. B., Kapadia, S. J., Karki, S., Kashyap, R., Kasprzack, M., Kastaun, W., Katsanevas, S., Katsavounidis, E., Katzman, W., Kaufer, S., Kawabe, K., Keerthana, N. V., Kéfélian, F., Keitel, D., Kennedy, R., Key, J. S., Khalili, F. Y., Khan, I., Khan, S., Khazanov, E. A., Khetan, N., Khursheed, M., Kijbunchoo, N., Kim, C., Kim, J. C., Kim, K., Kim, W., Kim, W. S., Kim, Y. M., Kimball, C., King, P. J., Kinley-Hanlon, M., Kirchhoff, R., Kissel, J. S., Kleybolte, L., Klika, J. H., Klimenko, S., Knowles, T. D., Koch, P., Koehlenbeck, S. M., Koekoek, G., Koley, S., Kondrashov, V., Kontos, A., Koper, N., Korobko, M., Korth, W. Z., Kovalam, M., Kozak, D. B., Krämer, C., Kringel, V., Krishnendu, N., Królak, A., Krupinski, N., Kuehn, G., Kumar, A., Kumar, P., Kumar, R., Kumar, R., Kuo, L., Kutynia, A., Kwang, S., Lackey, B. D.,

Laghi, D., Lai, K. H., Lam, T. L., Landry, M., Landry, P., Lane, B. B., Lang, R. N., Lange, J., Lantz, B., Lanza, R. K., Lartaux-Vollard, A., Lasky, P. D., Laxen, M., Lazzarini, A., Lazzaro, C., Leaci, P., Leavey, S., Lecoeuche, Y. K., Lee, C. H., Lee, H. K., Lee, H. M., Lee, H. W., Lee, J., Lee, K., Lehmann, J., Lenon, A. K., Leroy, N., Letendre, N., Levin, Y., Li, A., Li, J., Li, K. J., Li, T. G., Li, X., Lin, F., Linde, F., Linker, S. D., Littenberg, T. B., Liu, J., Liu, X., Llorens-Monteagudo, M., Lo, R. K., London, L. T., Longo, A., Lorenzini, M., Lorette, V., Lormand, M., Losurdo, G., Lough, J. D., Lousto, C. O., Lovelace, G., Lower, M. E., Lück, H., Lumaca, D., Lundgren, A. P., Lynch, R., Ma, Y., Macas, R., Macfoy, S., Macinnis, M., Macleod, D. M., Macquet, A., Magana Hernandez, I., Magana-Sandoval, F., Magee, R. M., Majorana, E., Maksimovic, I., Malik, A., Man, N., Mandic, V., Mangano, V., Mansell, G. L., Manske, M., Mantovani, M., Mapelli, M., Marchesoni, F., Marion, F., Márka, S., Márka, Z., Markakis, C., Markosyan, A. S., Markowitz, A., Maros, E., Marquina, A., Marsat, S., Martelli, F., Martin, I. W., Martin, R. M., Martinez, V., Martynov, D. V., Masalehdan, H., Mason, K., Massera, E., Masserot, A., Massinger, T. J., Masso-Reid, M., Mastrogiovanni, S., Matas, A., Matichard, F., Matone, L., Mavalvala, N., McCann, J. J., McCarthy, R., McClelland, D. E., McCormick, S., McCuller, L., McGuire, S. C., McIsaac, C., McIver, J., McManus, D. J., McRae, T., McWilliams, S. T., Meacher, D., Meadors, G. D., Mehmet, M., Mehta, A. K., Meidam, J., Mejuto Villa, E., Melatos, A., Mendell, G., Mercer, R. A., Mereni, L., Merfeld, K., Merilh, E. L., Merzougui, M., Meshkov, S., Messenger, C., Messick, C., Messina, F., Metzdorff, R., Meyers, P. M., Meylahn, F., Miani, A., Miao, H., Michel, C., Middleton, H., Milano, L., Miller, A. L., Millhouse, M., Mills, J. C., Milovich-Goff, M. C., Minazzoli, O., Minenkov, Y., Mishkin, A., Mishra, C., Mistry, T., Mitra, S., Mitrofanov, V. P., Mitselmakher, G., Mittleman, R., Mo, G., Moffa, D., Mogushi, K., Mohapatra, S. R., Molina-Ruiz, M., Mondin, M., Montani, M., Moore, C. J., Moraru, D., Morawski, F., Moreno, G., Morisaki, S., Mours, B., Mow-Lowry, C. M., Muciaccia, F., Mukherjee, A., Mukherjee, D., Mukherjee, S., Mukherjee, S., Mukund, N., Mullavey, A., Munch, J., Muniz, E. A., Muratore, M., Murray, P. G., Nagar, A., Nardecchia, I., Naticchioni, L., Nayak, R. K., Neil, B. F., Neilson, J., Nelemans, G., Nelson, T. J., Nery, M., Neunzert, A., Nevin, L., Ng, K. Y., Ng, S., Nguyen, C., Nguyen, P., Nichols, D., Nichols, S. A., Nissanke, S., Nocera, F., North, C., Nuttall, L. K., Obergaulinger, M., Oberling, J., O'Brien, B. D., Oganessian, G., Ogin, G. H., Oh, J. J., Oh, S. H., Ohme, F., Ohta, H., Okada, M. A., Oliver, M., Oppermann, P., Oram, R. J., O'Reilly, B., Ormiston, R. G., Ortega, L. F., O'Shaughnessy, R., Ossokine, S., Ottaway, D. J., Overmier, H., Owen, B. J., Pace, A. E., Pagano, G., Page, M. A., Pagliaroli, G., Pai, A., Pai, S. A., Palamos, J. R., Palashov, O., Palomba, C., Pan, H., Panda, P. K., Pang, P. T., Pankow, C., Pannarale, F., Pant, B. C., Paoletti, F., Paoli, A., Parida, A., Parker, W., Pascucci, D., Pasqualetti, A., Passaquieti, R., Passuello, D., Patil, M., Patricelli, B., Payne, E., Pearlstone, B. L., Pechsiri, T. C., Pedersen, A. J., Pedraza, M., Pedurand, R., Pele, A., Penn, S., Perego, A., Perez, C. J., Périgois, C., Perreca, A., Petermann, J., Pfeiffer, H. P., Phelps, M., Phukon, K. S., Piccinni, O. J., Pichot, M., Piergiovanni, F., Pierro, V., Pillant, G., Pinard, L., Pinto, I. M., Pirello, M., Pitkin, M., Plastino, W., Poggiani, R., Pong, D. Y., Ponrathnam, S., Popolizio, P., Porter, E. K., Powell, J., Prajapati, A. K., Prasad, J., Prasai, K., Prasanna, R., Pratten, G., Prestegard, T., Principe, M., Prodi, G. A., Prokhorov, L., Punturo, M., Puppo, P., Pürrer, M., Qi, H., Quetschke, V., Quinonez, P. J., Raab, F. J., Raaijmakers, G., Radkins, H., Radulesco, N., Raffai, P., Raja, S., Rajan, C., Rajbhandari, B., Rakhmanov, M., Ramirez, K. E., Ramos-Buades, A., Rana, J., Rao, K., Rapagnani, P., Raymond, V., Razzano, M., Read, J., Regimbau, T., Rei, L., Reid, S., Reitze, D. H., Rettengo, P., Ricci, F., Richardson, C. J., Richardson, J. W., Ricker, P. M., Riemenschneider, G., Riles, K., Rizzo, M., Robertson, N. A.,

- Robinet, F., Rocchi, A., Rolland, L., Rollins, J. G., Roma, V. J., Romanelli, M., Romano, R., Romel, C. L., Romie, J. H., Rose, C. A., Rose, D., Rose, K., Rosińska, D., Rosofsky, S. G., Ross, M. P., Rowan, S., Rüdiger, A., Ruggi, P., Rutins, G., Ryan, K., Sachdev, S., Sadecki, T., Sakellariadou, M., Salafia, O. S., Salconi, L., Saleem, M., Samajdar, A., Sammut, L., Sanchez, E. J., Sanchez, L. E., Sanchis-Gual, N., Sanders, J. R., Santiago, K. A., Santos, E., Sarin, N., Sassolas, B., Sathyaprakash, B. S., Sauter, O., Savage, R. L., Schale, P., Scheel, M., Scheuer, J., Schmidt, P., Schnabel, R., Schofield, R. M., Schönbeck, A., Schreiber, E., Schulte, B. W., Schutz, B. F., Scott, J., Scott, S. M., Seidel, E., Sellers, D., Sengupta, A. S., Sennett, N., Sentenac, D., Sequino, V., Sergeev, A., Setyawati, Y., Shaddock, D. A., Shaffer, T., Shahriar, M. S., Shaner, M. B., Sharma, A., Sharma, P., Shawhan, P., Shen, H., Shink, R., Shoemaker, D. H., Shoemaker, D. M., Shukla, K., Shyamsundar, S., Siellez, K., Sieniawska, M., Sigg, D., Singer, L. P., Singh, D., Singh, N., Singhal, A., Sintes, A. M., Sitmukhambetov, S., Skliris, V., Slagmolen, B. J., Slaven-Blair, T. J., Smith, J. R., Smith, R. J., Somala, S., Son, E. J., Soni, S., Sorazu, B., Sorrentino, F., Souradeep, T., Sowell, E., Spencer, A. P., Spera, M., Srivastava, A. K., Srivastava, V., Staats, K., Stachie, C., Standke, M., Steer, D. A., Steinke, M., Steinlechner, J., Steinlechner, S., Steinmeyer, D., Stevenson, S. P., Stocks, D., Stone, R., Stops, D. J., Strain, K. A., Stratta, G., Strigin, S. E., Strunk, A., Sturani, R., Stuver, A. L., Sudhir, V., Summerscales, T. Z., Sun, L., Sunil, S., Sur, A., Suresh, J., Sutton, P. J., Swinkels, B. L., Szczepańczyk, M. J., Tacca, M., Tait, S. C., Talbot, C., Tanner, D. B., Tao, D., Tápai, M., Tapia, A., Tasson, J. D., Taylor, R., Tenorio, R., Terkowski, L., Thomas, M., Thomas, P., Thondapu, S. R., Thorne, K. A., Thrane, E., Tiwari, S., Tiwari, S., Tiwari, V., Toland, K., Tonelli, M., Tornasi, Z., Torres-Forné, A., Torrie, C. I., Töyrä, D., Travasso, F., Traylor, G., Tringali, M. C., Tripathee, A., Trovato, A., Trozzo, L., Tsang, K. W., Tse, M., Tso, R., Tsukada, L., Tsuna, D., Tsutsui, T., Tuyenbayev, D., Ueno, K., Ugolini, D., Unnikrishnan, C. S., Urban, A. L., Usman, S. A., Vahlbruch, H., Vajente, G., Valdes, G., Valentini, M., Van Bakel, N., Van Beuzekom, M., Van Den Brand, J. F., Van Den Broeck, C., Van Der-Hyde, D. C., Van Der Schaaf, L., Van Heijningen, J. V., Van Veggel, A. A., Vardaro, M., Varma, V., Vass, S., Vasúth, M., Vecchio, A., Vedovato, G., Veitch, J., Veitch, P. J., Venkateswara, K., Venugopalan, G., Verkindt, D., Vetrano, F., Viceré, A., Viets, A. D., Vinciguerra, S., Vine, D. J., Vinet, J. Y., Vitale, S., Vo, T., Vocca, H., Vorvick, C., Vyatchanin, S. P., Wade, A. R., Wade, L. E., Wade, M., Walet, R., Walker, M., Wallace, L., Walsh, S., Wang, H., Wang, J. Z., Wang, S., Wang, W. H., Wang, Y. F., Ward, R. L., Warden, Z. A., Warner, J., Was, M., Watchi, J., Weaver, B., Wei, L. W., Weinert, M., Weinstein, A. J., Weiss, R., Wellmann, F., Wen, L., Wessel, E. K., Weßels, P., Westhouse, J. W., Wette, K., Whelan, J. T., Whiting, B. F., Whittle, C., Wilken, D. M., Williams, D., Williamson, A. R., Willis, J. L., Willke, B., Winkler, W., Wipf, C. C., Wittel, H., Woan, G., Woehler, J., Wofford, J. K., Wright, J. L., Wu, D. S., Wysocki, D. M., Xiao, S., Xu, R., Yamamoto, H., Yancey, C. C., Yang, L., Yang, Y., Yang, Z., Yap, M. J., Yazback, M., Yeeles, D. W., Yu, H., Yu, H., Yuen, S. H., Zadrozny, A. K., Zadrozny, A., Zanolin, M., Zappa, F., Zelenova, T., Zendri, J. P., Zevin, M., Zhang, J., Zhang, L., Zhang, T., Zhao, C., Zhao, G., Zhou, M., Zhou, Z., Zhu, X. J., Zimmerman, A. B., Zlochower, Y., Zucker, M. E., and Zweizig, J. (2020a). Model comparison from LIGO-Virgo data on GW170817's binary components and consequences for the merger remnant. *Class. Quantum Gravity*, 37(4):045006.
- Abbott, B. P., Abbott, R., Abbott, T. D., Acernese, F., Ackley, K., Adams, C., Adams, T., Addesso, P., Adhikari, R. X., Adya, V. B., Affeldt, C., Afrough, M., Agarwal, B., Agathos, M., Agatsuma, K., Aggarwal, N., Aguiar, O. D., Aiello, L., Ain, A., Ajith, P., Allen, B.,

Allen, G., Allocca, A., Altin, P. A., Amato, A., Ananyeva, A., Anderson, S. B., Anderson, W. G., Angelova, S. V., Antier, S., Appert, S., Arai, K., Araya, M. C., Areeda, J. S., Arnaud, N., Arun, K. G., Ascenzi, S., Ashton, G., Ast, M., Aston, S. M., Astone, P., Atallah, D. V., Aufmuth, P., Aulbert, C., Aultoneal, K., Austin, C., Avila-Alvarez, A., Babak, S., Bacon, P., Bader, M. K., Bae, S., Bailes, M., Baker, P. T., Baldaccini, F., Ballardin, G., Ballmer, S. W., Banagiri, S., Barayoga, J. C., Barclay, S. E., Barish, B. C., Barker, D., Barkett, K., Barone, F., Barr, B., Barsotti, L., Barsuglia, M., Barta, D., Barthelmy, S. D., Bartlett, J., Bartos, I., Bassiri, R., Basti, A., Batch, J. C., Bawaj, M., Bayley, J. C., Bazzan, M., Bécsy, B., Beer, C., Bejger, M., Belahcene, I., Bell, A. S., Berger, B. K., Bergmann, G., Bernuzzi, S., Bero, J. J., Berry, C. P., Bersanetti, D., Bertolini, A., Betzwieser, J., Bhagwat, S., Bhandare, R., Bilenko, I. A., Billingsley, G., Billman, C. R., Birch, J., Birney, R., Birnholtz, O., Biscans, S., Biscoveanu, S., Bisht, A., Bitossi, M., Biwer, C., Bizouard, M. A., Blackburn, J. K., Blackman, J., Blair, C. D., Blair, D. G., Blair, R. M., Bloemen, S., Bock, O., Bode, N., Boer, M., Bogaert, G., Bohe, A., Bondu, F., Bonilla, E., Bonnand, R., Boom, B. A., Bork, R., Boschi, V., Bose, S., Bossie, K., Bouffanais, Y., Bozzi, A., Bradaschia, C., Brady, P. R., Branchesi, M., Brau, J. E., Briant, T., Brillet, A., Brinkmann, M., Brisson, V., Brockill, P., Broida, J. E., Brooks, A. F., Brown, D. A., Brown, D. D., Brunett, S., Buchanan, C. C., Buikema, A., Bulik, T., Bulten, H. J., Buonanno, A., Buskulic, D., Buy, C., Byer, R. L., Cabero, M., Cadonati, L., Cagnoli, G., Cahillane, C., Calderón Bustillo, J., Callister, T. A., Calloni, E., Camp, J. B., Canepa, M., Canizares, P., Cannon, K. C., Cao, H., Cao, J., Capano, C. D., Capocasa, E., Carbognani, F., Caride, S., Carney, M. F., Carullo, G., Casanueva Diaz, J., Casentini, C., Caudill, S., Cavaglià, M., Cavalier, F., Cavalieri, R., Cella, G., Cepeda, C. B., Cerdá-Durán, P., Cerretani, G., Cesarini, E., Chamberlin, S. J., Chan, M., Chao, S., Charlton, P., Chase, E., Chassande-Mottin, E., Chatterjee, D., Chatziioannou, K., Cheeseboro, B. D., Chen, H. Y., Chen, X., Chen, Y., Cheng, H. P., Chia, H., Chincarini, A., Chiummo, A., Chmiel, T., Cho, H. S., Cho, M., Chow, J. H., Christensen, N., Chu, Q., Chua, A. J., Chua, S., Chung, A. K., Chung, S., Ciani, G., Ciolfi, R., Cirelli, C. E., Cirone, A., Clara, F., Clark, J. A., Clearwater, P., Cleva, F., Cocchieri, C., Coccia, E., Cohadon, P. F., Cohen, D., Colla, A., Collette, C. G., Cominsky, L. R., Constancio, M., Conti, L., Cooper, S. J., Corban, P., Corbitt, T. R., Cordero-Carrión, I., Corley, K. R., Cornish, N., Corsi, A., Cortese, S., Costa, C. A., Coughlin, M. W., Coughlin, S. B., Coulon, J. P., Countryman, S. T., Couvares, P., Covas, P. B., Cowan, E. E., Coward, D. M., Cowart, M. J., Coyne, D. C., Coyne, R., Creighton, J. D., Creighton, T. D., Cripe, J., Crowder, S. G., Cullen, T. J., Cumming, A., Cunningham, L., Cuoco, E., Dal Canton, T., Dálya, G., Danilishin, S. L., D'Antonio, S., Danzmann, K., Dasgupta, A., Da Silva Costa, C. F., Dattilo, V., Dave, I., Davier, M., Davis, D., Daw, E. J., Day, B., De, S., Debra, D., Degallaix, J., De Laurentis, M., Deléglise, S., Del Pozzo, W., Demos, N., Denker, T., Dent, T., De Pietri, R., Dergachev, V., De Rosa, R., Derosa, R. T., De Rossi, C., Desalvo, R., De Varona, O., Devenson, J., Dhurandhar, S., Díaz, M. C., Dietrich, T., Di Fiore, L., Di Giovanni, M., Di Girolamo, T., Di Lieto, A., Di Pace, S., Di Palma, I., Di Renzo, F., Doctor, Z., Dolique, V., Donovan, F., Dooley, K. L., Doravari, S., Dorrington, I., Douglas, R., Dovale Álvarez, M., Downes, T. P., Drago, M., Dreissigacker, C., Driggers, J. C., Du, Z., Ducrot, M., Dudi, R., Dupej, P., Dwyer, S. E., Edo, T. B., Edwards, M. C., Effler, A., Eggenstein, H. B., Ehrens, P., Eichholz, J., Eikenberry, S. S., Eisenstein, R. A., Essick, R. C., Estevez, D., Etienne, Z. B., Etzel, T., Evans, M., Evans, T. M., Factourovich, M., Fafone, V., Fair, H., Fairhurst, S., Fan, X., Farinon, S., Farr, B., Farr, W. M., Fauchon-Jones, E. J., Favata, M., Fays, M., Fee, C., Fehrmann, H., Feicht, J., Fejer, M. M., Fernandez-Galiana, A., Ferrante, I., Ferreira, E. C., Ferrini, F., Fidecaro, F., Finstad, D., Fiori, I., Fiorucci, D.,

Fishbach, M., Fisher, R. P., Fitz-Axen, M., Flaminio, R., Fletcher, M., Fong, H., Font, J. A., Forsyth, P. W., Forsyth, S. S., Fournier, J. D., Frasca, S., Frascioni, F., Frei, Z., Freise, A., Frey, R., Frey, V., Fries, E. M., Fritschel, P., Frolov, V. V., Fulda, P., Fyffe, M., Gabbard, H., Gadre, B. U., Gaebel, S. M., Gair, J. R., Gammaitoni, L., Ganija, M. R., Gaonkar, S. G., Garcia-Quiros, C., Garufi, F., Gateley, B., Gaudio, S., Gaur, G., Gayathri, V., Gehrels, N., Gemme, G., Genin, E., Gennai, A., George, D., George, J., Gergely, L., Germain, V., Ghonge, S., Ghosh, A., Ghosh, A., Ghosh, S., Giaime, J. A., Giardina, K. D., Giazotto, A., Gill, K., Glover, L., Goetz, E., Goetz, R., Gomes, S., Goncharov, B., González, G., Gonzalez Castro, J. M., Gopakumar, A., Gorodetsky, M. L., Gossan, S. E., Gosselin, M., Gouaty, R., Grado, A., Graef, C., Granata, M., Grant, A., Gras, S., Gray, C., Greco, G., Green, A. C., Gretarsson, E. M., Groot, P., Grote, H., Grunewald, S., Gruning, P., Guidi, G. M., Guo, X., Gupta, A., Gupta, M. K., Gushwa, K. E., Gustafson, E. K., Gustafson, R., Halim, O., Hall, B. R., Hall, E. D., Hamilton, E. Z., Hammond, G., Haney, M., Hanke, M. M., Hanks, J., Hanna, C., Hannam, M. D., Hannuksela, O. A., Hanson, J., Hardwick, T., Harms, J., Harry, G. M., Harry, I. W., Hart, M. J., Haster, C. J., Haughian, K., Healy, J., Heidmann, A., Heintze, M. C., Heitmann, H., Hello, P., Hemming, G., Hendry, M., Heng, I. S., Hennig, J., Heptonstall, A. W., Heurs, M., Hild, S., Hinderer, T., Ho, W. C., Hoak, D., Hofman, D., Holt, K., Holz, D. E., Hopkins, P., Horst, C., Hough, J., Houston, E. A., Howell, E. J., Hreibi, A., Hu, Y. M., Huerta, E. A., Huet, D., Hughey, B., Husa, S., Huttner, S. H., Huynh-Dinh, T., Indik, N., Inta, R., Intini, G., Isa, H. N., Isac, J. M., Isi, M., Iyer, B. R., Izumi, K., Jacqmin, T., Jani, K., Jaranowski, P., Jawahar, S., Jiménez-Forteza, F., Johnson, W. W., Johnson-Mcdaniel, N. K., Jones, D. I., Jones, R., Jonker, R. J., Ju, L., Junker, J., Kalaghatgi, C. V., Kalogera, V., Kamai, B., Kandhasamy, S., Kang, G., Kanner, J. B., Kapadia, S. J., Karki, S., Karvinen, K. S., Kasprzack, M., Kastaun, W., Katolik, M., Katsavounidis, E., Katzman, W., Kaufer, S., Kawabe, K., Kéfélian, F., Keitel, D., Kemball, A. J., Kennedy, R., Kent, C., Key, J. S., Khalili, F. Y., Khan, I., Khan, S., Khan, Z., Khazanov, E. A., Kijbunchoo, N., Kim, C., Kim, J. C., Kim, K., Kim, W., Kim, W. S., Kim, Y. M., Kimbrell, S. J., King, E. J., King, P. J., Kinley-Hanlon, M., Kirchhoff, R., Kissel, J. S., Kleybolte, L., Klimenko, S., Knowles, T. D., Koch, P., Koehlenbeck, S. M., Koley, S., Kondrashov, V., Kontos, A., Korobko, M., Korth, W. Z., Kowalska, I., Kozak, D. B., Krämer, C., Kringel, V., Krishnan, B., Królak, A., Kuehn, G., Kumar, P., Kumar, R., Kumar, S., Kuo, L., Kutynia, A., Kwang, S., Lackey, B. D., Lai, K. H., Landry, M., Lang, R. N., Lange, J., Lantz, B., Lanza, R. K., Larson, S. L., Lartaux-Vollard, A., Lasky, P. D., Laxen, M., Lazzarini, A., Lazzaro, C., Leaci, P., Leavey, S., Lee, C. H., Lee, H. K., Lee, H. M., Lee, H. W., Lee, K., Lehmann, J., Lenon, A., Leon, E., Leonardi, M., Leroy, N., Letendre, N., Levin, Y., Li, T. G., Linker, S. D., Littenberg, T. B., Liu, J., Liu, X., Lo, R. K., Lockerbie, N. A., London, L. T., Lord, J. E., Lorenzini, M., Lorette, V., Lormand, M., Losurdo, G., Lough, J. D., Lousto, C. O., Lovelace, G., Lück, H., Lumaca, D., Lundgren, A. P., Lynch, R., Ma, Y., Macas, R., Macfoy, S., Machenschalk, B., Macinnis, M., Macleod, D. M., Magaña Hernandez, I., Magaña-Sandoval, F., Magaña Zertuche, L., Magee, R. M., Majorana, E., Maksimovic, I., Man, N., Mandic, V., Mangano, V., Mansell, G. L., Manske, M., Mantovani, M., Marchesoni, F., Marion, F., Márka, S., Márka, Z., Markakis, C., Markosyan, A. S., Markowitz, A., Maros, E., Marquina, A., Marsh, P., Martelli, F., Martellini, L., Martin, I. W., Martin, R. M., Martynov, D. V., Marx, J. N., Mason, K., Massera, E., Masserot, A., Massinger, T. J., Masso-Reid, M., Mastrogiovanni, S., Matas, A., Matichard, F., Matone, L., Mavalvala, N., Mazumder, N., McCarthy, R., McClelland, D. E., McCormick, S., McCuller, L., McGuire, S. C., McIntyre, G., McIver, J., McManus, D. J., McNeill, L., McRae, T., McWilliams, S. T., Meacher, D., Meadors, G. D., Mehmet,

M., Meidam, J., Mejuto-Villa, E., Melatos, A., Mendell, G., Mercer, R. A., Merilh, E. L., Merzougui, M., Meshkov, S., Messenger, C., Messick, C., Metzdorff, R., Meyers, P. M., Miao, H., Michel, C., Middleton, H., Mikhailov, E. E., Milano, L., Miller, A. L., Miller, B. B., Miller, J., Millhouse, M., Milovich-Goff, M. C., Minazzoli, O., Minenkov, Y., Ming, J., Mishra, C., Mitra, S., Mitrofanov, V. P., Mitselmakher, G., Mittleman, R., Moffa, D., Moggi, A., Mogushi, K., Mohan, M., Mohapatra, S. R., Molina, I., Montani, M., Moore, C. J., Moraru, D., Moreno, G., Morisaki, S., Morriss, S. R., Mours, B., Mow-Lowry, C. M., Mueller, G., Muir, A. W., Mukherjee, A., Mukherjee, D., Mukherjee, S., Mukund, N., Mullavey, A., Munch, J., Muñiz, E. A., Muratore, M., Murray, P. G., Nagar, A., Napier, K., Nardecchia, I., Naticchioni, L., Nayak, R. K., Neilson, J., Nelemans, G., Nelson, T. J., Nery, M., Neunzert, A., Nevin, L., Newport, J. M., Newton, G., Ng, K. K., Nguyen, P., Nguyen, T. T., Nichols, D., Nielsen, A. B., Nissanke, S., Nitz, A., Noack, A., Nocera, F., Nolting, D., North, C., Nuttall, L. K., Oberling, J., O'Dea, G. D., Ogin, G. H., Oh, J. J., Oh, S. H., Ohme, F., Okada, M. A., Oliver, M., Oppermann, P., Oram, R. J., O'Reilly, B., Ormiston, R., Ortega, L. F., O'Shaughnessy, R., Ossokine, S., Ottaway, D. J., Overmier, H., Owen, B. J., Pace, A. E., Page, J., Page, M. A., Pai, A., Pai, S. A., Palamos, J. R., Palashov, O., Palomba, C., Pal-Singh, A., Pan, H., Pan, H. W., Pang, B., Pang, P. T., Pankow, C., Pannarale, F., Pant, B. C., Paoletti, F., Paoli, A., Papa, M. A., Parida, A., Parker, W., Pascucci, D., Pasqualetti, A., Passaquieti, R., Passuello, D., Patil, M., Patricelli, B., Pearlstone, B. L., Pedraza, M., Pedurand, R., Pekowsky, L., Pele, A., Penn, S., Perez, C. J., Perreca, A., Perri, L. M., Pfeiffer, H. P., Phelps, M., Piccinni, O. J., Pichot, M., Piergiovanni, F., Pierro, V., Pillant, G., Pinard, L., Pinto, I. M., Pirello, M., Pitkin, M., Poe, M., Poggiani, R., Popolizio, P., Porter, E. K., Post, A., Powell, J., Prasad, J., Pratt, J. W., Pratten, G., Predoi, V., Prestegard, T., Prijatelj, M., Principe, M., Privitera, S., Prix, R., Prodi, G. A., Prokhorov, L. G., Puncken, O., Punturo, M., Puppo, P., Pürrer, M., Qi, H., Quetschke, V., Quintero, E. A., Quitzow-James, R., Raab, F. J., Rabeling, D. S., Radkins, H., Raffai, P., Raja, S., Rajan, C., Rajbhandari, B., Rakhmanov, M., Ramirez, K. E., Ramos-Buades, A., Rapagnani, P., Raymond, V., Razzano, M., Read, J., Regimbau, T., Rei, L., Reid, S., Reitze, D. H., Ren, W., Reyes, S. D., Ricci, F., Ricker, P. M., Rieger, S., Riles, K., Rizzo, M., Robertson, N. A., Robie, R., Robinet, F., Rocchi, A., Rolland, L., Rollins, J. G., Roma, V. J., Romano, J. D., Romano, R., Romel, C. L., Romie, J. H., Rosińska, D., Ross, M. P., Rowan, S., Rüdiger, A., Ruggi, P., Rutins, G., Ryan, K., Sachdev, S., Sadecki, T., Sadeghian, L., Sakellariadou, M., Salconi, L., Saleem, M., Salemi, F., Samajdar, A., Sammut, L., Sampson, L. M., Sanchez, E. J., Sanchez, L. E., Sanchis-Gual, N., Sandberg, V., Sanders, J. R., Sassolas, B., Sathyaprakash, B. S., Saulson, P. R., Sauter, O., Savage, R. L., Sawadsky, A., Schale, P., Scheel, M., Scheuer, J., Schmidt, J., Schmidt, P., Schnabel, R., Schofield, R. M., Schönbeck, A., Schreiber, E., Schuette, D., Schulte, B. W., Schutz, B. F., Schwalbe, S. G., Scott, J., Scott, S. M., Seidel, E., Sellers, D., Sengupta, A. S., Sentenac, D., Sequino, V., Sergeev, A., Shaddock, D. A., Shaffer, T. J., Shah, A. A., Shahriar, M. S., Shaner, M. B., Shao, L., Shapiro, B., Shawhan, P., Sheperd, A., Shoemaker, D. H., Shoemaker, D. M., Siellez, K., Siemens, X., Sieniawska, M., Sigg, D., Silva, A. D., Singer, L. P., Singh, A., Singhal, A., Sintes, A. M., Slagmolen, B. J., Smith, B., Smith, J. R., Smith, R. J., Somala, S., Son, E. J., Sonnenberg, J. A., Sorazu, B., Sorrentino, F., Souradeep, T., Spencer, A. P., Srivastava, A. K., Staats, K., Staley, A., Steinke, M., Steinlechner, J., Steinlechner, S., Steinmeyer, D., Stevenson, S. P., Stone, R., Stops, D. J., Strain, K. A., Stratta, G., Strigin, S. E., Strunk, A., Sturani, R., Stuver, A. L., Summerscales, T. Z., Sun, L., Sunil, S., Suresh, J., Sutton, P. J., Swinkels, B. L., Szczepańczyk, M. J., Tacca, M., Tait, S. C., Talbot, C., Talukder, D., Tanner, D. B., Tápai, M., Taracchini, A., Tasson, J. D., Taylor, J. A., Taylor, R., Tewari, S. V., Theeg,

- T., Thies, F., Thomas, E. G., Thomas, M., Thomas, P., Thorne, K. A., Thorne, K. S., Thrane, E., Tiwari, S., Tiwari, V., Tokmakov, K. V., Toland, K., Tonelli, M., Tornasi, Z., Torres-Forné, A., Torrie, C. I., Töyrä, D., Travasso, F., Traylor, G., Trinastic, J., Tringali, M. C., Trozzo, L., Tsang, K. W., Tse, M., Tso, R., Tsukada, L., Tsuna, D., Tuyenbayev, D., Ueno, K., Ugolini, D., Unnikrishnan, C. S., Urban, A. L., Usman, S. A., Vahlbruch, H., Vajente, G., Valdes, G., Vallisneri, M., Van Bakel, N., Van Beuzekom, M., Van Den Brand, J. F., Van Den Broeck, C., Vander-Hyde, D. C., Van Der Schaaf, L., Van Heijningen, J. V., Van Veggel, A. A., Vardaro, M., Varma, V., Vass, S., Vasúth, M., Vecchio, A., Vedovato, G., Veitch, J., Veitch, P. J., Venkateswara, K., Venugopalan, G., Verkindt, D., Vetrano, F., Viceré, A., Viets, A. D., Vinciguerra, S., Vine, D. J., Vinet, J. Y., Vitale, S., Vo, T., Vocca, H., Vorvick, C., Vyatchanin, S. P., Wade, A. R., Wade, L. E., Wade, M., Walet, R., Walker, M., Wallace, L., Walsh, S., Wang, G., Wang, H., Wang, J. Z., Wang, W. H., Wang, Y. F., Ward, R. L., Warner, J., Was, M., Watchi, J., Weaver, B., Wei, L. W., Weinert, M., Weinstein, A. J., Weiss, R., Wen, L., Wessel, E. K., Weßels, P., Westerweck, J., Westphal, T., Wette, K., Whelan, J. T., Whitcomb, S. E., Whiting, B. F., Whittle, C., Wilken, D., Williams, D., Williams, R. D., Williamson, A. R., Willis, J. L., Willke, B., Wimmer, M. H., Winkler, W., Wipf, C. C., Wittel, H., Woan, G., Woehler, J., Wofford, J., Wong, K. W., Worden, J., Wright, J. L., Wu, D. S., Wysocki, D. M., Xiao, S., Yamamoto, H., Yancey, C. C., Yang, L., Yap, M. J., Yazback, M., Yu, H., Yu, H., Yvert, M., Zadrożny, A., Zanolin, M., Zelenova, T., Zendri, J. P., Zevin, M., Zhang, L., Zhang, M., Zhang, T., Zhang, Y. H., Zhao, C., Zhou, M., Zhou, Z., Zhu, S. J., Zhu, X. J., Zimmerman, A. B., Zucker, M. E., and Zweizig, J. (2017a). GW170817: Observation of Gravitational Waves from a Binary Neutron Star Inspiral. *Phys. Rev. Lett.*, 119(16):161101.
- Abbott, B. P., Abbott, R., Abbott, T. D., Acernese, F., Ackley, K., Adams, C., Adams, T., Addesso, P., Adhikari, R. X., Adya, V. B., Affeldt, C., Afrough, M., Agarwal, B., Agathos, M., Agatsuma, K., Aggarwal, N., Aguiar, O. D., Aiello, L., Ain, A., Ajith, P., Allen, B., Allen, G., Allocca, A., Aloy, M. A., Altin, P. A., Amato, A., Ananyeva, A., Anderson, S. B., Anderson, W. G., Angelova, S. V., Antier, S., Appert, S., Arai, K., Araya, M. C., Areeda, J. S., Arnaud, N., Arun, K. G., Ascenzi, S., Ashton, G., Ast, M., Aston, S. M., Astone, P., Atallah, D. V., Aufmuth, P., Aulbert, C., AultONeal, K., Austin, C., Avila-Alvarez, A., Babak, S., Bacon, P., Bader, M. K., Bae, S., Baker, P. T., Baldaccini, F., Ballardín, G., Ballmer, S. W., Banagiri, S., Barayoga, J. C., Barclay, S. E., Barish, B. C., Barker, D., Barkett, K., Barone, F., Barr, B., Barsotti, L., Barsuglia, M., Barta, D., Bartlett, J., Bartos, I., Bassiri, R., Basti, A., Batch, J. C., Bawaj, M., Bayley, J. C., Bazzan, M., Bécsy, B., Beer, C., Bejger, M., Belahcene, I., Bell, A. S., Berger, B. K., Bergmann, G., Bero, J. J., Berry, C. P., Bersanetti, D., Bertolini, A., Betzwieser, J., Bhagwat, S., Bhandare, R., Bilenko, I. A., Billingsley, G., Billman, C. R., Birch, J., Birney, R., Birnholtz, O., Biscans, S., Biscoveanu, S., Bisht, A., Bitossi, M., Biwer, C., Bizouard, M. A., Blackburn, J. K., Blackman, J., Blair, C. D., Blair, D. G., Blair, R. M., Bloemen, S., Bock, O., Bode, N., Boer, M., Bogaert, G., Bohe, A., Bondu, F., Bonilla, E., Bonnard, R., Boom, B. A., Bork, R., Boschi, V., Bose, S., Bossie, K., Bouffanais, Y., Bozzi, A., Bradaschia, C., Brady, P. R., Branchesi, M., Brau, J. E., Briant, T., Brilliet, A., Brinkmann, M., Brisson, V., Brockill, P., Broida, J. E., Brooks, A. F., Brown, D. A., Brown, D. D., Brunett, S., Buchanan, C. C., Buikema, A., Bulik, T., Bulten, H. J., Buonanno, A., Buskulic, D., Buy, C., Byer, R. L., Cabero, M., Cadonati, L., Cagnoli, G., Cahillane, C., Calderón Bustillo, J., Callister, T. A., Calloni, E., Camp, J. B., Canepa, M., Canizares, P., Cannon, K. C., Cao, H., Cao, J., Capano, C. D., Capocasa, E., Carbognani, F., Caride, S., Carney, M. F., Casanueva Diaz, J., Casentini, C., Caudill, S., Cavaglià, M., Cavalier, F., Cavalieri, R., Cella, G., Cepeda,

C. B., Cerdá-Durán, P., Cerretani, G., Cesarini, E., Chamberlin, S. J., Chan, M., Chao, S., Charlton, P., Chase, E., Chassande-Mottin, E., Chatterjee, D., Chatziioannou, K., Cheeseboro, B. D., Chen, H. Y., Chen, X., Chen, Y., Cheng, H. P., Chia, H., Chincarini, A., Chiummo, A., Chmiel, T., Cho, H. S., Cho, M., Chow, J. H., Christensen, N., Chu, Q., Chua, A. J., Chua, S., Chung, A. K., Chung, S., Ciani, G., Ciolfi, R., Cirelli, C. E., Cirone, A., Clara, F., Clark, J. A., Clearwater, P., Cleva, F., Cocchieri, C., Coccia, E., Cohadon, P. F., Cohen, D., Colla, A., Collette, C. G., Cominsky, L. R., Constancio, M., Conti, L., Cooper, S. J., Corban, P., Corbitt, T. R., Cordero-Carrión, I., Corley, K. R., Cornish, N., Corsi, A., Cortese, S., Costa, C. A., Coughlin, M. W., Coughlin, S. B., Coulon, J. P., Countryman, S. T., Couvares, P., Covas, P. B., Cowan, E. E., Coward, D. M., Cowart, M. J., Coyne, D. C., Coyne, R., Creighton, J. D., Creighton, T. D., Cripe, J., Crowder, S. G., Cullen, T. J., Cumming, A., Cunningham, L., Cuoco, E., Dal Canton, T., Dálya, G., Danilishin, S. L., D'Antonio, S., Danzmann, K., Dasgupta, A., da Silva Costa, C. F., Dattilo, V., Dave, I., Davier, M., Davis, D., Daw, E. J., Day, B., De, S., DeBra, D., Degallaix, J., de Laurentis, M., Deléglise, S., Del Pozzo, W., Demos, N., Denker, T., Dent, T., de Pietri, R., Dergachev, V., de Rosa, R., DeRosa, R. T., de Rossi, C., DeSalvo, R., de Varona, O., Devenson, J., Dhurandhar, S., Díaz, M. C., Di Fiore, L., Di Giovanni, M., Di Girolamo, T., Di Lieto, A., Di Pace, S., Di Palma, I., Di Renzo, F., Doctor, Z., Dolique, V., Donovan, F., Dooley, K. L., Doravari, S., Dorrington, I., Douglas, R., Dovalé Álvarez, M., Downes, T. P., Drago, M., Dreissigacker, C., Driggers, J. C., Du, Z., Ducrot, M., Dupej, P., Dwyer, S. E., Edo, T. B., Edwards, M. C., Effler, A., Eggenstein, H. B., Ehrens, P., Eichholz, J., Eikenberry, S. S., Eisenstein, R. A., Essick, R. C., Estevez, D., Etienne, Z. B., Etzel, T., Evans, M., Evans, T. M., Factourovich, M., Fafone, V., Fair, H., Fairhurst, S., Fan, X., Farinon, S., Farr, B., Farr, W. M., Fauchon-Jones, E. J., Favata, M., Fays, M., Fee, C., Fehrmann, H., Feicht, J., Fejer, M. M., Fernandez-Galiana, A., Ferrante, I., Ferreira, E. C., Ferrini, F., Fidecaro, F., Finstad, D., Fiori, I., Fiorucci, D., Fishbach, M., Fisher, R. P., Fitz-Axen, M., Flaminio, R., Fletcher, M., Fong, H., Font, J. A., Forsyth, P. W., Forsyth, S. S., Fournier, J. D., Frasca, S., Frascioni, F., Frei, Z., Freise, A., Frey, R., Frey, V., Fries, E. M., Fritschel, P., Frolov, V. V., Fulda, P., Fyffe, M., Gabbard, H., Gadre, B. U., Gaebel, S. M., Gair, J. R., Gammaitoni, L., Ganija, M. R., Gaonkar, S. G., Garcia-Quiros, C., Garufi, F., Gateley, B., Gaudio, S., Gaur, G., Gayathri, V., Gehrels, N., Gemme, G., Genin, E., Gennai, A., George, D., George, J., Gergely, L., Germain, V., Ghonge, S., Ghosh, A., Ghosh, A., Ghosh, S., Giaime, J. A., Giardina, K. D., Giazotto, A., Gill, K., Glover, L., Goetz, E., Goetz, R., Gomes, S., Goncharov, B., González, G., Gonzalez Castro, J. M., Gopakumar, A., Gorodetsky, M. L., Gossan, S. E., Gosselin, M., Gouaty, R., Grado, A., Graef, C., Granata, M., Grant, A., Gras, S., Gray, C., Greco, G., Green, A. C., Gretarsson, E. M., Groot, P., Grote, H., Grunewald, S., Gruning, P., Guidi, G. M., Guo, X., Gupta, A., Gupta, M. K., Gushwa, K. E., Gustafson, E. K., Gustafson, R., Halim, O., Hall, B. R., Hall, E. D., Hamilton, E. Z., Hammond, G., Haney, M., Hanke, M. M., Hanks, J., Hanna, C., Hannam, M. D., Hannuksela, O. A., Hanson, J., Hardwick, T., Harms, J., Harry, G. M., Harry, I. W., Hart, M. J., Haster, C. J., Haughian, K., Healy, J., Heidmann, A., Heintze, M. C., Heitmann, H., Hello, P., Hemming, G., Hendry, M., Heng, I. S., Hennig, J., Heptonstall, A. W., Heurs, M., Hild, S., Hinderer, T., Hoak, D., Hofman, D., Holt, K., Holz, D. E., Hopkins, P., Horst, C., Hough, J., Houston, E. A., Howell, E. J., Hreibi, A., Hu, Y. M., Huerta, E. A., Huet, D., Hughey, B., Husa, S., Huttner, S. H., Huynh-Dinh, T., Indik, N., Inta, R., Intini, G., Isa, H. N., Isac, J. M., Isi, M., Iyer, B. R., Izumi, K., Jacqmin, T., Jani, K., Jaranowski, P., Jawahar, S., Jiménez-Forteza, F., Johnson, W. W., Johnson-McDaniel, N. K., Jones, D. I., Jones, R., Jonker, R. J., Ju, L., Junker, J., Kalaghatgi, C. V., Kalogera, V., Kamai, B., Kandhasamy, S.,

Kang, G., Kanner, J. B., Kapadia, S. J., Karki, S., Karvinen, K. S., Kasprzack, M., Kastaun, W., Katolik, M., Katsavounidis, E., Katzman, W., Kaufer, S., Kawabe, K., Kéfélian, F., Keitel, D., Kemball, A. J., Kennedy, R., Kent, C., Key, J. S., Khalili, F. Y., Khan, I., Khan, S., Khan, Z., Khazanov, E. A., Kijbunchoo, N., Kim, C., Kim, J. C., Kim, K., Kim, W., Kim, W. S., Kim, Y. M., Kimbrell, S. J., King, E. J., King, P. J., Kinley-Hanlon, M., Kirchhoff, R., Kissel, J. S., Kleybolte, L., Klimenko, S., Knowles, T. D., Koch, P., Koehlenbeck, S. M., Koley, S., Kondrashov, V., Kontos, A., Korobko, M., Korth, W. Z., Kowalska, I., Kozak, D. B., Krämer, C., Kringel, V., Krishnan, B., Królak, A., Kuehn, G., Kumar, P., Kumar, R., Kumar, S., Kuo, L., Kutynia, A., Kwang, S., Lackey, B. D., Lai, K. H., Landry, M., Lang, R. N., Lange, J., Lantz, B., Lanza, R. K., Lartaux-Vollard, A., Lasky, P. D., Laxen, M., Lazzarini, A., Lazzaro, C., Leaci, P., Leavey, S., Lee, C. H., Lee, H. K., Lee, H. M., Lee, H. W., Lee, K., Lehmann, J., Lenon, A., Leonardi, M., Leroy, N., Letendre, N., Levin, Y., Li, T. G., Linker, S. D., Littenberg, T. B., Liu, J., Lo, R. K., Lockerbie, N. A., London, L. T., Lord, J. E., Lorenzini, M., Lorette, V., Lormand, M., Losurdo, G., Lough, J. D., Lousto, C. O., Lovelace, G., Lück, H., Lumaca, D., Lundgren, A. P., Lynch, R., Ma, Y., Macas, R., Macfoy, S., Machenschalk, B., MacInnis, M., Macleod, D. M., Magaña Hernandez, I., Magaña-Sandoval, F., Magaña Zertuche, L., Magee, R. M., Majorana, E., Maksimovic, I., Man, N., Mandic, V., Mangano, V., Mansell, G. L., Manske, M., Mantovani, M., Marchesoni, F., Marion, F., Márka, S., Márka, Z., Markakis, C., Markosyan, A. S., Markowitz, A., Maros, E., Marquina, A., Martelli, F., Martellini, L., Martin, I. W., Martin, R. M., Martynov, D. V., Mason, K., Massera, E., Masserot, A., Massinger, T. J., Masso-Reid, M., Mastrogiovanni, S., Matas, A., Matichard, F., Matone, L., Mavalvala, N., Mazumder, N., McCarthy, R., McClelland, D. E., McCormick, S., McCuller, L., McGuire, S. C., McIntyre, G., McIver, J., McManus, D. J., McNeill, L., McRae, T., McWilliams, S. T., Meacher, D., Meadors, G. D., Mehmet, M., Meidam, J., Mejuto-Villa, E., Melatos, A., Mendell, G., Mercer, R. A., Merilh, E. L., Merzougui, M., Meshkov, S., Messenger, C., Messick, C., Metzdorff, R., Meyers, P. M., Miao, H., Michel, C., Middleton, H., Mikhailov, E. E., Milano, L., Miller, A. L., Miller, B. B., Miller, J., Millhouse, M., Milovich-Goff, M. C., Minazzoli, O., Minenkov, Y., Ming, J., Mishra, C., Mitra, S., Mitrofanov, V. P., Mitselmakher, G., Mittleman, R., Moffa, D., Moggi, A., Mogushi, K., Mohan, M., Mohapatra, S. R., Montani, M., Moore, C. J., Moraru, D., Moreno, G., Morriss, S. R., Mours, B., Mow-Lowry, C. M., Mueller, G., Muir, A. W., Mukherjee, A., Mukherjee, D., Mukherjee, S., Mukund, N., Mullavey, A., Munch, J., Muñiz, E. A., Muratore, M., Murray, P. G., Napier, K., Nardecchia, I., Naticchioni, L., Nayak, R. K., Neilson, J., Nelemans, G., Nelson, T. J., Nery, M., Neunzert, A., Nevin, L., Newport, J. M., Newton, G., Ng, K. K., Nguyen, T. T., Nichols, D., Nielsen, A. B., Nissanke, S., Nitz, A., Noack, A., Nocera, F., Nolting, D., North, C., Nuttall, L. K., Oberling, J., O'Dea, G. D., Ogin, G. H., Oh, J. J., Oh, S. H., Ohme, F., Okada, M. A., Oliver, M., Oppermann, P., Oram, R. J., O'Reilly, B., Ormiston, R., Ortega, L. F., O'Shaughnessy, R., Ossokine, S., Ottaway, D. J., Overmier, H., Owen, B. J., Pace, A. E., Page, J., Page, M. A., Pai, A., Pai, S. A., Palamos, J. R., Palashov, O., Palomba, C., Pal-Singh, A., Pan, H., Pan, H. W., Pang, B., Pang, P. T., Pankow, C., Pannarale, F., Pant, B. C., Paoletti, F., Paoli, A., Papa, M. A., Parida, A., Parker, W., Pascucci, D., Pasqualetti, A., Passaquieti, R., Passuello, D., Patil, M., Patricelli, B., Pearlstone, B. L., Pedraza, M., Pedurand, R., Pekowsky, L., Pele, A., Penn, S., Perez, C. J., Perreca, A., Perri, L. M., Pfeiffer, H. P., Phelps, M., Piccinni, O. J., Pichot, M., Piergiovanni, F., Pierro, V., Pillant, G., Pinard, L., Pinto, I. M., Pirello, M., Pitkin, M., Poe, M., Poggiani, R., Popolizio, P., Porter, E. K., Post, A., Powell, J., Prasad, J., Pratt, J. W., Pratten, G., Predoi, V., Prestegard, T., Prijatelj, M., Principe, M., Privitera, S., Prodi, G. A., Prokhorov, L. G.,

Puncken, O., Punturo, M., Puppo, P., Pürrer, M., Qi, H., Quetschke, V., Quintero, E. A., Quitzow-James, R., Raab, F. J., Rabeling, D. S., Radkins, H., Raffai, P., Raja, S., Rajan, C., Rajbhandari, B., Rakhmanov, M., Ramirez, K. E., Ramos-Buades, A., Rapagnani, P., Raymond, V., Razzano, M., Read, J., Regimbau, T., Rei, L., Reid, S., Reitze, D. H., Ren, W., Reyes, S. D., Ricci, F., Ricker, P. M., Rieger, S., Riles, K., Rizzo, M., Robertson, N. A., Robie, R., Robinet, F., Rocchi, A., Rolland, L., Rollins, J. G., Roma, V. J., Romano, R., Romel, C. L., Romie, J. H., Rosińska, D., Ross, M. P., Rowan, S., Rüdiger, A., Ruggi, P., Rutins, G., Ryan, K., Sachdev, S., Sadecki, T., Sadeghian, L., Sakellariadou, M., Salconi, L., Saleem, M., Salemi, F., Samajdar, A., Sammut, L., Sampson, L. M., Sanchez, E. J., Sanchez, L. E., Sanchis-Gual, N., Sandberg, V., Sanders, J. R., Sassolas, B., Sathyaprakash, B. S., Saulson, P. R., Sauter, O., Savage, R. L., Sawadsky, A., Schale, P., Scheel, M., Scheuer, J., Schmidt, J., Schmidt, P., Schnabel, R., Schofield, R. M., Schönbeck, A., Schreiber, E., Schuette, D., Schulte, B. W., Schutz, B. F., Schwalbe, S. G., Scott, J., Scott, S. M., Seidel, E., Sellers, D., Sengupta, A. S., Sentenac, D., Sequino, V., Sergeev, A., Shaddock, D. A., Shaffer, T. J., Shah, A. A., Shahriar, M. S., Shaner, M. B., Shao, L., Shapiro, B., Shawhan, P., Sheperd, A., Shoemaker, D. H., Shoemaker, D. M., Siellez, K., Siemens, X., Sieniawska, M., Sigg, D., Silva, A. D., Singer, L. P., Singh, A., Singhal, A., Sintès, A. M., Slagmolen, B. J., Smith, B., Smith, J. R., Smith, R. J., Somala, S., Son, E. J., Sonnenberg, J. A., Sorazu, B., Sorrentino, F., Souradeep, T., Spencer, A. P., Srivastava, A. K., Staats, K., Staley, A., Steinke, M., Steinlechner, J., Steinlechner, S., Steinmeyer, D., Stevenson, S. P., Stone, R., Stops, D. J., Strain, K. A., Stratta, G., Strigin, S. E., Strunk, A., Sturani, R., Stuver, A. L., Summerscales, T. Z., Sun, L., Sunil, S., Suresh, J., Sutton, P. J., Swinkels, B. L., Szczepańczyk, M. J., Tacca, M., Tait, S. C., Talbot, C., Talukder, D., Tanner, D. B., Tápai, M., Taracchini, A., Tasson, J. D., Taylor, J. A., Taylor, R., Tewari, S. V., Theeg, T., Thies, F., Thomas, E. G., Thomas, M., Thomas, P., Thorne, K. A., Thorne, K. S., Thrane, E., Tiwari, S., Tiwari, V., Tokmakov, K. V., Toland, K., Tonelli, M., Tornasi, Z., Torres-Forné, A., Torrie, C. I., Töyrä, D., Travasso, F., Traylor, G., Trinastic, J., Tringali, M. C., Trozzo, L., Tsang, K. W., Tse, M., Tso, R., Tsukada, L., Tsuna, D., Tuyenbayev, D., Ueno, K., Ugolini, D., Unnikrishnan, C. S., Urban, A. L., Usman, S. A., Vahlbruch, H., Vajente, G., Valdes, G., van Bakel, N., van Beuzekom, M., van den Brand, J. F., van Den Broeck, C., Vander-Hyde, D. C., van der Schaaf, L., van Heijningen, J. V., van Veggel, A. A., Vardaro, M., Varma, V., Vass, S., Vasúth, M., Vecchio, A., Vedovato, G., Veitch, J., Veitch, P. J., Venkateswara, K., Venugopalan, G., Verkindt, D., Vetrano, F., Viceré, A., Viets, A. D., Vinciguerra, S., Vine, D. J., Vinet, J. Y., Vitale, S., Vo, T., Vocca, H., Vorvick, C., Vyatchanin, S. P., Wade, A. R., Wade, L. E., Wade, M., Walet, R., Walker, M., Wallace, L., Walsh, S., Wang, G., Wang, H., Wang, J. Z., Wang, W. H., Wang, Y. F., Ward, R. L., Warner, J., Was, M., Watchi, J., Weaver, B., Wei, L. W., Weinert, M., Weinstein, A. J., Weiss, R., Wen, L., Wessel, E. K., Weßels, P., Westerweck, J., Westphal, T., Wette, K., Whelan, J. T., Whitcomb, S. E., Whiting, B. F., Whittle, C., Wilken, D., Williams, D., Williams, R. D., Williamson, A. R., Willis, J. L., Willke, B., Wimmer, M. H., Winkler, W., Wipf, C. C., Wittel, H., Woan, G., Woehler, J., Wofford, J., Wong, K. W., Worden, J., Wright, J. L., Wu, D. S., Wysocki, D. M., Xiao, S., Yamamoto, H., Yancey, C. C., Yang, L., Yap, M. J., Yazback, M., Yu, H., Yu, H., Yvert, M., Zadrożny, A., Zanolin, M., Zelenova, T., Zendri, J. P., Zevin, M., Zhang, L., Zhang, M., Zhang, T., Zhang, Y. H., Zhao, C., Zhou, M., Zhou, Z., Zhu, S. J., Zhu, X. J., Zimmerman, A. B., Zucker, M. E., Zweizig, J., Burns, E., Veres, P., Kocevski, D., Racusin, J., Goldstein, A., Connaughton, V., Briggs, M. S., Blackburn, L., Hamburg, R., Hui, C. M., von Kienlin, A., McEnery, J., Preece, R. D., Wilson-Hodge, C. A., Bissaldi, E., Cleveland, W. H., Gibby, M. H., Giles, M. M., Kippen, R. M., McBreen, S.,

- Meegan, C. A., Pacieras, W. S., Poolakkil, S., Roberts, O. J., Stanbro, M., Savchenko, V., Ferrigno, C., Kuulkers, E., Bazzano, A., Bozzo, E., Brandt, S., Chenevez, J., Courvoisier, T. J., Diehl, R., Domingo, A., Hanlon, L., Jourdain, E., Laurent, P., Lebrun, F., Lutovinov, A., Mereghetti, S., Natalucci, L., Rodi, J., Roques, J. P., Sunyaev, R., and Ubertini, P. (2017b). Gravitational waves and gamma-rays from a binary neutron star merger: GW170817 and GRB 170817A. *ApJL*, 848(2):L13.
- Abbott, R., Abbott, T. D., Abraham, S., Acernese, F., Ackley, K., Adams, C., Adhikari, R. X., Adya, V. B., Affeldt, C., Agathos, M., Agatsuma, K., Aggarwal, N., Aguiar, O. D., Aich, A., Aiello, L., Ain, A., Ajith, P., Akcay, S., Allen, G., Allocca, A., Altin, P. A., Amato, A., Anand, S., Ananyeva, A., Anderson, S. B., Anderson, W. G., Angelova, S. V., Ansoldi, S., Antier, S., Appert, S., Arai, K., Araya, M. C., Areeda, J. S., Arène, M., Arnaud, N., Aronson, S. M., Arun, K. G., Asali, Y., Ascenzi, S., Ashton, G., Aston, S. M., Astone, P., Aubin, F., Aufmuth, P., Aultoneal, K., Austin, C., Avendano, V., Babak, S., Bacon, P., Badaracco, F., Bader, M. K., Bae, S., Baer, A. M., Baird, J., Baldaccini, F., Ballardín, G., Ballmer, S. W., Bals, A., Balsamo, A., Baltus, G., Banagiri, S., Bankar, D., Bankar, R. S., Barayoga, J. C., Barbieri, C., Barish, B. C., Barker, D., Barkett, K., Barneo, P., Barone, F., Barr, B., Barsotti, L., Barsuglia, M., Barta, D., Bartlett, J., Bartos, I., Bassiri, R., Basti, A., Bawaj, M., Bayley, J. C., Bazzan, M., Bécsy, B., Bejger, M., Belahcene, I., Bell, A. S., Beniwal, D., Benjamin, M. G., Bentley, J. D., Bergamin, F., Berger, B. K., Bergmann, G., Bernuzzi, S., Berry, C. P., Bersanetti, D., Bertolini, A., Betzwieser, J., Bhandare, R., Bhandari, A. V., Bidler, J., Biggs, E., Bilenko, I. A., Billingsley, G., Birney, R., Birnholtz, O., Biscans, S., Bisch, M., Biscoveanu, S., Bisht, A., Bissenbayeva, G., Bitossi, M., Bizouard, M. A., Blackburn, J. K., Blackman, J., Blair, C. D., Blair, D. G., Blair, R. M., Bobba, F., Bode, N., Boer, M., Boetzel, Y., Bogaert, G., Bondu, F., Bonilla, E., Bonnand, R., Booker, P., Boom, B. A., Bork, R., Boschi, V., Bose, S., Bossilkov, V., Bosveld, J., Bouffanais, Y., Bozzi, A., Bradaschia, C., Brady, P. R., Bramley, A., Branchesi, M., Brau, J. E., Breschi, M., Briant, T., Briggs, J. H., Brighenti, F., Brilliet, A., Brinkmann, M., Brockill, P., Brooks, A. F., Brooks, J., Brown, D. D., Brunett, S., Bruno, G., Bruntz, R., Buikema, A., Bulik, T., Bulten, H. J., Buonanno, A., Buscicchio, R., Buskulic, D., Byer, R. L., Cabero, M., Cadonati, L., Cagnoli, G., Cahillane, C., Calderón Bustillo, J., Callaghan, J. D., Callister, T. A., Calloni, E., Camp, J. B., Canepa, M., Cannon, K. C., Cao, H., Cao, J., Carapella, G., Carbognani, F., Caride, S., Carney, M. F., Carullo, G., Casanueva Diaz, J., Casentini, C., Castañeda, J., Caudill, S., Cavaglià, M., Cavalier, F., Cavalieri, R., Cella, G., Cerdá-Durán, P., Cesarini, E., Chaibi, O., Chakravarti, K., Chan, C., Chan, M., Chandra, K., Chao, S., Charlton, P., Chase, E. A., Chassande-Mottin, E., Chatterjee, D., Chaturvedi, M., Chatziioannou, K., Chen, H. Y., Chen, X., Chen, Y., Cheng, H. P., Cheong, C. K., Chia, H. Y., Chiadini, F., Chierici, R., Chincarini, A., Chiummo, A., Cho, G., Cho, H. S., Cho, M., Christensen, N., Chu, Q., Chua, S., Chung, K. W., Chung, S., Ciani, G., Ciecielag, P., Cieřlar, M., Ciobanu, A. A., Ciolfi, R., Cipriano, F., Cirone, A., Clara, F., Clark, J. A., Clearwater, P., Clesse, S., Cleva, F., Coccia, E., Cohadon, P. F., Cohen, D., Colleoni, M., Collette, C. G., Collins, C., Colpi, M., Constancio, M., Conti, L., Cooper, S. J., Corban, P., Corbitt, T. R., Cordero-Carrión, I., Corezzi, S., Corley, K. R., Cornish, N., Corre, D., Corsi, A., Cortese, S., Costa, C. A., Cotesta, R., Coughlin, M. W., Coughlin, S. B., Coulon, J. P., Countryman, S. T., Couvares, P., Covas, P. B., Coward, D. M., Cowart, M. J., Coyne, D. C., Coyne, R., Creighton, J. D., Creighton, T. D., Cripe, J., Croquette, M., Crowder, S. G., Cudell, J. R., Cullen, T. J., Cumming, A., Cummings, R., Cunningham, L., Cuoco, E., Curylo, M., Canton, T. D., Dálya, G., Dana, A., Daneshgaran-Bajastani, L. M., D'Angelo, B., Danilishin, S. L., D'Antonio, S.,

Danzmann, K., Darsow-Fromm, C., Dasgupta, A., Datrier, L. E., Dattilo, V., Dave, I., Davier, M., Davies, G. S., Davis, D., Daw, E. J., Debra, D., Deenadayalan, M., Degallaix, J., De Laurentis, M., Deléglise, S., Delfavero, M., De Lillo, N., Del Pozzo, W., Demarchi, L. M., D'Emilio, V., Demos, N., Dent, T., De Pietri, R., De Rosa, R., De Rossi, C., Desalvo, R., De Varona, O., Dhurandhar, S., Díaz, M. C., Diaz-Ortiz, M., Dietrich, T., Di Fiore, L., Di Fronzo, C., Di Giorgio, C., Di Giovanni, F., Di Giovanni, M., Di Girolamo, T., Di Lieto, A., Ding, B., Di Pace, S., Di Palma, I., Di Renzo, F., Divakarla, A. K., Dmitriev, A., Doctor, Z., Donovan, F., Dooley, K. L., Doravari, S., Dorrington, I., Downes, T. P., Drago, M., Driggers, J. C., Du, Z., Ducoin, J. G., Dupej, P., Durante, O., D'Urso, D., Dwyer, S. E., Easter, P. J., Eddolls, G., Edelman, B., Edo, T. B., Edy, O., Effler, A., Ehrens, P., Eichholz, J., Eikenberry, S. S., Eisenmann, M., Eisenstein, R. A., Ejlli, A., Errico, L., Essick, R. C., Estelles, H., Estevez, D., Etienne, Z. B., Etzel, T., Evans, M., Evans, T. M., Ewing, B. E., Fafone, V., Fairhurst, S., Fan, X., Farinon, S., Farr, B., Farr, W. M., Fauchon-Jones, E. J., Favata, M., Fays, M., Fazio, M., Feicht, J., Fejer, M. M., Feng, F., Fenyvesi, E., Ferguson, D. L., Fernandez-Galiana, A., Ferrante, I., Ferreira, E. C., Ferreira, T. A., Fidecaro, F., Fiori, I., Fiorucci, D., Fishbach, M., Fisher, R. P., Fittipaldi, R., Fitz-Axen, M., Fiumara, V., Flaminio, R., Floden, E., Flynn, E., Fong, H., Font, J. A., Forsyth, P. W., Fournier, J. D., Frasca, S., Frasconi, F., Frei, Z., Freise, A., Frey, R., Frey, V., Fritschel, P., Frolov, V. V., Fronzè, G., Fulda, P., Fyffe, M., Gabbard, H. A., Gadre, B. U., Gaebel, S. M., Gair, J. R., Galaudage, S., Ganapathy, D., Ganguly, A., Gaonkar, S. G., García-Quirós, C., Garufi, F., Gateley, B., Gaudio, S., Gayathri, V., Gemme, G., Genin, E., Gennai, A., George, D., George, J., Gergely, L., Ghonge, S., Ghosh, A., Ghosh, A., Ghosh, S., Giacomazzo, B., Giaime, J. A., Giardina, K. D., Gibson, D. R., Gier, C., Gill, K., Glanzer, J., Gniesmer, J., Godwin, P., Goetz, E., Goetz, R., Gohlke, N., Goncharov, B., González, G., Gopakumar, A., Gossan, S. E., Gosselin, M., Gouaty, R., Grace, B., Grado, A., Granata, M., Grant, A., Gras, S., Grassia, P., Gray, C., Gray, R., Greco, G., Green, A. C., Green, R., Gretarsson, E. M., Griggs, H. L., Grignani, G., Grimaldi, A., Grimm, S. J., Grote, H., Grunewald, S., Gruning, P., Guidi, G. M., Guimaraes, A. R., Guixé, G., Gulati, H. K., Guo, Y., Gupta, A., Gupta, A., Gupta, P., Gustafson, E. K., Gustafson, R., Haegel, L., Halim, O., Hall, E. D., Hamilton, E. Z., Hammond, G., Haney, M., Hanke, M. M., Hanks, J., Hanna, C., Hannam, M. D., Hannuksela, O. A., Hansen, T. J., Hanson, J., Harder, T., Hardwick, T., Haris, K., Harms, J., Harry, G. M., Harry, I. W., Hasskew, R. K., Haster, C. J., Haughian, K., Hayes, F. J., Healy, J., Heidmann, A., Heintze, M. C., Heinze, J., Heitmann, H., Hellman, F., Hello, P., Hemming, G., Hendry, M., Heng, I. S., Hennes, E., Hennig, J., Heurs, M., Hild, S., Hinderer, T., Hoback, S. Y., Hochheim, S., Hofgard, E., Hofman, D., Holgado, A. M., Holland, N. A., Holt, K., Holz, D. E., Hopkins, P., Horst, C., Hough, J., Howell, E. J., Hoy, C. G., Huang, Y., Hübner, M. T., Huerta, E. A., Huet, D., Hughey, B., Hui, V., Husa, S., Huttner, S. H., Huxford, R., Huynh-Dinh, T., Idzkowski, B., Iess, A., Inchauspe, H., Ingram, C., Intini, G., Isac, J. M., Isi, M., Iyer, B. R., Jacqmin, T., Jadhav, S. J., Jadhav, S. P., James, A. L., Jani, K., Janthapur, N. N., Jaranowski, P., Jariwala, D., Jaume, R., Jenkins, A. C., Jiang, J., Johns, G. R., Johnson-Mcdaniel, N. K., Jones, A. W., Jones, D. I., Jones, J. D., Jones, P., Jones, R., Jonker, R. J., Ju, L., Junker, J., Kalaghatgi, C. V., Kalogera, V., Kamai, B., Kandhasamy, S., Kang, G., Kanner, J. B., Kapadia, S. J., Karki, S., Kashyap, R., Kasprzack, M., Kastaun, W., Katsanevas, S., Katsavounidis, E., Katzman, W., Kaufer, S., Kawabe, K., Kéfélian, F., Keitel, D., Keivani, A., Kennedy, R., Key, J. S., Khadka, S., Khalili, F. Y., Khan, I., Khan, S., Khan, Z. A., Khazanov, E. A., Khetan, N., Khursheed, M., Kijbunchoo, N., Kim, C., Kim, G. J., Kim, J. C., Kim, K., Kim, W., Kim, W. S., Kim, Y. M., Kimball, C., King, P. J., Kinley-Hanlon, M., Kirchhoff, R., Kissel, J. S., Kleybolte, L., Klimenko, S., Knowles,

T. D., Knyazev, E., Koch, P., Koehlenbeck, S. M., Koekoek, G., Koley, S., Kondrashov, V., Kontos, A., Koper, N., Korobko, M., Korth, W. Z., Kovalam, M., Kozak, D. B., Kringel, V., Krishnendu, N. V., Królak, A., Krupinski, N., Kuehn, G., Kumar, A., Kumar, P., Kumar, R., Kumar, R., Kumar, S., Kuo, L., Kutynia, A., Lackey, B. D., Laghi, D., Lalande, E., Lam, T. L., Lamberts, A., Landry, M., Lane, B. B., Lang, R. N., Lange, J., Lantz, B., Lanza, R. K., La Rosa, I., Lartaux-Vollard, A., Lasky, P. D., Laxen, M., Lazzarini, A., Lazzaro, C., Leaci, P., Leavey, S., Lecoeuche, Y. K., Lee, C. H., Lee, H. M., Lee, H. W., Lee, J., Lee, K., Lehmann, J., Leroy, N., Letendre, N., Levin, Y., Li, A. K., Li, J., Li, K., Li, T. G., Li, X., Linde, F., Linker, S. D., Linley, J. N., Littenberg, T. B., Liu, J., Liu, X., Llorens-Monteaugudo, M., Lo, R. K., Lockwood, A., London, L. T., Longo, A., Lorenzini, M., Lorette, V., Lormand, M., Losurdo, G., Lough, J. D., Lousto, C. O., Lovelace, G., Lück, H., Lumaca, D., Lundgren, A. P., Ma, Y., Macas, R., Macfoy, S., Macinnis, M., Macleod, D. M., Macmillan, I. A., Macquet, A., Magaña Hernandez, I., Magaña-Sandoval, F., Magee, R. M., Majorana, E., Maksimovic, I., Malik, A., Man, N., Mandic, V., Mangano, V., Mansell, G. L., Manske, M., Mantovani, M., Mapelli, M., Marchesoni, F., Marion, F., Márka, S., Márka, Z., Markakis, C., Markosyan, A. S., Markowitz, A., Maros, E., Marquina, A., Marsat, S., Martelli, F., Martin, I. W., Martin, R. M., Martinez, V., Martynov, D. V., Masalehdan, H., Mason, K., Massera, E., Masserot, A., Massinger, T. J., Masso-Reid, M., Mastrogiovanni, S., Matas, A., Matichard, F., Mavalvala, N., Maynard, E., McCann, J. J., McCarthy, R., McClelland, D. E., McCormick, S., McCuller, L., McGuire, S. C., McIsaac, C., McIver, J., McManus, D. J., McRae, T., McWilliams, S. T., Meacher, D., Meadors, G. D., Mehmet, M., Mehta, A. K., Mejuto Villa, E., Melatos, A., Mendell, G., Mercer, R. A., Mereni, L., Merfeld, K., Merilh, E. L., Merritt, J. D., Merzougui, M., Meshkov, S., Messenger, C., Messick, C., Metzдорff, R., Meyers, P. M., Meylahn, F., Mhaske, A., Miani, A., Miao, H., Michaloliakos, I., Michel, C., Middleton, H., Milano, L., Miller, A. L., Millhouse, M., Mills, J. C., Milotti, E., Milovich-Goff, M. C., Minazzoli, O., Minenkov, Y., Mishkin, A., Mishra, C., Mistry, T., Mitra, S., Mitrofanov, V. P., Mitselmakher, G., Mittleman, R., Mo, G., Mogushi, K., Mohapatra, S. R., Mohite, S. R., Molina-Ruiz, M., Mondin, M., Montani, M., Moore, C. J., Moraru, D., Morawski, F., Moreno, G., Morisaki, S., Mours, B., Mow-Lowry, C. M., Mozzon, S., Muciaccia, F., Mukherjee, A., Mukherjee, D., Mukherjee, S., Mukherjee, S., Mukund, N., Mullavey, A., Munch, J., Muñoz, E. A., Murray, P. G., Nagar, A., Nardecchia, I., Naticchioni, L., Nayak, R. K., Neil, B. F., Neilson, J., Nelemans, G., Nelson, T. J., Nery, M., Neunzert, A., Ng, K. Y., Ng, S., Nguyen, C., Nguyen, P., Nichols, D., Nichols, S. A., Nissanke, S., Nitz, A., Nocera, F., Noh, M., North, C., Nothard, D., Nuttall, L. K., Oberling, J., O'Brien, B. D., Oganessian, G., Ogini, G. H., Oh, J. J., Oh, S. H., Ohme, F., Ohta, H., Okada, M. A., Oliver, M., Olivetto, C., Oppermann, P., Oram, R. J., O'Reilly, B., Ormiston, R. G., Ortega, L. F., O'Shaughnessy, R., Ossokine, S., Osthelder, C., Ottaway, D. J., Overmier, H., Owen, B. J., Pace, A. E., Pagano, G., Page, M. A., Pagliaroli, G., Pai, A., Pai, S. A., Palamos, J. R., Palashov, O., Palomba, C., Pan, H., Panda, P. K., Pang, P. T., Pankow, C., Pannarale, F., Pant, B. C., Paoletti, F., Paoli, A., Parida, A., Parker, W., Pascucci, D., Pasqualetti, A., Passaquieti, R., Passuello, D., Patricelli, B., Payne, E., Pearlstone, B. L., Pechsiri, T. C., Pedersen, A. J., Pedraza, M., Pele, A., Penn, S., Perego, A., Perez, C. J., Périgois, C., Perreca, A., Perriès, S., Petermann, J., Pfeiffer, H. P., Phelps, M., Phukon, K. S., Piccinni, O. J., Pichot, M., Piendibene, M., Piergiovanni, F., Pierro, V., Pillant, G., Pinard, L., Pinto, I. M., Piotrkowski, K., Pirello, M., Pitkin, M., Plastino, W., Poggiani, R., Pong, D. Y., Ponrathnam, S., Popolizio, P., Porter, E. K., Powell, J., Prajapati, A. K., Prasai, K., Prasanna, R., Pratten, G., Prestegard, T., Principe, M., Prodi, G. A., Prokhorov, L., Punturo, M., Puppo, P., Pürerer, M., Qi, H., Quetschke, V., Quinonez, P. J., Raab, F. J., Raaijmakers,

G., Radkins, H., Radulesco, N., Raffai, P., Rafferty, H., Raja, S., Rajan, C., Rajbhandari, B., Rakhmanov, M., Ramirez, K. E., Ramos-Buades, A., Rana, J., Rao, K., Rapagnani, P., Raymond, V., Razzano, M., Read, J., Regimbau, T., Rei, L., Reid, S., Reitze, D. H., Rettengo, P., Ricci, F., Richardson, C. J., Richardson, J. W., Ricker, P. M., Riemenschneider, G., Riles, K., Rizzo, M., Robertson, N. A., Robinet, F., Rocchi, A., Rodriguez-Soto, R. D., Rolland, L., Rollins, J. G., Roma, V. J., Romanelli, M., Romano, R., Romel, C. L., Romero-Shaw, I. M., Romie, J. H., Rose, C. A., Rose, D., Rose, K., Rosińska, D., Rosofsky, S. G., Ross, M. P., Rowan, S., Rowlinson, S. J., Roy, P. K., Roy, S., Roy, S., Ruggi, P., Rutins, G., Ryan, K., Sachdev, S., Sadecki, T., Sakellariadou, M., Salafia, O. S., Salconi, L., Saleem, M., Salemi, F., Samajdar, A., Sanchez, E. J., Sanchez, L. E., Sanchis-Gual, N., Sanders, J. R., Santiago, K. A., Santos, E., Sarin, N., Sassolas, B., Sathyaprakash, B. S., Sauter, O., Savage, R. L., Savant, V., Sawant, D., Sayah, S., Schaetzel, D., Schale, P., Scheel, M., Scheuer, J., Schmidt, P., Schnabel, R., Schofield, R. M., Schönbeck, A., Schreiber, E., Schulte, B. W., Schutz, B. F., Schwarm, O., Schwartz, E., Scott, J., Scott, S. M., Seidel, E., Sellers, D., Sengupta, A. S., Sennett, N., Sentenac, D., Sequino, V., Sergeev, A., Setyawati, Y., Shaddock, D. A., Shaffer, T., Sharifi, S., Shahriar, M. S., Sharma, A., Sharma, P., Shawhan, P., Shen, H., Shikauchi, M., Shink, R., Shoemaker, D. H., Shoemaker, D. M., Shukla, K., Shyamsundar, S., Siellez, K., Sieniawska, M., Sigg, D., Singer, L. P., Singh, D., Singh, N., Singha, A., Singhal, A., Sintès, A. M., Sipala, V., Skliris, V., Slagmolen, B. J., Slaven-Blair, T. J., Smetana, J., Smith, J. R., Smith, R. J., Somala, S., Son, E. J., Soni, S., Sorazu, B., Sordini, V., Sorrentino, F., Souradeep, T., Sowell, E., Spencer, A. P., Spera, M., Srivastava, A. K., Srivastava, V., Staats, K., Stachie, C., Standke, M., Steer, D. A., Steinke, M., Steinlechner, J., Steinlechner, S., Steinmeyer, D., Stevenson, S., Stocks, D., Stops, D. J., Stover, M., Strain, K. A., Stratta, G., Strunk, A., Sturani, R., Stuver, A. L., Sudhagar, S., Sudhir, V., Summerscales, T. Z., Sun, L., Sunil, S., Sur, A., Suresh, J., Sutton, P. J., Swinkels, B. L., Szczepańczyk, M. J., Tacca, M., Tait, S. C., Talbot, C., Tanasijczuk, A. J., Tanner, D. B., Tao, D., Tápai, M., Tapia, A., Tapia San Martin, E. N., Tasson, J. D., Taylor, R., Tenorio, R., Terkowski, L., Thirugnanasambandam, M. P., Thomas, M., Thomas, P., Thompson, J. E., Thondapu, S. R., Thorne, K. A., Thrane, E., Tinsman, C. L., Saravanan, T. R., Tiwari, S., Tiwari, S., Tiwari, V., Toland, K., Tonelli, M., Tornasi, Z., Torres-Forné, A., Torrie, C. I., Tosta E Melo, I., Töyrä, D., Travasso, F., Traylor, G., Tringali, M. C., Tripathee, A., Trovato, A., Trudeau, R. J., Tsang, K. W., Tse, M., Tso, R., Tsukada, L., Tsuna, D., Tsutsui, T., Turconi, M., Ubhi, A. S., Udall, R., Ueno, K., Ugolini, D., Unnikrishnan, C. S., Urban, A. L., Usman, S. A., Utina, A. C., Vahlbruch, H., Vajente, G., Valdes, G., Valentini, M., Van Bakel, N., Van Beuzekom, M., Van Den Brand, J. F., Van Den Broeck, C., Vander-Hyde, D. C., Van Der Schaaf, L., Van Heijningen, J. V., Van Veggel, A. A., Vardaro, M., Varma, V., Vass, S., Vasúth, M., Vecchio, A., Vedovato, G., Veitch, J., Veitch, P. J., Venkateswara, K., Venugopalan, G., Verkindt, D., Veske, D., Vetrano, F., Viceré, A., Viets, A. D., Vinciguerra, S., Vine, D. J., Vinet, J. Y., Vitale, S., Vivanco, F. H., Vo, T., Vocca, H., Vorvick, C., Vyatchanin, S. P., Wade, A. R., Wade, L. E., Wade, M., Walet, R., Walker, M., Wallace, G. S., Wallace, L., Walsh, S., Wang, J. Z., Wang, S., Wang, W. H., Ward, R. L., Warden, Z. A., Warner, J., Was, M., Watchi, J., Weaver, B., Wei, L. W., Weinert, M., Weinstein, A. J., Weiss, R., Wellmann, F., Wen, L., Weßels, P., Westhouse, J. W., Wette, K., Whelan, J. T., Whiting, B. F., Whittle, C., Wilken, D. M., Williams, D., Willis, J. L., Willke, B., Winkler, W., Wipf, C. C., Wittel, H., Woan, G., Woehler, J., Wofford, J. K., Wong, I. C., Wright, J. L., Wu, D. S., Wysocki, D. M., Xiao, L., Yamamoto, H., Yang, L., Yang, Y., Yang, Z., Yap, M. J., Yazback, M., Yeeles, D. W., Yu, H., Yu, H., Yuen, S. H., Zadrożny, A. K., Zadrożny, A., Zanolin, M., Zelenova, T., Zendri, J. P., Zevin, M., Zhang, J., Zhang, L., Zhang,

- T., Zhao, C., Zhao, G., Zhou, M., Zhou, Z., Zhu, X. J., Zimmerman, A. B., Zucker, M. E., and Zweizig, J. (2020b). GW190521: A Binary Black Hole Merger with a Total Mass of 150  $M_{\odot}$ . *Phys. Rev. Lett.*, 125(10):101102.
- Ade, P. A., Aghanim, N., Arnaud, M., Ashdown, M., Aumont, J., Baccigalupi, C., Banday, A. J., Barreiro, R. B., Bartlett, J. G., Bartolo, N., Battaner, E., Battye, R., Benabed, K., Benoît, A., Benoit-Lévy, A., Bernard, J. P., Bersanelli, M., Bielewicz, P., Bock, J. J., Bonaldi, A., Bonavera, L., Bond, J. R., Borrill, J., Bouchet, F. R., Boulanger, F., Bucher, M., Burigana, C., Butler, R. C., Calabrese, E., Cardoso, J. F., Catalano, A., Challinor, A., Chamballu, A., Chary, R. R., Chiang, H. C., Chluba, J., Christensen, P. R., Church, S., Clements, D. L., Colombi, S., Colombo, L. P., Combet, C., Coulais, A., Crill, B. P., Curto, A., Cuttaia, F., Danese, L., Davies, R. D., Davis, R. J., De Bernardis, P., De Rosa, A., De Zotti, G., Delabrouille, J., Désert, F. X., Di Valentino, E., Dickinson, C., Diego, J. M., Dolag, K., Dole, H., Donzelli, S., Doré, O., Douspis, M., Ducout, A., Dunkley, J., Dupac, X., Efstathiou, G., Elsner, F., Enßlin, T. A., Eriksen, H. K., Farhang, M., Fergusson, J., Finelli, F., Forni, O., Frailis, M., Fraisse, A. A., Franceschi, E., Frejsel, A., Galeotta, S., Galli, S., Ganga, K., Gauthier, C., Gerbino, M., Ghosh, T., Giard, M., Giraud-Héraud, Y., Giusarma, E., Gjerløw, E., González-Nuevo, J., Górski, K. M., Gratton, S., Gregorio, A., Gruppuso, A., Gudmundsson, J. E., Hamann, J., Hansen, F. K., Hanson, D., Harrison, D. L., Helou, G., Henrot-Versillé, S., Hernández-Monteagudo, C., Herranz, D., Hildebrandt, S. R., Hivon, E., Hobson, M., Holmes, W. A., Hornstrup, A., Hovest, W., Huang, Z., Huppenberger, K. M., Hurier, G., Jaffe, A. H., Jaffe, T. R., Jones, W. C., Juvela, M., Keihänen, E., Keskitalo, R., Kisner, T. S., Kneissl, R., Knoche, J., Knox, L., Kunz, M., Kurki-Suonio, H., Lagache, G., Lähteenmäki, A., Lamarre, J. M., Lasenby, A., Lattanzi, M., Lawrence, C. R., Leahy, J. P., Leonardi, R., Lesgourgues, J., Levrier, F., Lewis, A., Liguori, M., Lilje, P. B., Linden-Vørnle, M., López-Caniego, M., Lubin, P. M., Macías-Pérez, J. F., Maggio, G., Maino, D., Mandolesi, N., Mangilli, A., Marchini, A., Maris, M., Martin, P. G., Martinelli, M., Martínez-González, E., Masi, S., Matarrese, S., McGehee, P., Meinhold, P. R., Melchiorri, A., Melin, J. B., Mendes, L., Mennella, A., Migliaccio, M., Millea, M., Mitra, S., Miville-Deschênes, M. A., Moneti, A., Montier, L., Morgante, G., Mortlock, D., Moss, A., Munshi, D., Murphy, J. A., Naselsky, P., Nati, F., Natoli, P., Netterfield, C. B., Nørgaard-Nielsen, H. U., Noviello, F., Novikov, D., Novikov, I., Oxborrow, C. A., Paci, F., Pagano, L., Pajot, F., Paladini, R., Paoletti, D., Partridge, B., Pasian, F., Patanchon, G., Pearson, T. J., Perdereau, O., Perotto, L., Perrotta, F., Pettorino, V., Piacentini, F., Piat, M., Pierpaoli, E., Pietrobon, D., Plaszczyński, S., Pointecouteau, E., Polenta, G., Popa, L., Pratt, G. W., Prézeau, G., Prunet, S., Puget, J. L., Rachen, J. P., Reach, W. T., Rebolo, R., Reinecke, M., Remazeilles, M., Renault, C., Renzi, A., Ristorcelli, I., Rocha, G., Rosset, C., Rossetti, M., Roudier, G., Rouillé D'orfeuille, B., Rowan-Robinson, M., Rubinó-Martín, J. A., Rusholme, B., Said, N., Salvatelli, V., Salvati, L., Sandri, M., Santos, D., Savelainen, M., Savini, G., Scott, D., Seiffert, M. D., Serra, P., Shellard, E. P., Spencer, L. D., Spinelli, M., Stolyarov, V., Stompor, R., Sudiwala, R., Sunyaev, R., Sutton, D., Suur-Uski, A. S., Sygnet, J. F., Tauber, J. A., Terenzi, L., Toffolatti, L., Tomasi, M., Tristram, M., Trombetti, T., Tucci, M., Tuovinen, J., Türler, M., Umaga, G., Valenziano, L., Valiviita, J., Van Tent, F., Vielva, P., Villa, F., Wade, L. A., Wandelt, B. D., Wehus, I. K., White, M., White, S. D., Wilkinson, A., Yvon, D., Zacchei, A., and Zonca, A. (2016). Planck 2015 results: XIII. Cosmological parameters. *A&A*, 594:A13.
- Aghanim, N., Akrami, Y., Ashdown, M., Aumont, J., Baccigalupi, C., Ballardini, M., Banday, A. J., Barreiro, R. B., Bartolo, N., Basak, S., Battye, R., Benabed, K., Bernard, J. P., Bersanelli,

- M., Bielewicz, P., Bock, J. J., Bond, J. R., Borrill, J., Bouchet, F. R., Boulanger, F., Bucher, M., Burigana, C., Butler, R. C., Calabrese, E., Cardoso, J. F., Carron, J., Challinor, A., Chiang, H. C., Chluba, J., Colombo, L. P., Combet, C., Contreras, D., Crill, B. P., Cuttaia, F., De Bernardis, P., De Zotti, G., Delabrouille, J., Delouis, J. M., Di Valentino, E., Diego, J. M., Doré, O., Douspis, M., Ducout, A., Dupac, X., Dusini, S., Efstathiou, G., Elsner, F., Enßlin, T. A., Eriksen, H. K., Fantaye, Y., Farhang, M., Fergusson, J., Fernandez-Cobos, R., Finelli, F., Forastieri, F., Frailis, M., Fraisse, A. A., Franceschi, E., Frolov, A., Galeotta, S., Galli, S., Ganga, K., Génova-Santos, R. T., Gerbino, M., Ghosh, T., González-Nuevo, J., Górski, K. M., Gratton, S., Gruppuso, A., Gudmundsson, J. E., Hamann, J., Handley, W., Hansen, F. K., Herranz, D., Hildebrandt, S. R., Hivon, E., Huang, Z., Jaffe, A. H., Jones, W. C., Karacik, A., Keihänen, E., Keskitalo, R., Kiiveri, K., Kim, J., Kisner, T. S., Knox, L., Krachmalnicoff, N., Kunz, M., Kurki-Suonio, H., Lagache, G., Lamarre, J. M., Lasenby, A., Lattanzi, M., Lawrence, C. R., Le Jeune, M., Lemos, P., Lesgourgues, J., Levrier, F., Lewis, A., Liguori, M., Lilje, P. B., Lilley, M., Lindholm, V., López-Cañiego, M., Lubin, P. M., Ma, Y. Z., Maciás-Pérez, J. F., Maggio, G., Maino, D., Mandolesi, N., Mangilli, A., Marcos-Caballero, A., Maris, M., Martin, P. G., Martinelli, M., Martínez-González, E., Matarrese, S., Mauri, N., McEwen, J. D., Meinhold, P. R., Melchiorri, A., Mennella, A., Migliaccio, M., Millea, M., Mitra, S., Miville-Deschênes, M. A., Molinari, D., Montier, L., Morgante, G., Moss, A., Natoli, P., Nørgaard-Nielsen, H. U., Pagano, L., Paoletti, D., Partridge, B., Patanchon, G., Peiris, H. V., Perrotta, F., Pettorino, V., Piacentini, F., Polastri, L., Polenta, G., Puget, J. L., Rachen, J. P., Reinecke, M., Remazeilles, M., Renzi, A., Rocha, G., Rosset, C., Roudier, G., Rubiño-Martín, J. A., Ruiz-Granados, B., Salvati, L., Sandri, M., Savelainen, M., Scott, D., Shellard, E. P., Sirignano, C., Sirri, G., Spencer, L. D., Sunyaev, R., Suur-Uski, A. S., Tauber, J. A., Tavagnacco, D., Tenti, M., Toffolatti, L., Tomasi, M., Trombetti, T., Valenziano, L., Valiviita, J., Van Tent, B., Vibert, L., Vielva, P., Villa, F., Vittorio, N., Wandelt, B. D., Wehus, I. K., White, M., White, S. D., Zacchei, A., and Zonca, A. (2020). Planck 2018 results: VI. Cosmological parameters. *A&A*, 641:A6.
- Akiyama, K., Alberdi, A., Alef, W., Asada, K., Azulay, R., Baczko, A.-K., Ball, D., Baloković, M., Barrett, J., Bintley, D., Blackburn, L., Boland, W., Bouman, K. L., Bower, G. C., Bremer, M., Brinkerink, C. D., Brissenden, R., Britzen, S., Broderick, A. E., Brogiere, D., Bronzwaer, T., Byun, D.-Y., Carlstrom, J. E., Chael, A., Chan, C.-k., Chatterjee, S., Chatterjee, K., Chen, M.-T., Chen, Y., Cho, I., Christian, P., Conway, J. E., Cordes, J. M., Crew, G. B., Cui, Y., Davelaar, J., Laurentis, M. D., Deane, R., Dempsey, J., Desvignes, G., Dexter, J., Doeleman, S. S., Eatough, R. P., Falcke, H., Fish, V. L., Fomalont, E., Fraga-Encinas, R., Freeman, W. T., Friberg, P., Fromm, C. M., Gómez, J. L., Galison, P., Gammie, C. F., García, R., Gentaz, O., Georgiev, B., Goddi, C., Gold, R., Gu, M., Gurwell, M., Hada, K., Hecht, M. H., Hesper, R., Ho, L. C., Ho, P., Honma, M., Huang, C.-W. L., Huang, L., Hughes, D. H., Ikeda, S., Inoue, M., Issaoun, S., James, D. J., Jannuzi, B. T., Janssen, M., Jeter, B., Jiang, W., Johnson, M. D., Jorstad, S., Jung, T., Karami, M., Karuppusamy, R., Kawashima, T., Keating, G. K., Kettenis, M., Kim, J.-Y., Kim, J., Kim, J., Kino, M., Koay, J. Y., Koch, P. M., Koyama, S., Kramer, M., Kramer, C., Krichbaum, T. P., Kuo, C.-Y., Lauer, T. R., Lee, S.-S., Li, Y.-R., Li, Z., Lindqvist, M., Liu, K., Liuzzo, E., Lo, W.-P., Lobanov, A. P., Loinard, L., Lonsdale, C., Lu, R.-S., MacDonald, N. R., Mao, J., Markoff, S., Marrone, D. P., Marscher, A. P., Martí-Vidal, I., Matsushita, S., Matthews, L. D., Medeiros, L., Menten, K. M., Mizuno, Y., Mizuno, I., Moran, J. M., Moriyama, K., Moscibrodzka, M., Müller, C., Nagai, H., Nagar, N. M., Nakamura, M., Narayan, R., Narayanan, G., Natarajan, I., Neri, R., Ni, C., Noutsos,

- A., Okino, H., Olivares, H., Ortiz-León, G. N., Oyama, T., Özel, F., Palumbo, D. C. M., Patel, N., Pen, U.-L., Pesce, D. W., Piétu, V., Plambeck, R., PopStefanija, A., Porth, O., Prather, B., Preciado-López, J. A., Psaltis, D., Pu, H.-Y., Ramakrishnan, V., Rao, R., Rawlings, M. G., Raymond, A. W., Rezzolla, L., Ripperda, B., Roelofs, F., Rogers, A., Ros, E., Rose, M., Roshanineshat, A., Rottmann, H., Roy, A. L., Ruszczyk, C., Ryan, B. R., Rygl, K. L. J., Sánchez, S., Sánchez-Arguelles, D., Sasada, M., Savolainen, T., Schloerb, F. P., Schuster, K.-F., Shao, L., Shen, Z., Small, D., Sohn, B. W., SooHoo, J., Tazaki, F., Tiede, P., Tilanus, R. P. J., Titus, M., Toma, K., Torne, P., Trent, T., Trippe, S., Tsuda, S., van Bemmell, I., van Langevelde, H. J., van Rossum, D. R., Wagner, J., Wardle, J., Weintraub, J., Wex, N., Wharton, R., Wielgus, M., Wong, G. N., Wu, Q., Young, K., Young, A., Younsi, Z., Yuan, F., Yuan, Y.-F., Zensus, J. A., Zhao, G., Zhao, S.-S., Zhu, Z., Algaba, J.-C., Allardi, A., Amestica, R., Anczarski, J., Bach, U., Baganoff, F. K., Beaudoin, C., Benson, B. A., Berthold, R., Blanchard, J. M., Blundell, R., Bustamente, S., Cappallo, R., Castillo-Domínguez, E., Chang, C.-C., Chang, S.-H., Chang, S.-C., Chen, C.-C., Chilson, R., Chuter, T. C., Rosado, R. C., Coulson, I. M., Crawford, T. M., Crowley, J., David, J., Derome, M., Dexter, M., Dornbusch, S., Dudevoir, K. A., Dzib, S. A., Eckart, A., Eckert, C., Erickson, N. R., Everett, W. B., Faber, A., Farah, J. R., Fath, V., Folkers, T. W., Forbes, D. C., Freund, R., Gómez-Ruiz, A. I., Gale, D. M., Gao, F., Geertsema, G., Graham, D. A., Greer, C. H., Grosslein, R., Gueth, F., Haggard, D., Halverson, N. W., Han, C.-C., Han, K.-C., Hao, J., Hasegawa, Y., Henning, J. W., Hernández-Gómez, A., Herrero-Illana, R., Heyminck, S., Hirota, A., Hoge, J., Huang, Y.-D., Impellizzeri, C. M. V., Jiang, H., Kamble, A., Keisler, R., Kimura, K., Kono, Y., Kubo, D., Kuroda, J., Lacasse, R., Laing, R. A., Leitch, E. M., Li, C.-T., Lin, L. C.-C., Liu, C.-T., Liu, K.-Y., Lu, L.-M., Marson, R. G., Martin-Cocher, P. L., Massingill, K. D., Matulonis, C., McColl, M. P., McWhirter, S. R., Messias, H., Meyer-Zhao, Z., Michalik, D., Montaña, A., Montgomerie, W., Mora-Klein, M., Muders, D., Nadolski, A., Navarro, S., Neilsen, J., Nguyen, C. H., Nishioka, H., Norton, T., Nowak, M. A., Nystrom, G., Ogawa, H., Oshiro, P., Oyama, T., Parsons, H., Paine, S. N., Peñalver, J., Phillips, N. M., Poirier, M., Pradel, N., Primiani, R. A., Raffin, P. A., Rahlin, A. S., Reiland, G., Risacher, C., Ruiz, I., Sáez-Madaín, A. F., Sassella, R., Schellart, P., Shaw, P., Silva, K. M., Shiokawa, H., Smith, D. R., Snow, W., Souccar, K., Sousa, D., Sridharan, T. K., Srinivasan, R., Stahm, W., Stark, A. A., Story, K., Timmer, S. T., Vertatschitsch, L., Walther, C., Wei, T.-S., Whitehorn, N., Whitney, A. R., Woody, D. P., Wouterloot, J. G. A., Wright, M., Yamaguchi, P., Yu, C.-Y., Zeballos, M., Zhang, S., and Ziurys, L. (2019a). First M87 Event Horizon Telescope Results. I. The Shadow of the Supermassive Black Hole. *ApJ*, 875(1):L1.
- Akiyama, K., Alberdi, A., Alef, W., Asada, K., Azulay, R., Baczko, A.-K., Ball, D., Baloković, M., Barrett, J., Bintley, D., Blackburn, L., Boland, W., Bouman, K. L., Bower, G. C., Bremer, M., Brinkerink, C. D., Brissenden, R., Britzen, S., Broderick, A. E., Brogiere, D., Bronzwaer, T., Byun, D.-Y., Carlstrom, J. E., Chael, A., Chan, C.-k., Chatterjee, S., Chatterjee, K., Chen, M.-T., Chen, Y., Cho, I., Christian, P., Conway, J. E., Cordes, J. M., Crew, G. B., Cui, Y., Davelaar, J., De Laurentis, M., Deane, R., Dempsey, J., Desvignes, G., Dexter, J., Doleman, S. S., Eatough, R. P., Falcke, H., Fish, V. L., Fomalont, E., Fraga-Encinas, R., Friberg, P., Fromm, C. M., Gómez, J. L., Galison, P., Gammie, C. F., García, R., Gentaz, O., Georgiev, B., Goddi, C., Gold, R., Gu, M., Gurwell, M., Hada, K., Hecht, M. H., Hesper, R., Ho, L. C., Ho, P., Honma, M., Huang, C.-W. L., Huang, L., Hughes, D. H., Ikeda, S., Inoue, M., Issaoun, S., James, D. J., Jannuzi, B. T., Janssen, M., Jeter, B., Jiang, W., Johnson, M. D., Jorstad, S., Jung, T., Karami, M., Karuppusamy, R., Kawashima, T., Keating, G. K.,

- Kettenis, M., Kim, J.-Y., Kim, J., Kim, J., Kino, M., Koay, J. Y., Koch, P. M., Koyama, S., Kramer, M., Kramer, C., Krichbaum, T. P., Kuo, C.-Y., Lauer, T. R., Lee, S.-S., Li, Y.-R., Li, Z., Lindqvist, M., Liu, K., Liuzzo, E., Lo, W.-P., Lobanov, A. P., Loinard, L., Lonsdale, C., Lu, R.-S., MacDonald, N. R., Mao, J., Markoff, S., Marrone, D. P., Marscher, A. P., Martí-Vidal, I., Matsushita, S., Matthews, L. D., Medeiros, L., Menten, K. M., Mizuno, Y., Mizuno, I., Moran, J. M., Moriyama, K., Moscibrodzka, M., Müller, C., Nagai, H., Nagar, N. M., Nakamura, M., Narayan, R., Narayanan, G., Natarajan, I., Neri, R., Ni, C., Noutsos, A., Okino, H., Olivares, H., Ortiz-León, G. N., Oyama, T., Özel, F., Palumbo, D. C. M., Patel, N., Pen, U.-L., Pesce, D. W., Piétu, V., Plambeck, R., PopStefanija, A., Porth, O., Prather, B., Preciado-López, J. A., Psaltis, D., Pu, H.-Y., Ramakrishnan, V., Rao, R., Rawlings, M. G., Raymond, A. W., Rezzolla, L., Ripperda, B., Roelofs, F., Rogers, A., Ros, E., Rose, M., Roshanineshat, A., Rottmann, H., Roy, A. L., Ruzsczyk, C., Ryan, B. R., Rygl, K. L. J., Sánchez, S., Sánchez-Arguelles, D., Sasada, M., Savolainen, T., Schloerb, F. P., Schuster, K.-F., Shao, L., Shen, Z., Small, D., Sohn, B. W., SooHoo, J., Tazaki, F., Tiede, P., Tilanus, R. P. J., Titus, M., Toma, K., Torne, P., Trent, T., Trippe, S., Tsuda, S., van Bemmell, I., van Langevelde, H. J., van Rossum, D. R., Wagner, J., Wardle, J., Weintroub, J., Wex, N., Wharton, R., Wielgus, M., Wong, G. N., Wu, Q., Young, A., Young, K., Younsi, Z., Yuan, F., Yuan, Y.-F., Zensus, J. A., Zhao, G., Zhao, S.-S., Zhu, Z., Algaba, J.-C., Allardi, A., Amestica, R., Bach, U., Beaudoin, C., Benson, B. A., Berthold, R., Blanchard, J. M., Blundell, R., Bustamente, S., Cappallo, R., Castillo-Domínguez, E., Chang, C.-C., Chang, S.-H., Chang, S.-C., Chen, C.-C., Chilson, R., Chuter, T. C., Rosado, R. C., Coulson, I. M., Crawford, T. M., Crowley, J., David, J., Derome, M., Dexter, M., Dornbusch, S., Dudevoir, K. A., Dzib, S. A., Eckert, C., Erickson, N. R., Everett, W. B., Faber, A., Farah, J. R., Fath, V., Folkers, T. W., Forbes, D. C., Freund, R., Gómez-Ruiz, A. I., Gale, D. M., Gao, F., Geertsema, G., Graham, D. A., Greer, C. H., Grosslein, R., Gueth, F., Halverson, N. W., Han, C.-C., Han, K.-C., Hao, J., Hasegawa, Y., Henning, J. W., Hernández-Gómez, A., Herrero-Illana, R., Heyminck, S., Hirota, A., Hoge, J., Huang, Y.-D., Impellizzeri, C. M. V., Jiang, H., Kamble, A., Keisler, R., Kimura, K., Kono, Y., Kubo, D., Kuroda, J., Lacasse, R., Laing, R. A., Leitch, E. M., Li, C.-T., Lin, L. C.-C., Liu, C.-T., Liu, K.-Y., Lu, L.-M., Marson, R. G., Martin-Cocher, P. L., Massingill, K. D., Matulonis, C., McColl, M. P., McWhirter, S. R., Messias, H., Meyer-Zhao, Z., Michalik, D., Montaña, A., Montgomerie, W., Mora-Klein, M., Muders, D., Nadolski, A., Navarro, S., Nguyen, C. H., Nishioka, H., Norton, T., Nystrom, G., Ogawa, H., Oshiro, P., Oyama, T., Padin, S., Parsons, H., Paine, S. N., Peñalver, J., Phillips, N. M., Poirier, M., Pradel, N., Primiani, R. A., Raffin, P. A., Rahlin, A. S., Reiland, G., Risacher, C., Ruiz, I., Sáez-Madaín, A. F., Sassella, R., Schellart, P., Shaw, P., Silva, K. M., Shiokawa, H., Smith, D. R., Snow, W., Souccar, K., Sousa, D., Sridharan, T. K., Srinivasan, R., Stahm, W., Stark, A. A., Story, K., Timmer, S. T., Vertatschitsch, L., Walther, C., Wei, T.-S., Whitehorn, N., Whitney, A. R., Woody, D. P., Wouterloot, J. G. A., Wright, M., Yamaguchi, P., Yu, C.-Y., Zeballos, M., and Ziurys, L. (2019b). First M87 Event Horizon Telescope Results. II. Array and Instrumentation. *ApJ*, 875(1):L2.
- Akiyama, K., Alberdi, A., Alef, W., Asada, K., Azulay, R., Baczko, A.-K., Ball, D., Baloković, M., Barrett, J., Bintley, D., Blackburn, L., Boland, W., Bouman, K. L., Bower, G. C., Bremer, M., Brinkerink, C. D., Brissenden, R., Britzen, S., Broderick, A. E., Brogiere, D., Bronzwaer, T., Byun, D.-Y., Carlstrom, J. E., Chael, A., Chan, C.-k., Chatterjee, S., Chatterjee, K., Chen, M.-T., Chen, Y., Cho, I., Christian, P., Conway, J. E., Cordes, J. M., Crew, G. B., Cui, Y., Davelaar, J., De Laurentis, M., Deane, R., Dempsey, J., Desvignes, G., Dexter, J., Doeleman,

- S. S., Eatough, R. P., Falcke, H., Fish, V. L., Fomalont, E., Fraga-Encinas, R., Friberg, P., Fromm, C. M., Gómez, J. L., Galison, P., Gammie, C. F., García, R., Gentaz, O., Georgiev, B., Goddi, C., Gold, R., Gu, M., Gurwell, M., Hada, K., Hecht, M. H., Hesper, R., Ho, L. C., Ho, P., Honma, M., Huang, C.-W. L., Huang, L., Hughes, D. H., Ikeda, S., Inoue, M., Issaoun, S., James, D. J., Jannuzi, B. T., Janssen, M., Jeter, B., Jiang, W., Johnson, M. D., Jorstad, S., Jung, T., Karami, M., Karuppusamy, R., Kawashima, T., Keating, G. K., Kettenis, M., Kim, J.-Y., Kim, J., Kim, J., Kino, M., Koay, J. Y., Koch, P. M., Koyama, S., Kramer, M., Kramer, C., Krichbaum, T. P., Kuo, C.-Y., Lauer, T. R., Lee, S.-S., Li, Y.-R., Li, Z., Lindqvist, M., Liu, K., Liuzzo, E., Lo, W.-P., Lobanov, A. P., Loinard, L., Lonsdale, C., Lu, R.-S., MacDonald, N. R., Mao, J., Markoff, S., Marrone, D. P., Marscher, A. P., Martí-Vidal, I., Matsushita, S., Matthews, L. D., Medeiros, L., Menten, K. M., Mizuno, Y., Mizuno, I., Moran, J. M., Moriyama, K., Moscibrodzka, M., Müller, C., Nagai, H., Nagar, N. M., Nakamura, M., Narayan, R., Narayanan, G., Natarajan, I., Neri, R., Ni, C., Noutsos, A., Okino, H., Olivares, H., Ortiz-León, G. N., Oyama, T., Özel, F., Palumbo, D. C. M., Patel, N., Pen, U.-L., Pesce, D. W., Piétu, V., Plambeck, R., PopStefanija, A., Porth, O., Prather, B., Preciado-López, J. A., Psaltis, D., Pu, H.-Y., Ramakrishnan, V., Rao, R., Rawlings, M. G., Raymond, A. W., Rezzolla, L., Ripperda, B., Roelofs, F., Rogers, A., Ros, E., Rose, M., Roshanineshat, A., Rottmann, H., Roy, A. L., Ruszczyk, C., Ryan, B. R., Rygl, K. L. J., Sánchez, S., Sánchez-Arguelles, D., Sasada, M., Savolainen, T., Schloerb, F. P., Schuster, K.-F., Shao, L., Shen, Z., Small, D., Sohn, B. W., SooHoo, J., Tazaki, F., Tiede, P., Tilanus, R. P. J., Titus, M., Toma, K., Torne, P., Trent, T., Trippe, S., Tsuda, S., van Bemmell, I., van Langevelde, H. J., van Rossum, D. R., Wagner, J., Wardle, J., Weintraub, J., Wex, N., Wharton, R., Wielgus, M., Wong, G. N., Wu, Q., Young, A., Young, K., Younsi, Z., Yuan, F., Yuan, Y.-F., Zensus, J. A., Zhao, G., Zhao, S.-S., Zhu, Z., Cappallo, R., Farah, J. R., Folkers, T. W., Meyer-Zhao, Z., Michalik, D., Nadolski, A., Nishioka, H., Pradel, N., Primiani, R. A., Souccar, K., Vertatschitsch, L., and Yamaguchi, P. (2019c). First M87 Event Horizon Telescope Results. III. Data Processing and Calibration. *ApJ*, 875(1):L3.
- Akiyama, K., Alberdi, A., Alef, W., Asada, K., Azulay, R., Baczko, A.-K., Ball, D., Baloković, M., Barrett, J., Bintley, D., Blackburn, L., Boland, W., Bouman, K. L., Bower, G. C., Bremer, M., Brinkerink, C. D., Brissenden, R., Britzen, S., Broderick, A. E., Brogiere, D., Bronzwaer, T., Byun, D.-Y., Carlstrom, J. E., Chael, A., Chan, C.-k., Chatterjee, S., Chatterjee, K., Chen, M.-T., Chen, Y., Cho, I., Christian, P., Conway, J. E., Cordes, J. M., Crew, G. B., Cui, Y., Davelaar, J., De Laurentis, M., Deane, R., Dempsey, J., Desvignes, G., Dexter, J., Doleman, S. S., Eatough, R. P., Falcke, H., Fish, V. L., Fomalont, E., Fraga-Encinas, R., Freeman, W. T., Friberg, P., Fromm, C. M., Gómez, J. L., Galison, P., Gammie, C. F., García, R., Gentaz, O., Georgiev, B., Goddi, C., Gold, R., Gu, M., Gurwell, M., Hada, K., Hecht, M. H., Hesper, R., Ho, L. C., Ho, P., Honma, M., Huang, C.-W. L., Huang, L., H. Hughes, D., Ikeda, S., Inoue, M., Issaoun, S., James, D. J., Jannuzi, B. T., Janssen, M., Jeter, B., Jiang, W., Johnson, M. D., Jorstad, S., Jung, T., Karami, M., Karuppusamy, R., Kawashima, T., Keating, G. K., Kettenis, M., Kim, J.-Y., Kim, J., Kim, J., Kino, M., Koay, J. Y., Koch, P. M., Koyama, S., Kramer, M., Kramer, C., Krichbaum, T. P., Kuo, C.-Y., Lauer, T. R., Lee, S.-S., Li, Y.-R., Li, Z., Lindqvist, M., Liu, K., Liuzzo, E., Lo, W.-P., Lobanov, A. P., Loinard, L., Lonsdale, C., Lu, R.-S., MacDonald, N. R., Mao, J., Markoff, S., Marrone, D. P., Marscher, A. P., Martí-Vidal, I., Matsushita, S., Matthews, L. D., Medeiros, L., Menten, K. M., Mizuno, Y., Mizuno, I., Moran, J. M., Moriyama, K., Moscibrodzka, M., Müller, C., Nagai, H., Nagar, N. M., Nakamura, M., Narayan, R., Narayanan, G., Natarajan, I., Neri, R., Ni, C., Noutsos, A., Okino, H., Olivares,

- H., Oyama, T., Özel, F., Palumbo, D. C. M., Patel, N., Pen, U.-L., Pesce, D. W., Piétu, V., Plambeck, R., PopStefanija, A., Porth, O., Prather, B., Preciado-López, J. A., Psaltis, D., Pu, H.-Y., Ramakrishnan, V., Rao, R., Rawlings, M. G., Raymond, A. W., Rezzolla, L., Ripperda, B., Roelofs, F., Rogers, A., Ros, E., Rose, M., Roshanineshat, A., Rottmann, H., Roy, A. L., Ruszczyk, C., Ryan, B. R., Rygl, K. L. J., Sánchez, S., Sánchez-Arguelles, D., Sasada, M., Savolainen, T., Schloerb, F. P., Schuster, K.-F., Shao, L., Shen, Z., Small, D., Sohn, B. W., SooHoo, J., Tazaki, F., Tiede, P., Tilanus, R. P. J., Titus, M., Toma, K., Torne, P., Trent, T., Trippe, S., Tsuda, S., van Bemmell, I., van Langevelde, H. J., van Rossum, D. R., Wagner, J., Wardle, J., Weintraub, J., Wex, N., Wharton, R., Wielgus, M., Wong, G. N., Wu, Q., Young, A., Young, K., Younsi, Z., Yuan, F., Yuan, Y.-F., Zensus, J. A., Zhao, G., Zhao, S.-S., Zhu, Z., Farah, J. R., Meyer-Zhao, Z., Michalik, D., Nadolski, A., Nishioka, H., Pradel, N., Primiani, R. A., Souccar, K., Vertatschitsch, L., and Yamaguchi, P. (2019d). First M87 Event Horizon Telescope Results. IV. Imaging the Central Supermassive Black Hole. *ApJ*, 875(1):L4.
- Akiyama, K., Alberdi, A., Alef, W., Asada, K., Azulay, R., Bacsko, A.-K., Ball, D., Baloković, M., Barrett, J., Bintley, D., Blackburn, L., Boland, W., Bouman, K. L., Bower, G. C., Bremer, M., Brinkerink, C. D., Brissenden, R., Britzen, S., Broderick, A. E., Brogiere, D., Bronzwaer, T., Byun, D.-Y., Carlstrom, J. E., Chael, A., Chan, C.-k., Chatterjee, S., Chatterjee, K., Chen, M.-T., Chen, Y., Cho, I., Christian, P., Conway, J. E., Cordes, J. M., Crew, G. B., Cui, Y., Davelaar, J., De Laurentis, M., Deane, R., Dempsey, J., Desvignes, G., Dexter, J., Doeleman, S. S., Eatough, R. P., Falcke, H., Fish, V. L., Fomalont, E., Fraga-Encinas, R., Friberg, P., Fromm, C. M., Gómez, J. L., Galison, P., Gammie, C. F., García, R., Gentaz, O., Georgiev, B., Goddi, C., Gold, R., Gu, M., Gurwell, M., Hada, K., Hecht, M. H., Hesper, R., Ho, L. C., Ho, P., Honma, M., Huang, C.-W. L., Huang, L., Hughes, D. H., Ikeda, S., Inoue, M., Issaoun, S., James, D. J., Jannuzi, B. T., Janssen, M., Jeter, B., Jiang, W., Johnson, M. D., Jorstad, S., Jung, T., Karami, M., Karuppusamy, R., Kawashima, T., Keating, G. K., Kettenis, M., Kim, J.-Y., Kim, J., Kim, J., Kino, M., Koay, J. Y., Koch, P. M., Koyama, S., Kramer, M., Kramer, C., Krichbaum, T. P., Kuo, C.-Y., Lauer, T. R., Lee, S.-S., Li, Y.-R., Li, Z., Lindqvist, M., Liu, K., Liuzzo, E., Lo, W.-P., Lobanov, A. P., Loinard, L., Lonsdale, C., Lu, R.-S., MacDonald, N. R., Mao, J., Markoff, S., Marrone, D. P., Marscher, A. P., Martí-Vidal, I., Matsushita, S., Matthews, L. D., Medeiros, L., Menten, K. M., Mizuno, Y., Mizuno, I., Moran, J. M., Moriyama, K., Moscibrodzka, M., Müller, C., Nagai, H., Nagar, N. M., Nakamura, M., Narayan, R., Narayanan, G., Natarajan, I., Neri, R., Ni, C., Noutsos, A., Okino, H., Olivares, H., Oyama, T., Özel, F., Palumbo, D. C. M., Patel, N., Pen, U.-L., Pesce, D. W., Piétu, V., Plambeck, R., PopStefanija, A., Porth, O., Prather, B., Preciado-López, J. A., Psaltis, D., Pu, H.-Y., Ramakrishnan, V., Rao, R., Rawlings, M. G., Raymond, A. W., Rezzolla, L., Ripperda, B., Roelofs, F., Rogers, A., Ros, E., Rose, M., Roshanineshat, A., Rottmann, H., Roy, A. L., Ruszczyk, C., Ryan, B. R., Rygl, K. L. J., Sánchez, S., Sánchez-Arguelles, D., Sasada, M., Savolainen, T., Schloerb, F. P., Schuster, K.-F., Shao, L., Shen, Z., Small, D., Sohn, B. W., SooHoo, J., Tazaki, F., Tiede, P., Tilanus, R. P. J., Titus, M., Toma, K., Torne, P., Trent, T., Trippe, S., Tsuda, S., van Bemmell, I., van Langevelde, H. J., van Rossum, D. R., Wagner, J., Wardle, J., Weintraub, J., Wex, N., Wharton, R., Wielgus, M., Wong, G. N., Wu, Q., Young, A., Young, K., Younsi, Z., Yuan, F., Yuan, Y.-F., Zensus, J. A., Zhao, G., Zhao, S.-S., Zhu, Z., Anczarski, J., Baganoff, F. K., Eckart, A., Farah, J. R., Haggard, D., Meyer-Zhao, Z., Michalik, D., Nadolski, A., Neilsen, J., Nishioka, H., Nowak, M. A., Pradel, N., Primiani, R. A., Souccar, K., Vertatschitsch, L., Yamaguchi, P., and Zhang, S. (2019e). First M87 Event Horizon Telescope Results. V. Physical Origin of the Asymmetric Ring. *ApJ*, 875(1):L5.

- Akiyama, K., Alberdi, A., Alef, W., Asada, K., Azulay, R., Baczko, A.-K., Ball, D., Baloković, M., Barrett, J., Bintley, D., Blackburn, L., Boland, W., Bouman, K. L., Bower, G. C., Bremer, M., Brinkerink, C. D., Brissenden, R., Britzen, S., Broderick, A. E., Brogiere, D., Bronzwaer, T., Byun, D.-Y., Carlstrom, J. E., Chael, A., Chan, C.-k., Chatterjee, S., Chatterjee, K., Chen, M.-T., Chen, Y., Cho, I., Christian, P., Conway, J. E., Cordes, J. M., Crew, G. B., Cui, Y., Davelaar, J., De Laurentis, M., Deane, R., Dempsey, J., Desvignes, G., Dexter, J., Doleman, S. S., Eatough, R. P., Falcke, H., Fish, V. L., Fomalont, E., Fraga-Encinas, R., Friberg, P., Fromm, C. M., Gómez, J. L., Galison, P., Gammie, C. F., García, R., Gentaz, O., Georgiev, B., Goddi, C., Gold, R., Gu, M., Gurwell, M., Hada, K., Hecht, M. H., Hesper, R., Ho, L. C., Ho, P., Honma, M., Huang, C.-W. L., Huang, L., Hughes, D. H., Ikeda, S., Inoue, M., Issaoun, S., James, D. J., Jannuzi, B. T., Janssen, M., Jeter, B., Jiang, W., Johnson, M. D., Jorstad, S., Jung, T., Karami, M., Karuppusamy, R., Kawashima, T., Keating, G. K., Kettenis, M., Kim, J.-Y., Kim, J., Kim, J., Kino, M., Koay, J. Y., Koch, P. M., Koyama, S., Kramer, M., Kramer, C., Krichbaum, T. P., Kuo, C.-Y., Lauer, T. R., Lee, S.-S., Li, Y.-R., Li, Z., Lindqvist, M., Liu, K., Liuzzo, E., Lo, W.-P., Lobanov, A. P., Loinard, L., Lonsdale, C., Lu, R.-S., MacDonald, N. R., Mao, J., Markoff, S., Marrone, D. P., Marscher, A. P., Martí-Vidal, I., Matsushita, S., Matthews, L. D., Medeiros, L., Menten, K. M., Mizuno, Y., Mizuno, I., Moran, J. M., Moriyama, K., Moscibrodzka, M., Müller, C., Nagai, H., Nagar, N. M., Nakamura, M., Narayan, R., Narayanan, G., Natarajan, I., Neri, R., Ni, C., Noutsos, A., Okino, H., Olivares, H., Oyama, T., Özel, F., Palumbo, D. C. M., Patel, N., Pen, U.-L., Pesce, D. W., Piétu, V., Plambeck, R., PopStefanija, A., Porth, O., Prather, B., Preciado-López, J. A., Psaltis, D., Pu, H.-Y., Ramakrishnan, V., Rao, R., Rawlings, M. G., Raymond, A. W., Rezzolla, L., Ripperda, B., Roelofs, F., Rogers, A., Ros, E., Rose, M., Roshanineshat, A., Rottmann, H., Roy, A. L., Ruszczyk, C., Ryan, B. R., Rygl, K. L. J., Sánchez, S., Sánchez-Arguelles, D., Sasada, M., Savolainen, T., Schloerb, F. P., Schuster, K.-F., Shao, L., Shen, Z., Small, D., Sohn, B. W., SooHoo, J., Tazaki, F., Tiede, P., Tilanus, R. P. J., Titus, M., Toma, K., Torne, P., Trent, T., Trippe, S., Tsuda, S., van Bemmell, I., van Langevelde, H. J., van Rossum, D. R., Wagner, J., Wardle, J., Weintraub, J., Wex, N., Wharton, R., Wielgus, M., Wong, G. N., Wu, Q., Young, A., Young, K., Younsi, Z., Yuan, F., Yuan, Y.-F., Zensus, J. A., Zhao, G., Zhao, S.-S., Zhu, Z., Farah, J. R., Meyer-Zhao, Z., Michalik, D., Nadolski, A., Nishioka, H., Pradel, N., Primiani, R. A., Souccar, K., Vertatschitsch, L., and Yamaguchi, P. (2019f). First M87 Event Horizon Telescope Results. VI. The Shadow and Mass of the Central Black Hole. *ApJ*, 875(1):L6.
- Amaro-Seoane, P., Audley, H., Babak, S., Baker, J., Barausse, E., Bender, P., Berti, E., Binetruy, P., Born, M., Bortoluzzi, D., Camp, J., Caprini, C., Cardoso, V., Colpi, M., Conklin, J., Cornish, N., Cutler, C., Danzmann, K., Dolesi, R., Ferraioli, L., Ferroni, V., Fitzsimons, E., Gair, J., Gesa Bote, L., Giardini, D., Gibert, F., Grimaldi, C., Halluin, H., Heinzl, G., Hertog, T., Hewitson, M., Holley-Bockelmann, K., Hollington, D., Hueller, M., Inchauspe, H., Jetzer, P., Karnesis, N., Killow, C., Klein, A., Klipstein, B., Korsakova, N., Larson, S. L., Livas, J., Lloro, I., Man, N., Mance, D., Martino, J., Mateos, I., McKenzie, K., McWilliams, S. T., Miller, C., Mueller, G., Nardini, G., Nelemans, G., Nofrarias, M., Petiteau, A., Pivato, P., Plagnol, E., Porter, E., Reiche, J., Robertson, D., Robertson, N., Rossi, E., Russano, G., Schutz, B., Sesana, A., Shoemaker, D., Slutsky, J., Sopuerta, C. F., Sumner, T., Tamanini, N., Thorpe, I., Troebels, M., Vallisneri, M., Vecchio, A., Vetrugno, D., Vitale, S., Volonteri, M., Wanner, G., Ward, H., Wass, P., Weber, W., Ziemer, J., and Zweifel, P. (2017). Laser Interferometer Space Antenna. *arXiv e-print*, *arXiv:1702.00786*.
- Antonini, F. and Merritt, D. (2012). Dynamical friction around supermassive black holes. *ApJ*,

745(1):83.

- Appel, A. W., Appel, and W., A. (1985). An Efficient Program for Many-Body Simulation. *SJSSC*, 6(1):85–103.
- Arca Sedda, M., Berczik, P., Capuzzo-Dolcetta, R., Fragione, G., Sobolenko, M., and Spurzem, R. (2019). Supermassive black holes coalescence mediated by massive perturbers: implications for gravitational waves emission and nuclear cluster formation. *MNRAS*, 484(1):520–542.
- Arca-Sedda, M. and Capuzzo-Dolcetta, R. (2014). Dynamical friction in cuspy galaxies. *ApJ*, 785(1):51, 17.
- Arzoumanian, Z., Baker, P. T., Blumer, H., Bécsy, B., Brazier, A., Brook, P. R., Burke-Spolaor, S., Chatterjee, S., Chen, S., Cordes, J. M., Cornish, N. J., Crawford, F., Cromartie, H. T., DeCesar, M. E., Demorest, P. B., Dolch, T., Ellis, J. A., Ferrara, E. C., Fiore, W., Fonseca, E., Garver-Daniels, N., Gentile, P. A., Good, D. C., Hazboun, J. S., Holzgado, A. M., Islo, K., Jennings, R. J., Jones, M. L., Kaiser, A. R., Kaplan, D. L., Kelley, L. Z., Key, J. S., Laal, N., Lam, M. T., Lazio, T. W., Lorimer, D. R., Luo, J., Lynch, R. S., Madison, D. R., McLaughlin, M. A., Mingarelli, C. M., Ng, C., Nice, D. J., Pennucci, T. T., Pol, N. S., Ransom, S. M., Ray, P. S., Shapiro-Albert, B. J., Siemens, X., Simon, J., Spiewak, R., Stairs, I. H., Stinebring, D. R., Stovall, K., Sun, J. P., Swiggum, J. K., Taylor, S. R., Turner, J. E., Vallisneri, M., Vigeland, S. J., and Witt, C. A. (2020). The NANOGrav 12.5-year Data Set: Search for An Isotropic Stochastic Gravitational-Wave Background. *ApJL*, 905(2):L34.
- Arzoumanian, Z., Brazier, A., Burke-Spolaor, S., Chamberlin, S. J., Chatterjee, S., Christy, B., Cordes, J. M., Cornish, N. J., Crowter, K., Demorest, P. B., Deng, X., Dolch, T., Ellis, J. A., Ferdman, R. D., Fonseca, E., Garver-Daniels, N., Gonzalez, M. E., Jenet, F., Jones, G., Jones, M. L., Kaspi, V. M., Koop, M., Lam, M. T., Lazio, T. J. W., Levin, L., Lommen, A. N., Lorimer, D. R., Luo, J., Lynch, R. S., Madison, D. R., McLaughlin, M. A., McWilliams, S. T., Mingarelli, C. M. F., Nice, D. J., Palliyaguru, N., Pennucci, T. T., Ransom, S. M., Sampson, L., Sanidas, S. A., Sesana, A., Siemens, X., Simon, J., Stairs, I. H., Stinebring, D. R., Stovall, K., Swiggum, J., Taylor, S. R., Vallisneri, M., van Haasteren, R., Wang, Y., and Zhu, W. W. (2016). THE NANOGrav NINE-YEAR DATA SET: LIMITS ON THE ISOTROPIC STOCHASTIC GRAVITATIONAL WAVE BACKGROUND. *ApJ*, 821(1):13.
- Avramov, B., Berczik, P., Meiron, Y., Acharya, A., and Just, A. (2021). Properties of loss cone stars in a cosmological galaxy merger remnant. *A&A*, 649(A41):17.
- Baker, J., Bellovary, J., Bender, P. L., Berti, E., Caldwell, R., Camp, J., Conklin, J. W., Cornish, N., Cutler, C., DeRosa, R., Eracleous, M., Ferrara, E. C., Francis, S., Hewitson, M., Holley-Bockelmann, K., Hornschemeier, A., Hogan, C., Kamai, B., Kelly, B. J., Key, J. S., Larson, S. L., Livas, J., Manthripragada, S., McKenzie, K., McWilliams, S. T., Mueller, G., Natarajan, P., Numata, K., Rioux, N., Sankar, S. R., Schnittman, J., Shoemaker, D., Shoemaker, D., Slutsky, J., Spero, R., Stebbins, R., Thorpe, I., Vallisneri, M., Ware, B., Wass, P., Yu, A., and Ziemer, J. (2019). The laser interferometer space antenna: Unveiling the millihertz gravitational wave sky. *arXiv e-print*, *arXiv:1907.06482*.
- Bañados, E., Venemans, B. P., Decarli, R., Farina, E. P., Mazzucchelli, C., Walter, F., Fan, X., Stern, D., Schlafly, E., Chambers, K. C., Rix, H.-W., Jiang, L., McGreer, I., Simcoe, R., Wang, F., Yang, J., Morganson, E., Rosa, G. D., Greiner, J., Baloković, M., Burgett, W. S.,

- Cooper, T., Draper, P. W., Flewelling, H., Hodapp, K. W., Jun, H. D., Kaiser, N., Kudritzki, R.-P., Magnier, E. A., Metcalfe, N., Miller, D., Schindler, J.-T., Tonry, J. L., Wainscoat, R. J., Waters, C., and Yang, Q. (2016). The PAN-STARRS1 distant  $z > 5.6$  Quasar Survey: More than 100 Quasars within the First Gyr of the Universe. *ApJS*, 227(1):11.
- Bañados, E., Venemans, B. P., Mazzucchelli, C., Farina, E. P., Walter, F., Wang, F., Decarli, R., Stern, D., Fan, X., Davies, F. B., Hennawi, J. F., Simcoe, R. A., Turner, M. L., Rix, H. W., Yang, J., Kelson, D. D., Rudie, G. C., and Winters, J. M. (2018). An 800-million-solar-mass black hole in a significantly neutral Universe at a redshift of 7.5. *Nature*, 553(7689):473–476.
- Barnes, J. and Hut, P. (1986). A hierarchical  $O(N \log N)$  force-calculation algorithm. *Nature*, 324(6096):446–449.
- Barrows, R. S., Comerford, J. M., Greene, J. E., and Pooley, D. (2016). Spatially Offset Active Galactic Nuclei. I. Selection and spectroscopic properties. *ApJ*, 829(1):37.
- Bédorf, J., Gaburov, E., and Portegies Zwart, S. (2012a). A sparse octree gravitational N-body code that runs entirely on the GPU processor. *J. Comput. Phys.*, 231(7):2825–2839.
- Bédorf, J., Gaburov, E., and Zwart, S. P. (2012b). Bonsai: A GPU Tree-Code. In Capuzzo-Dolcetta, R., Limongi, M., and Tornambe, A., editors, *Adv. Comput. Astrophys. Methods, Tools, Outcome*, page 325. Astronomical Society of the Pacific Conference Series.
- Begelman, M., Blandford, R., and Rees, M. (1980). Massive black hole binaries in active galactic nuclei. *Nature*, 287(5780):307–309.
- Belleman, R. G., Bédorf, J., and Portegies Zwart, S. F. (2008). High performance direct gravitational N-body simulations on graphics processing units II: An implementation in CUDA. *New Astronomy*, 13(2):103–112.
- Berczik, P., Merritt, D., and Spurzem, R. (2005). Long-Term Evolution of Massive Black Hole Binaries. II. Binary Evolution in Low-Density Galaxies. *ApJ*, 633(2):680–687.
- Berczik, P., Merritt, D., Spurzem, R., and Bischof, H.-P. (2006). Efficient Merger of Binary Supermassive Black Holes in Nonaxisymmetric Galaxies. *ApJL*, 642(1):L21–L24.
- Berczik, P., Nitadori, K., Zhong, S., Spurzem, R., Hamada, T., Wang, X., Berentzen, I., Veles, A., and Ge, W. (2011). High performance massively parallel direct N-body simulations on large GPU clusters. In *Int. Conf. High Perform. Comput.*, pages 8–18.
- Bertola, F. and Capaccioli, M. (1977). Dynamics of early-type galaxies. II. The rotation curve of the S0 galaxy NGC 128. *ApJ*, 211:697–706.
- Biava, N., Colpi, M., Capelo, P. R., Bonetti, M., Volonteri, M., Tamfal, T., Mayer, L., and Sesana, A. (2019). The lifetime of binary black holes in Sérsic galaxy models. *MNRAS*, 487(4):4985–4994.
- Binney, J. (2005). Rotation and anisotropy of galaxies revisited. *MNRAS*, 363(3):937–942.
- Binney, J. and Tremaine, S. (1987). *Galactic dynamics*. Princeton University Press, Princeton, USA.
- Blanchet, L. (2014). Gravitational radiation from post-newtonian sources and inspiralling compact binaries. *Living Rev. Relativ.*, 17(1):2.

- Blanchet, L. and Iyer, B. (2003). Third post-Newtonian dynamics of compact binaries: Equations of motion in the center-of-mass frame. *Class. Quantum Gravity*, 20(4):755–776.
- Blecha, L., Briskin, W., Burke-Spolaor, S., Civano, F., Comerford, J., Darling, J., Lazio, T. J. W., and Maccarone, T. J. (2019). Detecting Offset Active Galactic Nuclei. *Astro2020 Decad. Surv. Astron. Astrophys. Sci. white Pap. no. 318*.
- Blecha, L., Cox, T. J., Loeb, A., and Hernquist, L. (2011). Recoiling Black Holes in Merging Galaxies: Relationship to AGN Lifetimes, Starbursts, and the M-sigma Relation. *MNRAS*, 412(4):2154–2182.
- Blümlein, J., Maier, A., Marquard, P., and Schäfer, G. (2021). The fifth-order post-Newtonian Hamiltonian dynamics of two-body systems from an effective field theory approach: Potential contributions. *Nucl. Phys. B*, 965:115352.
- Bogdanović, T. (2015). Supermassive Black Hole Binaries: The Search Continues. In *Gravitational Wave Astrophys.*, volume 40, page 103.
- Bonetti, M., Bortolas, E., Lupi, A., and Dotti, M. (2021). Dynamical evolution of massive perturbers in realistic multi-component galaxy models I: implementation and validation. *MNRAS*, 502(3):3554–3568.
- Bonetti, M., Bortolas, E., Lupi, A., Dotti, M., and Raimundo, S. I. (2020a). Dynamical friction-driven orbital circularization in rotating discs: A semi-analytical description. *MNRAS*, 494(2):3053–3059.
- Bonetti, M., Haardt, F., Sesana, A., and Barausse, E. (2016). Post-Newtonian evolution of massive black hole triplets in galactic nuclei - I. Numerical implementation and tests. *MNRAS*, 461(4):4419–4434.
- Bonetti, M., Haardt, F., Sesana, A., and Barausse, E. (2018). Post-Newtonian evolution of massive black hole triplets in galactic nuclei - II. Survey of the parameter space. *MNRAS*, 477(3):3910–3926.
- Bonetti, M., Rasskazov, A., Sesana, A., Dotti, M., Haardt, F., Leigh, N. W., Arca Sedda, M., Fragione, G., and Rossi, E. (2020b). On the eccentricity evolution of massive black hole binaries in stellar backgrounds. *MNRAS*, 493(1):L114–L119.
- Bonetti, M., Sesana, A., Haardt, F., Barausse, E., and Colpi, M. (2019). Post-Newtonian evolution of massive black hole triplets in galactic nuclei-IV. Implications for LISA. *MNRAS*, 486(3):4044–4060.
- Bortolas, E., Bonetti, M., Dotti, M., Lupi, A., Capelo, P. R., Mayer, L., and Sesana, A. (2021). The role of bars on the dynamical-friction driven inspiral of massive perturbers. *arXiv e-print, arXiv:2103.07486*.
- Bortolas, E., Capelo, P. R., Zana, T., Mayer, L., Bonetti, M., Dotti, M., Davies, M. B., and Madau, P. (2020). Global torques and stochasticity as the drivers of massive black hole pairing in the young Universe. *MNRAS*, 498(3):3601–3615.
- Bortolas, E., Gualandris, A., Dotti, M., and Read, J. (2018a). The influence of massive black hole binaries on the morphology of merger remnants. *MNRAS*, 477(2):2310–2325.

- Bortolas, E., Gualandris, A., Dotti, M., Spera, M., and Mapelli, M. (2016). Brownian motion of massive black hole binaries and the final parsec problem. *MNRAS*, 461(1):1023–1031.
- Bortolas, E., Mapelli, M., and Spera, M. (2018b). Star cluster disruption by a massive black hole binary. *MNRAS*, 474(1):1054–1064.
- Buonanno, A. and Damour, T. (1999). Effective one-body approach to general relativistic two-body dynamics. *Phys. Rev. D - Part. Fields, Gravit. Cosmol.*, 59(8):1–24.
- Bustamante, S. and Springel, V. (2019). Spin evolution and feedback of supermassive black holes in cosmological simulations. *MNRAS*, 490(3):4133–4153.
- Callegari, S., Kazantzidis, S., Mayer, L., Colpi, M., Bellovary, J. M., Quinn, T., and Wadsley, J. (2011). Growing massive black hole pairs in minor mergers of disk galaxies. *ApJ*, 729(2):85.
- Callegari, S., Mayer, L., Kazantzidis, S., Colpi, M., Governato, F., Quinn, T., and Wadsley, J. (2009). Pairing of Supermassive Black Holes in unequal-mass galaxy mergers. *ApJL*, 696(1):89–92.
- Campanelli, M., Lousto, C. O., Zlochower, Y., and Merritt, D. (2007). Maximum gravitational recoil. *Phys. Rev. Lett.*, 98(23):231102.
- Canton, T. D., Mangiagli, A., Noble, S. C., Schnittman, J., Ptak, A., Klein, A., Sesana, A., and Camp, J. (2019). Detectability of modulated X-rays from LISA’s supermassive black hole mergers. *ApJ*, 886(2):146.
- Cappellari, M., Emsellem, E., Bacon, R., Bureau, M., Davies, R. L., de Zeeuw, P., Falcón-Barroso, J., Krajnović, D., Kuntschner, H., McDermid, R. M., Peletier, R. F., Sarzi, M., van den Bosch, R. C., and van de Ven, G. (2007). The SAURON project - X. The orbital anisotropy of elliptical and lenticular galaxies: revisiting the  $(V/\sigma, \{ \in \})$  diagram with integral-field stellar kinematics. *MNRAS*, 379(2):418–444.
- Cervantes-Cota, J. L., Galindo-Uribarri, S., and Smoot, G. F. (2016). A Brief History of Gravitational Waves. *Universe*, 2(3):22.
- Chandrasekhar, S. (1943). Dynamical Friction. I. General Considerations: the Coefficient of Dynamical Friction. *ApJ*, 97:255.
- Chatterjee, P., Hernquist, L., and Loeb, A. (2003). Effects of Wandering on the Coalescence of Black Hole Binaries in Galactic Centers. *ApJ*, 592(1):32–41.
- Clutton-Brock, M. (1972). The gravitational field of flat galaxies. *Ap&SS*, 16(1):101–119.
- Clutton-Brock, M. (1973). The gravitational field of three-dimensional galaxies. *Ap&SS*, 23(1):55–69.
- Colpi, M., Holley-Bockelmann, K., Bogdanović, T., Natarajan, P., Bellovary, J., Sesana, A., Tremmel, M., Schnittman, J., Comerford, J., Barausse, E., Berti, E., Volonteri, M., Khan, F. M., McWilliams, S. T., Burke-Spolaor, S., Hazboun, J. S., Conklin, J., Mueller, G., and Larson, S. (2019). Astro2020 Science White Paper: The Gravitational Wave View of Massive Black Holes. *arXiv e-print, arXiv:1903.06867*.
- Cuadra, J., Armitage, P., Alexander, R., and Begelman, M. (2009). Massive black hole binary mergers within subparsec scale gas discs. *MNRAS*, 393(4):1423–1432.

- Cui, X. and Yu, Q. (2014). Orbital orientation evolution of massive binary black holes at the centres of non-spherical galaxies. *MNRAS*, 437(1):777–789.
- Dahal, P. K. (2020). Review of pulsar timing array for gravitational wave research. *JA&A*, 41(1):8.
- Damour, T. and Deruelle, N. (1985). General relativistic celestial mechanics of binary systems. I. The post-Newtonian motion. *AHNS*, 43(1):107–132.
- Darbha, S., Coughlin, E. R., Kasen, D., and Quataert, E. (2018). Gravitational interactions of stars with supermassive black hole binaries - I. Tidal disruption events. *MNRAS*, 477(3):4009–4034.
- Davies, M. B., Coleman Miller, M., and Bellovary, J. M. (2011). Supermassive black hole formation via gas accretion in nuclear stellar clusters. *ApJL*, 740(2):42.
- Davies, R. I., Mueller Sanchez, F., Genzel, R., Tacconi, L. J., Hicks, E. K. S., Friedrich, S., and Sternberg, A. (2007). A Close Look at Star Formation around Active Galactic Nuclei. *ApJ*, 671(2):1388–1412.
- De Rosa, A., Vignali, C., Bogdanović, T., Capelo, P. R., Charisi, M., Dotti, M., Husemann, B., Lusso, E., Mayer, L., Paragi, Z., Runnoe, J., Sesana, A., Steinborn, L., Bianchi, S., Colpi, M., del Valle, L., Frey, S., Gabányi, K., Giustini, M., Guainazzi, M., Haiman, Z., Herrera Ruiz, N., Herrero-Illana, R., Iwasawa, K., Komossa, S., Lena, D., Loiseau, N., Perez-Torres, M., Piconcelli, E., and Volonteri, M. (2019). The quest for dual and binary supermassive black holes: A multi-messenger view.
- Degraf, C. and Sijacki, D. (2020). Cosmological simulations of massive black hole seeds: Predictions for next-generation electromagnetic and gravitational wave observations. *MNRAS*, 491(4):4973–4992.
- Dehnen, W. (1993). A family of potential-density pairs for spherical galaxies and bulges. *MNRAS*, 265(1):250–256.
- Desvignes, G., Caballero, R. N., Lentati, L., Verbiest, J. P., Champion, D. J., Stappers, B. W., Janssen, G. H., Lazarus, P., Osłowski, S., Babak, S., Bassa, C. G., Brem, P., Burgay, M., Cognard, I., Gair, J. R., Graikou, E., Guillemot, L., Hessels, J. W., Jessner, A., Jordan, C., Karuppusamy, R., Kramer, M., Lassus, A., Lazaridis, K., Lee, K. J., Liu, K., Lyne, A. G., McKee, J., Mingarelli, C. M., Perrodin, D., Petiteau, A., Possenti, A., Purver, M. B., Rosado, P. A., Sanidas, S., Sesana, A., Shaifullah, G., Smits, R., Taylor, S. R., Theureau, G., Tiburzi, C., Van Haasteren, R., and Vecchio, A. (2016). High-precision timing of 42 millisecond pulsars with the European Pulsar Timing Array. *MNRAS*, 458(3):3341–3380.
- Dey, L., Gopakumar, A., Valtonen, M., Zola, S., Susobhanan, A., Hudec, R., Pihajoki, P., Pursimo, T., Berdyugin, A., Piirola, V., Ciprini, S., Nilsson, K., Jermak, H., Kidger, M., and Komossa, S. (2019). The unique blazar OJ 287 and its massive binary black hole central engine. *Universe*, 5(5):108.
- Di Matteo, T., King, A., and Cornish, N. J. (2019). *Black Hole Formation and Growth*, volume 48 of *Saas-Fee Advanced Course*. Springer Berlin Heidelberg, Berlin, Heidelberg.
- Dubois, Y., Pichon, C., Welker, C., Le Borgne, D., Devriendt, J., Laigle, C., Codis, S., Pogosyan, D., Arnouts, S., Benabed, K., Bertin, E., Blaizot, J., Bouchet, F., Cardoso, J. F., Colombi,

- S., De Lapparent, V., Desjacques, V., Gavazzi, R., Kassin, S., Kimm, T., McCracken, H., Milliard, B., Peirani, S., Prunet, S., Rouberol, S., Silk, J., Slyz, A., Sousbie, T., Teysier, R., Tresse, L., Treyer, M., Vibert, D., and Volonteri, M. (2014). Dancing in the dark: Galactic properties trace spin swings along the cosmic web. *MNRAS*, 444(2):1453–1468.
- Dullo, B. T., Graham, A. W., and Knapen, J. H. (2017). A remarkably large depleted core in the Abell 2029 BCG IC 1101. *MNRAS*, 471(2):2321–2333.
- Dyson, F. W., Eddington, A. S., and Davidson, C. (1920). IX. A determination of the deflection of light by the sun’s gravitational field, from observations made at the total eclipse of May 29, 1919. *Philos. Trans. R. Soc. London. Ser. A, Contain. Pap. a Math. or Phys. Character*, 220(571-581):291–333.
- Einstein, A., Infeld, L., Hoffmann, B., Einstein, A., Infeld, L., and Hoffmann, B. (1938). The Gravitational Equations and the Problem of Motion. *Ann. Math. Second Ser.*, 39(1):65–100.
- Ellis, J. and Lewicki, M. (2021). Cosmic String Interpretation of NANOGrav Pulsar Timing Data. *Phys. Rev. Lett.*, 126(4):041304.
- Escala, A., Larson, R. B., Coppi, P. S., and Mardones, D. (2005). The Role of Gas in the Merging of Massive Black Holes in Galactic Nuclei. II. Black Hole Merging in a Nuclear Gas Disk. *ApJ*, 630(1):152–166.
- Favata, M. (2009). Nonlinear gravitational-wave memory from binary black hole mergers. *ApJ*, 696(2):159–162.
- Faye, G., Blanchet, L., and Buonanno, A. (2006). Higher-order spin effects in the dynamics of compact binaries. I. Equations of motion. *Phys. Rev. D*, 74(10):104033.
- Feldmann, R. and Mayer, L. (2015). The Argo simulation - I. Quenching of massive galaxies at high redshift as a result of cosmological starvation. *MNRAS*, 446(2):1939–1956.
- Ferrarese, L. and Ford, H. (2005). Supermassive black holes in galactic nuclei: Past, present and future research. *Space Sci. Rev.*, 116(3-4):523–624.
- Fiacconi, D., Feldmann, R., and Mayer, L. (2015). The Argo simulation - II. The early build-up of the Hubble sequence. *MNRAS*, 446(2):1957–1972.
- Foffa, S., Porto, R. A., Rothstein, I., and Sturani, R. (2019). Conservative dynamics of binary systems to fourth Post-Newtonian order in the EFT approach I: Regularized Lagrangian. *Phys. Rev. D*, 100(2):024048.
- Foord, A., Gültekin, K., Nevin, R., Comerford, J. M., Hodges-Kluck, E., Scott Barrows, R., Goulding, A. D., and Greene, J. E. (2020). A second look at 12 candidate Dual AGNs using BAYMAX. *ApJ*, 892(1):21.
- Foord, A., Gültekin, K., Reynolds, M. T., Hodges-Kluck, E., Cackett, E. M., Comerford, J. M., King, A. L., Miller, J. M., and Runnoe, J. C. (2019). A Bayesian Analysis of SDSS J0914+0853, a Low-Mass Dual AGN Candidate. *ApJ*, 877(1):17.
- Foord, A., Gültekin, K., Runnoe, J. C., and Koss, M. J. (2021). AGN triality of triple mergers: Multi-wavelength classifications. *ApJ*, 907(2):14.
- Gaburov, E., Harfst, S., and Zwart, S. P. (2009). SAPPORO: A way to turn your graphics cards into a GRAPE-6. *New Astronomy*, 14(7):630–637.

- Genzel, R., Schödel, R., Ott, T., Eckart, A., Alexander, T., Lacombe, F., Rouan, D., and Aschenbach, B. (2003). Near-infrared flares from accreting gas around the supermassive black hole at the Galactic Centre. *Nature*, 425(6961):934–937.
- Gerhard, O. O. E. and Binney, J. (1985). Triaxial galaxies containing massive black holes or central density cusps. *MNRAS*, 216(2):467–502.
- Ghez, A. M., Klein, B. L., Morris, M., and Becklin, E. E. (1998). High Proper-Motion Stars in the Vicinity of Sagittarius A\*: Evidence for a Supermassive Black Hole at the Center of Our Galaxy. *ApJ*, 509(2):678–686.
- Gilmozzi, R. and Spyromilio, J. (2007). The European Extremely Large Telescope (E-ELT). *The Messenger*, 127:11.
- Goicovic, F. G., Maureira-Fredes, C., Sesana, A., Amaro-Seoane, P., and Cuadra, J. (2018). Accretion of clumpy cold gas onto massive black hole binaries: a possible fast route to binary coalescence. *MNRAS*, 479(3):3438–3455.
- Goicovic, F. G., Sesana, A., Cuadra, J., and Stasyszyn, F. (2017). Infalling clouds on to supermassive black hole binaries - II. Binary evolution and the final parsec problem. *MNRAS*, 472(1):514–531.
- Graham, A. W. and Scott, N. (2013). The Mbh-LSpheroid relation at high and low masses, the quadratic growth of black holes, and intermediate-mass black hole candidates. *ApJ*, 764(2).
- Gualandris, A., Dotti, M., and Sesana, A. (2012). Massive black hole binary plane reorientation in rotating stellar systems. *MNRAS*, 420(1):L38–L42.
- Gualandris, A. and Merritt, D. (2008). Ejection of Supermassive Black Holes from Galaxy Cores. *ApJ*, 678(2):780–797.
- Gualandris, A., Read, J. I., Dehnen, W., and Bortolas, E. (2017). Collisionless loss-cone refilling: there is no final parsec problem. *MNRAS*, 464(2):2301–2310.
- Gürlebeck, N. (2015). No-hair theorem for black holes in astrophysical environments. *Phys. Rev. Lett.*, 114(15).
- Habouzit, M., Li, Y., Somerville, R. S., Genel, S., Pillepich, A., Volonteri, M., Davé, R., Rosas-Guevara, Y., McAlpine, S., Peirani, S., Hernquist, L., Anglés-Alcázar, D., Reines, A., Bower, R., Dubois, Y., Nelson, D., Pichon, C., and Vogelsberger, M. (2020). Supermassive black holes in cosmological simulations I: MBH - Mst relation and black hole mass function. *MNRAS*, 503(2):1940–1975.
- Haiman, Z. (2013). The Formation of the First Massive Black Holes. *ASSL*, 396:293–341.
- Hamada, T. and Iitaka, T. (2007). The Chamomile Scheme: An Optimized Algorithm for N-body simulations on Programmable Graphics Processing Units. *arXiv e-print, arXiv:astro-ph/0703100*.
- Harfst, S., Gualandris, A., Merritt, D., Spurzem, R., Portegies Zwart, S., and Berczik, P. (2007). Performance analysis of direct N-body algorithms on special-purpose supercomputers. *New Astronomy*, 12(5):357–377.
- Häring, N. and Rix, H.-W. (2004). On the Black Hole Mass-Bulge Mass Relation. *ApJ*, 604(2):L89–L92.

- Heggie, D. C. (1975). Binary Evolution in Stellar Dynamics. *MNRAS*, 173(3):729–787.
- Hemsendorf, M., Sigurdsson, S., and Spurzem, R. (2002). Collisional Dynamics around Binary Black Holes in Galactic Centers. *ApJ*, 581(2):1256–1270.
- Hernquist, L. (1990). An analytical model for spherical galaxies and bulges. *ApJ*, 356:359.
- Hernquist, L. and Ostriker, J. P. (1992). A Self-consistent Field Method for Galactic Dynamics. *ApJ*, 386:375.
- Hickox, R. C. and Alexander, D. M. (2018). Obscured Active Galactic Nuclei. *ARA&A*, 56:625–671.
- Hills, J. G. (1983). The effect of low-velocity, low-mass intruders (collisionless gas) on the dynamical evolution of a binary system. *AJ*, 88:1269.
- Hobbs, G. and Dai, S. (2017). Gravitational wave research using pulsar timing arrays. *National Science Review*, 4(5):707–717.
- Hoffman, L. and Loeb, A. (2007). Dynamics of triple black hole systems in hierarchically merging massive galaxies. *MNRAS*, 377(3):957–976.
- Holley-Bockelmann, K. and Khan, F. M. (2015). Galaxy Rotation and Rapid Supermassive Binary Coalescence. *ApJ*, 810(2):139.
- Holmberg, E. (1941). On the Clustering Tendencies among the Nebulae. II. a Study of Encounters Between Laboratory Models of Stellar Systems by a New Integration Procedure. *ApJ*, 94:385.
- Holz, D. E. and Hughes, S. A. (2005). Using Gravitational-Wave Standard Sirens. *ApJ*, 629(1):15–22.
- Hulse, R. A. and Taylor, J. H. (1975). Discovery of a pulsar in a binary system. *ApJ*, 195:L51.
- Ikape, M. (2016). *Dynamical Evolution of Supermassive Binary Black Holes in Galactic Nuclei*.
- Illingworth, G. (1977). Rotation (?) in 13 elliptical galaxies. *ApJL*, 218:L43–L47.
- Isi, M., Giesler, M., Farr, W. M., Scheel, M. A., and Teukolsky, S. A. (2019). Testing the no-hair theorem with GW150914. *Phys. Rev. Lett.*, 123(11):111102.
- Islam, R. R., Taylor, J. E., and Silk, J. (2004). Massive black hole remnants of the first stars - II. Optical and X-ray signatures in present-day galactic haloes. *MNRAS*, 354(2):443–456.
- Ito, T., Makino, J., Ebisuzaki, T., and Sugimoto, D. (1990). A special-purpose N-body machine GRAPE-1. *Comput. Phys. Commun.*, 60(2):187–194.
- Iwasawa, M., Funato, Y., and Makino, J. (2006). Evolution of Massive Black Hole Triples. I. Equal-Mass Binary-Single Systems. *ApJ*, 651(2):1059–1067.
- Just, A., Khan, F., Berczik, P., Ernst, A., and Spurzem, R. (2011). Dynamical friction of massive objects in galactic centres. *MNRAS*, 411(1):653–674.
- Katz, M. L., Kelley, L. Z., Dosopoulou, F., Berry, S., Blecha, L., and Larson, S. L. (2020). Probing massive black hole binary populations with LISA. *MNRAS*, 491(2):2301–2317.

- Kelley, L. Z., Blecha, L., and Hernquist, L. (2017a). Massive black hole binary mergers in dynamical galactic environments. *MNRAS*, 464(3):3131–3157.
- Kelley, L. Z., Blecha, L., Hernquist, L., Sesana, A., and Taylor, S. R. (2017b). The gravitational wave background from massive black hole binaries in Illustris: Spectral features and time to detection with pulsar timing arrays. *MNRAS*, 471(4):4508–4526.
- Kelly, B. C., Bechtold, J., Trump, J. R., Vestergaard, M., and Siemiginowska, A. (2008). Observational Constraints on the Dependence of Radio-Quiet Quasar X-ray Emission on Black Hole Mass and Accretion Rate. *ApJS*, 176(2):355–373.
- Kerr, R. P. (1963). Gravitational field of a spinning mass as an example of algebraically special metrics. *Phys. Rev. Lett.*, 11(5):237–238.
- Khan, F. M., Berczik, P., and Just, A. (2018a). Gravitational wave driven mergers and coalescence time of supermassive black holes. *A&A*, 615:A71.
- Khan, F. M., Berczik, P., and Just, A. (2018b). Gravitational wave driven mergers and coalescence time of supermassive black holes. *A&A*, 615:A71.
- Khan, F. M., Berentzen, I., Berczik, P., Just, A., Mayer, L., Nitadori, K., and Callegari, S. (2012a). Formation and Hardening of Supermassive Black Hole Binaries in Minor Mergers of Disk Galaxies. *ApJ*, 756(1):30.
- Khan, F. M., Capelo, P. R., Mayer, L., and Berczik, P. (2018c). Dynamical Evolution and Merger Timescales of LISA Massive Black Hole Binaries in Disk Galaxy Mergers. *ApJ*, 868(2):97.
- Khan, F. M., Fiacconi, D., Mayer, L., Berczik, P., and Just, A. (2016). Swift Coalescence of Supermassive Black Holes in Cosmological Mergers of Massive Galaxies. *ApJ*, 828(2):73.
- Khan, F. M., Holley-Bockelmann, K., Berczik, P., and Just, A. (2013). Supermassive Black Hole Binary Evolution in Axisymmetric Galaxies: The Final Parsec Problem is Not a Problem. *ApJ*, 773(2):100.
- Khan, F. M., Just, A., and Merritt, D. (2011). Efficient Merger of Binary Supermassive Black Holes in Merging Galaxies. *ApJ*, 732(2):89.
- Khan, F. M., Mirza, M. A., and Holley-Bockelmann, K. (2020). Inward bound: the incredible journey of massive black holes as they pair and merge - I. The effect of mass ratio in flattened rotating galactic nuclei. *MNRAS*, 492(1):256–267.
- Khan, F. M., Preto, M., Berczik, P., Berentzen, I., Just, A., and Spurzem, R. (2012b). Mergers of Unequal-mass Galaxies: Supermassive Black Hole Binary Evolution and Structure of Merger Remnants. *ApJ*, 749(2):147.
- King, A. R., Pringle, J. E., and Hofmann, J. A. (2008). The evolution of black hole mass and spin in active galactic nuclei. *MNRAS*, 385(3):1621–1627.
- Kollatschny, W., Weilbacher, P., Ochmann, M., Chelouche, D., Monreal-Ibero, A., Bacon, R., and Contini, T. (2020). NGC 6240: A triple nucleus system in the advanced or final state of merging. *A&A*, 633:A79.
- Kormendy, J. and Ho, L. C. (2013). Coevolution (or not) of supermassive black holes and host galaxies. *ARA&A*, 51(1):511–653.

- Kozai, Y. (1962). Secular perturbations of asteroids with high inclination and eccentricity. *AJ*, 67(9):591.
- Krolik, J. H., Volonteri, M., Dubois, Y., and Devriendt, J. (2019). Population Estimates for Electromagnetically-Distinguishable Supermassive Binary Black Holes. *ApJ*, 879(2):12.
- Kulier, A., Ostriker, J. P., Natarajan, P., Lackner, C. N., and Cen, R. (2015). Understanding black hole mass assembly via accretion and mergers at late times in cosmological simulations. *ApJ*, 799(2):178.
- Kustaanheimo, P. and Stiefel, E. (1965). Perturbation theory of Kepler motion based on spinor regularization. *J. Reine Angew. Math.*, 218:204–219.
- Latif, M. A. and Ferrara, A. (2016). Formation of supermassive black hole seeds. *Publ. Astron. Soc. Aust.*, 33:16.
- Latif, M. A., Schleicher, D. R. G., Schmidt, W., and Niemeyer, J. C. (2013). The characteristic black hole mass resulting from direct collapse in the early universe. *MNRAS*, 436(4):2989–2996.
- Lehner, L. and Pretorius, F. (2014). Numerical relativity and astrophysics. *ARA&A*, 52:661–694.
- Lezhnin, K. and Vasiliev, E. (2019). Evolution of supermassive black hole binaries and tidal disruption rates in non-spherical galactic nuclei. *MNRAS*, 484(2):2851–2865.
- Li, K., Ballantyne, D. R., and Bogdanović, T. (2021). The Detectability of Kiloparsec Scale Dual AGNs: The Impact of Galactic Structure and Black Hole Orbital Properties. *arXiv e-print*, *arXiv:2103.02862*.
- Li, S., Berczik, P., Chen, X., Liu, F., Spurzem, R., and Qiu, Y. (2019). Direct N-body Simulations of Tidal Disruption Rate Evolution in Equal-mass Galaxy Mergers. *ApJ*, 883(2):132.
- Li, S., Liu, F., Berczik, P., Chen, X., and Spurzem, R. (2012). Interaction of Recoiling Supermassive Black Holes with Stars in Galactic Nuclei. *ApJ*, 748(1):65.
- Li, S., Liu, F., Berczik, P., and Spurzem, R. (2017). Boosted Tidal Disruption by Massive Black Hole Binaries During Galaxy Mergers from the View of N-Body Simulation. *ApJ*, 834(2):195.
- Lidov, M. L. (1962). The evolution of orbits of artificial satellites of planets under the action of gravitational perturbations of external bodies. *Planetary and Space Science*, 9(10):719–759.
- Lorentz, H. A. and Droste, J. (1937). The Motion of a System of Bodies under the Influence of their Mutual Attraction, According to Einstein’s Theory. In *Collect. Pap.*, pages 330–355. Springer Netherlands.
- Lousto, C. O. and Zlochower, Y. (2007). Further insight into gravitational recoil. *Phys. Rev. D - Part. Fields, Gravit. Cosmol.*, 77(4):044028.
- Lousto, C. O., Zlochower, Y., Dotti, M., and Volonteri, M. (2012). Gravitational recoil from accretion-aligned black-hole binaries. *Phys. Rev. D - Part. Fields, Gravit. Cosmol.*, 85(8):084015.
- Luo, J., Chen, L. S., Duan, H. Z., Gong, Y. G., Hu, S., Ji, J., Liu, Q., Mei, J., Milyukov, V., Sazhin, M., Shao, C. G., Toth, V. T., Tu, H. B., Wang, Y., Wang, Y., Yeh, H. C., Zhan, M. S.,

- Zhang, Y., Zharov, V., and Zhou, Z. B. (2016). TianQin: A space-borne gravitational wave detector. *Class. Quantum Gravity*, 33(3):035010.
- Lupi, A., Colpi, M., Devecchi, B., Galanti, G., and Volonteri, M. (2014). Constraining the high-redshift formation of black hole seeds in nuclear star clusters with gas inflows. *MNRAS*, 442(4):3616–3626.
- Madau, P. and Rees, M. J. (2001). Massive Black Holes as Population III Remnants. *ApJ*, 551(1):L27–L30.
- Magorrian, J., Tremaine, S., Richstone, D., Bender, R., Bower, G., Dressler, A., Faber, S. M., Gebhardt, K., Green, R., Grillmair, C., Kormendy, J., and Lauer, T. (1998). The Demography of Massive Dark Objects in Galaxy Centers. *AJ*, 115(6):2285–2305.
- Makino, J. (1991). Optimal order and time-step criterion for Aarseth-type N-body integrators. *ApJ*, 369:200.
- Makino, J. and Aarseth, S. J. (1992). On a Hermite Integrator with Ahmad-Cohen Scheme for Gravitational Many-Body Problems. *PASJ*, 44:141–151.
- Makino, J., Taiji, M., Makino, J., and Taiji, M. (1998). Scientific Simulations with Special-Purpose Computers—the GRAPE Systems. *sssc*, page 248.
- Mannerkoski, M., Johansson, P. H., Pihajoki, P., Rantala, A., and Naab, T. (2019). Gravitational Waves from the Inspiral of Supermassive Black Holes in Galactic-scale Simulations. *ApJ*, 887(1):35.
- Mannerkoski, M., Johansson, P. H., Rantala, A., Naab, T., and Liao, S. (2021). Resolving the Complex Evolution of a Supermassive Black Hole Triplet in a Cosmological Simulation. *arXiv e-print*, *arXiv:2103.16254*.
- Mapelli, M. (2016). Massive black hole binaries from runaway collisions: The impact of metallicity. *MNRAS*, 459(4):3432–3446.
- Marinacci, F., Vogelsberger, M., Pakmor, R., Torrey, P., Springel, V., Hernquist, L., Nelson, D., Weinberger, R., Pillepich, A., Naiman, J., and Genel, S. (2018). First results from the IllustrisTNG simulations: Radio haloes and magnetic fields. *MNRAS*, 480(4):5113–5139.
- Mayer, L., Kazantzidis, S., Madau, P., Colpi, M., Quinn, T., and Wadsley, J. (2007). Rapid formation of supermassive black hole binaries in galaxy mergers with gas. *Science*, 316(5833):1874–1877.
- McGee, S., Sesana, A., and Vecchio, A. (2020). Linking gravitational waves and X-ray phenomena with joint LISA and Athena observations. *Nature Astronomy*, 4(1):26–31.
- McWilliams, S. T., Ostriker, J. P., and Pretorius, F. (2014). Gravitational waves and stalled satellites from massive galaxy mergers at  $z \leq 1$ . *ApJ*, 789(2):156.
- Meiron, Y. and Laor, A. (2010). The stellar kinematic signature of massive black hole binaries. *MNRAS*, 407(3):1497–1513.
- Meiron, Y. and Laor, A. (2013). The kinematic signature of the inspiral phase of massive binary black holes. *MNRAS*, 433(3):2502–2510.

- Meiron, Y., Li, B., Holley-Bockelmann, K., and Spurzem, R. (2014). Expansion Techniques for Collisionless Stellar Dynamical Simulations. *ApJ*, 792(2):98.
- Memmesheimer, R.-M., Gopakumar, A., and Schäfer, G. (2004). Third post-Newtonian accurate generalized quasi-Keplerian parametrization for compact binaries in eccentric orbits. *Phys. Rev. D - Part. Fields, Gravit. Cosmol.*, 70(10):17.
- Menon, H., Wesolowski, L., Zheng, G., Jetley, P., Kale, L., Quinn, T., and Governato, F. (2015). Adaptive techniques for clustered N-body cosmological simulations. *Comput. Astrophys. Cosmol.*, 2(1):1.
- Merritt, D. (2013a). *Dynamics and Evolution of Galactic Nuclei*. Princeton University Press, Princeton and Oxford.
- Merritt, D. (2013b). Loss-cone dynamics. *Class. Quantum Gravity*, 30(24):244005.
- Merritt, D. (2015). Gravitational Encounters and the Evolution of Galactic Nuclei. IV. Captures Mediated by Gravitational-Wave Energy Loss. *ApJ*, 814(1):57, 12.
- Merritt, D. and Poon, M. (2004). Chaotic Loss Cones and Black Hole Fueling. *ApJ*, 606(2):788–798.
- Merritt, D. and Vasiliev, E. (2011). Orbits Around Black Holes in Triaxial Nuclei. *ApJ*, 726(2):61.
- Merritt, D. and Wang, J. (2005). Loss Cone Refilling Rates in Galactic Nuclei. *ApJL*, 621(2):L101–L104.
- Middleton, H., Sesana, A., Chen, S., Vecchio, A., Del Pozzo, W., and Rosado, P. A. (2021). Massive black hole binary systems and the NANOGrav 12.5 year results. *MNRAS: Letters*, 502(1):L99–L103.
- Mikkola, S. and Aarseth, S. (2002). A Time-Transformed Leapfrog Scheme. *CeMDA*, 84(4):343–354.
- Mikkola, S. and Aarseth, S. J. (1993). An implementation of N-body chain regularization. *Celest. Mech. Dyn. Astron.*, 57(3):439–459.
- Mikkola, S., Aarseth, S. J., Mikkola, S., and Aarseth, S. J. (1990). A chain regularization method for the few-body problem. Technical Report 4.
- Mikkola, S. and Merritt, D. (2006). Algorithmic regularization with velocity-dependent forces. *MNRAS*, 372(1):219–223.
- Mikkola, S. and Merritt, D. (2008). Implementing Few-Body Algorithmic Regularization with Post-Newtonian Terms. *AJ*, 135(6):2398–2405.
- Milosavljević, M. and Merritt, D. (2001). Formation of Galactic Nuclei. *ApJ*, 563(1):34–62.
- Milosavljević, M. and Merritt, D. (2003a). Long-Term Evolution of Massive Black Hole Binaries. *ApJ*, 596(2):860–878.
- Milosavljević, M. and Merritt, D. (2003b). The Final Parsec Problem. In Centrella, J. M., editor, *Astrophys. Gravitational Wave Sources*, volume 686 of *American Institute of Physics Conference Series*, pages 201–210.

- Mirza, M., Tahir, A., Khan, F., Holley-Bockelmann, H., Baig, A., Berczik, P., and Chishtie, F. (2017). Galaxy rotation and supermassive black hole binary evolution. *MNRAS*, 470(1):940–947.
- Mo, H., van den Bosch, F. C., and White, S. (2010). *Galaxy Formation and Evolution*. Cambridge University Press, Cambridge, UK.
- Morganti, R. (2017). The Many Routes to AGN Feedback. *Front. Astron. Sp. Sci.*, 4:42.
- Naiman, J. P., Pillepich, A., Springel, V., Ramirez-Ruiz, E., Torrey, P., Vogelsberger, M., Pakmor, R., Nelson, D., Marinacci, F., Hernquist, L., Weinberger, R., and Genel, S. (2018). First results from the IllustrisTNG simulations: A tale of two elements - Chemical evolution of magnesium and europium. *MNRAS*, 477(1):1206–1224.
- Nasim, I., Gualandris, A., Read, J., Dehnen, W., Delorme, M., and Antonini, F. (2020). Defeating stochasticity: coalescence timescales of massive black holes in galaxy mergers. *MNRAS*, 497(1):739–746.
- Nelson, D., Pillepich, A., Springel, V., Weinberger, R., Hernquist, L., Pakmor, R., Genel, S., Torrey, P., Vogelsberger, M., Kauffmann, G., Marinacci, F., and Naiman, J. (2018). First results from the IllustrisTNG simulations: The galaxy colour bimodality. *MNRAS*, 475(1):624–647.
- Nelson, D., Springel, V., Pillepich, A., Rodriguez-Gomez, V., Torrey, P., Genel, S., Vogelsberger, M., Pakmor, R., Marinacci, F., Weinberger, R., Kelley, L., Lovell, M., Diemer, B., and Hernquist, L. (2019). The IllustrisTNG simulations: Public data release. *Comput. Astrophys. Cosmol.*, 6(1):29.
- Newville, M., Stensitzki, T., Allen, D. B., and Ingargiola, A. (2014). LMFIT: Non-Linear Least-Square Minimization and Curve-Fitting for Python. *Zenodo*, DOI 10.5281/ZENODO.11813.
- Nguyen, K., Bogdanović, T., Runnoe, J. C., Taylor, S. R., Sesana, A., Eracleous, M., and Sigurdsson, S. (2020). Pulsar timing array constraints on the merger timescale of subparsec supermassive black hole binary candidates. *ApJL*, 900(2):7.
- Nitadori, K. (2009). *New approaches to high-performance N-body*. PhD thesis, University of Tokyo.
- Nitadori, K. and Makino, J. (2008). 6th and 8th Order Hermite Integrator for N-body Simulations. *New Astronomy*, 13(7):498–507.
- Nyland, L., Harris, M., and Prins, J. (2007). Chapter 31. Fast N-Body Simulation with CUDA | NVIDIA Developer. *GPU Gems, NVIDIA Dev.*, pages 3:677–695.
- Ogiya, G., Hahn, O., Mingarelli, C. M., and Volonteri, M. (2020). Accelerated orbital decay of supermassive black hole binaries in merging nuclear star clusters. *MNRAS*, 493(3):3676–3689.
- Padovani, P., Alexander, D. M., Assef, R. J., De Marco, B., Giommi, P., Hickox, R. C., Richards, G. T., Smolčić, V., Hatziminaoglou, E., Mainieri, V., and Salvato, M. (2017). Active galactic nuclei: what’s in a name? *A&AR*, 25(1):2.
- Perets, H. B. and Alexander, T. (2007). Massive perturbers and the efficient merger of binary massive black holes. *ApJ*, 677(1):146–159.
- Perets, H. B., Mastrobuono-Battisti, A., Meiron, Y., and Gualandris, A. (2018). Spiral arms,

- warping, and clumps formation in the galactic center young stellar disk. *arXiv e-print, arXiv:1802.00012*.
- Peschken, N., Łokas, E. L., and Athanassoula, E. (2020). Disc galaxies formed from major mergers in Illustris. *MNRAS*, 493(1):1375–1387.
- Peters, P. and Mathews, J. (1963). Gravitational Radiation from Point Masses in a Keplerian Orbit. *Phys. Rev.*, 131(1):435–440.
- Peters, P. C. (1964). Gravitational radiation and the motion of two point masses. *Phys. Rev.*, 136(4B):1224–1232.
- Pfister, H., Volonteri, M., Dubois, Y., Dotti, M., and Colpi, M. (2019). The erratic dynamical life of black hole seeds in high-redshift galaxies. *MNRAS*, 486(1):101–111.
- Pillepich, A., Nelson, D., Hernquist, L., Springe, V., Rüdiger Pakmor, Torrey, P., Weinberger, R., Gene, S., Naiman, J. P., Marinacci, F., and Vogelsberger, M. (2018a). First results from the illustriTNG simulations: The stellar mass content of groups and clusters of galaxies. *MNRAS*, 475(1):648–675.
- Pillepich, A., Springel, V., Nelson, D., Genel, S., Naiman, J., Pakmor, R., Hernquist, L., Torrey, P., Vogelsberger, M., Weinberger, R., and Marinacci, F. (2018b). Simulating galaxy formation with the IllustrisTNG model. *MNRAS*, 473(3):4077–4106.
- Poisson, E. (2004). The motion of point particles in curved spacetime. *Living Rev. Relativ.*, 7(1):6.
- Poisson, E. and Will, C. M. (2014). *Gravity*. Cambridge University Press, Cambridge, UK.
- Poole, G. B., Mutch, S. J., Croton, D. J., and Wyithe, S. (2017). Convergence properties of halo merger trees; Halo and substructure merger rates across cosmic history. *MNRAS*, 472(3):3659–3682.
- Portegies Zwart, S. F. and McMillan, S. L. W. (2002). The Runaway Growth of Intermediate-Mass Black Holes in Dense Star Clusters. *ApJ*, 576(2):899–907.
- Preto, M., Berentzen, I., Berczik, P., and Spurzem, R. (2011). Fast Coalescence of Massive Black Hole Binaries from Mergers of Galactic Nuclei: Implications for Low-frequency Gravitational-wave Astrophysics. *ApJL*, 732(2):L26.
- Punturo, M., Abernathy, M., Acernese, F., Allen, B., Andersson, N., Arun, K., Barone, F., Barr, B., Barsuglia, M., Beker, M., Beveridge, N., Birindelli, S., Bose, S., Bosi, L., Braccini, S., Bradaschia, C., Bulik, T., Calloni, E., Cella, G., Chassande Mottin, E., Chelkowski, S., Chincarini, A., Clark, J., Coccia, E., Colacino, C., Colas, J., Cumming, A., Cunningham, L., Cuoco, E., Danilishin, S., Danzmann, K., De Luca, G., De Salvo, R., Dent, T., De Rosa, R., Di Fiore, L., Di Virgilio, A., Doets, M., Fafone, V., Falferi, P., Flaminio, R., Franc, J., Frasconi, F., Freise, A., Fulda, P., Gair, J., Gemme, G., Gennai, A., Giazotto, A., Glampedakis, K., Granata, M., Grote, H., Guidi, G., Hammond, G., Hannam, M., Harms, J., Heinert, D., Hendry, M., Heng, I., Hennes, E., Hild, S., Hough, J., Husa, S., Huttner, S., Jones, G., Khalili, F., Kokeyama, K., Kokkotas, K., Krishnan, B., Lorenzini, M., Lück, H., Majorana, E., Mandel, I., Mandic, V., Martin, I., Michel, C., Minkenov, Y., Morgado, N., Mosca, S., Mours, B., Müller-Ebhardt, H., Murray, P., Nawrodt, R., Nelson, J., Oshaughnessy, R., Ott, C. D., Palomba, C., Paoli, A., Parguez, G., Pasqualetti, A., Passaquieti, R., Passuello, D., Pinard,

- L., Poggiani, R., Popolizio, P., Prato, M., Puppo, P., Rabeling, D., Rapagnani, P., Read, J., Regimbau, T., Rehbein, H., Reid, S., Rezzolla, L., Ricci, F., Richard, F., Rocchi, A., Rowan, S., Rüdigger, A., Sassolas, B., Sathyaprakash, B., Schnabel, R., Schwarz, C., Seidel, P., Sintes, A., Somiya, K., Speirits, F., Strain, K., Strigin, S., Sutton, P., Tarabrin, S., Thüring, A., Van Den Brand, J., Van Leewen, C., Van Veggel, M., Van Den Broeck, C., Vecchio, A., Veitch, J., Vetrano, F., Vicere, A., Vyatchanin, S., Willke, B., Woan, G., Wolfango, P., and Yamamoto, K. (2010). The Einstein Telescope: A third-generation gravitational wave observatory. *Class. Quantum Gravity*, 27(19):194002.
- Quinlan, G. D. (1996). The dynamical evolution of massive black hole binaries I. Hardening in a fixed stellar background. *New Astronomy*, 1(1):35–56.
- Quinlan, G. D. and Hernquist, L. (1997). The dynamical evolution of massive black hole binaries - II. Self-consistent N-body integration. *New Astronomy*, 2(6):533–554.
- Rantala, A., Johansson, P. H., Naab, T., Thomas, J., and Frigo, M. (2018). The Formation of Extremely Diffuse Galaxy Cores by Merging Supermassive Black Holes. *ApJ*, 864(2):113.
- Rantala, A., Pihajoki, P., Johansson, P. H., Naab, T., Lahén, N., and Sawala, T. (2017). Post-Newtonian Dynamical Modeling of Supermassive Black Holes in Galactic-scale Simulations. *ApJ*, 840(1):53.
- Rantala, A., Pihajoki, P., Mannerkoski, M., Johansson, P. H., and Naab, T. (2020). MSTAR - A fast parallelized algorithmically regularized integrator with minimum spanning tree coordinates. *MNRAS*, 492(3):4131–4148.
- Rasskazov, A. and Kocsis, B. (2019). The Rate of Stellar Mass Black Hole Scattering in Galactic Nuclei. *ApJ*, 881(1):20.
- Rasskazov, A. and Merritt, D. (2017). Evolution of Binary Supermassive Black Holes in Rotating Nuclei. *ApJ*, 837(2):135.
- Read, J. I., Goerdt, T., Moore, B., Pontzen, A. P., Stadel, J., and Lake, G. (2006). Dynamical friction in constant density cores: a failure of the Chandrasekhar formula. *MNRAS*, 373(4):1451–1460.
- Reardon, D. J., Hobbs, G., Coles, W., Levin, Y., Keith, M. J., Bailes, M., Bhat, N. D., Burke-Spolaor, S., Dai, S., Kerr, M., Lasky, P. D., Manchester, R. N., Osłowski, S., Ravi, V., Shannon, R. M., van Straten, W., Toomey, L., Wang, J., Wen, L., You, X. P., and Zhu, X. J. (2016). Timing analysis for 20 millisecond pulsars in the Parkes Pulsar Timing Array. *MNRAS*, 455(2):1751–1769.
- Rees, M. J. (1984). Black Hole Models for Active Galactic Nuclei. *ARA&A*, 22(1):471–506.
- Reitze, D., Adhikari, R. X., Ballmer, S., Barish, B., Barsotti, L., Billingsley, G. L., Brown, D. A., Chen, Y., Coyne, D., Eisenstein, R., Evans, M., Fritschel, P., Hall, E. D., Lazzarini, A., Lovelace, G., Read, J., Sathyaprakash, B. S., Shoemaker, D., Smith, J., Torrie, C., Vitale, S., Weiss, R., Wipf, C., and Zucker, M. (2019). Cosmic explorer: The U.S. Contribution to gravitational-wave astronomy beyond LIGO. *BAAS*, 51(7):35.
- Reynolds, C. S. (2020). Observational Constraints on Black Hole Spin. *arXiv e-print, arXiv:2011.08948*.

- Reynolds, C. S. and Fabian, A. C. (2007). Broad iron K-alpha emission lines as a diagnostic of black hole spin. *ApJ*, 675(2):1048–1056.
- Ricarte, A., Tremmel, M., Natarajan, P., Zimmer, C., and Quinn, T. (2021). Origins and demographics of wandering black holes. *MNRAS*, 503(4):6098–6111.
- Robinson, I., Schild, A., and Schucking, E. L. (1965). Quasi-stellar sources and gravitational collapse. *Proc. 1st Texas Symp. Relativ. Astrophys. Chicago Univ. Chicago Press. 1965, Ed. by Ivor Robinson, Alfred Schild, E.L. Schucking.*
- Rodriguez, C., Taylor, G., Zavala, R., Peck, A., Pollack, L., and Romani, R. (2006). A Compact Supermassive Binary Black Hole System. *ApJ*, 646(1):49–60.
- Rodriguez-Gomez, V., Genel, S., Vogelsberger, M., Sijacki, D., Pillepich, A., Sales, L. V., Torrey, P., Snyder, G., Nelson, D., Springel, V., Ma, C. P., and Hernquist, L. (2015). The merger rate of galaxies in the Illustris simulation: A comparison with observations and semi-empirical models. *MNRAS*, 449(1):49–64.
- Roedig, C. and Sesana, A. (2014). Migration of massive black hole binaries in self-gravitating discs: retrograde versus prograde. *MNRAS*, 439(4):3476–3489.
- Rusli, S. P., Erwin, P., Saglia, R. P., Thomas, J., Fabricius, M., Bender, R., and Nowak, N. (2013). Depleted Galaxy Cores and Dynamical Black Hole Masses. *AJ*, 146(6):160.
- Salpeter, E. (1964). ACCRETION OF INTERSTELLAR MATTER BY MASSIVE OBJECTS. *ApJ*, 140:796–800.
- Sathyaprakash, B. S. and Schutz, B. F. (2009). Physics, astrophysics and cosmology with gravitational waves. *Living Rev. Relativ.*, 12(1):2.
- Sayeb, M., Blecha, L., Kelley, L. Z., Gerosa, D., Kesden, M., and Thomas, J. (2021). Massive black hole binary inspiral and spin evolution in a cosmological framework. *MNRAS*, 501(2):2531–2546.
- Schaye, J., Crain, R. A., Bower, R. G., Furlong, M., Schaller, M., Theuns, T., Dalla Vecchia, C., Frenk, C. S., McCarthy, I. G., Helly, J. C., Jenkins, A., Rosas-Guevara, Y. M., White, S. D., Baes, M., Booth, C. M., Camps, P., Navarro, J. F., Qu, Y., Rahmati, A., Sawala, T., Thomas, P. A., and Trayford, J. (2015). The EAGLE project: Simulating the evolution and assembly of galaxies and their environments. *MNRAS*, 446(1):521–554.
- Schmidt, M. (1963). 3C 273: A star-like object with large red-shift. *Nature*, 197(4872):1040.
- Sesana, A. (2010). Self Consistent Model for the Evolution of Eccentric Massive Black Hole Binaries in Stellar Environments: Implications for Gravitational Wave Observations. *ApJ*, 719(1):851–864.
- Sesana, A., Gualandris, A., and Dotti, M. (2011). Massive black hole binary eccentricity in rotating stellar systems. *MNRAS: Letters*, 415(1):L35–L39.
- Sesana, A., Haardt, F., and Madau, P. (2006). Interaction of Massive Black Hole Binaries with Their Stellar Environment. I. Ejection of Hypervelocity Stars. *ApJ*, 651(1):392–400.
- Sesana, A., Haardt, F., and Madau, P. (2008). Interaction of Massive Black Hole Binaries with Their Stellar Environment. III. Scattering of Bound Stars. *ApJ*, 686(1):432–447.

- Sesana, A. and Khan, F. M. (2015). Scattering experiments meet N-body - I. A practical recipe for the evolution of massive black hole binaries in stellar environments. *MNRAS*, 454(1):L66–L70.
- Shakura, N. I. and Sunyaev, R. A. (1973). Reprint of 1973A&A....24..337S. Black holes in binary systems. Observational appearance. *A&A*, 500:33–51.
- Shankar, F., Bernardi, M., Richardson, K., Marsden, C., Sheth, R. K., Allevato, V., Graziani, L., Mezcuca, M., Ricci, F., Penny, S. J., La Franca, F., and Pacucci, F. (2019). Black hole scaling relations of active and quiescent galaxies: Addressing selection effects and constraining virial factors. *MNRAS*, 485(1):1278–1292.
- Shapiro, S. L. and Teukolsky, S. A. (1983). *Black Holes, White Dwarfs, and Neutron Stars*. John Wiley and Sons, New York, USA.
- Sillanpaa, A., Haarala, S., Valtonen, M. J., Sundelius, B., and Byrd, G. G. (1988). OJ 287 - Binary pair of supermassive black holes. *ApJ*, 325:628.
- Smith, A. and Bromm, V. (2019). Supermassive Black Holes in the Early Universe. *Contemp. Phys.*, 60(2):111–126.
- Souza Lima, R., Mayer, L., Capelo, P. R., Bortolas, E., and Quinn, T. R. (2020). The Erratic Path to Coalescence of LISA Massive Black Hole Binaries in Subparsec-resolution Simulations of Smooth Circumnuclear Gas Disks. *ApJ*, 899(2):126.
- Spera, M. and Mapelli, M. (2017). Very massive stars, pair-instability supernovae and intermediate-mass black holes with the SEVN code. *MNRAS*, 470(4):4739–4749.
- Springel, V. (2005). The cosmological simulation code GADGET-2. *MNRAS*, 364(4):1105–1134.
- Springel, V. (2010). E pur si muove: Galilean-invariant cosmological hydrodynamical simulations on a moving mesh. *MNRAS*, 401(2):791–851.
- Springel, V., Pakmor, R., Pillepich, A., Weinberger, R., Nelson, D., Hernquist, L., Vogelsberger, M., Genel, S., Torrey, P., Marinacci, F., and Naiman, J. (2018). First results from the IllustrisTNG simulations: Matter and galaxy clustering. *MNRAS*, 475(1):676–698.
- Springel, V., Pakmor, R., Zier, O., and Reinecke, M. (2020). Simulating cosmic structure formation with the GADGET-4 code. *arXiv e-print*, *arXiv: 2010.03567*.
- Springel, V., White, S. D., Tormen, G., and Kauffmann, G. (2001). Populating a cluster of galaxies - I. Results at  $z = 0$ . *MNRAS*, 328(3):726–750.
- Spurzem, R. (1999). Direct N -body simulations. *J. Comput. Appl. Math.*, 109(1-2):407–432.
- Stone, N. C., Vasiliev, E., Kesden, M., Rossi, E. M., Perets, H. B., and Amaro-Seoane, P. (2020). Rates of Stellar Tidal Disruption.
- Szego, G. (1975). *Orthogonal Polynomials*. American Mathematical Society, Providence, Rhode Island, USA.
- Tagoshi, H., Ohashi, A., and Owen, B. J. (2001). Gravitational field and equations of motion of spinning compact binaries to 2.5 post-Newtonian order. *Phys. Rev. D*, 63(4):044006.

- Tamfal, T., Capelo, P. R., Kazantzidis, S., Mayer, L., Potter, D., Stadel, J., and Widrow, L. M. (2018). Formation of LISA Black Hole Binaries in Merging Dwarf Galaxies: The Imprint of Dark Matter.
- Tanikawa, A. and Umemura, M. (2011). Successive Merger of Multiple Massive Black Holes in a Primordial Galaxy. *ApJL*, 728(2):L31.
- Thomas, J., Jesseit, R., Naab, T., Saglia, R., Burkert, A., and Bender, R. (2007). Axisymmetric orbit models of N-body merger remnants: a dependency of reconstructed mass on viewing angle. *MNRAS*, 381(4):1672–1696.
- Thomas, J., Jesseit, R., Saglia, R., Bender, R., Burkert, A., Corsini, E., Gebhardt, K., Magorrian, J., Naab, T., Thomas, D., and Wegner, G. (2009). The flattening and the orbital structure of early-type galaxies and collisionless N-body binary disc mergers. *MNRAS*, 393(2):641–652.
- Tremmel, M., Governato, F., Volonteri, M., Pontzen, A., and Quinn, T. R. (2018a). Wandering Supermassive Black Holes in Milky-Way-mass Halos. *ApJL*, 857(2):L22.
- Tremmel, M., Governato, F., Volonteri, M., Quinn, T., and Pontzen, A. (2018b). Dancing to CHANGA: a self-consistent prediction for close SMBH pair formation time-scales following galaxy mergers. *MNRAS*, 475(4):4967–4977.
- Valiante, R., Colpi, M., Schneider, R., Mangiagli, A., Bonetti, M., Cerini, G., Fairhurst, S., Haardt, F., Mills, C., and Sesana, A. (2021). Unveiling early black hole growth with multi-frequency gravitational wave observations. *MNRAS*, 500(3):4095–4109.
- Vasiliev, E. (2014). Rates of capture of stars by supermassive black holes in non-spherical galactic nuclei. *Class. Quantum Gravity*, 31(24):467–502.
- Vasiliev, E. (2016). Evolution of binary supermassive black holes and the final-parsec problem. In *Proc. of the IAU*, volume 10, pages 92–100. Cambridge University Press.
- Vasiliev, E. (2019). AGAMA: Action-based galaxy modelling architecture. *MNRAS*, 482(2):1525–1544.
- Vasiliev, E., Antonini, F., and Merritt, D. (2014). The Final-parsec Problem in Nonspherical Galaxies Revisited. *ApJ*, 785(2):163.
- Vasiliev, E., Antonini, F., and Merritt, D. (2015). The Final-parsec Problem in the Collisionless Limit. *ApJ*, 810(1):49.
- Verbiest, J. P., Lentati, L., Hobbs, G., Van Haasteren, R., Demorest, P. B., Janssen, G. H., Wang, J. B., Desvignes, G., Caballero, R. N., Keith, M. J., Champion, D. J., Arzoumanian, Z., Babak, S., Bassa, C. G., Bhat, N. D., Brazier, A., Brem, P., Burgay, M., Burke-Spolaor, S., Chamberlin, S. J., Chatterjee, S., Christy, B., Cognard, I., Cordes, J. M., Dai, S., Dolch, T., Ellis, J. A., Ferdman, R. D., Fonseca, E., Gair, J. R., Garver-Daniels, N. E., Gentile, P., Gonzalez, M. E., Graikou, E., Guillemot, L., Hessels, J. W., Jones, G., Karuppusamy, R., Kerr, M., Kramer, M., Lam, M. T., Lasky, P. D., Lassus, A., Lazarus, P., Lazio, T. J., Lee, K. J., Levin, L., Liu, K., Lynch, R. S., Lyne, A. G., Mckee, J., McLaughlin, M. A., McWilliams, S. T., Madison, D. R., Manchester, R. N., Mingarelli, C. M., Nice, D. J., Osłowski, S., Palliyaguru, N. T., Pennucci, T. T., Perera, B. B., Perrodin, D., Possenti, A., Petiteau, A., Ransom, S. M., Reardon, D., Rosado, P. A., Sanidas, S. A., Sesana, A., Shaifullah, G., Shannon, R. M., Siemens, X., Simon, J., Smits, R., Spiewak, R., Stairs, I. H., Stappers,

- B. W., Stinebring, D. R., Stovall, K., Swiggum, J. K., Taylor, S. R., Theureau, G., Tiburzi, C., Toomey, L., Vallisneri, M., Van Straten, W., Vecchio, A., Wang, Y., Wen, L., You, X. P., Zhu, W. W., and Zhu, X. J. (2016). The international pulsar timing array: First data release. *MNRAS*, 458(2):1267–1288.
- Verbiest, J. P. W., Osłowski, S., and Burke-Spolaor, S. (2021). Pulsar Timing Array Experiments. *arXiv e-print, arXiv: 2101.10081*.
- Vestergaard, M., Fan, X., Tremonti, C. A., Osmer, P. S., and Richards, G. T. (2008). Mass Functions of the Active Black Holes in Distant Quasars from the Sloan Digital Sky Survey Data Release 3. *ApJ*, 674(1):L1–L4.
- Vogelsberger, M., Genel, S., Springel, V., Torrey, P., Sijacki, D., Xu, D., Snyder, G., Bird, S., Nelson, D., and Hernquist, L. (2014). Properties of galaxies reproduced by a hydrodynamic simulation. *Nature*, 509(7499):177–182.
- Vogelsberger, M., Marinacci, F., Torrey, P., and Puchwein, E. (2020). Cosmological simulations of galaxy formation. *Nature Reviews Physics*, 2(1):42–66.
- Volonteri, M. (2010). Formation of supermassive black holes. *A&AR*, 18(3):279–315.
- Volonteri, M. and Bellovary, J. (2012). Black holes in the early Universe. *Reports Prog. Phys.*, 75(12).
- von Hoerner, S. (1960). Die numerische Integration des n-Körper-Problemes für Sternhaufen. I. *Z. Astrophys.*, 50:184–214.
- Wadsley, J., Stadel, J., and Quinn, T. (2004). Gasoline: a flexible, parallel implementation of TreeSPH. *New Astronomy*, 9(2):137–158.
- Wang, H.-T., Jiang, Z., Sesana, A., Barausse, E., Huang, S.-J., Wang, Y.-F., Feng, W.-F., Wang, Y., Hu, Y.-M., Mei, J., and Luo, J. (2019). Science with the TianQin observatory: Preliminary results on massive black hole binaries. *Phys. Rev. D*, 100(4).
- Wang, L., Berczik, P., Spurzem, R., and Kouwenhoven, M. (2014). The Link between Ejected Stars, Hardening and Eccentricity Growth of Super Massive Black Holes in Galactic Nuclei. *ApJ*, 780(2):164.
- Wang, L., Spurzem, R., Aarseth, S., Giersz, M., Askar, A., Berczik, P., Naab, T., Schadow, R., and Kouwenhoven, M. B. (2016). The DRAGON simulations: Globular cluster evolution with a million stars. *MNRAS*, 458(2):1450–1465.
- Wang, R., Ruan, W.-H., Yang, Q., Guo, Z.-K., Cai, R.-G., and Hu, B. (2020). Hubble parameter estimation via dark sirens with the LISA-Taiji network. *arXiv e-print, arXiv: 2010.14732*.
- Weinberger, R., Springel, V., Pakmor, R., Nelson, D., Genel, S., Pillepich, A., Vogelsberger, M., Marinacci, F., Naiman, J., Torrey, P., and Hernquist, L. (2018). Supermassive black holes and their feedback effects in the IllustrisTNG simulation. *MNRAS*, 479(3):4056–4072.
- Weltman, A., Bull, P., Camera, S., Kelley, K., Padmanabhan, H., Pritchard, J., Raccanelli, A., Riemer-Sørensen, S., Shao, L., Andrianomena, S., Athanassoula, E., Bacon, D., Barkana, R., Bertone, G., Bøhm, C., Bonvin, C., Bosma, A., Brügggen, M., Burigana, C., Calore, F., Cembranos, J. A., Clarkson, C., Connors, R. M., Cruz-Dombriz, D. L., Dunsby, P. K., Fonseca, J., Fornengo, N., Gaggero, D., Harrison, I., Larena, J., Ma, Y. Z., Maartens, R., Méndez-Isla,

- M., Mohanty, S. D., Murray, S., Parkinson, D., Pourtsidou, A., Quinn, P. J., Regis, M., Saha, P., Sahlén, M., Sakellariadou, M., Silk, J., Trombetti, T., Vazza, F., Venumadhav, T., Vidotto, F., Villaescusa-Navarro, F., Wang, Y., Weniger, C., Wolz, L., Zhang, F., and Gaensler, B. M. (2020). Fundamental physics with the Square Kilometre Array.
- White, S. D. M. and Frenk, C. S. (1991). Galaxy formation through hierarchical clustering. *ApJ*, 379:52.
- White, S. D. M. and Rees, M. J. (1978). Core condensation in heavy halos: a two-stage theory for galaxy formation and clustering. *MNRAS*, 183(3):341–358.
- Will, C. M. (2011). On the unreasonable effectiveness of the post-Newtonian approximation in gravitational physics. *Proc. Natl. Acad. Sci. U. S. A.*, 108(15):5938–5945.
- Xu, G. (1995). A New Parallel N-Body Gravity Solver: TPM. *ApJS*, 98:355.
- Yang, J., Wang, F., Fan, X., Hennawi, J. F., Davies, F. B., Yue, M., Banados, E., Wu, X.-B., Venemans, B., Barth, A. J., Bian, F., Boutsia, K., Decarli, R., Farina, E. P., Green, R., Jiang, L., Li, J.-T., Mazzucchelli, C., and Walter, F. (2020). Poniuu’ena: A Luminous  $z=7.5$  Quasar Hosting a 1.5 Billion Solar Mass Black Hole. *ApJL*, 897(1):L14.
- Yu, Q. (2002). Evolution of massive binary black holes. *MNRAS*, 331(4):935–958.
- Zel’dovich, Y. B. and Novikov, I. (1964). The Radiation of Gravity Waves by Bodies Moving in the Field of a Collapsing Star. *Sov. Phys. Dokl.*, 9:246.
- Zhang, X. and Lu, Y. (2017). On the Mean Radiative Efficiency of Accreting Massive Black Holes in AGNs And QSOs. *Sci. China Physics, Mech. Astron.*, 60(10):109511.
- Zhong, S., Berczik, P., and Spurzem, R. (2014). Super Massive Black Hole in Galactic Nuclei with Tidal Disruption of Stars. *ApJ*, 792(2):137.
- Zinchenko, I. A., Berczik, P., Grebel, E. K., Pilyugin, L. S., and Just, A. (2015). On the Influence of Minor Mergers on the Radial Abundance Gradient in Disks of Milky Way-like Galaxies. *ApJ*, 806(2):17.
- Zwick, L., Capelo, P. R., Bortolas, E., Vazquez-Aceves, V., Mayer, L., and Amaro-Seoane, P. (2021). Improved gravitational radiation time-scales II: spin-orbit contributions and environmental perturbations. *MNRAS*, 000:1–14.
- Zwick, L., Zwick, L., Capelo, P. R., Bortolas, E., Mayer, L., Amaro-Seoane, P., Amaro-Seoane, P., Amaro-Seoane, P., and Amaro-Seoane, P. (2020). Improved gravitational radiation time-scales: Significance for LISA and LIGO-Virgo sources. *MNRAS*, 495(2):2321–2331.



## COLOPHON

This thesis was typeset in  $\text{\LaTeX}$  using the integrated  $\text{\LaTeX}$  editing environment *Texmaker*. The graphics was prepared with the Python plotting library *Matplotlib* and with the *OpenOffice Impress* instrumentary. The bibliography was generated with *Mendeley*.